UNIVERSITY OF LEEDS

Scale Interactions of Organised Convection in West Africa

Fran Morris

Submitted in accordance with the requirements for the degree of PhD in School of Earth and Environment

The University of Leeds

Faculty of Environment

School of Earth and Environment

August 2023

Abstract

Moist convection drives energy and moisture transfer across a range of scales, from microscopic phase changes within clouds, to latent heat release over hundreds of kilometres in tropical cyclones and thunderstorms. The complex feedbacks arising from scale interactions between moist convective processes are a source of major uncertainty in global climate models, and moist convection often drives high-impact weather with devastating effects.

Mesoscale convective systems (MCSs) are an example of high-impact organised convection, large enough to generate their own mesoscale circulations which can modulate synoptic-scale weather patterns, which in turn can modulate initiation and development of MCSs, leading to complex feedbacks. In West Africa, MCSs are the primary source of seasonal precipitation variability. The region is also home to well-characterised synoptic systems such as the African Easterly Jet and African Easterly Waves, which makes it a perfect natural laboratory for investigating convection-circulation feedbacks.

The thesis focuses on the use of regional high-resolution simulations which can, to some extent, represent mesoscale convection explicitly without a deep convection parameterisation, referred to as 'convection-permitting' (CP) simulations. Throughout the thesis, several techniques are used to explore moist convective scale interactions using such CP simulations. The first results chapter explores one such technique to diagnose scale interactions: the circulation budget. The chapter examines how the closure of the circulation budget varies under changing environmental conditions, output timesteps, and spatial resolution. Having confirmed that instantaneous circulation budget terms are a valid quantification of atmospheric vorticity accumulation and tilting, the following chapter divides the terms into mean and anomalous components to understand the effects of different scales of atmospheric processes on synoptic-scale circulation in West Africa. It also highlights the representation of the dynamics of MCSs in the region and

the vortex structures associated with them in CP and parameterised simulations, and how such dynamical structures feed back on larger circulations. A third results chapter examines the statistics of the vortex structures and their potential for undergoing tropical cyclogenesis based on their size, vorticity intensity, and thermodynamic properties, highlighting another route for mesoscale convection to evolve into synoptic-scale systems.

The fourth results chapter utilises a dataset of tracked MCSs in a CP simulation and a parameterised simulation to examine the environments where MCSs are likely to be initiated, and how environments have been modulated by MCSs when they dissipate. Mechanisms for feedbacks between MCSs and themselves are explored, highlighting the roles of soil moisture feedbacks and low-level moisture in MCS initiation. The role of these mechanisms is further emphasised in the final results chapter, which compares CP simulations initialised with and without convective-scale atmospheric structures and evaluates how differences between their forecasts emerge. The comparison also demonstrates differences in the evolution of kinetic energy at different scales, and illustrates an transfer of energy upscale associated with the diurnal cycle of convection.

The work in this thesis demonstrates the capacity of convective-scale models for representing mesoscale-to-synoptic convective scale interactions, justifying further exploration of convective-scale models on larger domains despite the associated computational cost. Results could also inform development of parameterisations which account for the upscale impacts of organised mesoscale convection, thus improve atmospheric modelling across temporal and spatial scales.

Intellectual Property

The candidate confirms that the work submitted is her own and that appropriate credit has been given where reference has been made to the work of others.

This copy has been supplied on the understanding that it is copyright material and that no quotation from the thesis may be published without proper acknowledgement.

Material in chapter 5 (and some of the content of the literature review in chapter 2) is based on the following article: Morris, F. A., Schwendike, J., Parker, D. J., and Bain, C. L. (Accepted: 2023) How is synoptic-scale circulation influenced by the dynamics of mesoscale convection in convection-permitting simulations over West Africa? Journal of the Atmospheric Sciences. ISSN 0022-4928 (In Press)

The candidate is the lead author of the article. She performed the scientific analysis, wrote the manuscript, and generated the figures. Co-authors provided suggestions for the methods to be used, as well as editorial corrections to the manuscript.

Signed 

Acknowledgements

First of all, I would like to say a huge thank you to my supervisors: Juliane Schwendike, Doug Parker, and Caroline Bain. I want to thank them for their constant support and advice over the past four years, for dealing with every crisis of confidence, encouraging me to get the monster of a first paper submitted, and for allowing me to take advantage of so many different opportunities over the course of my PhD - as well as for teaching me that sometimes saying no to things is a good idea too.

Next I am incredibly grateful for the Atmosphere and Cloud Dynamics group in Leeds, for putting up with my lengthy emails and semi-mandatory semi-regular quizzes over several long years of semi-lockdown. I learned so much from so many ludicrously clever people and had a lot of fun doing so. It's very difficult to not just make an extensive list of everyone who has had the joy of explaining things to me, so that's what I will do: thank you Leo, Declan, Leif, Steef, Beth, Craig, Julia, Cathryn, John, Alan, Jonathan, Ben, and especially Sam for tolerating questions about simulations run several years ago. This thanks would of course not be complete without another shoutout to my supervisory Schwendike-squad siblings, Amethyst, Ashar, and Michael.

There are of course some incredible colleagues outside of Leeds who I would also like to thank: EODG, especially Adam and Isabelle, for the sage advice on academia, and without whom I almost certainly would not have even applied to do a PhD. Also, James Warner, whose brilliant and exciting warm-starting simulations over Africa are an essential cornerstone of the results in this thesis, and who I'm sure will continue to be recognised in many Africa MAC meetings to come.

I also want to say a huge thank you to my parents and siblings. I am incredibly grateful to have a brilliant, funny, and thoughtful sister and brother, and throughout my life I have been so lucky to have amazingly supportive parents. Without their help, I would never be where I

am today.

Finally, I'd like to thank the friends who kept me sane through it all: my housemate, Emily, who was there for me through every stressful moment of research and travel and chaos. The Mammoths, for the socials, the fun, and for reminding me to never take anything too seriously. Lauren, the best friend a girl could hope to have. And of course Sam, for everything.

Contents

1 Introduction **1**

2 Contemporary Understanding of Scale Interactions of Mesoscale Convection in West Africa and the Tropics **7**

2.1 Convection and Tropical Meteorology 8

2.2 Dynamics of Deep Tropical Convection 10

2.3 Mesoscale Convective Systems 11

2.3.1 Characteristics of MCSs 14

2.3.2 Tropical Cyclones 19

2.4 Meteorology of West Africa 20

2.5 Modelling Convection Over West Africa 23

2.6 Summary and Thesis Outlook 26

3 Data and Methodology **28**

3.1 The Met Office Unified Model 28

3.1.1 Hardy et al. (2021)'s Typhoon Nepartak Simulations 30

3.1.2 CP4-Africa 31

3.1.3 'Warm-Starting' Simulations 33

3.2 Storm Tracking 38

3.3 Observational data 39

3.3.1 JET2000 39

3.3.2 Global Precipitation Measurement (GPM) 39

3.4 ERA5 Reanalysis 40

4 Closing the Circulation Budget **41**

4.1 The Circulation Budget . . . 42
4.2 Data, Methodology, and Case Selection . . . 45
4.3 Closing the Circulation Budget . . . 49
4.4 Sensitivity to Region Size . . . 52
4.5 Impact of Friction . . . 54
4.6 Impact of Temporal Resolution . . . 56
4.7 Impact of Spatial Resolution . . . 60
4.8 Impact of Varying Both Spatial and Temporal Resolution . . . 64
4.9 Comparison to ERA5 Reanalysis . . . 66
4.10 Evaluation and Conclusions . . . 69

5 Circulation Budget Analysis of Scale Interactions in West Africa 72
5.1 Scale Separation Using the Circulation Budget . . . 73
5.2 Data and Domain selection . . . 74
5.3 Circulation Budget Diurnal Cycle over West Africa . . . 74
5.4 Dynamics of Mesoscale Precipitating Features . . . 81
5.4.1 Vortex Tilting by Precipitating Features on the Mesoscale . . . 81
5.4.2 Vorticity Accumulation by Precipitating Features on the Mesoscale . . . 91
5.4.3 Comparison to Observations . . . 94
5.5 Summary and Conclusions . . . 98

6 North Atlantic vortex populations in CP models 102
6.1 Data and methodology . . . 103
6.1.1 Data . . . 103
6.1.2 Vortex Identification . . . 104
6.1.3 Thermodynamic Metrics . . . 105
6.2 Vortex Statistics . . . 106
6.2.1 Vortex Frequency and Intensity . . . 106
6.2.2 Vortex Thermodynamics . . . 113
6.3 Conclusions and Future Outlook . . . 116

7 Initiation and dissipation environments of MCSs in CP4-Africa 119
7.1 MCS Populations in CP4 and R25 . . . 120

7.2 Initiation Environments of MCSs in CP4 and R25 121
7.2.1 Composites Illustrating Mean Initiation Environments 121
7.2.2 Statistics Describing Initiation Environments 124
7.3 Dissipation Environments of MCSs 125
7.4 Conclusions and MCS Feedbacks 125

8 Practical Implications of Convective Feedbacks in an NWP Model 139
8.1 Case Study 1: Forecast Initialised at 18 UTC on 17 June 2020 141
8.1.1 Explaining Differences Between Warm-Started and Cold-Started Forecasts 143
8.1.2 Upscale Impacts of Forecast Differences 149
8.2 Case Study 2: Forecast Initialised at 18 UTC on 7 August 2020 156
8.3 Overall Impact of Convective Feedbacks on Forecasts 162
8.4 Summary and discussion 166

9 Discussion and Conclusions 170
9.1 Answering the Research Questions 171
9.2 Summary of Key Results and Implications 176
9.3 Limitations and Future Outlook 178

References 181

List of Acronyms

4D-VAR	Four-dimensional data assimilation technique
AEJ	African Easterly Jet
AEW	African Easterly Wave
AMMA	African Monsoon Multidisciplinary Analysis
CMIP6	Coupled Model Intercomparison Project phase 6
CP	Convection-permitting
CP4	CP4-Africa, a convection-permitting climate configuration of the MetUM described in Stratton et al. (2018)
DA	Data assimilation
ECMWF	European Centre for Medium-range Weather Forecasts
ERA5	ECMWF reanalysis data product
ENDGame	Even Newer Dynamics for General atmospheric modelling of the environment, the MetUM's dynamical core from GA6.0 onwards
FSS	Fractional skill score
GA	Global Atmosphere, a type of MetUM configuration for global domains
GCM	Global climate model
GL	Global Land, a type of MetUM configuration for the land surface model associated with global domains
GPM	Global Precipitation Measurement
HIW	High-impact weather
IFS	Integrated Forecasting System, ECMWF's weather and climate model
IMERG	Integrated Multi-satellitE Retrievals for GPM retrieval

IPCC	Intergovernmental Panel on Climate Change
JULES	Joint UK Land Environment Simulator
LAM	Local area model
LBC	Lateral boundary condition
LHS	Left-hand side
MetUM	Met Office Unified Model
MCS	Mesoscale convective system
MetUM	Met Office Unified Model
MJO	Madden-Julian Oscillation
MOGREPS-G	Met Office Global Ensemble Prediction System
NWP	Numerical weather prediction
OLR	Outgoing longwave radiation
PC2	Prognostic cloud 2, a cloud scheme
PV	Potential vorticity
R25	A companion climate simulation to CP4, with a deep convection parameterisation, described in Stratton et al. (2018)
RAL	Regional Atmosphere-Land, a type of MetUM configuration for nested regional domains
RCP	Representative Concentration Pathway
RHS	Right-hand side
RIJ	Rear inflow jet
SST	Sea-surface temperature
TAM	Tropical Africa Model, an operational CP configuration of the MetUM running over tropical Africa
TC	Tropical cyclone
TEJ	Tropical Easterly Jet
UTC	Coordinated universal time
WAM	West African Monsoon

List of Figures

2.1 Figure 10 from Feng et al. (2021), showing annual averages of (a) MCS frequency, (b) total MCS precipitation, and (c) fraction of precipitation associated with MCSs, using their dataset of tracked MCSs from 2001 to 2019. Dark grey contours indicate orography above 1000 m. Regions where missing brightness temperature data made MCS tracking impossible are indicated by light grey contours and labelled. 13

2.2 Figure 14 from Houze (2004). Schematic of an archetypal 'squall line with trailing stratiform'. The mesoscale flows that characterise its dynamics are shown as black arrows. Intermediate and strong radar reflectivity is indicated by medium and dark shading respectively, and 'H' and 'L' denote pressure highs and lows in the system respectively. 14

2.3 Based on figures from Moncrieff (1992). (a) Schematic of "triple branch circulation" of storm-relative streamlines within in a westward-propagating organised convective system. An overturning updraught at the front of the storm and a jump updraught flowing from the front to the rear of the storm are illustrated in red, and the downdraughts in blue. (b) Normalised vertical profiles of momentum flux, $\Lambda = \frac{\langle \rho u_m w_m \rangle}{\rho U_0^2}$. u_m and w_m are the storm-relative zonal and vertical velocities, ρ is the density of the inflowing air, and U_0 is the relative velocity of the inflow. Shown for triple branch circulation with an overturning updraught and overturning downdraught (dashed line), circulation without an overturning updraught (solid line), and circulation without an overturning downdraught (dotted line). 18

3.1 Map showing illustration of the CP4-Africa domain, defined in Stratton et al. (2018). The filled contours show the orography of the terrain. The thick black line outlines the CP4 regional domain. 31

3.2 A flowchart illustrating the process of warm-starting a new regional simulation run (cycle n+1) using the previous global and regional runs (cycle n). 35

3.3 Domain of warm-starting experiment shown by thick black line. 37

4.1 Schematic illustrations of the processes that cause changes in circulation via (a) vorticity accumulation and (b) vortex tilting. In (b), an example shear profile is illustrated by the dark red arrows; this does not necessarily reflect the shear in the Maritime Continent (the region that the case study focuses on) at all times. Instead it represents a shear profile typical of background flow in West Africa, the focus of the thesis as a whole. 44

4.2 A snapshot of absolute vorticity (η, in $s^{-1} \times 10^5$) at 700 hPa, at 01 UTC on 05 July 2016, as simulated by a MetUM ensemble member. Case study regions are outlined by the black (8×8 °), blue (6×6 °), and cyan (4×4 °) boxes labelled A (Typhoon Nepartak), B (an oceanic MCS), C (an MCS over land), and D (oceanic region with least active convection). 46

4.3 The circulation budget terms calculated around the 8×8 ° black boxes labelled a–d in figure 4.2, at 01 UTC on 05 July 2016 in the simulation. The thinner coloured lines indicate the circulation budget terms calculated at each pressure level: the vorticity accumulation term (blue), the tilting term (orange), and the friction term (green). The thick black line is the sum of the three RHS terms. The thick grey line is the circulation tendency $\frac{\partial \Gamma}{\partial t}$ at the same time around the box, calculated at time output interval Δt=5 minutes. 50

4.4 Ratio of the variance of residual (RHS budget terms subtracted from LHS $\frac{\partial \Gamma}{\partial t}$ circulation tendency) to variance of the signal (LHS circulation tendency), σ_r^2/σ_s^2, for each time that the circulation budget was calculated over the four regions illustrated in figure 4.2, for the three sizes of box, (a) 8×8°, (b) 6×6°, and (c) 4×4° boxes. Different coloured lines represent the different regions (mid-blue for the TC region, purple for the MCS, green for the land, and cyan for the inactive ocean). The solid lines show the variance ratio excluding the friction term on the RHS, and the dashed lines show the calculations including the friction term. A solid grey line indicates where $\frac{\sigma^2(\text{residual})}{\sigma^2(\text{signal})}$=1, the point at which variation in the difference between the signals is indistinguishable from variation in the signal itself. Note the difference in y-axis scale across the three plots. 51

4.5 Ratios of the variance of the residual (RHS - LHS of the circulation budget equation) to the variance of the signal (LHS of the circulation budget), σ_r^2/σ_s^2, for the regions (a)–(d) depicted in figure 4.2 in corresponding subfigures, and different domain sizes for each regions illustrated by the differently-coloured bars: black for the 8×8° regions, blue for the 6×6° regions, and cyan for the 4×4° regions. 53

4.6 Similarly to figure 4.3, circulation budget terms not including friction calculated around the 8×8° black boxes labelled (a)–(d) in figure 4.2, at 01 UTC on 05 July in the simulation. The thinner coloured lines indicate the circulation budget terms calculated at each pressure level: the vorticity accumulation term (blue) and the tilting term (orange). The thick black line is the sum of the two terms. The thick grey line is the circulation tendency $\frac{\partial \Gamma}{\partial t}$ at the same time around the box. 55

4.7 Ratios between the variance of the residuals between the RHS and LHS of the circulation budget equation, and the variance of the RHS of the circulation budget, σ_r^2/σ_s^2, calculated for the four 8×8° regions (a-d) shown in figure 4.2. 57

4.8 Circulation tendency for various Δt calculated around the 8×8° black boxes labelled a–d in figure 4.2, at 01 UTC on 05 July in the simulation. The dashed black line indicates the RHS sum of circulation budget terms while the coloured lines represent different Δt as illustrated in the key in subfigure (d). 58

4.9 Mean of ratios of variance of residual (LHS-RHS) to variance of signal (RHS) for different Δt on the LHS, σ_r^2/σ_s^2, taken over the 12 time periods the circulation budget was calculated at. Circulation budget terms and circulation were calculated around the regions (a)–(d) shown in figure 4.2. 59

4.10 RHS of circulation budget profiles calculated for different spatial resolutions Δx, shown for the time snapshotted and regions a–d outlined in figure 4.2. The native grid resolution is the highest resolution shown, 0.04 °. 62

4.11 Mean of ratios of variance of residual (LHS-RHS) to variance of signal (RHS) for different Δx on the LHS, σ_r^2/σ_s^2, taken over the 12 time periods the circulation budget was calculated at. Circulation budget terms and circulation were calculated around the regions a–d shown in figure 4.2, at the respective grid resolutions Δx corresponding to each bar. The native grid resolution is the highest resolution shown, 0.04 °. 63

4.12 Mean of ratios of variance of residual (LHS-RHS) to variance of signal (RHS), σ_r^2/σ_s^2, for different Δx (x-axis) and Δt (y-axis), taken over the 12 time periods the circulation budget was calculated at, around the regions (a)–(d) shown in figure 4.2. 65

4.13 A snapshot of absolute vorticity (η, in $s^{-1} \times 10^5$) at 700 hPa, at 01 UTC on 05 July 2016, as calculated by ERA5 reanalysis. Case study regions are outlined by the black (8×8 °), blue (6×6 °), and cyan (4×4 °) boxes labelled A (Typhoon Nepartak), B (an oceanic MCS), C (an MCS over land), and D (oceanic region with least active convection). 66

4.14 Similarly to figure 4.6, circulation budget terms from the ERA5 reanalysis, not including the friction term, calculated around the 8×8 ° black boxes labelled (a)–(d) in figure 4.13, at 01 UTC on 05 July in the simulation. The thinner coloured lines indicate the circulation budget terms calculated at each pressure level: the vorticity accumulation term (blue) and the tilting term (orange). The thick black line is the sum of the two terms. The thick grey line is the circulation tendency $\frac{\partial \Gamma}{\partial t}$ at the same time around the box. 67

4.15 Mean of ratios of variance of residual (LHS-RHS) to variance of signal (RHS) σ_r^2/σ_s^2 in ERA5, taken over the 12 time periods the circulation budget was calculated at, around the regions (a)–(d) shown in figure 4.13. 68

5.1 Orography (filled contours) and mean rainfall (line contours, labelled in mm h^{-1}) in July and August 1998-2006 for (a) CP4 and (b) R25. The region of interest analysed here is outlined by the black box. 75

5.2 Orography (filled contours) and mean zonal wind (line contours, labelled in m s^{-1}) in July and August 1998-2006 for CP4 (red) and R25 (blue). The region of interest analysed here is outlined by the black box. 76

5.3 Mean diurnal cycle (repeated for two full days) of (a-b) circulation (normalised by area) Γ (s^{-1}; filled contours) and (c-d) normalised circulation tendency $\frac{\partial \Gamma}{\partial t}$ ($s^{-1}h^{-1}$; filled contours) around the synoptic region illustrated in figure 5.1. The mean is calculated over all points in the border of the selected synoptic region for each time in the diurnal cycle. Also shown is rainfall fraction (fraction of grid cells with a precipitation rate of 1mm h^{-1} or greater; black solid line) and estimated convective boundary layer height (dashed black line). (a) and (c) show these features in CP4, (b) and (d) in R25. The diagram also indicates the regions selected for "afternoon" (12–18 UTC) and "overnight" (21–3 UTC) convection in lined and dotted hashed regions respectively. 77

5.4 Mean diurnal cycle (repeated for two full days) of circulation budget terms. The mean is calculated over all points in the border of the selected synoptic region (black rectangle in figures 5.1 and 5.2) for each time in the diurnal cycle. The 'anomalous' terms are the integral of deviations from these mean values. (a-b) "Synoptic accumulation" term $-\oint_C \bar{\boldsymbol{u}}\bar{\eta} \cdot \hat{\boldsymbol{n}} dl$, (c-d) "Anomalous accumulation" $-\oint_C \boldsymbol{u'}\eta' \cdot \hat{\boldsymbol{n}}\boldsymbol{dl}$, (e-f) "Synoptic tilting" $\oint_C \bar{\omega}\hat{\boldsymbol{k}} \times \frac{\partial \bar{\boldsymbol{u}}}{\partial p} \cdot \hat{\boldsymbol{n}} dl$, (g-h) "Anomalous tilting" $\oint_C \omega'\hat{\boldsymbol{k}} \times \frac{\partial \boldsymbol{u'}}{\partial p} \cdot \hat{\boldsymbol{n}} dl$. The left column shows results for CP4 and the right column shows results for R25. 78

5.5 Composites of tilting term integrand $\left(\omega \frac{\partial v}{\partial p}\right)$ anomaly across a meridional (north-south) cross-section of 500 km centred on grid cells precipitating at a rate of 1mm h^{-1} or greater. The composited integrands contribute to the tilting integral through the eastern and western edges of the box. 84

5.6 Composites of tilting term integrand $\left(\omega \frac{\partial u}{\partial p}\right)$ anomaly across a zonal (east-west) cross-section of 500 km centred on grid cells precipitating at a rate of 1mm h^{-1} or greater. The composited integrands contribute to the tilting integral through the northern and southern edges of the box. 85

5.7 Composite of mean fields in a zonal cross-section extending 250 km to the west and east around grid cells precipitating at a rate of 1mm h^{-1} or greater, as averaged through afternoon convection 12–18 UTC (top row) and overnight convection 21–3 UTC (bottom row), for CP4 (left column) and R25 (right column). Vertical velocity in Pa s^{-1} is shown by filled contours. Vector arrows show storm-relative wind speeds such that the zonal and vertical components are on the same scale in the plane of the cross section. The thick overlaid arrows are schematic illustrations of the jump updraughts (yellow), overturning updraughts (pink) and overturning downdraughts (purple), with the hatched region showing the approximate height of the AEJ. 86

5.8 Vertical profiles of the mean product of composited storm-relative zonal velocity u_m and vertical velocity ω_m for CP4 (red lines) and R25 (blue lines) through afternoon convection 12–18 UTC (solid lines) and overnight convection 21–3 UTC (dashed lines). The mean values are calculated at each pressure level for the entire width of the zonal composites in figures 5.9–5.7. The hatched region represents the typical height of the AEJ. 89

5.9 Composites of relative vorticity anomaly (filled contours) and divergence anomaly (line contours) across a meridional (north-south) cross-section of 500 km around grid cells precipitating at a rate of 1 mm h^{-1} or greater. Divergence anomaly is labelled in s^{-1} $\times 10^6$; dashed lines represent negative values (convergence). Thick black dot-dash line shows the product of the divergence and vorticity anomalies, averaged meridionally across the composite. 92

5.10 Cross-section of dropsonde profiles of (a) zonal and (b) meridional velocity (m s^{-1}) for flight A781 on the JET2000 campaign. The position of the storm that the flight travelled behind is marked at 11 ° N with a black dashed line. The positions at which dropsondes were dropped are shown by the black pips at the top. 95

5.11 (a) Meridional cross-section of the relative vorticity term contributed by latitudinal change in zonal velocity, $-\frac{\partial u}{\partial y}$ (shading), and the horizontal divergence from meridional velocity variation $\frac{\partial v}{\partial y}$ (line contours, labelled in s^{-1} $\times 10^6$), spanning 500 km centred on the storm at 11 ° N (black dashed line). (b) Meridional cross-section of relative vorticity and divergence anomaly in composites around grid cells precipitating at a rate > 1mm h^{-1} in CP4 at 9–12 UTC over the same pressure range as (a). (c) As in (b) but for R25. 96

5.12 (a) Vertical profile of convective momentum flux $< u_m \omega_m >$ measured by the dropsondes in the JET2000 campaign at 11 ° N. (b) Vertical profile of convective momentum flux $< u_m \omega_m >$ calculated using storm-relative winds from composites around grid cells precipitating at a rate of 1mm h^{-1} or greater at 9–12 UTC in CP4 (red line) and R25 (blue line). 97

5.13 Schematic illustrating the effects of vorticity accumulation and vortex tilting linked to convection on the circulation budget. Top row shows synoptic (diurnal mean) effects and bottom row shows anomalous effects. Storms are illustrated in the location in the box where they impact each term. Red (blue) arrows indicate reinforcement of (anti)cyclonic circulation. Objects, and illustrative arrows, are not to scale. 100

6.1 Snapshot of 850 hPa relative vorticity on 5th September 2006 at 15 UTC (filled contours) in (a) CP4 and (b) R25. (Note that the plot does not correspond to the actual date since the simulations are free-running climate models). Vortices identified with kinematic vorticity number $W_k > 1$ are outlined in black contours. Thick black outline indicates regions of interest over land and sea. 104

6.2 Histogram showing frequency of vortices, on a logarithmic scale, with different values of area. Median values for each model and region are shown by the vertical lines. Dashed darker lines represent CP4 and the lighter, solid lines represent R25. Sea region is shown in blue and land in red. Grey line indicates an area of 25,000 km^2. 106

6.3 Histogram showing frequency of vortices, on a logarithmic scale, with different values of mean relative vorticity at 850 hPa (left column), mean specific humidity at 850 hPa (middle column), and mean total column water (TCW; right column). Dashed darker lines represent CP4 and the lighter, solid lines represent R25. Sea region is shown in blue and land in red. The vertical lines indicate the respective medians of each distribution (for relative vorticity, medians are calculated for both positive and negative vortices). The top row indicates statistics for all vortices, and the bottom row limits the population to vortices with an area of 25,000 km^2 or greater. 108

6.4 2-D histogram showing the ratio of number vortices in the land region to number of vortices in the sea region in given bins of area (x-axis) and mean relative vorticity (y-axis), for (a) CP4 and (b) R25. Colours indicate whether the ratio is greater than 1.2 (more vortices over land, green), between 0.8 and 1.2 (around the same number of vortices over land and ocean, orange), or less than 0.8 (more vortices over sea, blue). The opacity of each box is proportional to the total frequency of vortices in each box in both simulations. Bins are only shown if there are at least 10 total vortices over land and sea in the given bin. The grey dashed lines illustrate levels of constant circulation. 109

6.5 Composites of the relative vorticity anomaly (filled contours, s^{-1}) around centres of positive vortices at the time that the vortices identified using the $W_k > 1$ threshold over land, and composited around the same location as time goes on, thus showing the average vorticity field evolution around a given identified vortex. The centroid of the identified vortex is at coordinate (0,0). Vortices in CP4 are shown in the left column and R25 are shown in the right column. 111

6.6 Composites of the relative vorticity anomaly (filled contours, s^{-1}) and vertical velocity (line contours; Pa s^{-1}) in a 500-km north-south (meridional) cross-section centred around grid cells where the rainfall rate exceeds 1 mm h^{-1}. 112

6.7 Histograms showing the frequency of vortices with different values of $-|V_L^T|$ (left column) and $-|V_U^T|$ (right column) for all vortices (top row) and only vortices with area $> 25{,}000\,\mathrm{km}^2$. The dashed darker lines indicate vortex populations in CP4 and the lighter, solid lines indicate vortex populations in R25. Sea region is shown in blue and land in red. The vertical lines indicate the medians of corresponding distributions. 114

6.8 Two-dimensional histograms with $-|V_L^T|$ on the x-axis and $-|V_U^T|$ on the y-axis, for the vortices with area $> 25{,}000\,\mathrm{km}^2$ identified over the land (left column) and sea (right column) in CP4 (top row) and R25 (bottom row). The fill colour of each box represents fraction of the vortices which lie in each box of the histogram on the colorbar. 115

7.1 Density of initiations (top row) and tracks (bottom row) of MCSs in CP4 (left column) and R25 (right column), indicated by filled contours. The grid orography for each simulation is shown in labelled line contours. 129

7.2 Left column shows composites of specific humidity anomaly (filled contours) and horizontal divergence anomaly (line contours, labelled in units of $\mathrm{s}^{-1} \times 10^5$) along zonal (east-west) cross-sections through MCS centroids at initiation in CP4 (top row) and R25 (bottom row). Right column shows, instead of initiation centroids, composites around random points at the times of initiations of storms. 130

7.3 Composites of relative vorticity anomaly (filled contours) and wind anomaly (vectors) along zonal (east-west) cross-sections through MCS centroids at and leading up to time of initiation in CP4 (top row) and R25 (bottom row). 131

7.4 Composites of relative vorticity anomaly (filled contours) and wind anomaly (vectors) along meridional (north-south) cross-sections through MCS centroids at and leading up to time of initiation in CP4 (top row) and R25 (bottom row). 132

7.5 Composites of soil moisture anomaly (filled contours) in 500-km squares centred on MCS centroids at and leading up to time of initiation in CP4 (top row) and R25 (bottom row). 132

7.6 Composites of land surface temperature (LST; filled contours) in 500-km squares centred on MCS centroids at and leading up to time of initiation in CP4 (top row) and R25 (bottom row). 133

7.7 Composites of land surface temperature (LST; filled contours) in 500-km squares centred on random points at and leading up to time of each MCS initiation in CP4 (top row) and R25 (bottom row). 134
7.8 Maximum value of relative vorticity anomaly ($\zeta \times 10^5$) in 500-km squares centred on centroid of MCS at its initiation leading up to time of each MCS initiation in CP4 (orange lines) and R25 (blue lines). 135
7.9 Variance of soil moisture anomaly in 500-km squares centred on centroid of MCS at its initiation leading up to time of each MCS initiation in CP4 (orange lines) and R25 (blue lines). 135
7.10 Composites of relative vorticity anomaly (filled contours) and wind anomaly (vectors) along zonal (east-west) cross-sections through the centroid of MCS at dissipation and for 3 and 6 hours after dissipation at the same point, in CP4 (top row) and R25 (bottom row). 136
7.11 Composites of specific humidity anomaly (filled contours) and wind anomaly (vectors) along zonal (east-west) cross-sections through the centroid of MCS at dissipation and for 3 and 6 hours after dissipation at the same point, in CP4 (top row) and R25 (bottom row). 137
7.12 Composites of anomalous MCS track density within the 24 hours before initiation around centroids at MCS initiation (left column) and random points at the time of MCS initiations (right column) in CP4 (top row) and R25 (bottom row). The composite excludes centroids of storms as they are being composited around. . . 138

8.1 Three-hourly averages of precipitation rate at 12-hour intervals (represented by each row) from 18 UTC on 17 June 2020 onwards. The left column shows the Global Precipitation Measurement (GPM) final-run gridded product. The middle and right columns show the precipitation in the warm- and cold-started simulations respectively, both regridded to the same resolution as GPM. 142
8.2 Relative vorticity ζ at 700 hPa at forecast hours T+0 (top row), T+3 (middle row), and T+6 (bottom row), for the cold-start simulation (right column) and closest approximations for warm-started output (left column), after initialisation at 18 UTC on 17 June 2020. Rainfall contours at 0.5 $\mathrm{mm\,h^{-1}}$ are shown by the black line contour. 144

8.3 Wind at 925 hPa (shown by black vectors) and relative humidity at 925 hPa at T+18 (top row), T+21 (middle row), and T+27 (bottom row), for the cold-start simulation (right column) and closest approximations for warm-started output (left column) after initialisation at 18 UTC on 17 June 2020. Rainfall contours at 0.5 mm h^{-1} are shown by the black line contour. 146

8.4 Soil moisture at 0.05 m below the surface at T+12 (top row), T+24 (middle row), and T+36 (bottom row), for the cold-started (right column) and warm-started (left column) simulations after initialisation at 18 UTC on 17 June 2020. Rainfall contours at 0.5 mm h^{-1} are shown by the black line contour. 148

8.5 Wind vectors (black vectors and greyscale shading) representing the difference between the warm- and cold-started simulations at T+13 (top row), T+25 (middle row), and T+37 (bottom row) after initialisation at 18 UTC on 17 June 2020 for 700 hPa and 200 hPa (right column). The warm-started simulation's 3-hourly mean rainfall rate is shown by the coloured contours. 150

8.6 Hovmöller plots of curvature vorticity (filled contours) averaged over (a–b) 15–22.5 ° N at 850 hPa and (c–d) 5–12.5 ° N at 700 hPa, plotted for each longitude against forecast hour, for the warm-started simulations (left column) and cold-started simulations (right column). The location of AEWs in longitude and time are plotted by black lines. 151

8.7 Spectral energy density plotted against wavenumber on a log-log plot, for the first four forecast hours (indicated by row; T+1, 4, 7, and 10 for the warm-started simulation and T+0, 3, 6, and 9 for the cold-started simulation) after initiation of the simulation at 18 UTC on 17 June 2020. Spectra are shown at three different pressure levels (indicated by column; 850 hPa, 700 hPa, and 200 hPa), for the warm-started and cold-started initialisations (orange and blue lines respectively) as well as forecasts at the same time from the closest driving global model initialisation (grey lines). The spectra are smoothed using a variable-size uniform filter along their length to limit noise (raw signals are shown in faded colours behind the lines). Reference lines showing the archetypal $E(k) \sim k^{-\frac{5}{3}}$ relationship (with arbitrary scalings to approximate observed amplitudes in the plots) are in black. 153

8.8 Rate of change of the logarithm of spectral energy density (filled contours) plotted against log(wavelength) on the x-axis and forecast hour on the y-axis for the forecast initialised at 18 UTC on 17 June 2020, with the warm-started regional forecast (left column), cold-started regional forecast (middle column), and global model (right column). Global model spectra are only shown above the model's native grid spacing (≈33 km). 154

8.9 Three-hourly averages of precipitation rate at 12-hour intervals (represented by each row) from 18 UTC on 7 August 2020 onwards. The left column shows the Global Precipitation Measurement (GPM) final-run gridded product. The middle and right columns show the precipitation in the warm- and cold-started simulations respectively, both regridded to the same resolution as GPM. 157

8.10 Hovmöller plots of curvature vorticity (filled contours) averaged over (a–b) 15–22.5 ° N at 850 hPa and (c–d) 5–12.5 ° N at 700 hPa, plotted for each longitude against forecast hour since initialisation at 18 UTC , for the warm-started simulations (left column) and cold-started simulations (right column). The location of African Easterly Waves (AEWs) in longitude and time are plotted by black lines. 158

8.11 Rate of change of the logarithm of spectral energy density (filled contours) plotted against log(wavelength) on the x-axis and forecast hour on the y-axis for the forecast initialised at 18 UTC on 7 August 2020, with the warm-started regional forecast (left column), cold-started regional forecast (middle column), and global model (right column). Global model spectra are only shown above the model's native grid spacing (≈33 km). 159

8.12 As for figure 8.3, for the initialisation at 18 UTC on 7 August 2020. Wind vectors at 925 hPa (shown by black vectors) and relative humidity at 925 hPa at T+3 (top row), T+6 (middle row), and T+9 (bottom row), for the cold-start simulation (right column) and closest approximations for warm-started output (left column). Rainfall contours at 0.5 mm h^{-1} are shown by the black line contour. 160

8.13 Soil moisture at 0.05 m below the surface at T+12 (top row), T+24 (middle row), and T+36 (bottom row), for the cold-started (right column) and warm-started (left column) simulations after initialisation at 18 UTC on 17 June 2020. Rainfall contours at 0.5 mm h^{-1} are shown by the black line contour. 161

8.14 Plotted as in figure 8.7 energy density plotted against wavenumber on a log-log plot over the full three-month experiment, for the first four forecast hours (indicated by row; T+1, 4, 7, and 10 for the warm-started simulation and T+0, 3, 6, and 9 for the cold-started simulation) at three different pressure levels (indicated by column; 850 hPa, 700 hPa, and 200 hPa), for the warm-started and cold-started initialisations (orange and blue lines respectively) as well as forecasts at the same time from the closest driving global model initialisation (grey lines). The spectra are smoothed using a variable-size uniform filter along their length to limit noise (raw signals are shown in faded colours behind the lines). Reference lines showing the archetypal $E(k) \sim k^{-\frac{5}{3}}$ relationship (with arbitrary scalings to approximate observed amplitudes in the plots) are in black. 163

8.15 Rate of change of the logarithm of total spectral energy density across all initialisations at 18 UTC (filled contours) plotted against log(wavelength) on the x-axis and forecast hour on the y-axis for warm-started (left column) and cold-started (central column) initialisation, with the difference between the two in the right column 165

8.16 Rate of change of the logarithm of total spectral energy density across all initialisations at 18 UTC (filled contours) plotted against log(wavelength) on the x-axis and forecast hour on the y-axis for warm-started and cold-started CP simulations, driving model simulations, and the difference between the warm-started and cold-started simulations and the driving simulation (right two columns). Spectra only shown above native resolution of driving simulation ($\approx 33\,\text{km} \approx 10^{4.5}\,\text{m}$). 167

List of Tables

5.1 Number of grid cells precipitating at a rate of 1mm h^{-1} or greater along each edge of the synoptic box for the two regimes of convection. 82

Chapter 1

Introduction

The motions of Earth's atmosphere span a vast range of scales, from phase changes at the microscopic scale of cloud droplets to clusters of storms spanning hundreds of kilometres across continents and oceans. Connecting these scales is the process of moist convection. While dry convection is a ubiquitous means of heat transfer within any body containing fluids across the universe, the addition of water and its phase changes to the process adds complexity that builds the unique properties of Earth's weather and climate systems. The latent heat release associated with condensation in moist ascent drives some of the most intense and high-impact weather (HIW) on the planet in the form of thunderstorms and tropical cyclones (TCs), as well as controlling planetary-scale moisture and temperature distributions. The forecasting of moist convection is therefore essential for not only short-range numerical weather prediction (NWP), but for the accurate representation of atmospheric dynamics in global climate models (GCMs). However, moist convection remains one of the major sources of uncertainty in climate sensitivity (Stevens and Bony 2013; Sherwood et al. 2014).

Moist convective processes drive runaway ascent which results in the formation of deep cumulonimbus clouds associated with HIW. On scales of hundreds of kilometres, moist convection can become 'organised', a term which refers to systems that are longer-lived than an individual convective updraught (with a typical lifespan of around half an hour) and grow upscale in a systematic way to form mesoscale (or larger) structures. Examples of organised convection include mesoscale convective systems (MCSs) and supercell thunderstorms. Organised convection can and does occur all over Earth, but in this thesis, the focus is on the behaviour of organised mesoscale convection in the tropics.

One meteorological definition of the tropics is the region of Earth where variability in weather is modulated predominantly by the diurnal cycle rather than by seasonal changes (the definition results in a complex map, so other methods are often used; see Galvin 2016). Strong latent heating from solar radiation and high atmospheric moisture content drive moist convection that occurs on a daily basis, typically peaking in the local mid-afternoon. Often, such convection organises into coherent systems which can last beyond the diurnal afternoon precipitation peak and persist overnight.

Contemporary understanding of tropical organised convection is limited, however, for a number of reasons. Firstly, historically there are far fewer observations of tropical weather, so the development of tropical meteorology knowledge lags significantly behind understanding of midlatitude meteorology (Bechtold 2019). Furthermore, long-term challenges exist for sustainable operational forecasting in tropical regions, such as inconsistent communications with and maintenance of in-situ sensors (Parker et al. 2008). It remains challenging to facilitate field campaigns and other high-quality measurements of tropical weather due to economic, political, and logistical constraints. The resulting lack of in-situ observations means that the internal dynamics of tropical convection are somewhat under-explored.

Secondly, weather that is dominated by convection is inherently more challenging to predict than midlatitude weather systems. In the midlatitudes, it is possible to reduce the equations describing the atmosphere by applying the quasi-geostrophic approximation, but the approximation relies on the assumption that the Coriolis parameter is large compared to inertial forces, which is not true in the tropics as the Coriolis parameter becomes negligible (Holton and Hakim 2013c). Under quasi-geostrophy, it is possible to understand large-scale atmospheric motions using the framework of potential vorticity, and consider convection-related disturbances as a source of potential vorticity (e.g. Plant et al. 2003). In the tropics, no similar framework exists, and as a result the interactions between convection and the larger-scale circulations are more difficult to diagnose. Furthermore, the timescales of convection are much faster than the slow-moving quasi-geostrophic motions of synoptic-scale features in the midlatitudes.

Thirdly, and crucially, there is evidence that there are feedbacks involved in the interactions between mesoscale organised convection which are yet to be comprehensively understood, in part due to the aforementioned two challenges. Satellite observations indicate that convection couples to modes of synoptic- and planetary-scale variability in the tropical atmosphere, such as

African Easterly Waves (AEWs; Mekonnen et al. 2006), equatorial waves (Kiladis et al. 2009), and the Madden-Julian Oscillation (MJO; Wheeler and Hendon 2004). However, mechanisms for these couplings remain uncertain. To accurately forecast convection, it is necessary to understand its impact on synoptic systems and further feedbacks on subsequent convection, by interrogating the scale interactions between these features.

Without understanding scale interactions between synoptic systems and mesoscale convection, the quality of NWP forecasts in the tropics is limited. Forecasting convection with the correct timing, location, and intensity has long been a challenge in the tropics, and while skill has significantly increased there are still advances to be made in operational forecasting. In the tropics, MCSs are an example of poorly-forecasted HIW. MCSs are organised convective thunderstorms on the order of hundreds of kilometres, often associated with sustained intense precipitation and strong winds (Houze 2018). MCSs can cause flooding and high winds which lead to property damage, injury, and loss of life. Furthermore, forecasting precipitation, large proportions of which can come from MCSs (Feng et al. 2021), is essential for the agricultural industries in tropical regions. For example, the prediction of monsoon onset will significantly modulate planned planting and harvesting times (Kniveton et al. 2009; Dunning et al. 2018). When such a high proportion of the season's rainfall can come from just a handful of MCSs, forecasting each one correctly is crucial to know whether a year's rainfall will be abundant or if the season will be a drought (Vellinga et al. 2016). TCs are another example of HIW events, also causing strong winds and torrential rainfall, particularly to coastal regions. While TC forecasting has improved significantly in the past two decades, predicting their formation, intensity, and intraseasonal variability remains a major challenge of tropical forecasting. Capturing interactions between convection across scales during TC genesis and development is crucial to improving predictions.

The value of understanding scale interactions of convection is not just limited to short- and medium-range forecasting. Cloud-circulation feedbacks are also a major source of uncertainty in GCMs. Projections of precipitation under different warming scenarios in the tropics vary between simulations, and in Africa some scenarios are not even constrained within a consistent decrease or increase in precipitation in a warming climate (Moon and Ha 2020). The projections are sensitive to parameterisations of convection, which are required to represent the sub-grid-scale processes of convection in GCMs with resolutions of tens of kilometres.

In recent years, increases in available computational power have allowed higher-resolution models to be run at regional and even global scales (Stevens et al. 2019). Such models are referred to as 'convection-permitting' (CP), 'convective-scale', or 'storm-resolving' simulations. CP simulations can, to some extent, explicitly resolve updraughts of mesoscale convection. Therefore, the deep convection parameterisation schemes which are necessary to resolve sub-gridscale processes in coarser resolution models can be switched off. While CP models do not resolve shallow convection, and even the representation of deep convection is limited (Prein et al. 2015; Kendon et al. 2021), the models may still provide valuable insight into the dynamics of tropical convection and the interactions between mesoscale convection and synoptic-scale systems. However, there remain practical challenges to the use of CP models for operational forecasting, such as errors introduced in initialisation in high-resolution simulations due to challenges in assimilating data across multiple scales, and a requirement for high-quality downscaling of driving models to provide realistic boundary conditions (Hu et al. 2023). Furthermore, while it is now possible to run global-scale high-resolution simulations, the process has a significant computational and therefore carbon cost. Computing power might be more effectively utilised in other areas of meteorological prediction and research, such as running ensemble simulations or developing parameterisations. The need to run computationally-demanding CP simulations must be justified.

This thesis aims to make progress towards an understanding of how mesoscale organised convection interacts with synoptic systems in the tropics. The thesis particularly focuses on the dynamics of West Africa, where in the summer months the surface temperature gradient between the moist Sahel and dry Sahara produces a midlevel atmospheric jet (African Easterly Jet; AEJ) along which barotropic-baroclinic disturbances (AEWs) propagate, which can be intensified and triggered by MCSs. The region is a useful natural laboratory to examine scale interactions between such synoptic-scale disturbances and MCSs. Knowledge of the dynamics of MCSs, the conditions conducive to their formation, and how synoptic-scale systems such as atmospheric jets and monsoon winds respond to them could be applied to other tropical regions such as South America, South East Asia, and other parts of Africa. The thesis also has a focus on utilising the outputs of CP models to understand the added value such simulations can provide for interrogating the mesoscale dynamics of convection, to justify whether the computational cost of running future high-resolution simulations is worthwhile or necessary.

The questions that the thesis aims to address are as follows:

1. How can the modulation of synoptic-scale atmospheric dynamics by organised mesoscale convection be measured?
2. How does organised convection in West Africa modulate synoptic-scale dynamics both locally (e.g. AEJ, AEWs, monsoon wind) and downstream into the Atlantic Ocean (e.g. modulating TC genesis)?
3. Which environmental conditions, on the mesoscale and on larger scales, affect the initiation and development of MCSs in West Africa?
4. How do MCSs in West Africa interact with each other across temporal and spatial scales?

To answer most of these questions, it is necessary to compare the meso- and synoptic-scale environments in situations where organised convection does and does not exist. As a proxy for the existence or lack of organised convective systems, one can examine simulations where organised convection is represented more realistically (i.e. CP simulations) and less realistically (traditional simulations with deep convection parameterisation, which do not often accurately represent the dynamics of convection compared to observations). Specifically, much of the analysis presented uses output from regional configurations of the Met Office Unified Model (MetUM) with and without convection parameterisations. Another approach taken is using the spin-up period of high-resolution models. When initialised from global analysis, it takes time for convective structures to appear in CP simulations. Comparing the classic spin-up period to a novel initialisation technique which allows for convective structure to be included at initialisation, the effect of pre-existing convection on synoptic-scale motions can be investigated. Furthermore, a limited set of observations allow us to evaluate the use of CP models for simulating convective dynamics.

In this thesis, a literature review (chapter 2) summarises contemporary research on tropical organised convection, dynamics of MCSs, West African meteorology and the challenges of modelling in the region. Chapter 3 catalogues the data used throughout the thesis and relevant techniques used for MCS identification and tracking. In chapter 4, the 'circulation budget' technique is evaluated as a method for quantifying synoptic-scale changes to circulation in a region, and comment on the practical implications of its use (working towards answering question 1), before utilising the technique in chapter 5 to diagnose processes that modulate the circu-

lation over West Africa over the diurnal cycle. Chapter 5 also divides the circulation budget into mean and anomalous terms, characterises mesoscale dynamics of precipitating convection, and draws conclusions about the effect of mesoscale convection on the synoptic circulation as a result (addressing the first part of question 2). Following the convection downstream, chapter 6 evaluates how TC precursor vortices are represented in a CP simulation compared to a parameterised simulation (second part of question 2). Chapter 7 then attempts to address question 3 by using a dataset of tracked MCSs in a high-resolution simulation to characterise the environmental conditions associated with MCS initiation and intensification. Continuing to address the feedbacks between MCSs, Chapter 8 quantifies the impact of the existence of convection at the initialisation of NWP simulations by examining CP simulations which use novel initialisation techniques (working to address question 4). Finally, chapter 9 presents a discussion of the results and the conclusions, as well as suggestions for future directions of research based on the results within the thesis.

Chapter 2

Contemporary Understanding of Scale Interactions of Mesoscale Convection in West Africa and the Tropics

The understanding and prediction of tropical convection is a long-standing but essential challenge of meteorology and climate science. In the tropics, the dominant source of energy that drives synoptic-scale systems is from latent heat release associated with convection, rather than from available potential energy stored as latitudinal temperature gradients which drives systems in the midlatitudes (Holton and Hakim 2013c). Tropical variability is primarily on a diurnal timescale due to the daily cycle of convection that occurs across the tropics, but recent developments in understanding synoptic-scale and larger tropical weather systems have improved skill in intraseasonal and even intradecadal predictions in the tropics. Many of the longer-lived disturbances are strongly coupled with convective activity, and there are scale interactions between convection on the mesoscale up to synoptic- and even planetary-scales via teleconnections between the tropics, subtropics, and midlatitudes. The scale interactions of tropical convection is an active and ongoing area of research, and are the central theme of the thesis.

Many tropical regions exhibit examples of scale interactions, but as discussed in the previous chapter, the thesis focuses on West Africa. West Africa has a unique climatology whereby

the land surface temperature gradient sets up a jet in thermal wind balance, along which convectively-coupled disturbances propagate. It is also a region where organised convective systems contribute major proportions of seasonal rainfall, so it makes an excellent testbed for examining the interactions of these mesoscale convective systems (MCSs) with the synoptic-scale features of the region.

This chapter presents a literature review summarising the current state of knowledge in the fields of tropical convection and the simulation thereof, with a specific focus on West Africa. The review covers key features of tropical meteorology that affect convection and its organisation, atmospheric convection and its role in numerical weather prediction (NWP) and climate, developments in the understanding of convective organisation and the dynamics of MCSs, and the particular meteorology of West Africa, and summarises the contemporary successes and challenges of modelling tropical convection.

2.1 Convection and Tropical Meteorology

Traditionally, the definition of the global tropics is defined as the area covered by the latitudes between the Tropics of Cancer and Capricorn (at 23.45 ° N and 23.45 ° S respectively; Galvin 2016). Riehl (1979) introduced an alternative meteorological definition: that the tropics is an area where the diurnal temperature variability exceeds the annual temperature variability across seasons. Tropical meteorology has developed rapidly over the past decades, with the advent of satellite observations adding value not only to practically forecasting tropical weather, but also providing a foundation for theoretical developments in the field (Bauer et al. 2015).

However, theoretical understanding of tropical meteorology continues to lag that of meteorology in the midlatitudes, not only due to practical constraints (Parker et al. 2008), but also because of the lack of a fundamental unifying theory to describe the atmospheric motion, analogous to quasi-geostrophic theory in the midlatitudes. Quasi-geostrophic theory supposes that the only deviation from geostrophic balance (a balance between Coriolis and pressure gradient forces) is contributed by inertia, and that the inertial contribution is small relative to the Coriolis contribution (e.g. Holton and Hakim 2013b). In the tropics, where the Coriolis force is small itself, the approximation collapses. As a result, tropical meteorology requires understanding of various planetary- and synoptic-scale systems which each contribute to tropical variability across timescales (Li and Hsu 2018).

Convection is a key element of tropical meteorology for multiple reasons. To start with, latent heat release associated with moist convection is the primary source of energy in the tropics (Galvin 2016). As a result, convection can trigger and couple to the synoptic-scale systems which drive most variability in the tropics, such as atmospheric waves. The mechanisms for such couplings are a topic of thriving research.

Furthermore, convection is a key element of even larger, planetary-scale circulations. The difference between the insolation received at the equator and at the poles results induces the Hadley circulation, where the air at the equator is subject to stronger heating and rises, then moves poleward. As it travels towards the poles, the air cools and subsides. Meanwhile, to drive the rising air at the equator, there is low-level convergence, forming a region commonly referred to as the inter-tropical convergence zone (ITCZ). The thermally-direct picture of the Hadley cell is something of an oversimplification since the observed tropical atmosphere's temperature profile is stable above 600 hPa, so above 600 hPa, ascent of air parcels would cool the atmosphere. Therefore cumulonimbus clouds associated with deep convection are required to transport air parcels upwards through pseudo-adiabatic motions in 'hot towers' (Simpson et al. 1998), which is corroborated by observations of the ITCZ as a band of strong convection, indicated by low brightness temperatures, at equatorial latitudes (Holton and Hakim 2013c).

Variations in sea surface temperatures (SSTs) on a planetary scale, driven by ocean currents, lead to variation in the latent heating across longitudes. Such variations lead to zonally-asymmetric circulations such as an east-west circulation over the equator referred to as the Walker circulation. Another source of planetary-scale variability strongly coupled to convection is the Madden-Julian Oscillation (MJO). The MJO is a 'convective envelope' which propagates eastward around the globe along the equator at a speed of around $5\,\mathrm{ms}^{-1}$, with a period of 30–60 days (Li and Hsu 2018). It is described as existing in 8 phases, where there is a pronounced rainfall maximum associated with a different region in each phase. The MJO was first noted as an observational phenomenon, and several theories exist that attempt to describe the mechanism of its propagation and convective coupling, but a consensus on a theoretical description of the system has not yet been reached (Zhang et al. 2020). Not only does tropical convection couple strongly to the above modes of variability, but also independent convective systems can produce extremely high-impact weather conditions. Mesoscale convective systems (MCSs) are prevalent in the tropics over land as discussed at length in section 2.3, squall lines

can have devastating impacts, so forecasting them accurately is crucial. Much attention has also been paid, historically, to predicting and forecasting tropical cyclones (TCs), some of the most destructive natural phenomena on Earth, which are discussed further in section 2.3.2.

Monsoons are another key meteorological feature of the tropics which control seasonal variability in precipitation in various tropical regions. Historically, monsoons were purely identified as seasonal shifts in precipitation characteristics in separate geographic regions, caused by seasonal changes to land-sea temperature contrasts. In recent decades, the term monsoon has shifted to refer to any seasonal reversal of circulation (Holton and Hakim 2013c). A combination of observations and idealised simulations support a newer perspective of monsoons existing as part of an integrated global monsoon system associated with the seasonal shift of the ITCZ and other tropical and subtropical regions of convergence (Wang and Ding 2008). Variations between the regional monsoon systems are associated with differing responses to local forcings (such as orography and SSTs), and it is suggested that the varying extents of monsoons can be limited by energetic constraints (Geen et al. 2020).

Generally, studies describe six major monsoon systems: the South Asian Monsoon, the South American Monsoon, the Australian Monsoon, the North American Monsoon, the South African Monsoon, and the West African Monsoon (WAM). The latter is of most interest for the purposes of the literature review since the thesis will focus on convection in West Africa. More details about the dynamics of the WAM are discussed in section 2.4.

2.2 Dynamics of Deep Tropical Convection

Atmospheric convection is ubiquitous throughout the tropics. It is largely categorised into 'deep' and 'shallow' convection. Shallow convection has a limited vertical extent and describes such phenomena as cumulus and stratocumulus clouds, while deep convection has a far greater vertical extent, creating cumulonimbus clouds. The runaway ascent associated with deep convection is only limited by the tropopause: the atmospheric boundary demarcating the top of the troposphere and bottom of the stratosphere, where the temperature of the atmosphere reaches a local minimum. Deep convection may be associated with a single updraught, often referred to as a single convective cell. Deep convection may also be 'organised': multiple convective cells will cluster together to form systems which are larger and longer-lived than an individual cell. As a result, convection in the atmosphere exists on many scales and in the form of various

structures, from disorganised and randomly-distributed clouds to lines and bands of cloud, up to planetary-scale cloud envelopes (Holloway et al. 2017).

Convection can become organised through various mechanisms, such as through environmental wind shear, variance in humidity in the atmosphere associated with nearby cloud, cold pools, synoptic-scale wave features, and more (Pscheidt et al. 2019). However, idealised modelling studies have also shown that cloud clusters can organise themselves without environmental inhomogeneities in a process referred to as convective self-aggregation, implying that convective organisation is an inherent instability of an atmosphere in some equilibrium (Holloway et al. 2017). Examples of organised convection include frontal systems in the midlatitudes, and tropical-extratropical cloud bands which occur in the subtropics. This thesis focuses on two types of organised convection which occur in the tropics: TCs and MCSs. Both of these are high-impact weather (HIW) systems which can bring extreme precipitation and high winds to a region, and in fact the genesis of many TCs can be traced back to MCSs. TCs are unique in their warm-core rapidly-rotating structure, with convection surrounding their well-defined centre, and they typically form over tropical or subtropical waters such as the tropical North Atlantic Ocean.

The accurate representation of convection in atmospheric models is not only important due to the severe impacts that such systems can have on humanity, but also because of the impacts of convection on the climate system (Bony et al. 2015). In the recent Intergovernmental Panel on Climate Change (IPCC) sixth Assessment Report (AR6) report, confidence in high tropical cloud (such as anvils which can form as a result of tropical deep convection) feedbacks is low, as is land-cloud feedback (Forster et al. 2021). Furthermore, projections of how tropical precipitation will be modulated by warming depend on representations of convection (Pendergrass and Hartmann 2014), as will the change in frequency or intensity of HIW systems such as MCSs (Seneviratne et al. 2021). To understand how climate change scenarios will affect weather systems, it is essential to represent convection accurately, and to do so, it is necessary to interrogate its dynamics and scale interactions.

2.3 Mesoscale Convective Systems

Mesoscale convective systems (MCSs) are a type of organised convection manifesting in the form of a multicellular thunderstorm on the scale of hundreds of kilometres, which can last up to

several days. The precise definition of what qualifies as an MCS varies from study to study, but generally it is agreed that an MCS is a cumulonimbus cloud system which produces a contiguous rainfall area which reaches 100 km or more in scale along at least one axis (Houze 2004). Crucially, an MCS continues to sustain itself over a lifetime that exceeds that of individual convective cores, so MCSs are a form of organised convection.

Forecasting MCSs is important for multiple reasons. Firstly, their impacts are extensive and the systems can be extremely hazardous, associated with lightning (Sen Roy and Balling Jr 2013), flooding (e.g. Engel et al. 2017; Miller et al. 2022; Osei et al. 2023), and high winds (Ashley et al. 2019; Schumacher and Rasmussen 2020). As a result, accurate forecasting can save lives, and can further benefit various industries including agriculture, the energy sector, and fisheries (Roberts et al. 2022). Furthermore, since MCSs produce high quantities of precipitation, changes to the number of systems forecasted within a season can be the difference between a year of drought or severe flooding (Vellinga et al. 2016; Schumacher and Rasmussen 2020).

The development of radar, followed by the advent of the satellite era, has allowed for the creation of algorithms that track and quantify MCSs across the globe. Methods utilise geostationary satellite data to identify MCSs by tracking cold-cloud regions (indicating high-level cloud anvils) using brightness temperatures (e.g. Roca et al. 2014; Huang et al. 2018), or use low-orbit instruments to track storm properties such as precipitation (e.g. Nesbitt et al. 2006), with more recent sophisticated algorithms integrating both types of measurements (Feng et al. 2021). Typically, algorithms depend on timestep image detection and then characterise continuous systems as those which have an overlap above a specific threshold between consecutive timesteps.

In the tropics, MCSs contribute 50–90% of the annual rainfall (Schumacher and Rasmussen 2020). Figure 2.1 shows that while the number of MCSs in West Africa is not as high as in other regions in the tropics, with only around 30–50 storms occurring each year, they comprise up to 70% of the annual rainfall (Maranan et al. 2018; Feng et al. 2021), making them an essential factor in the region's climate. The importance of MCSs to annual rainfall in West Africa is one of the reasons the region was selected for study; more details of the implications of MCSs in West African meteorology and the choice of region are discussed in section 2.4.

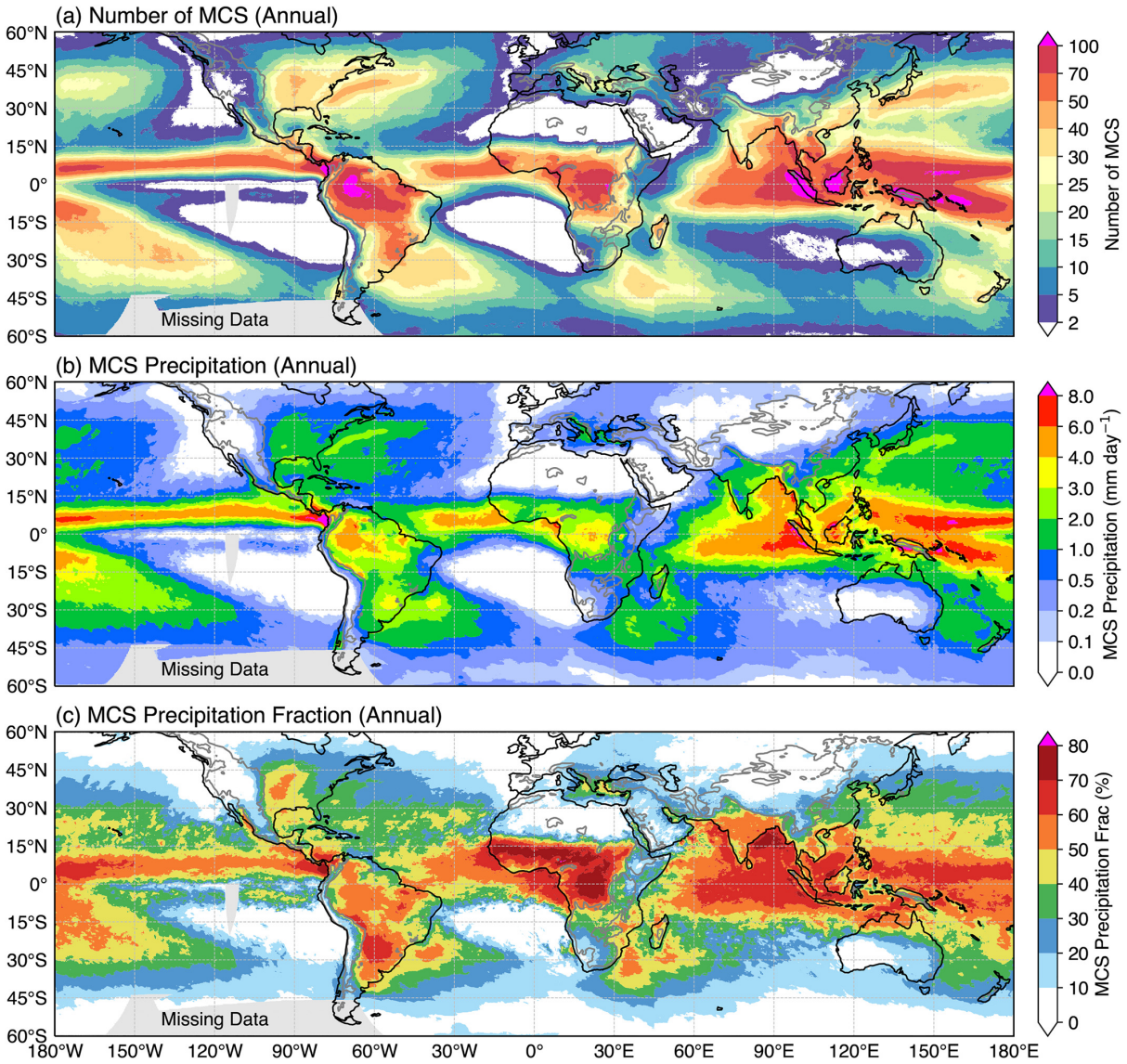

Figure 2.1: Figure 10 from Feng et al. (2021), showing annual averages of (a) MCS frequency, (b) total MCS precipitation, and (c) fraction of precipitation associated with MCSs, using their dataset of tracked MCSs from 2001 to 2019. Dark grey contours indicate orography above 1000 m. Regions where missing brightness temperature data made MCS tracking impossible are indicated by light grey contours and labelled.

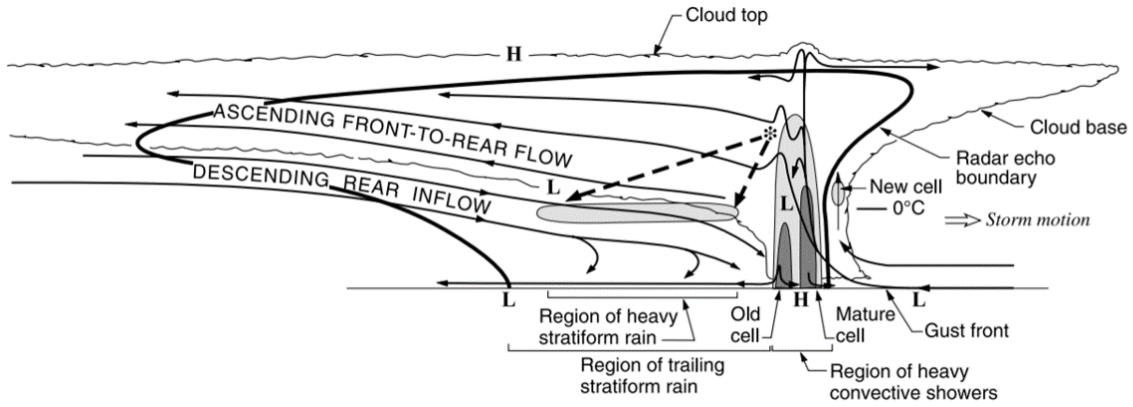

Figure 2.2: Figure 14 from Houze (2004). Schematic of an archetypal 'squall line with trailing stratiform'. The mesoscale flows that characterise its dynamics are shown as black arrows. Intermediate and strong radar reflectivity is indicated by medium and dark shading respectively, and 'H' and 'L' denote pressure highs and lows in the system respectively.

2.3.1 Characteristics of MCSs

The devastating impacts of MCSs are a result of not only the large areas and long lifetimes of the storms, but also result from their dynamical effects. In order to be self-sustaining, it is necessary for an MCS to have certain dynamical features in order to prevent updraughts from dissipating as a single convective cell would. An example of a self-sustaining MCS structure is that of the squall line. Not all MCSs are categorised as squall lines, and many have more complex configurations of convective and stratiform cloud, but the squall-line MCS is one of the most frequent MCS archetypes, especially over West Africa, since it is favoured by the pre-existence of strong background vertical wind shear which is an essential part of West African climatology (see section 2.4).

Squall line structure

Squall-line MCSs are divided into two regions characterised by distinct rainfall paradigms: a convective rainfall region contributing intense precipitation, co-located with updraughts forming the intense and deep convective cores, and a generally more uniform stratiform region with weaker rainfall, with stratiform cloud produced by the remnants of decayed convective cores (Schumacher and Houze 2003; Houze 2004). Typically the convective cores will align themselves perpendicular relative to the direction of travel, with the stratiform region 'trailing' behind. Figure 2.2 shows a cross-section of the typical squall line structure. The convective and stratiform regions have different heating profiles, with stronger heating closer to the ground in the convective region but elevated in the stratiform region, often with a region of cooling below it,

described as a 'top-heavy' heating profile (Schumacher et al. 2004).

As the MCS propagates, new convective cores as part of the same system can be triggered as air is lifted over the moist, dense air of cold pools (sometimes referred to as 'gust fronts') ahead of the storm. The regeneration of convective cores as the storm propagates is encouraged by the front-to-rear inflow, a circulation observed in many MCSs but particularly prominent in squall lines. The front-to-rear inflow moves air upwards over the cold pool, flowing into the front of the storm relative to the storm's motion. Along with the front-to-rear inflow, another characteristic mesoscale circulation in a typical squall line is the rear-inflow jet (RIJ), a jet which flows into the convective region from behind the storm, descending, which is generated as convergence is forced due to the low pressure at and behind the convective line (Schumacher and Rasmussen 2020).

Within an MCS, it is possible for a mesoscale convective vortex (MCV) to form in the base of the stratiform cloud, creating a midlevel, warm-core low pressure centre within the system (Bartels and Maddox 1991). MCVs may also exist at the end of a convective line as 'book-end' or 'line-end' vortices, strengthening the rear-inflow jet (Skamarock et al. 1994). Beyond the storm, MCVs have been observed to persist for several days after their associated MCS has dissipated. Persistent MCVs not only have the potential to form TCs if they move over oceans, but some studies indicate that such vortices can re-trigger convection and create new MCSs (Davis and Galarneau 2009).

Even in the absence of distinct MCVs, MCSs exhibit characteristic vorticity features. In both observations and models, dipoles of relative and potential vorticity associated with cumulus-scale convective cells are seen (Chagnon and Gray 2009; Oertel and Schemm 2021). Dynamically, the dipole pattern arises due to the convective updraught tilting background horizontal vorticity associated with ambient vertical wind shear, illustrated in more detail in Holton and Hakim (2013a).

A key requirement for the formation of squall lines is that the environment must be such that the newly-generated developing cells are not immediately counteracted by downdraughts from existing convective cells. New cells must be generated ahead of the mature cells in order for the storm to be sustained. Therefore, for the archetypal squall line, some vertical wind shear in the low levels of the atmosphere is necessary for sustained convection, as argued by Rotunno et al. (1988), who suggest that the shear also acts to balance the cold-pool vorticity in the storm's

lower levels so that it can sustain itself.

Lafore and Moncrieff (1989) argue that because MCSs are characterised by their mesoscale circulations, the convection-scale shear balance was insufficient to explain how the system sustains itself and that "system-scale baroclinic vorticity generation cannot be neglected;" that is to say, the entire system's balance cannot be ascribed entirely to such a small part of the system as a cold pool. More recently, it has been argued by Alfaro (2017) that the shear is important because it increases the relative proportion of moist and convectively unstable air parcels as a fraction of the total storm-relative inflow, which naturally leads to more triggering of new convective cells. However, it is well-established that shear plays a role in the maintenance of organised convection, indicated by both idealised modelling (Bickle et al. 2022) and observational and reanalysis studies (Klein et al. 2021b; Baidu et al. 2022).

MCS initiation

In order for deep moist convection that generates MCSs to trigger, several conditions are required: sufficient atmospheric moisture to produce clouds and precipitation, atmospheric instability that supports the continued ascent of air parcels through convection after the initial lift, the existence of background shear in order to prevent the immediate dissipation of the convective cells (as discussed in the previous subsection), and some form of lifting to drive the ascent of air required for convection to begin (Schumacher and Rasmussen 2020). The initial lift may be encouraged, in the midlatitudes, by frontal systems, but in the tropics other triggers are required.

An example is orographic lift as air moves upwards over ascending terrain. Houze (2012) summarises the nuances of how orography may affect convection: not only may uphill ascent trigger deep convection, but it can also act to maintain the stratiform regions of MCSs. Flows from higher terrain at midlevels can cap the boundary layer to contribute further instability and create more favourable environments for convection near mountainous regions. Furthermore, overnight subsidence associated with divergence around mountainous regions can also contribute to forming MCSs. In West Africa in particular, the Guinea Highlands contribute to deep convective development associated with a rainfall maximum off the West coast of the region (Hamilton et al. 2017).

Often, larger atmospheric drivers will trigger convection, such as synoptic- and planetary-scale

disturbances such as atmospheric waves which are associated with convergence. Convergence across various scales in the boundary layer typically precedes deep convection by several hours (Mapes and Lin 2005; Birch et al. 2014a), so these larger-scale features can provide favourable environments for convective initiation. Equatorial waves are an example of planetary-scale modes which modulate organised convection, often described as 'convectively-coupled' since they are largely in phase with large clusters of convection (Kiladis et al. 2009), and have been linked to extreme precipitation (Ferrett et al. 2020; Senior et al. 2023), and are associated with increased frequencies of organised convective systems (Cheng et al. 2023).

Sometimes MCSs can be generated as a result of features from MCSs which have already formed. For example, MCSs may produce gravity waves, which cause vertical velocity disturbances in the atmosphere and propagate outwards from and at a faster speed than their parent MCS. These can then go forth to trigger convection in lines which result in the formation of new convection (e.g. Liu and Moncrieff 2004; Birch et al. 2013). Liu and Moncrieff (2004) specifically argue that gravity waves have an especially strong impact in the tropics due to the weaker Coriolis effect. MCSs also generate 'cold pools', which are effectively density currents resulting from the evaporation of rain as it reaches the ground, and which propagate outwards from a storm. The existence of cold pools has been linked to higher precipitation rates, with deeper and wider updraughts, in deep convection (Böing et al. 2012). Cold pools not only allow for the mechanical lifting of unstable air to trigger convection, but also through moisture accumulation on the edge of the pools reducing convective inhibition for developing convective cells (Torri et al. 2015). Collisions between cold pools result in even stronger updraughts linked to organised systems (Meyer and Haerter 2020).

Another feature associated with MCS formation are patterns in soil moisture. Taylor et al. (2011) show that 37% of MCS initiations in West Africa happen over the steepest 25% of land surface temperature anomaly gradients, associated with sharp boundaries between warmer, drier soil and cooler, wetter soil. The warmer, drier soils provide a higher sensible heat flux to the atmosphere than the cooler, wetter soils, driving updraughts. Therefore, patches of dry soil surrounded by wetter soil induces convergence of moist low-level air which fuels further moist convection. There is no observational evidence for positive feedbacks between moist soil and convective initiation, despite global models indicating otherwise (Taylor et al. 2012). Higher-resolution regional models appear to have a more realistic representation of the feedbacks

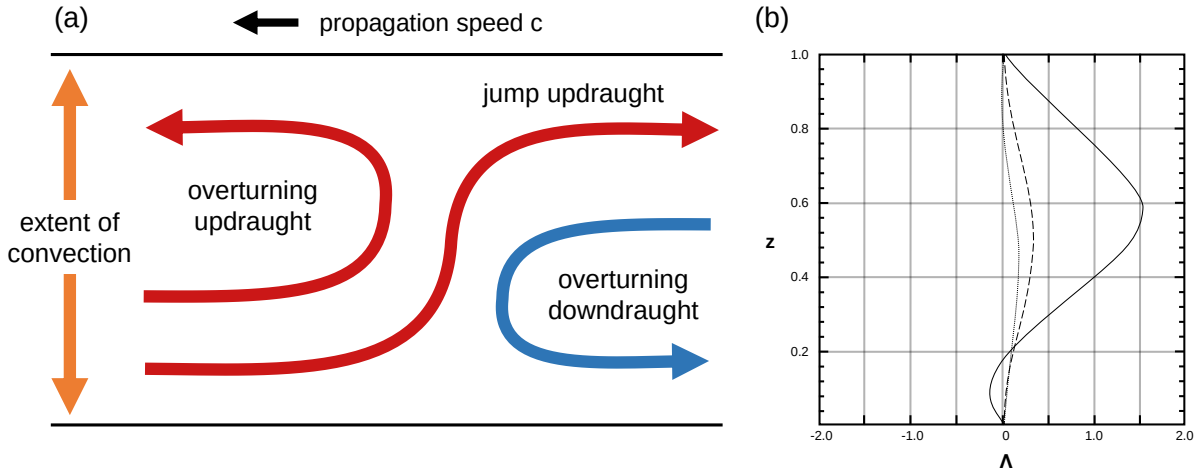

Figure 2.3: Based on figures from Moncrieff (1992). (a) Schematic of "triple branch circulation" of storm-relative streamlines within in a westward-propagating organised convective system. An overturning updraught at the front of the storm and a jump updraught flowing from the front to the rear of the storm are illustrated in red, and the downdraughts in blue. (b) Normalised vertical profiles of momentum flux, $\Lambda = \frac{\langle \rho u_m w_m \rangle}{\rho U_0^2}$. u_m and w_m are the storm-relative zonal and vertical velocities, ρ is the density of the inflowing air, and U_0 is the relative velocity of the inflow. Shown for triple branch circulation with an overturning updraught and overturning downdraught (dashed line), circulation without an overturning updraught (solid line), and circulation without an overturning downdraught (dotted line).

(Taylor et al. 2013). Beyond initiation, dry soils can serve to intensify MCSs more than moist soils (Klein and Taylor 2020), again due to the higher sensible heat flux produced by dry soils compared to wet soils.

It is possible that, earlier in rainy seasons, both the effects of cold pool and soil moisture feedbacks are more marked. Since the air is typically drier, cold pool moisture is enhanced (Provod et al. 2016), and where early season precipitating systems provide starker soil moisture gradients compared to the drier soils that exist before wet season onset (Hu et al. 2021).

Convective momentum transport in MCSs

Moncrieff (1992) outlines a theory for momentum transport properties associated with propagating coherent cloud structures, from a two-dimensional framework considering the conservation of key quantities along streamlines. As illustrated in figure 2.3a, archetypal squall line systems are characterised by a triple-branch circulation of storm-relative winds, with a jump-like updraught flow through the system combined with an overturning updraught at the front of the storm and an overturning downdraught towards the rear. Depending on the type of convection, sometimes there may be weaker downdraughts or updraughts. Assuming sheared background

flow, the heat and momentum transport induced by an organised convective system can be deduced. Normalised vertical profiles of the convective momentum flux induced by the archetypal three-branch circulation as well as by two other limiting regimes with no overturning updraught and no overturning downdraught in each case respectively, are shown in figure 2.3b. Idealised simulations have recreated the up and downgradient momentum transport in such systems (Badlan et al. 2017), and implementing the framework in MCS parameterisation schemes has resulted in improved tropical dynamics (Moncrieff et al. 2017; Moncrieff 2019).

2.3.2 Tropical Cyclones

Tropical cyclones (TCs) are some of the most devastating natural disasters on the planet. TCs are low-pressure systems in the form of approximately axisymmetric vortical towers of rotating convection. Tropical convection is therefore fundamental to TC genesis and propagation (Holton and Hakim 2013a). The systems require some degree of Coriolis force in order for the rotation to spin up and grow, but also must form over warm oceans with SSTs of at least 26.5 °C, and sufficiently warm water over a depth of 50 m, which is far more likely to occur in the tropics than at higher latitudes, so almost all TCs formed in the latitude band of 5–30 ° N, although they often travel outside of these latitudes later in their lifetimes (Emanuel 2003). Approximately 80 TCs occur each year in tropical basins of the Atlantic, Pacific, and Indian Oceans (Ramsay 2017).

TCs are characterised a cloudless central 'eye' of the storm, surrounded by an eyewall which contains the most vigorous convection, and then continued convection in cloud bands which wrap around the storm, separated by bands of subsidence, with strong winds at the eyewall decreasing in velocity over the radius of the storm (Emanuel 2003). Another crucial feature of their structure is thermodynamic: TCs are typically several degrees warmer than their environment, with a peak in temperature anomaly at their centre where their pressure is lowest. Their positive temperature anomaly is why TCs are referred to as warm-core phenomena, and is a key feature that distinguishes TCs from midlatitude cyclones, which are cold-cored (Shea and Gray 1973).

The particular relevance of TCs to West Africa is in their initiation. While TCs are in themselves organised convection, they do not occur over West Africa as they form over the ocean. West Africa's meteorology is tied to TC formation in the North Atlantic Basin. In order to form, many studies propose that TCs require an initial atmospheric disturbance, or a 'seed' from

which the system evolves (Emanuel 2003), and several such disturbances can form over West Africa, as will be discussed in the following section 2.4. In addition to a disturbance, TCs also require the high SSTs discussed previously, a conditionally unstable atmosphere in order to facilitate deep convection, a moist mid-troposphere, and relatively weak wind shear (Hakim and Patoux 2021).

Progress has been made in the past decades in improving forecasted TC tracks, but forecasts of TC intensity have shown less improvement until around 2010 (DeMaria et al. 2014; Montgomery and Smith 2017; Cangialosi et al. 2020). Projections of future changes in TC frequency, intensity, and hence their impact are relatively uncertain. The IPCC AR6 report predicts an increase in the precipitation associated with TCs with high confidence, but there is only medium confidence that the frequency of TCs will decrease or stay the same under warming scenarios (Douville et al. 2021). Major challenges remain in forecasting the genesis of TCs and TC-like disturbances. While many case studies show how TCs grow from tropical disturbances off the coast of West Africa, understanding which disturbances will become TCs, and the processes they must undergo in order to do so, is an ongoing research question (Tang et al. 2020).

2.4 Meteorology of West Africa

Chapter 1 provides a brief overview of the motivation to study West Africa in particular. Because of its distinctive synoptic-scale features, and the key role that MCSs play in its boreal summer climate, West Africa makes for an excellent natural laboratory to investigate the impacts of organised convection on synoptic-scale circulation.

In West Africa, the climate is primarily controlled by the WAM (Cornforth et al. 2017). In winter, the WAM mean flow is northeasterly and in summer, it reverses and becomes southwesterly, advecting cool moist air from the Gulf of Guinea inland and providing the moisture essential for convective conditions. The WAM onset typically occurs in late June, with the meridional maximum in precipitation making a sharp jump from its quasi-stable position at 5 ° N during May–June to a new position at 10 ° N in July–August (Sultan and Janicot 2003). Monsoon activity may be modulated by planetary-scale modes of variability including equatorial waves or the MJO (Matthews 2004; Lavender and Matthews 2009).

A key feature of the WAM system is the African Easterly Jet (AEJ), a midtropospheric jet over

West Africa peaking in velocity at 600-700 hPa. Its latitude varies on a seasonal scale, moving from over the coast of southern West Africa in January up to approximately 15° N in July (Cornforth et al. 2017). The AEJ is maintained as a result of thermal wind balance, caused by the difference in land surface temperature between the hot, dry Sahara to the north, and the cooler, moist Sahel to its south. The distinct orography of the region also is crucial to the AEJ's existence (Wu et al. 2009).

Another easterly jet exists over tropical West Africa: the Tropical Easterly Jet (TEJ). The TEJ is a feature of the South Asian Monsoon, extending from the South China Sea to West Africa, with a core jet strength descending from around 100 hPa to 200 hPa as it travels southwest towards equatorial Africa (e.g. Sathiyamoorthy et al. 2007). In Africa it is most prominent as an easterly climatological wind at 200 hPa typically observed from June to September.

The AEJ is important for regional weather forecasting for two key reasons. Firstly, the jet itself induces vertical shear as it opposes the low-level monsoon flow below it, which results in favourable conditions for convective organisation as discussed in section 2.3. Secondly, its barotropic and baroclinic instabilities are the source of African Easterly Waves (AEWs), which play a crucial role in the weather systems in the region. AEWs are westward-propagating disturbances to the AEJ with periods of around 3-5 days and wavelengths of around 2000–4000 km. AEWs develop and propagate over tropical North West Africa during the northern hemisphere summer, with phase speeds of around 6–8 $\mathrm{m\,s^{-1}}$ (Cornforth et al. 2017). Along the AEJ there are two stormtracks where AEWs propagate. To the north of the jet is a lower-level track with maximum amplitude at around 850 hPa, associated with dry, shallow convection. To the south of the jet there is a mid-level track with maximum amplitude, associated with precipitating deep convection (Brannan and Martin 2019). The two tracks tend to eventually merge over the Atlantic (Diedhiou et al. 1998).

It has been shown in observational and reanalysis studies (e.g. Schwendike and Jones 2010) that vortices associated with MCSs and AEWs can travel off the coast of West Africa into the North Atlantic, where they can develop into tropical depressions and potentially undergo tropical cyclogenesis (Thorncroft and Hodges 2001). Others studies link TC frequency to AEW energy (Russell et al. 2017). Despite observational evidence of many cases where AEWs go on to become TCs, some modelling studies indicate that suppressing AEW formation in global climate models (GCMs) and regional models does not affect TC number on a seasonal level

(Patricola et al. 2018; Danso et al. 2022).

Furthermore, AEWs induce favourable conditions for convective activity, often initiating mesoscale organised convection due to enhanced low-level convergence, wind shear, and rising motion (Fink 2003). Many studies have confirmed that moist convection is affected by AEWs, with some estimates suggesting that over 60% of observed summer squall lines in the region are associated with AEWs (Cornforth et al. 2017). The initiation of convection tends to occur in the northerlies, ahead of the AEW troughs, or in the southerlies behind the troughs, but MCSs can occur throughout the waveform (Fink 2003; Mekonnen et al. 2006). Observations have suggested that weaker convective systems occur in the southerlies and more intense storms in the northerlies at the front of the trough (Semunegus et al. 2017).

Modelling studies suggest that convection is one of the key factors in initiating and sustaining AEWs (Berry and Thorncroft 2005; Hsieh and Cook 2007; Berry and Thorncroft 2012) and indeed where organised convection is colocated with an AEW trough, the wave is more likely to develop and undergo tropical cyclogenesis (Enyew and Mekonnen 2021). Also, MCSs may trigger AEWs upstream; for example, after orographic triggering of convection at the Darfur Mountains or in the Ethiopian Highlands, both of which are near the entrance of the AEJ (Kiladis et al. 2006; Mekonnen and Rossow 2018).

Some studies suggest that the AEW life cycle and growth mechanism can be described by the diabatic Rossby wave model (Parker and Thorpe 1995; Moore and Montgomery 2005); others argue that the background baroclinicity is not strong enough to support the required isentropic lift (Russell and Aiyyer 2020). Others suggest a stratiform instability theory for AEW maintenance, suggesting positive feedback loops associated with wave-coupled convection, either through negative feedback loops of convective inhibition (CIN; where CIN is lower, convection is more likely, and convection will produce stratiform precipitation that cools the lower troposphere and further reduces CIN; see Mapes 2000), or through midtropospheric moisture feedbacks (where convection occurs, it will generate a moisture anomaly that results in further convective heating; see Kuang 2008). Russell and Aiyyer (2020) elaborate on the theory to propose 'rotational stratiform instability', suggesting that the potential vorticity anomalies associated with MCVs in the trailing stratiform regions of squall-line MCSs (see section 2.3.1) contribute to AEW maintenance. Tomassini (2018) agrees that the potential vorticity signature contributes to how an MCS's circulations have upscale effects on an MCS, alongside the

downscale support that the synoptic wave signature lends to maintaining the MCS structure, and further highlights that the dynamical and thermodynamical processes coupling the AEWs and MCSs occur across scales, making the interactions between the two challenging to model using sub-grid parameterisations.

2.5 Modelling Convection Over West Africa

Because of the complex interactions between meso- and synoptic-scale features over West Africa, simulating the region both in climate projections and in NWP is difficult. The unique challenges of understanding and therefore simulating West African meteorology are perhaps most starkly highlighted by the lack of consensus among climate models as to how the weather systems may change in the future. Precipitation projections for future climate scenarios highlight West Africa as a region of particular uncertainty. While Coupled Model Intercomparison Project phase 6 (CMIP6) simulations agree that there will be increased rainfall in the eastern-central Sahel and decreased rainfall in the western Sahel under warming scenarios (Monerie et al. 2020), the magnitude of projection varies wildly and appears highly sensitive to the convection parameterisation used (Hill et al. 2017; Douville et al. 2021). Another crucial example of the lack of predictability of West Africa as a region is outlined in Roehrig et al. (2013), where 1-day rainfall correlation coefficients are positive almost everywhere in the world during July–September except for West Africa, where they are negative. The result reflects the variability of precipitation in West Africa inherent to a region dominated by a small number of MCSs (Vellinga et al. 2016).

It is also important to consider not only the long-term climate projections in West Africa, but also the necessity of understanding the interactions between organised convection and synoptic circulation in the context of NWP, or short-to-medium range weather forecasting. The prediction of rainfall on subseasonal scales is of huge importance for the millions of people who live in the region, both in terms of the risks (such as flooding and lightning) that are associated with organised convective systems, and the importance of predicting monsoon onset for the selection of planting dates for the agricultural industry in the region (e.g. Singh et al. 2018; Nkiaka et al. 2020). Skill in forecasting precipitation is poor (Fink et al. 2011; Vogel et al. 2020), to the extent that even modern, state-of-the-art global ensemble predictions of rainfall are no better predictions based simply on climatological statistics (Vogel et al. 2021). The lack of forecasting

skill appears to emerge from a lack of representation of adequate convective organisation over the region.

Forecasting MCSs and organised convection has historically been a challenge for GCMs due to the limitations of the traditional convection parameterisation schemes which are employed to represent sub-gridscale processes. However, in the advent of improved computational capacity, higher resolution models can be run, meaning that convection is no longer necessarily a process that exclusively occurs on scales smaller than the horizontal grid spacing of the model. Such models can potentially contribute value to the simulation of organised convection and its upscale impacts.

Convection-permitting (CP) models (sometimes referred to as models with explicit convection, convective-scale models, convection-allowing models, storm-resolving models, or k-scale models) are weather or climate simulations of sufficiently high resolution to explicitly simulate deep convection without a deep convective parameterisation. Historically, due to high computational cost, CP models have been run over limited domains, but in recent years, improved computational capacity has allowed for the running of regional and even some global CP models (e.g. Satoh et al. 2017; Stevens et al. 2019; Kendon et al. 2021; Takayabu et al. 2022).

Explicit convection has been shown generate more realistic convective structures, improve diurnal timing of rainfall, and allow a more detailed representation of the dynamics associated with convective processes. Since deep convection dominates weather patterns from local to planetary scales in the global tropics, and large-scale circulations are intrinsically coupled to convective activity, the tropics benefits significantly from the advantages of CP modelling. In particular, West Africa stands to have its climate projections improved with the introduction of CP models since its uncertainty in existing climate models is dominated by the dynamical response of the climate to warming (Monerie et al. 2020), which will be explicitly represented where convection exists.

Errors in AEW forecasts can be attributed to the limitations of convection schemes (Elless and Torn 2019) and initial studies of CP models show that they are able to aid understanding of the interactions between AEWs and MCSs (Tomassini et al. 2017; Tomassini 2018; Tomassini 2020). Regional convection-permitting models studies (e.g. the Cascade Project, Pearson et al. 2010) demonstrate the added value of representing convective dynamics explicitly, even on relatively coarse scales, in tropical West Africa (e.g. Marsham et al. 2013; Taylor et al. 2013; Birch et al.

2014a; Birch et al. 2014b). Representation of convection has been shown to impact how models represent the WAM, which can have far-reaching impacts, even affecting forecasts in the North Atlantic-European sector (Pante and Knippertz 2019).

Furthermore, simulations using CP models have demonstrated improved capacity over models with deep convection parameterisations for representing TCs. Simulations from the DYnamics of the Atmospheric general circulation Modeled On Non-hydrostatic Domains (DYAMOND) CP model intercomparison project (Stevens et al. 2019) and comparisons to counterpart simulations with deep convection parameterisations indicate that the absence of a deep convective parameterisation leads to demonstrable improvements in representation of the number of TCs, as well as their intensity (Judt et al. 2021). However, it is uncertain as to why CP models seem to generate a more accurate number of TCs than parameterised simulations compared to observed numbers.

When putting CP models into operational practice, there are challenges associated with initialisation of the simulations and how best to assimilate data across scales. An overview of progress in the field is described in Hu et al. (2023). Where convective-scale models are simply initialised from global reanalyses, there is a 'spin-up' period where the model must start to generate small-scale structure that is not represented in the global data with which it is initialised (Lean et al. 2008), during which errors in the large-scale state increase further (Woodhams et al. 2018).

Data assimilation (DA) traditionally requires extensive analysis of background error covariances in order for increments of observational information to be applied. On a global scale, geostrophic and hydrostatic balances are incorporated into the error modelling, but such balances are invalid under convective conditions and on small scales. In the tropics in particular, a lack of high-quality high-resolution observations with well-quantified uncertainties provides a further challenge. Crucially, the inherent challenge of multiscale interactions means that DA is difficult. To address the challenge of multiscale DA, blending techniques have been trialled, which nudge high-resolution forecasts on small scales towards global reanalyses (some examples are summarised in Gustafsson et al. 2018). One such blending-style effort to counteract the impacts of model spin-up time without incorporating DA methods directly is 'warm-starting', trialled by Short and Petch (2022) over Darwin. An example of such simulations are described in more detail in Chapter 3. In data-sparse regions, such techniques which limit the requirement for deep knowledge of the background error covariances and high-resolution observations are of

potentially significant value.

Nonetheless, the current generation of CP models have inherent disadvantages that extend beyond the challenge of initialisation (Kendon et al. 2021). Rainfall is often too intense, as are updraughts, and the organisation of convection is still sensitive to other parameterisations such as microphysics (Feng et al. 2018) and boundary layer schemes (Christensen and Driver 2021). These sub-km parameterisations are still required, and most are currently not well-tuned to CP simulations. CP models also suffer from inaccuracies in land-surface interactions, and most are not ocean-coupled due to constraints in computational capacity. CP models can also be sensitive to the choice in model timestep (Barrett et al. 2019), and the lateral boundary forcing for regional CP models must be high quality otherwise it can introduce serious errors.

Chapter 8 of the IPCC AR6 'Physical Science Basis' report, however, states that there is currently 'high' confidence that using CP models will help improve projections of precipitation in models (Douville et al. 2021). The thesis explores the value the CP models can indeed add to the forecasting of convection in West Africa, specifically in the context of the upscale impacts of organised convection in the region.

2.6 Summary and Thesis Outlook

This literature review has provided an overview of the developments in tropical meteorology over the past few decades, and a summary of the key elements of West African meteorology during the monsoon season in boreal summer. It has also outlined current understanding of the dynamics of MCSs and tropical cyclogenesis associated with West African weather patterns in the North Atlantic Ocean. In recent years, the development of CP models, in conjunction with ever-increasing capacity for high-resolution satellite observations, has allowed for major improvements to be made in the understanding and simulation of mesoscale organised convection in the tropics.

Results indicate that modelling more realistic convection can add value to simulations both on NWP and climate timescales, both on local and extended scales, but there remain gaps in this line of research. For example, mechanisms through which mesoscale convection feeds back onto synoptic-scale circulation remain a key question. It is also challenging to isolate the effects of convection artificially in simulations or through analysis of observations, and there is a need for

the development of further tools to analyse scale interactions in the atmosphere. Convincing evidence that organised mesoscale convection drives an upscale energy cascade would be important for the motivation of further (computationally expensive) high-resolution convective-scale simulations on large regional or global domains.

In the context of West Africa, it is of interest to understand the interaction between MCSs and AEWs. Several mechanisms have been proposed for thermodynamic interactions that facilitate their coupling, but there are few studies that approach the interaction between MCSs and synoptic circulation in the region from a dynamical perspective. The effect of MCSs on the formation of future MCSs has been studied to some extent, as well as the initiating conditions associated with MCSs, but a holistic description of the effects of MCSs on initiation of future MCSs is lacking. Furthermore, there is a lack of consensus on how AEWs or MCSs transform from cold-core vortex structures to warm-cored TC precursor vortices as they propagate off the West African coast.

As a result, the thesis will aim to address the literature gaps by exploring potential new diagnostics for characterising scale interactions, and using the diagnostics to draw conclusions about the mesoscale dynamics of convection in CP simulations relative to parameterised simulations and the implications of their differences for synoptic-scale circulation. Investigations will analyse vortices and MCS tracks in CP models and parameterised counterparts to investigate the added value of convective-scale simulation to predict initiations of MCSs and TCs, and feedbacks of MCSs on future MCS initiations will be examined. Finally, the research will explore the upscale and downstream impacts of convection by comparing simulations where convection is and is not present at initialisation using output from trials of a novel initialisation technique.

Chapter 3

Data and Methodology

In order to further understanding of tropical organised convection and its upscale impacts, high-resolution state-of-the-art models are used to simulate the dynamics of such convection. Since there are few high-resolution observational datasets that characterise the internal structure of tropical mesoscale organised convection, it is largely modelling that is used in this thesis to investigate the internal dynamics and scale interactions of organised convection in the tropics, with some observation and reanalysis data used for comparisons in chapters 4, 5, and 8.

The following chapter summarises the datasets used to investigate tropical convection in the thesis. Firstly, the chapter outlines the setup of the UK Met Office's Unified Model (MetUM) and describe the configurations of the experiments analysed in the following chapters. Tracked storm datasets in MetUM simulations are described. Finally there is an overview of the observational data both from JET2000, as featured in chapter 5, satellite precipitation data used in chapter 8, and reanalysis data used in chapter 4.

3.1 The Met Office Unified Model

The Met Office Unified Model (MetUM) was developed with the aim to model the atmosphere and earth system seamlessly across both weather and climate timescales (Brown et al. 2012). The model is flexible and can be configured for various scenarios at various resolutions on regional or global grids, and with different parameterisations.

The dynamical core of the MetUM, Even Newer Dynamics for General atmospheric modelling of the environment (ENDGame), solves equations for a deep, non-hydrostatic, fully-

compressible atmosphere. Prognostic variables (three-dimensional wind vectors, potential temperature, Exner pressure, dry density, and moist prognostics) are stored using an Arakawa-C grid (Arakawa and Lamb 1977) staggering in the horizontal and Charney-Phillips (Charney and Phillips 1953) staggering in the vertical, on terrain-following hybrid height vertical coordinates. To calculate modelled fields, ENDGame uses a semi-Lagrangian formulation (the equations solved for key prognostic variables are Lagrangian in formulation, but are solved on a fixed Eulerian grid), with semi-implicit time integration (Staniforth and Côté 1991; Wood et al. 2014; Walters et al. 2019). Introduced in the Global Atmosphere (GA) 6.0 configuration, ENDGame improved tropical variability and representation of tropical cylones (TCs) and other such phenomena (Walters et al. 2017). The GA model releases are consistent with the release of Global Land (GL) configurations of the Joint UK Land Environment Simulator (JULES; see Best et al. 2011; Clark et al. 2011), which simulate the land surfaces that are coupled to the atmosphere in the simulations (e.g. GL7.0, see Walters et al. 2019).

The MetUM can be configured for regional use in the form of local area models (LAMs) with restricted domains. In a similar way to the releases of the GA configurations, regional model configurations of the MetUM are defined and released. Such regional simulations can be run at kilometre-scale resolution, without a deep convection parameterisation, and can be convection-permitting (CP). The first Regional Atmosphere Land configuration (RAL1) is described by Bush et al. (2020). Crucial differences between the global and regional configurations are in the coordinate system (in the regional model, coordinates are rotated such that the 'equator' of the rotated-pole grid runs through the centre of the domain) and the considerations that must be made to account for boundary effects on the edges of a regional domain: imposed lateral boundary conditions (LBCs) from the driving model that the domain is nested within must be blended with the regional model solution (see Davies 1976).

The RAL1 release is comprised of two sub-releases, RAL1-M and RAL1-T, which are configured specifically for midlatitude and tropical domains respectively. Key differences include stronger turbulent mixing in RAL1-T to ensure that convective cells develop at a realistic time and to an appropriate size, and a smaller number of below-tropopause vertical levels in RAL1-T since the troposphere is deeper in the tropics (Bush et al. 2020). A second release, RAL2, was described in (Bush et al. 2023). RAL2 increases the number of vertical levels from 70 in RAL1 to 90 in order to unify the vertical level set across both RAL2-M and RAL2-T configurations, and

implements changes to the boundary layer and turbulence schemes. The newer configuration, RAL3, is under development and looks to unify the configurations for the midlatitudes and tropics, so there will not be sub-configurations as for RAL1 and RAL2.

The following subsections describe the specific MetUM experiments investigated later in the thesis.

3.1.1 Hardy et al. (2021)'s Typhoon Nepartak Simulations

For the purposes of evaluating the circulation budget methodology on convective-scale simulations, a dataset with high time resolution output was necessary. A subset of ensemble runs were selected, taken from an experiment run over South East Asia (SEA) using the MetUM as outlined in Hardy et al. (2021). The experiment ran a twelve-member CP ensemble simulating the rapid intensification of Typhoon Nepartak in 2016, on a 4.4 km grid, based on the RAL1-T configuration of the MetUM but with reduced air-sea drag at high wind speeds, a change later implemented in the development of RAL2-T.

Ensemble members were one-way nested within corresponding Met Office global ensemble prediction system (MOGREPS-G; Bowler et al. 2008), configured using GA6.1. The MOGREPS-G ensemble members are created by perturbing the Met Office's global analysis state using an ensemble Kalman filter (Bishop et al. 2001). Their initial state is interpolated from the global onto the finer regional grid, and the MOGREPS-G members drive each regional ensemble member's LBCs on an hourly basis. The CP simulations did not include any additional stochastic parameterisations or perturbations, so the ensemble spread is entirely derived from the differences at initialisation and at the boundaries provided by the driving MOGREPS-G ensemble. Forecasts were re-initialised every 12 hours from 1200 coordinated universal time (UTC) 2 July 2016 to 0000 UTC 4 July 2016. The first 24 hours of each simulation are ignored since the model takes around 24 hours to spin-up convective structure.

While the simulations had limited success accurately replicating the intensification of the storm compared to observations (Hardy et al. 2021), they still prove a useful tool for our purposes. Firstly, the model output parameters include turbulent stress tensor components which can be used to estimate frictional terms, which are an element of the circulation budget. Secondly, the model timestep for the regional simulations was 75 seconds, and of the twelve ensemble members, one was simulated with a time output interval of 5 minutes, which was appropriate

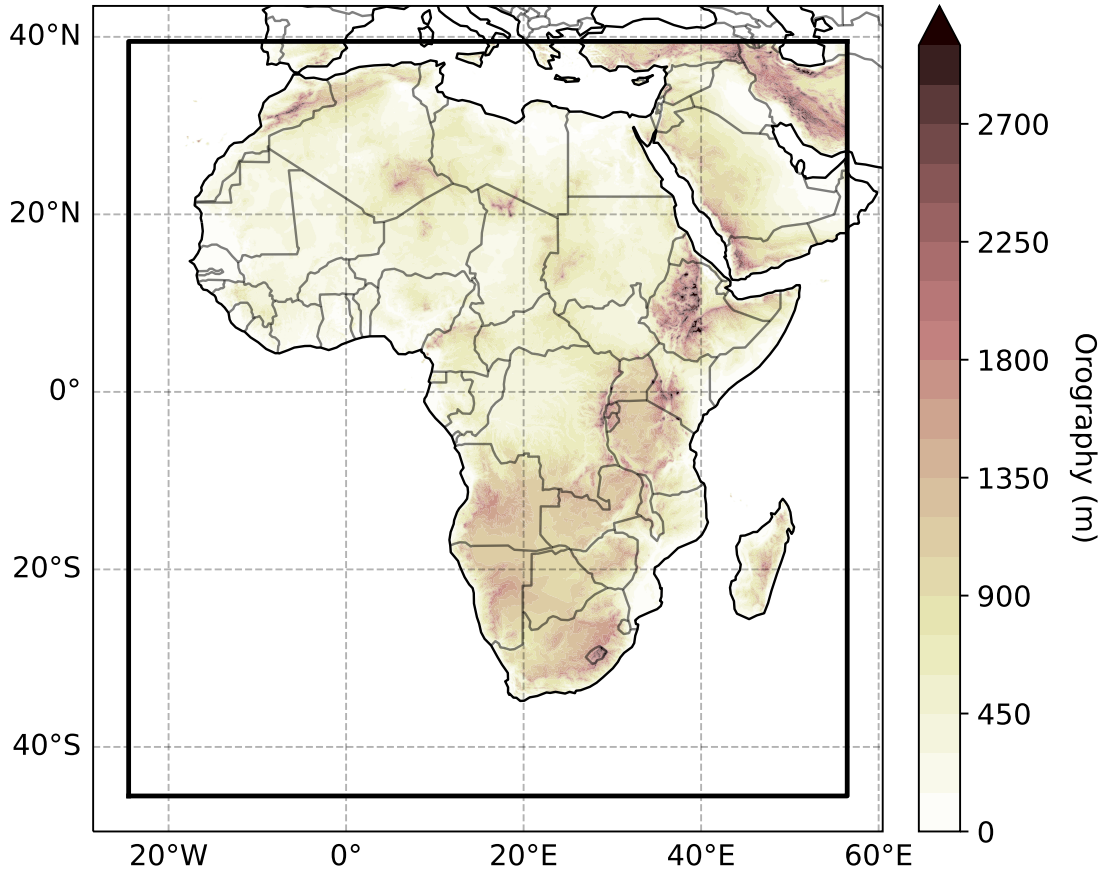

Figure 3.1: Map showing illustration of the CP4-Africa domain, defined in Stratton et al. (2018). The filled contours show the orography of the terrain. The thick black line outlines the CP4 regional domain.

for our aim: evaluating the impact of higher time output resolution on an analysis technique that has potential for investigating scale interactions of convection.

3.1.2 CP4-Africa

CP4-Africa (CP4) refers to a CP simulation covering the African continent (see figure 3.1) with a resolution of 4.4 km at the equator. A similar regional simulation with parameterised convection and a resolution of 25 km at the equator was also run, referred to hereafter as R25. The original experiment (outlined in Stratton et al. 2018) compared 10-year free-running 'current climate' simulations with 10-year free-running 'future climate' simulations with projected climatological changes in line with Representative Concentration Pathway (RCP) 8.5 applied in the form of sea surface temperature (SST) forcings. Mostly, in this thesis, the data used is from the

current-climate configurations of CP4 and R25.

CP4 builds on work done as part of the Cascade project (Pearson et al. 2010), which was connected with the African Monsoon Multidisciplinary Analysis (AMMA) campaign. The Cascade project used various configurations of the UM to run convection-permitting simulations over West Africa for a period in 2006 at several horizontal resolutions. Initial results indicated that convection-permitting simulations were far more effective at representing convection than their parameterised counterparts (Taylor et al. 2013; Birch et al. 2014b; Birch et al. 2015).

LBCs are supplied by a 25-km grid spacing GCM configured similarly to R25 through one-way nesting. R25 is largely based on the GA7.0 configuration described in the previous section (Walters et al. 2019), with the 6A convection scheme. Since CP4 is able to directly simulate deep convection, it instead uses the Smith (1990) diagnostic large-sale cloud scheme and Wilson and Ballard (1999) microphysics scheme. CP4 uses a blended boundary layer scheme (Boutle et al. 2014) which combines the schemes of Lock et al. (2000) and Smagorinsky (1963), which are better suited to low- and high-resolution models respectively, whereas R25 does not require a blended scheme. Full details of the model setup can be found in Stratton et al. (2018).

CP4 and R25 Evaluation

With a 4.4 km grid, CP4 cannot explicitly represent dynamics of shallow convection or congestus clouds, but it does improve diurnal precipitation timing and intensity relative to the 6A convection scheme used in R25 (Stratton et al. 2018; Kendon et al. 2019), especially when rainfall is regridded to 25-km resolution (Berthou et al. 2019), although there are noticeable biases such as a strong wet bias over the tropical ocean (Stratton et al. 2018).

CP4 also improves representation of the WAM and frequency of MCSs compared to observations (Stratton et al. 2018; Berthou et al. 2019). The CP4 MCSs have more realistic lifetimes, spatial distributions, and propagation directions compared to R25, but are smaller and propagate slower than observed systems (Crook et al. 2019). Fitzpatrick et al. (2020) and Klein et al. (2021a) note that the response of the MCSs to shear is not as expected, with no correlation between shear and precipitation despite observational and idealised model evidence that shear facilitates MCS organisation (e.g. Rotunno et al. 1988; Bickle et al. 2022; Baidu et al. 2022).

3.1.3 'Warm-Starting' Simulations

In March 2019, a Met Office simulation referred to as the 'Tropical Africa Model' (TAM) was made operational. The TAM is a deterministic operational forecasting model at 4.4 km resolution with no deep convection parameterisation, which covers the majority of tropical Africa. With the RAL1-T configuration, the PC2 prognostic cloud scheme is used (Wilson et al. 2008). The model is one-way nested within the MetUM GA6.1 configuration, which produces a new global analysis every 6 hours using hybrid incremental 4D-Var data assimilation (Rawlins et al. 2007).

At 06 and 18 UTC each day, the regional model is initialised using the downscaled global analyses. No new data are assimilated at initialisation onto the native scale of the regional model grid, but the global model updates the LBCs of the domain every 3 hours, and the operational sea surface temperature and sea ice analysis (OSTIA) is used to update sea and lake surface temperatures on a daily basis.

The use of a CP operational model has benefits in terms of a more realistic distribution and diurnal timing of rainfall and convective storms (Hanley et al. 2021; Mittermaier et al. 2022). However, there are disadvantages: a characteristic lack of light rainfall and overestimation of the most intense rain rates is observed, and crucially, in all assessment of the TAM, one of the major challenges is the 'spin-up period'. The first 6–24 hours of the simulation are reported to have insufficient convection present, since convective structure is not present in the global reanalysis data used to reinitialise the model, so convection and therefore precipitation take some time to develop within the model (Lean et al. 2008). The effect of the spin-up period is to reduce the utility of forecasts at short lead time, which means that forecasters tend to use simulations which have been initialised earlier, where convection has had time to 'spin-up' fully, but these prior initialisations lack more recent information available from global reanalysis and are likely to deviate more significantly from the true large-scale state (Woodhams et al. 2018).

Data assimilation (DA) on convective scales may be a solution to the problem posed by the spin-up period, but in the tropics and particularly in regions such as West Africa, observational data are sparse. High-quality and high-resolution observational data are required for effective convective-scale data assimilation, and even where such data are available, DA on kilometre scales in the tropics is challenging in itself due to the nonlinear nature of tropical convection (Gustafsson et al. 2018), and is particularly challenging in understudied regions since a well-

calibrated DA scheme requires background-error covariances to be calculated from existing simulations. Furthermore, DA is computationally expensive; if its benefits could be limited then it is not worth the extra cost. As a result, alternative methods for convective-scale initialisation have been trialled which blend other forms of regional information with global reanalysis data; for example, by using high-resolution model output from previous initialisations of the regional model.

The implementation of such a technique in the MetUM was termed 'warm-starting' in a seminal paper on the method by Short and Petch (2022). Warm-starting blends smaller-scale structures from the previous model run with the global reanalysis data, allowing for the assimilation of new larger-scale information while reducing the spin-up period by providing some existing convective-scale structure at smaller scales. Details of the process are outlined in the following subsection. By contrast, the traditional form of initialising models simply by regridding global analyses to the regional grid is referred to as 'cold-starting'. Short and Petch (2022) showed significant improvements in fractional skill score (FSS) by applying the warm-starting technique to a regional simulation over Darwin, for a relatively cheap computational cost of applying the technique.

Warm-Starting Implementation

For regional modelling, two simulations are run: a driving global model, and a regional simulation whose LBCs are driven by the global model. These two simulations are used to generate a new initialisation (cycle $n + 1$) from a previous model cycle (cycle n); a visual reference is provided in the form of a flowchart in figure 3.2, which has been created based on the process of generating a warm-started simulation described in Short and Petch (2022).

To begin initialising a new cycle of the driving global model, a dump from the previous run's T+3 forecast is taken, and increments from the 4D-VAR global analysis are applied (see Rawlins et al. 2007), effectively giving a short forecast with slightly more information applied than at initialisation of the previous cycle. This forecast is assigned to be (cycle length - 3) hours before the 'initialisation' of the new cycle; for example, since Short and Petch (2022) use a 6-hour cycle length, the forecast 'begins' is at T-3 for cycle $n + 1$. Meanwhile, the regional model cycle n continues to be driven by the evolving global model in cycle n.

The new cycle $n + 1$ T-3 forecast is integrated forward up to the T+0 'initialisation', and the

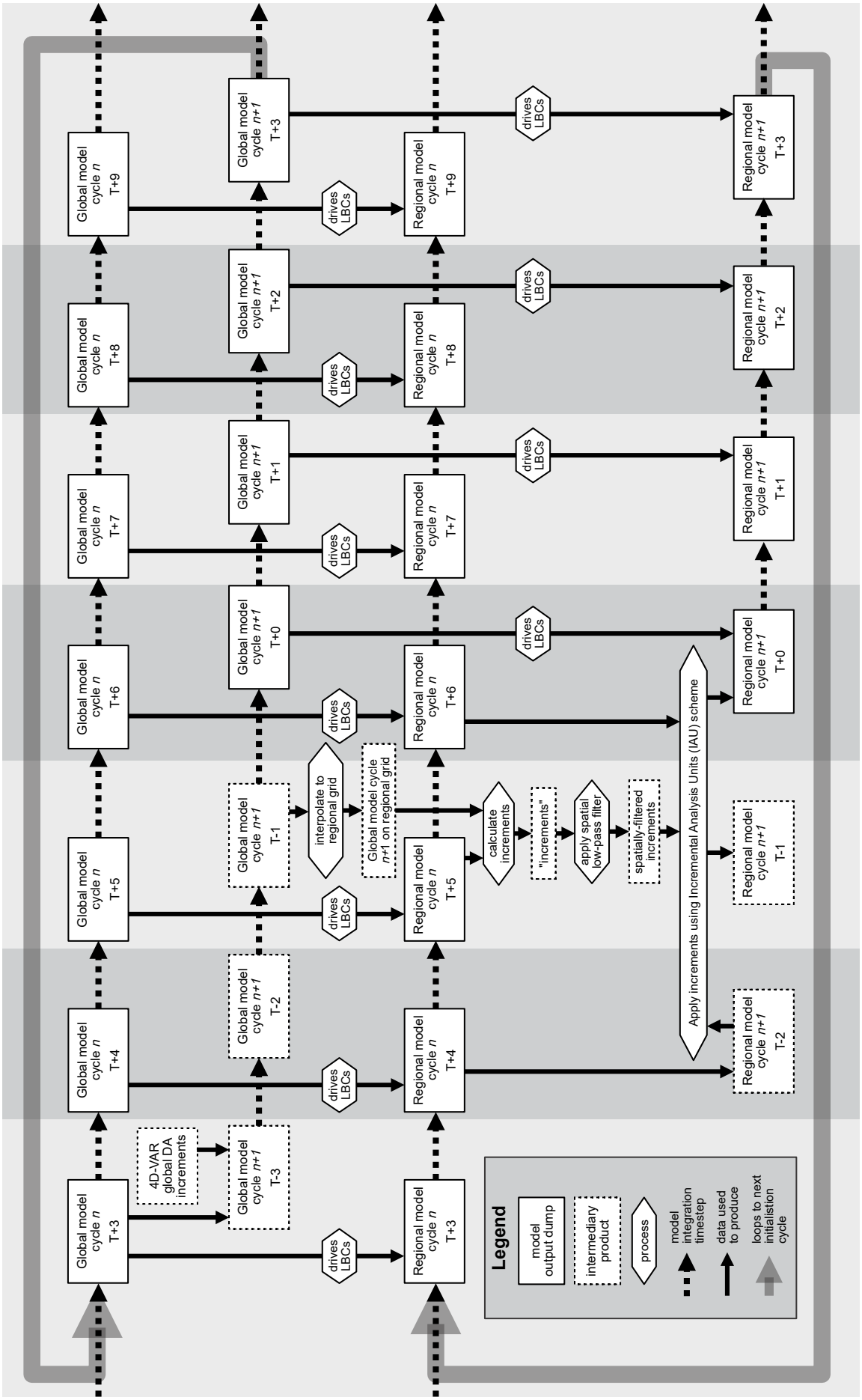

Figure 3.2: A flowchart illustrating the process of warm-starting a new regional simulation run (cycle n+1) using the previous global and regional runs (cycle n).

resulting global cycle $n+1$ forecasts at T-2, T-1, and T+0 are interpolated onto the regional grid. The regional forecasts from cycle n at T+4, T+5, and T+6, are subtracted from the interpolated global cycle $n+1$ forecasts at T-2, T-1, and T+0 respectively. A low-pass sixth-order implicit tangent spatial filter $\hat{\alpha}(k)$ is then applied to these 'increments':

$$\hat{\alpha}(k) = \left[1 + \epsilon \tan^6\left(\frac{k\Delta}{2}\right)\right]^{-1} \tag{3.1}$$

where $\epsilon = \tan^{-6}\left(\frac{k_c\Delta}{2}\right)$, and k_c is a characteristic wavenumber defined such that $\hat{\alpha}(k) = 0.5$ and associated with a particular spatial scale $\lambda_c = \frac{2\pi}{k_c}$. Physically, the filtering means that large-scale structure with $\lambda > \lambda_c$ is dominated by the global analysis, while on smaller scales, $\lambda < \lambda_c$, features from the previous regional simulation cycle are retained. Short and Petch (2022) tested several values of λ_c, with the most skilful forecasts occurring for a value of $\lambda_c = 400\,\text{km}$.

After the filtering, the increments are then added to the regional model cycle n simulations over a set time window (Short and Petch (2022) selected two hours) using the incremental analysis update scheme (Bloom et al. 1996) in order to avoid introducing instabilities associated with high-frequency gravity wave disturbances with a period smaller than the length of the time window. During the time window, the LBCs begin to be updated from the new global forecast cycle $n+1$ rather than the previous cycle. Once the increments have been applied, the model is run to the desired forecast length, and used for the initialisation of the next cycle.

The technique is applied to a subset of the prognostic variables: u and v wind components, potential temperature, density, Exner pressure, and moisture. Moisture is treated differently by the global and regional models, so when increments are computed between them, relevant variables must be converted accordingly. Global total specific humidity q_T is calculated by taking the sum of specific humidity q, cloud liquid water fraction q_l, and cloud ice fraction q_i, and increments of q_T are added to the specific humidity field q in the regional model because the lack of a deep convection scheme allows the regional model to independently distribute moisture across phases. Soil moisture also undergoes nudging towards the global reanalysis, but no spatial filtering is applied.

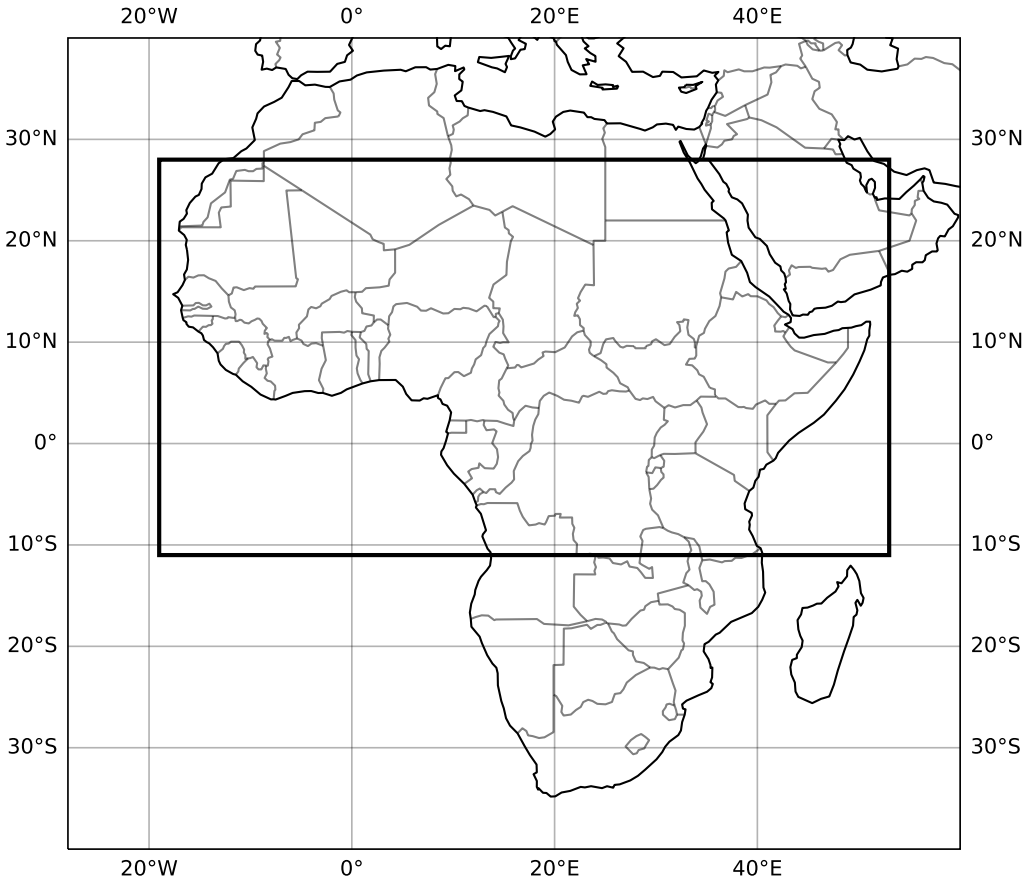

Figure 3.3: Domain of warm-starting experiment shown by thick black line.

Warm-Starting Simulations in West Africa

Warner et al. (2023) carried out a similar experiment over an African domain, configuring a model setup analogous to the TAM. They showed demonstrable improvements in the skill of rainfall prediction not only in the first 12–24 hours of the spin-up period, but also beyond into the later hours of the forecast, which are specifically associated with the initialisation technique. To explain why the warm-starting technique shows improvements in these simulations, chapter 8 examines the dynamics of the simulations and their control counterparts.

In Warner et al. (2023), several experiments were run. Based on the results of Short and Petch (2022), the key warm-starting experiment was run with a characteristic filtering scale of $\lambda_c = 400\,\text{km}$ and 6-hourly cycling. The simulation was run throughout June–August 2020 (capturing the evolution to maturity of the WAM) over the TAM domain (see figure 3.3, along with a corresponding 'cold-started' simulation (initialised by interpolating global reanalysis onto the regional grid), and a free-running simulation, whose LBCs are updated by a global model forecast which is reinitialised every six hours. The driving global model is a MetUM configuration using GA6.1 (Walters et al. 2017). In addition, further warm-starting trials were run for June 2020 with $\lambda_c = 200\,\text{km}$, one with 6-hourly cycling as for the longer experiment and one with 12-hourly cycling.

3.2 Storm Tracking

To examine the dynamics of MCSs over their life cycle, from initiation to mature phase and decay, it was necessary to use a dataset of tracked MCSs. Chapter 7 utilises the dataset of MCSs tracked using outgoing longwave radiation (OLR) in CP4 identified by Crook et al. (2019).

The storm-tracking algorithm used is based on the algorithm described in Stein et al. (2014). For each timestep, cloud clusters are identified as contiguous regions where the OLR $< 167\,\text{W}\,\text{m}^{-2}$, equivalent to a brightness temperature of $< 233\,\text{K}$. Between timesteps, a velocity field is calculated by cross-correlating images, and the field is used to advect the first timestep towards the second timestep, where, if the fractional overlap between an advected cluster and a cluster in the second timestep exceeds 0.6, the clusters are deemed to be part of the same storm. When a new cluster has no overlap with an advected cluster from the previous timestep, it is considered a storm initiation, and once an advected cluster does not overlap with any clusters

in the following image, the storm is considered to stop existing. Where multiple clusters from the first timestep overlap a single cluster in the second timestep, the storms are said to merge, and similarly, if a single cluster from the first timestep overlaps two in the second timestep, the two clusters are said to have split from the first storm.

Only storms with a maximum area that exceeds 5,000 km^2, and a lifespan of at least 6 hours, are categorised as MCSs. Under these criteria, 20,135 MCSs were identified between June and September throughout the ten years of the CP4 current-climate simulation, with 21,061 in R25.

3.3 Observational data

In addition to the MetUM simulations used in the thesis, chapter 5 also examine some observational data, both from in-situ measurements (JET2000 data) and satellite measurements.

3.3.1 JET2000

JET2000 was a 7-day field campaign at the end of August 2000, during which 35 hours of flying were undertaken using the Met Office's MRF C-130 aircraft, with the aim of characterising the dynamics of African Easterly Waves (AEWs) along the African Easterly Jet (AEJ). The C-130 aircraft took dynamical and thermodynamical measurements, as well as observing aerosols and radiation, and throughout the flights 112 dropsondes were deployed over key sections of flights at 0.5-1 ° resolution (Thorncroft et al. 2003).

Flight A781 on 29 August 2000 (flight 3 listed in their table 1), which flew both ahead of and behind an approaching mesoscale convective system, provides the data used in chapter 5. The western leg of the box-pattern flown by flight A781 passed in front of the storm, while the eastern leg travelled along a constant longitude of approximately 2.2 ° E and passed behind the MCS located at roughly 11 ° N. During the passage, 34 dropsondes were released, which give details of the vertical profile associated with the dynamics of the decaying storm.

3.3.2 Global Precipitation Measurement (GPM)

The Global Precipitation Measurement (GPM) mission is an international satellite mission which gathers data to facilitate global retrievals of precipitation rates which utilise a range of instruments (Hou et al. 2014). In chapter 8, the Integrated Multi-satellitE Retrievals for GPM (IMERG) retrieval Version 06B final product (Huffman et al. 2019) is compared to modelled

precipitation. The product uses data from both passive microwave and activate radar radiometer satellite instruments and is output at 0.1 ° grid-spacing every half hour. The simulations are regridded to the IMERG grid and the IMERG product is averaged over each full hour for a more accurate comparison.

3.4 ERA5 Reanalysis

The European Centre for Medium-range Weather Forecasting (ECMWF)'s ERA5 dataset is a reanalysis of atmospheric fields covering the time from January 1940 to the present. A deterministic reanalysis is produced using 4D-VAR DA along with forecasts from ECMWF's Integrated Forecasting System (IFS) model on 137 model levels from the surface up to 0.01 hPa at a horizontal grid resolution of 0.25 ° (Hersbach et al. 2020). ERA5 also includes an ensemble at lower resolution which is used for the DA process and to provide a relative random uncertainty associated with the deterministic high-resolution simulation. The IFS configuration used in ERA5 uses a convection parameterisation originally based on Tiedtke (1989) with some adaptations. In chapter 4, its winds on pressure levels are used as a comparison for the Hardy et al. (2021) MetUM simulations (see section 3.1.1).

Chapter 4

Closing the Circulation Budget

The first results chapter evaluates a method that can be used to interrogate the processes that lead to variation in circulation. In the contemporary era of high-volume data output from high-resolution convective-scale models, the question of how exactly to diagnose the interactions between mesoscale convection and synoptic systems - the key topic that this thesis aims to address - is an underappreciated challenge (Kendon et al. 2021). It is necessary to develop methods to quantify dynamical changes across scales in model simulations.

Calculating the circulation budget is one such method to evaluate variation in synoptic-scale circulation in terms of vorticity-related processes. Circulation Γ is the contour integral of horizontal velocity $\boldsymbol{u} = (u, v)$ around some closed contour C, equivalent to the surface integral of absolute vertical vorticity η contained in a region S enclosed by C:

$$\Gamma = \oint_C \boldsymbol{u} \cdot d\boldsymbol{l} = \iint_S \eta dA \tag{4.1}$$

Circulation, therefore, is a large-scale quantity encapsulating smaller-scale dynamics within a region, making it a powerful tool for examining scale interactions. By formulating a circulation budget, and analysing the magnitude of different terms, one can evaluate the changes to circulation which are associated with different processes. Any missing terms can be calculated by calculating the difference between the two sides of the budget equation to obtain a residual proxy for a missing term. It is of interest to evaluate how close the values of either side of the equation are, having calculated any terms which can be directly determined from model

outputs. The question of how well-matched the sides of the equation are referred to hereafter as the 'closure' of the circulation budget.

Here, the circulation budget is calculated in a numerical weather prediction (NWP) non-idealised model over Southeast Asia using various temporal and spatial resolutions, in order to understand the capacity for practical applications of the circulation budget to typical model output products. The model in question was generated in Hardy et al. (2021) and is described in more detail in section 3.1.1. Evaluating the use of the circulation budget technique for different model output time intervals is of interest because, as the spatial resolution of models increases with the advent of convective-scale high-resolution simulations, the volume of output data also increases, and compromises are often made in terms of model output timestep to limit the volume of data due to storage constraints. Understanding whether the instantaneous values of circulation budget terms accurately sum to the circulation tendency at a given timestep, regardless of the output frequency, may motivate the use of the circulation budget for further analysis of the interactions between convection and circulation as proposed by Haynes and McIntyre (1987).

Section 4.1 explains the circulation budget's derivation and outlines the meaning of the terms within it. Section 4.2 describes the model setup and errors that may be introduced in the methodology used, and justifies the case selection. In section 4.3, the analysis evaluates how well the circulation budget is closed at the highest temporal and spatial resolutions available over several case studies. Sections 4.4 and 4.5 discuss the sensitivity of the analysis to the size of the selected domain and features of its boundary, and to the inclusion of estimated frictional terms respectively. Then, the effect of the output model timestep (section 4.6) and the spatial resolution of the model grid (section 4.7) on the closure of the circulation budget is evaluated, with a comparison to ERA5 reanalysis data in section 4.9. A holistic evaluation of the technique and its applications is presented in section 4.10.

4.1 The Circulation Budget

The circulation budget is derived by integrating the vorticity budget. The equation for absolute vorticity η (sum of relative vorticity ζ and planetary vorticity f), can be written in flux-form:

$$\frac{\partial \eta}{\partial t} = -\nabla_{xy} \cdot \boldsymbol{J} \qquad \text{where} \qquad \boldsymbol{J} = \begin{pmatrix} u\eta + \omega \frac{\partial v}{\partial p} - G \\ v\eta - \omega \frac{\partial u}{\partial p} + F \end{pmatrix} = \boldsymbol{u}\eta - \omega \hat{\boldsymbol{k}} \times \frac{\partial \boldsymbol{u}}{\partial p} + \hat{\boldsymbol{k}} \times \boldsymbol{F}. \tag{4.2}$$

∇_{xy} is the differential operator in the x- and y-directions, $\boldsymbol{F} = (F, G)$ is frictional forces, and $\hat{\boldsymbol{k}}$ is the unit vector along the p-axis. Terms represent the accumulation of vorticity horizontally through the sides of a 2-D box on consistent pressure surfaces ($\boldsymbol{u}\eta$), the vertical tilting of horizontal vorticity into the vertical vorticity component ($-\omega\hat{\boldsymbol{k}} \times \dfrac{\partial \boldsymbol{u}}{\partial p}$), and frictional terms ($\hat{\boldsymbol{k}} \times \boldsymbol{F}$). Equation 4.2 is specifically the flux-form vorticity budget under the assumptions of a shallow atmosphere in hydrostatic balance, in pressure coordinates.

Integrating over a closed pressure surface S enclosed by contour C gives

$$\frac{\partial \Gamma}{\partial t} = -\oiint_S \nabla_{xy} \cdot \left(\boldsymbol{u}\eta - \omega\hat{\boldsymbol{k}} \times \frac{\partial \boldsymbol{u}}{\partial p} + \hat{\boldsymbol{k}} \times \boldsymbol{F} \right) dS. \tag{4.3}$$

Through the divergence theorem, equation 4.3 can be converted into a contour integral.

$$\frac{\partial \Gamma}{\partial t} = -\oint_C \left(\underbrace{\boldsymbol{u}\eta}_{\substack{\text{vorticity} \\ \text{accumulation}}} \quad \underbrace{-\omega\hat{\boldsymbol{k}} \times \frac{\partial \boldsymbol{u}}{\partial p}}_{\substack{\text{vortex} \\ \text{tilting}}} + \underbrace{\hat{\boldsymbol{k}} \times \boldsymbol{F}}_{\text{friction}} \right) \cdot \hat{\boldsymbol{n}} dl. \tag{4.4}$$

Equations 4.3 and 4.4 represent the circulation budget. The terms in each equation allow us to characterise how different processes at different scales govern changes to synoptic-scale circulation. Similar techniques have been used to analyse the circulation budgets associated with tropical cyclones (e.g. Raymond et al. 2014) and MCSs (e.g. Davis and Galarneau 2009).

Figure 4.1 is a schematic illustration of the processes involved in the (a) vorticity accumulation and (b) vortex tilting terms. The vorticity accumulation term accounts for any ways in which the vertical vorticity is modulated by horizontal winds on pressure surfaces. This includes advection of vorticity anomalies into or out of the domain, and also the stretching of vorticity anomalies due to convergence in the domain. Vortex tilting relies on the presence of horizontal vorticity and some vertical velocity. A localised vertical velocity can effectively 'tilt' horizontal vorticity into the vertical, which is illustrated in figure 4.1b through the concept of vortex tube lifting by an updraught on the edge of a domain. For positive $\dfrac{\partial \boldsymbol{u}}{\partial p}$, as illustrated in the schematic, an updraught (negative ω) on the southern edge of the domain will induce a positive vertical vorticity anomaly inside the domain, which will increase the circulation (equation 4.1 implies that a positive vorticity anomaly inside region S increases circulation). The positive circulation tendency induced corresponds to a positive sign overall for the tilting term when integrated,

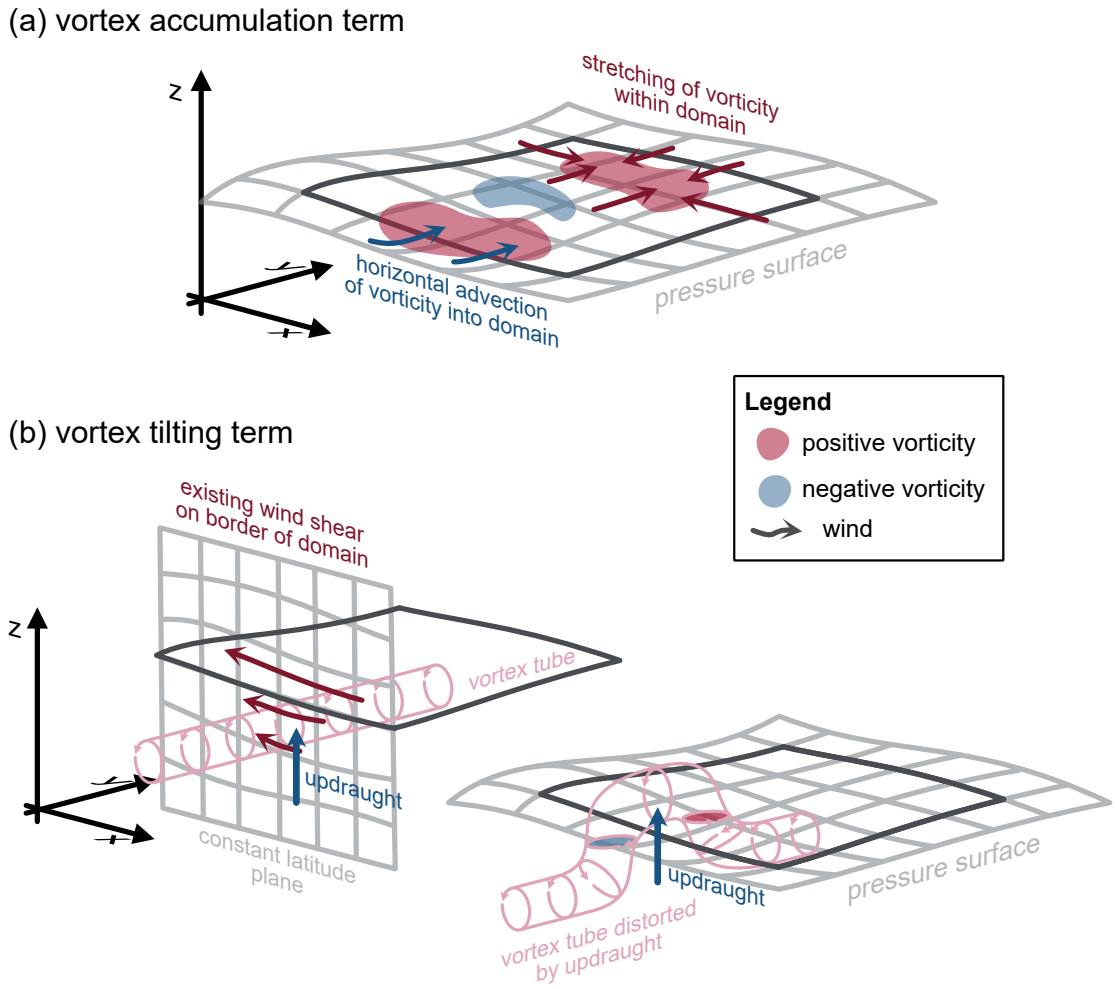

Figure 4.1: Schematic illustrations of the processes that cause changes in circulation via (a) vorticity accumulation and (b) vortex tilting. In (b), an example shear profile is illustrated by the dark red arrows; this does not necessarily reflect the shear in the Maritime Continent (the region that the case study focuses on) at all times. Instead it represents a shear profile typical of background flow in West Africa, the focus of the thesis as a whole.

anticlockwise, along the southern edge with x increasing.

Mathematically, for a shallow and hydrostatic atmosphere, equation 4.4 should be exact: the instantaneous values of the right-hand side (RHS) accumulation, tilting, and friction terms should sum to an accurate time derivative of circulation (left-hand side; LHS). For this reason, an approach to calculating any circulation budget terms for which model output data is not available (for example, commonly, the friction term) is to calculate the residual between the LHS and incomplete RHS, to estimate the term which has not been directly calculated. However, the residual technique is not frequently used because it is uncertain how closely the sides of the equation match: referred to hereafter as the 'closure' of the circulation budget.

Sources of error in the circulation budget closure emerge from several factors. Firstly, contemporary models no longer assume a shallow or hydrostatic atmosphere, so there will be errors introduced from non-hydrostatic deep atmosphere terms. Secondly, inaccuracies may be introduced when calculating terms in the equation on both sides using traditional model output, which are linked to logistical constraints such as temporal or spatial output resolution, or the presence of parameterisations in simulations. These sources of error are discussed in more detail in the following section.

It is possible to calculate the vorticity budget for a domain, but for the purposes of answering the questions pertinent to this thesis, the circulation budget was a more appropriate choice. As noted by equation 4.1, circulation is able to link processes that happen within a domain (changes in vorticity anomalies) to a measure that summarises the circulation pattern within the domain, and thus it is a measure that inherently accounts for processes across spatial scales. Furthermore, the circulation and circulation tendency act as a single measure of circulation for a selected region, whereas vorticity budgets are calculated at each grid point. The single value not only allows for more straightforward comparison across models, cases, and times, but also automatically damps out some of the noisier values that emerge in grid-cell-by-grid-cell measures.

4.2 Data, Methodology, and Case Selection

This chapter uses data from a MetUM ensemble run to examine Typhoon Nepartak (2016), published in Hardy et al. (2021) and described in more detail in chapter 3. The data was used

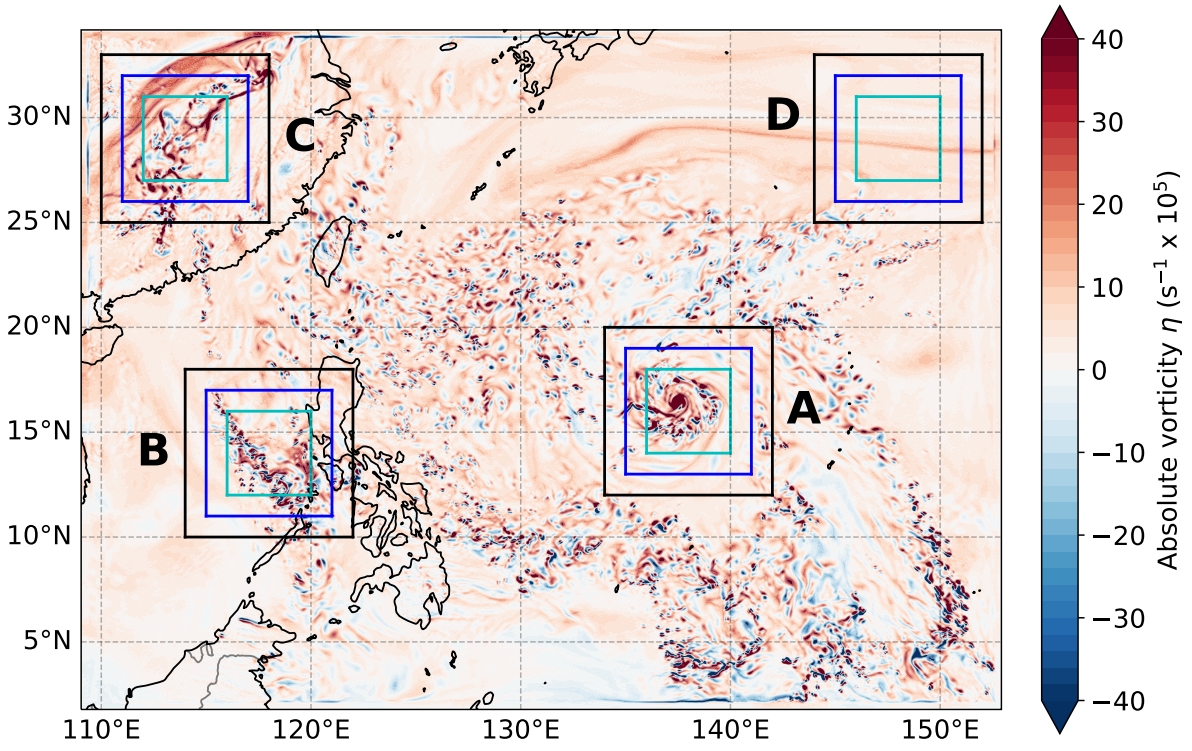

Figure 4.2: A snapshot of absolute vorticity (η, in $s^{-1} \times 10^5$) at 700 hPa, at 01 UTC on 05 July 2016, as simulated by a MetUM ensemble member. Case study regions are outlined by the black (8×8 °), blue (6×6 °), and cyan (4×4 °) boxes labelled A (Typhoon Nepartak), B (an oceanic MCS), C (an MCS over land), and D (oceanic region with least active convection).

because of its convective-scale 4.4-km spatial resolution and high output time resolution, at 5-minute intervals. The high frequency output time interval allows for the simulation of different model output timesteps for the calculations. The ensemble member is initialised at 12 UTC on 02 July 2016 and runs until 00 UTC on 06 July 2016.

Consider regions illustrated in figure 4.2, labelled A–D. The regions cover (A) the mature phase of Nepartak, (B) an MCS organised into a squall line which is largely positioned over the ocean, (C) an area over the land, and (D) an area over the ocean with minimal active convection. For each region we consider three boxes of different sizes (8×8 °, 6×6 °, and 4×4 °) in order to test the sensitivity of the budget to the area of the region. Circulation around each box was calculated at each of the 5-minute model output intervals for the duration of the simulation, from 13 UTC on 02 July to 07 UTC on 05 July. Once circulation had been calculated, circulation tendency was estimated through centred finite-difference numerical differentiation of circulation with respect to output time. However, the output time intervals, Δt, were varied in this calculation, from the highest-resolution time output of 5 minutes down to a Δt of 6 hours. While the model

was not output at 6-hour time intervals, this simulated the accuracy of circulation tendency calculated using finite-difference methods for lower output time resolutions.

Later in the chapter ERA5 reanalysis data is analysed for the same time period. The temporal output resolution is 1-hourly and the spatial resolution is 0.1 °. More detail is given in section 3.4 of chapter 3.

Instantaneous circulation budget terms were calculated at the same 6-hourly intervals over the simulated period at various pressure levels. The terms calculated were vorticity accumulation ($-\oint_C \boldsymbol{u}\eta \cdot \hat{\boldsymbol{n}}\boldsymbol{dl}$), vortex tilting ($\oint_C \omega\hat{\boldsymbol{k}} \times \frac{\partial \boldsymbol{u}}{\partial p} \cdot \hat{\boldsymbol{n}} dl$), and friction $-\oint \hat{\boldsymbol{k}} \times \boldsymbol{F} \cdot \hat{\boldsymbol{n}} dl$. The friction coefficients $\boldsymbol{F}$ were calculated using the model's output of the xz- and yz-components of turbulent wind stress, τ_{xz} and τ_{yz}, following the definition used in the calculations in Hardy et al. (2021):

$$F_{xv} = \frac{1}{\rho}\frac{\partial \tau_{xz}}{\partial z}; \qquad F_{yv} = \frac{1}{\rho}\frac{\partial \tau_{yz}}{\partial z}. \tag{4.5}$$

Here, F_{xv} and F_{yv} denote the components of frictional force per unit mass in the y and x directions, such that $\hat{\boldsymbol{k}} \times \boldsymbol{F} = F_{yv}\hat{\boldsymbol{i}} - F_{xv}\hat{\boldsymbol{j}}$. It should be noted that equation 4.5 is specifically formulated for the case of a mixed planetary boundary level over the ocean. Therefore, these terms may not be valid outside of the boundary layer, or over land, where more complex surface fluxes may interfere.

The nature of the output data from the MetUM simulation studied does impose some limitations on the accuracy of the budget closure. To begin with, the MetUM simulates a non-hydrostatic, fully-compressible, deep atmosphere, so terms that are usually neglected through scale analysis to reduce equations to those of a shallow, incompressible, and hydrostatic atmosphere (for example, the component of Coriolis acceleration proportional to the cosine of latitude; see White et al. 2005) will mean that the RHS terms of equation 4.4 do not sum to the exact circulation tendency.

Furthermore, the model output produced vertical velocity in height coordinates for the 5-minute time resolution, which had to be converted into vertical velocity in pressure coordinates, ω using MetPy (May et al. 2016). The conversion process again assumes hydrostatic conditions, which may introduce inaccuracies. Also, all dynamical fields were output on hybrid height levels, so had to be interpolated onto pressure levels, carried out using linear interpolation in one dimension (again calculated using MetPy). For ERA5, ω was output, and all variables were

available on pressure levels, so the same interpolation was not necessary.

Inexact time derivatives are also typically a significant source of error in the LHS $\frac{\partial \Gamma}{\partial t}$ term, for several reasons. Firstly, there are different techniques in calculus used internally to the model and in the post-processing analysis. The internal MetUM solver within its dynamical core is a semi-implicit semi-Lagrangian solver, meaning that integrals and derivatives are taken along trajectories (Wood et al. 2014). Furthermore, Arakawa C-grid staggering means that variables u, v, and p are calculated at different points in the grid during the dynamical calculations at each model timestep. Meanwhile, the post-processing analysis in this chapter uses a central point finite difference method to calculate gradients of the model output, regridded using linear interpolation to various horizontal grid spacings with consistent differences in latitude and longitude across the grid. The linear regridding itself may result in aliasing of small-scale features onto a coarser scale grid which will introduce inaccurate values when circulation is calculated by integrating around regions.

Naturally such differences in computational techniques will result in different outputs. However, the major source of error is the limitation in accuracy of any time derivatives by the size of the smallest model output interval. The model output interval is 5 minutes, compared to a model calculation timestep of 75 seconds. Since the output interval is four times larger than the model calculation timestep, the derivatives taken of the model output data are inherently relatively inexact compared to internal model derivatives.

As well as this, even with perfect interpolation, ignoring errors introduced by assuming hydrostatic equilibrium, and with perfectly exact time derivatives, a model's circulation budget still may not close. In a model, equations are solved numerically, which means that outputs are subject to truncation and numerical diffusion, limiting accuracy. Furthermore, sub-grid scale processes such as turbulence and convective processes may be obscured by parameterisations (for example, the boundary layer or convection schemes respectively) which simply represent the bulk output of smaller-scale process on the model grid. Realistically, no model explicitly represents processes at all scales, so there will always be unresolved sub-grid scale processes that will introduce differences between the sides of the circulation budget equation. ERA5 also has the added complication of data assimilation, which means that the model is being updated continuously with observations, which can push the model away from precisely solving the equations of the dynamical core as it would do were it a free-running model.

The following sections focus on varying the techniques used to calculate the circulation budget in order to investigate how some of these factors affect the budget's closure.

4.3 Closing the Circulation Budget

To illustrate the calculation, the circulation budget is calculated at the instant at which the snapshot in figure 4.2 was taken. Figure 4.3 shows vertical profiles in regions (a)–(d) for the 8×8 ° boxes shown in black in figure 4.2. The circulation budget terms are shown in the faded coloured lines, with their sum shown as the thick black line, denoting the total of the RHS of equation 4.4.

For the most part, and certainly in the cases of regions (a) and (c), the major contribution to the sum is from the vorticity accumulation term, shown in blue, which accounts for the effect of convergence and divergence causing vortex stretching and the advection of vorticity anomalies in or out of the box. For (a), the tropical cyclone exhibits a characteristic pattern of convergence and enhanced cyclonic circulation up to around 550 hPa, where the pattern reverses and becomes anticyclonic with the upper-level outflow. The tilting term (orange) is usually the next-largest term at most levels and for most cases, and is typically the effect of subsidence and ascent at the edges of the box tilting horizontal vorticity into the vertical. The friction term (green) is the smallest term most of the time, but can be very noisy.

For the four regions at the selected time, the circulation tendency $\frac{\partial \Gamma}{\partial t}$ is calculated at the output time resolution. The highest-possible output time resolution (5 minutes) is used to attempt to get the most accurate value of circulation tendency possible. The estimated circulation tendency (shown as the grey line in figure 4.3) does not match the RHS sum of circulation budget terms exactly, but it captures many of the major features of the vertical profile, largely matching the sign and following fluctuations in amplitude.

It is helpful to quantify the errors over the vertical profile between the instantaneously-calculated circulation budget and the differentiated circulation tendency, not only for the 01 UTC on 05 July 2016 instance, but also for the other 12 6-hourly intervals across the simulation. To do so, the ratio between the variance of the residual (difference between the RHS and LHS of equation 4.4) and the variance of the LHS of the equation was calculated. The metric is a means of expressing the extent to which the residual's variance compares to the signal's variance. If the

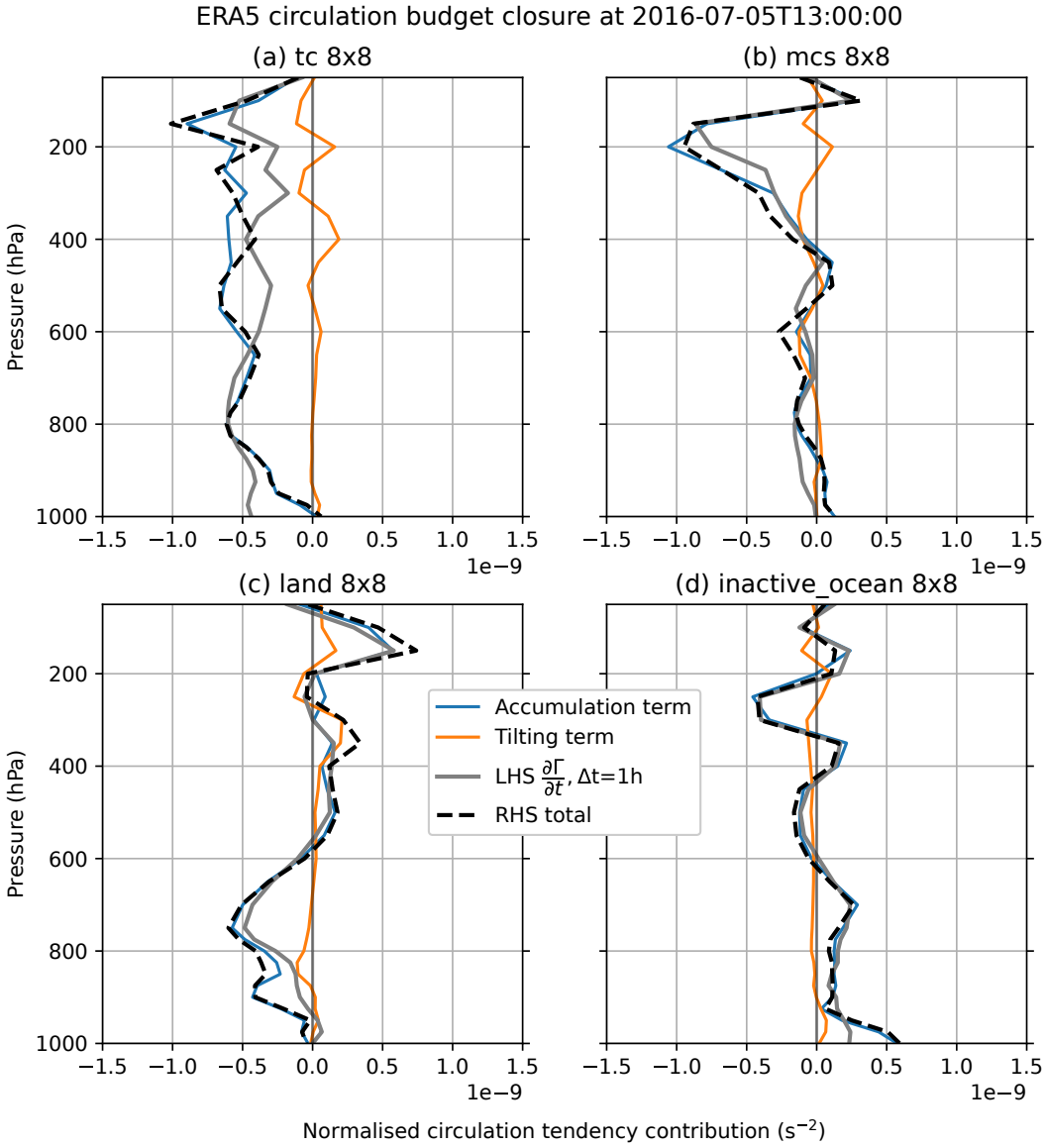

Figure 4.3: The circulation budget terms calculated around the 8×8 ° black boxes labelled a–d in figure 4.2, at 01 UTC on 05 July 2016 in the simulation. The thinner coloured lines indicate the circulation budget terms calculated at each pressure level: the vorticity accumulation term (blue), the tilting term (orange), and the friction term (green). The thick black line is the sum of the three RHS terms. The thick grey line is the circulation tendency $\frac{\partial \Gamma}{\partial t}$ at the same time around the box, calculated at time output interval Δt=5 minutes.

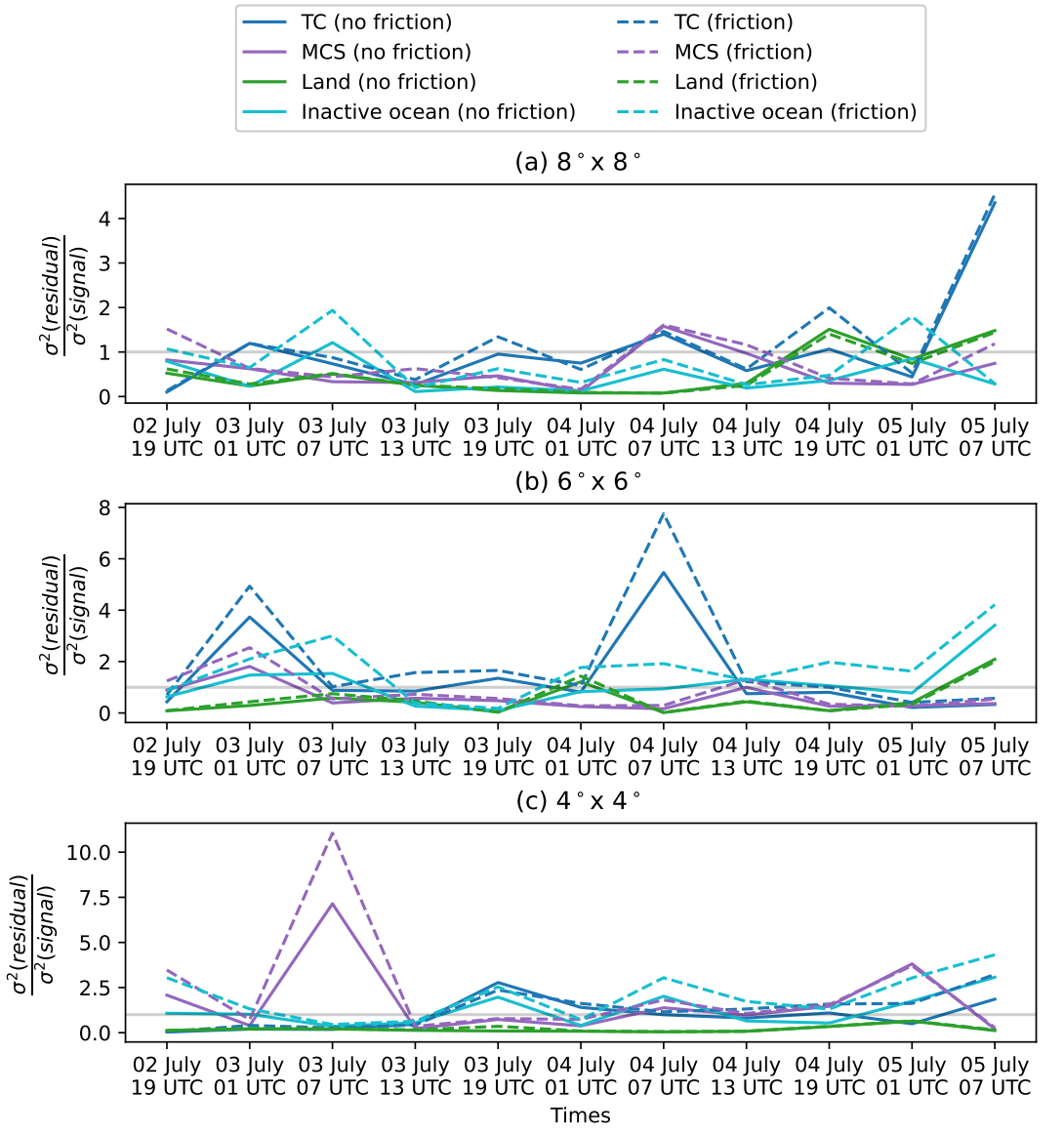

Figure 4.4: Ratio of the variance of residual (RHS budget terms subtracted from LHS $\frac{\partial \Gamma}{\partial t}$ circulation tendency) to variance of the signal (LHS circulation tendency), σ_r^2/σ_s^2, for each time that the circulation budget was calculated over the four regions illustrated in figure 4.2, for the three sizes of box, (a) 8×8°, (b) 6×6°, and (c) 4×4° boxes. Different coloured lines represent the different regions (mid-blue for the TC region, purple for the MCS, green for the land, and cyan for the inactive ocean). The solid lines show the variance ratio excluding the friction term on the RHS, and the dashed lines show the calculations including the friction term. A solid grey line indicates where $\frac{\sigma^2(\text{residual})}{\sigma^2(\text{signal})}$=1, the point at which variation in the difference between the signals is indistinguishable from variation in the signal itself. Note the difference in y-axis scale across the three plots.

ratio is greater than one, then the variance of the residual is greater than the variance of the signal, implying that it would be impossible to distinguish the difference in signal between the RHS and LHS from the signal itself. As a shorthand going forward, the ratio is referred to as σ_r^2/σ_s^2, where σ_r^2 is the variance of the residual and σ_s^2 is the variance of the signal.

Figure 4.4 shows the value of the ratio for each instantaneous time for which the budget was calculated. The ratios of residual to signal variance are different for different domain sizes, and different depending on the time at which they are taken. The ratio seems to increase as the box size decreases from the 8×8 ° to 4×4 ° regions. It also varies depending on whether friction is used to calculate the sum of the RHS budget terms. The latter two features are examined in more detail in the following few sections.

Nonetheless, the fact that the instantaneous circulation budget seems to, in many cases, follow the calculated circulation tendency is reassuring. It suggests that, were the circulation tendency calculated using a smaller model output timestep Δt, the two sides of the equation could be exactly equal. The similarity of patterns justifies that it is reasonable to take the instantaneous terms as a reasonably close approximation to the instantaneous derivative of circulation.

4.4 Sensitivity to Region Size

It is worth examining how the method responds to a changing domain size, so the circulation budget calculations were tested not only on the 8×8 ° regions (black squares in figure 4.2) but also smaller 6×6 ° (blue) and 4×4 ° (cyan) regions centred on the same features. To evaluate the error associated with each domain size, σ_r^2/σ_s^2 is calculated across the different-sized regions for the specific time shown in figure 4.2. The ratios are shown in figure 4.5.

For several of the cases (particularly the (a) TC and (b) MCS cases), there is an increase in the error ratio as the size of the domain decreases. An increase in error as domain size decreases makes intuitive sense because, where there are fewer grid points in the domain, each grid point will contribute more significantly to the mean value. Over larger domains, the small-scale noise will be averaged out and will not be reflected in the overall total. However, the inverse relationship of area and error is not reflected in the inactive ocean, and does not entirely hold for any of the regions, although it varies significantly between the regions themselves. Figure 4.2 shows the 700 hPa absolute vorticity across the region, which is a useful indicator of the

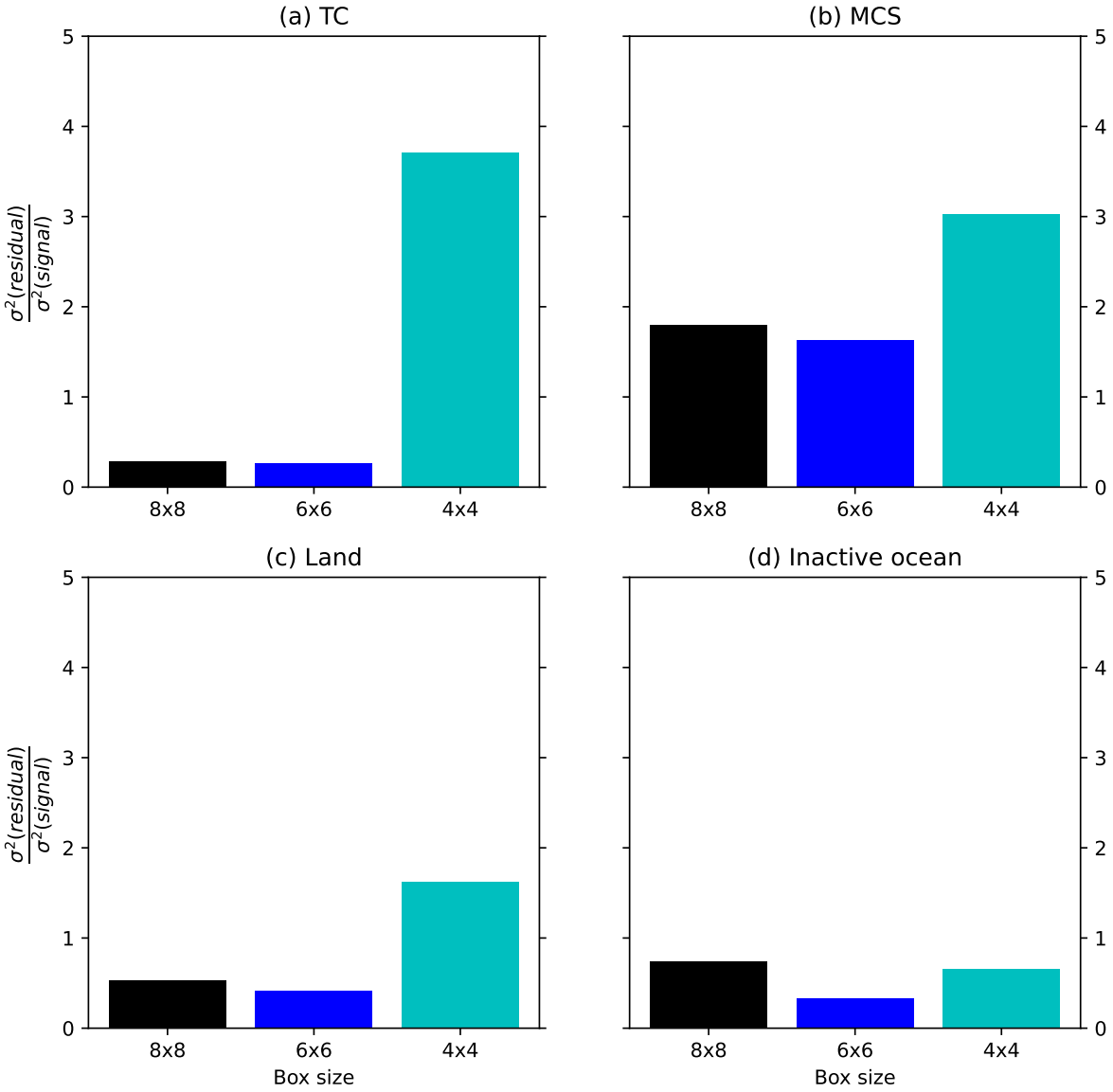

Figure 4.5: Ratios of the variance of the residual (RHS - LHS of the circulation budget equation) to the variance of the signal (LHS of the circulation budget), σ_r^2/σ_s^2, for the regions (a)–(d) depicted in figure 4.2 in corresponding subfigures, and different domain sizes for each regions illustrated by the differently-coloured bars: black for the $8\times8^\circ$ regions, blue for the $6\times6^\circ$ regions, and cyan for the $4\times4^\circ$ regions.

location of convection where there is strong vorticity, as discussed in section 2.3.1.

Differences in error between the domains are likely related to the variation of dynamics along the edges of the regions. Where the border of a region intersects convection, there are more errors introduced into both the circulation tendency term and separate budget terms leading to a poorer closure. Convection is a highly non-hydrostatic process, so the assumptions of hydrostatic equilibrium do not hold, inducing errors as discussed in section 4.2, and particularly in a CP model, instantaneous values of dynamical fields near convection are likely to be noisy. The introduction of such errors can be seen as the $4\times4^\circ$ TC box begins to intersect the TC structure, and even within the $8\times8^\circ$ MCS box there is error introduced since the domain intersects convective structure on the southern edge of the box. The oceanic region (d) is particularly low in error, and has a larger error fraction in its $8\times8^\circ$ domain than its smaller domains since the former intersects some scattered convection to the south.

4.5 Impact of Friction

Often, simulations do not output quantities which allow for the explicit calculation of friction, and in fact, in many cases, calculations of frictional forces are at best crude estimates based on approximations which rarely hold. For this reason, it is common to use the residual between the total circulation tendency and the circulation budget terms to estimate the contribution of friction to the budget. However, if the budget terms including the friction term do not add up to the calculated circulation tendency, or at least close to it, then the use of the technique is called into question.

The calculations of friction contributions are based on the xz- and yz-components of the wind stress tensor, which are output on the MetUM's native hybrid height levels. Using these levels to calculate the vertical derivatives, and the density field, one can calculate the horizontal friction terms as in equation 4.5. These terms can then be used to calculate the integral of the friction term in the circulation budget.

Figure 4.3 shows that the friction term (green line) is often noisy, often introducing spikes in the RHS total profile (black line) which do not necessarily bring the value closer to closure. Of interest is the fact that the friction term does not seem to significantly decrease in magnitude further away from the ground; typically friction is expected to be at its peak in the boundary

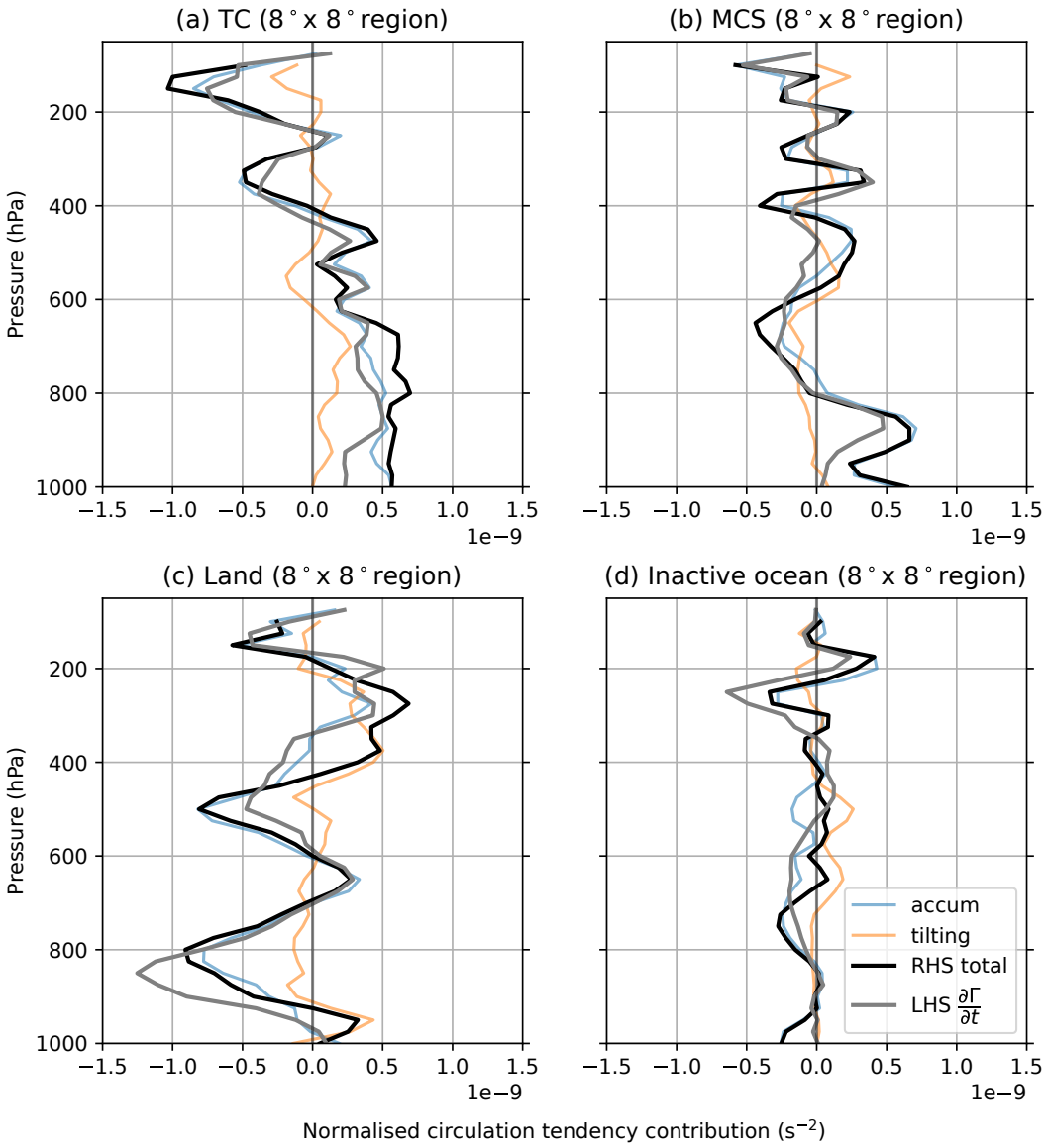

Figure 4.6: Similarly to figure 4.3, circulation budget terms not including friction calculated around the 8×8 ° black boxes labelled (a)–(d) in figure 4.2, at 01 UTC on 05 July in the simulation. The thinner coloured lines indicate the circulation budget terms calculated at each pressure level: the vorticity accumulation term (blue) and the tilting term (orange). The thick black line is the sum of the two terms. The thick grey line is the circulation tendency $\frac{\partial \Gamma}{\partial t}$ at the same time around the box.

layer where there is most turbulence. The term seems particularly erratic over land, where the assumptions made in its calculation hold less convincingly and boundary layer dynamics are complicated by orography, surface flux from different surface characteristics, and other inhomogeneities. Meanwhile, figure 4.6 shows the sum of the circulation budget terms at the same time and in the same regions as in figure 4.3, without the friction term being included. The erratic tendencies that it introduces are removed and overall it appears that the sum of just the accumulation and tilting terms are closer to the circulation tendency profile (grey line).

To compare the impact of including the friction term over the entire time period of the simulation, the mean of σ_r^2/σ_s^2 was calculated over all times for the four $8\times8^\circ$ domains, illustrated in figure 4.7. It appears that the inclusion of friction leads to a slightly increased error (less accurate closure of the circulation budget) for the MCS and land regions, whereas it decreases the error slightly in the TC and inactive ocean regions. The changes are, however, somewhat marginal in almost all cases. It is possible that the estimation of the friction term breaks down where there is convection on the boundaries of the region, inducing inhomogeneous and non-isotropic turbulent motions which do not produce reliable estimates for Reynolds stress. Because the improvement in circulation budget closure associated with the inclusion of the friction term calculation appears overall negligible, and for easier comparison to ERA5 data in later sections, where the relevant terms to calculate the friction term are not available, henceforth the RHS of the circulation budget equation is calculated ignoring the friction term.

4.6 Impact of Temporal Resolution

An aim of this chapter is to evaluate the circulation budget closure as it might be calculated in typical model outputs. Outputs were selected at larger time intervals in order to simulate different output timesteps Δt: as well as the model's native 5-minute timestep, we selected outputs at 10-minute, 20-minute, 30-minute, 1-hour, 3-hour, and 6-hour time intervals. From these selections, circulation tendencies were calculated for each of the Δt. The circulation budget terms were only calculated once, as for instantaneous model outputs the values would remain the same regardless of the time output interval.

The vertical profiles for calculations of circulation tendency at different time intervals, compared to the sum of the circulation budget terms calculated instantaneously, are shown in figure 4.8. At time resolutions up to around 30 minutes, the spatial pattern does not degrade much and

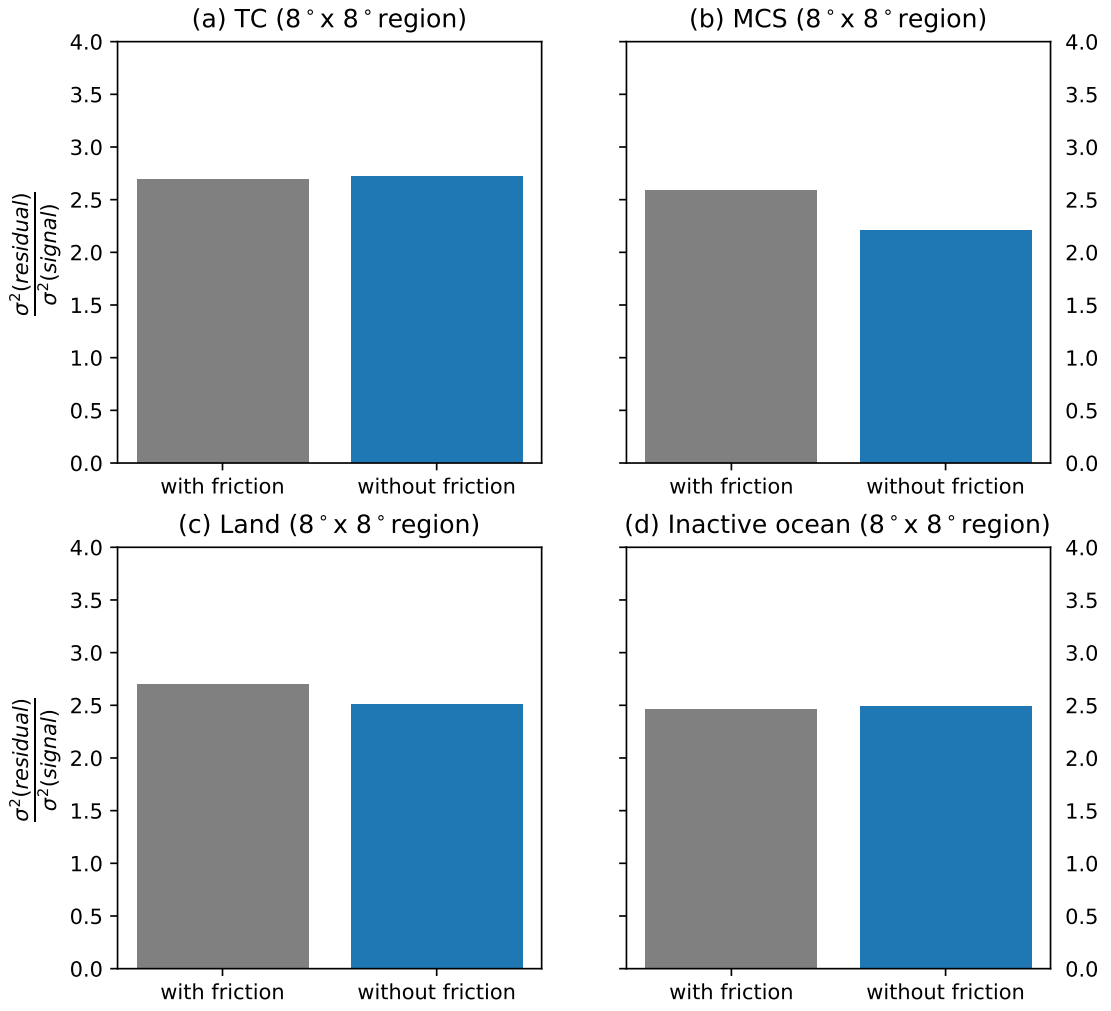

Figure 4.7: Ratios between the variance of the residuals between the RHS and LHS of the circulation budget equation, and the variance of the RHS of the circulation budget, σ_r^2/σ_s^2, calculated for the four 8×8 ° regions (a-d) shown in figure 4.2.

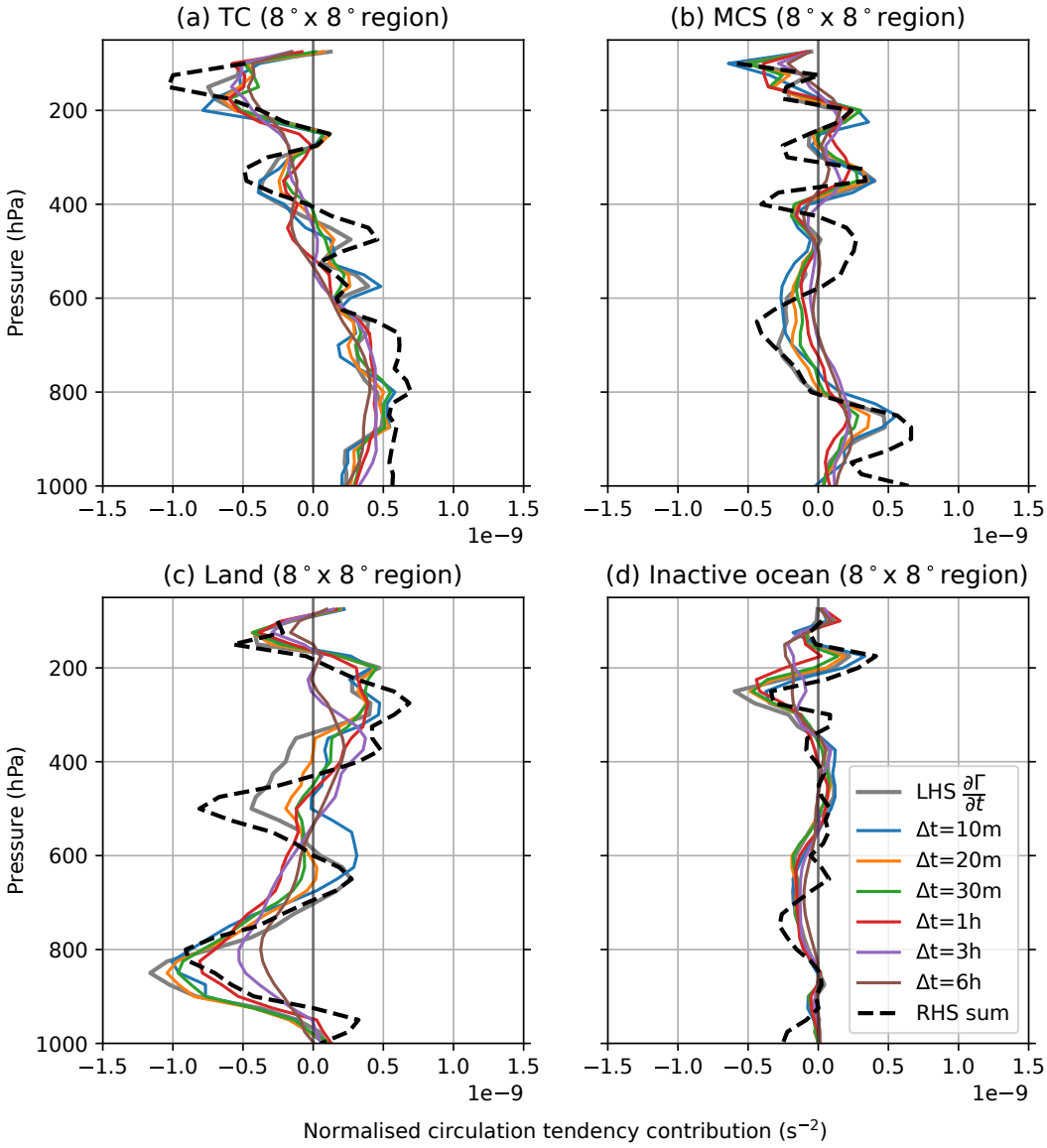

Figure 4.8: Circulation tendency for various Δt calculated around the 8×8 ° black boxes labelled a–d in figure 4.2, at 01 UTC on 05 July in the simulation. The dashed black line indicates the RHS sum of circulation budget terms while the coloured lines represent different Δt as illustrated in the key in subfigure (d).

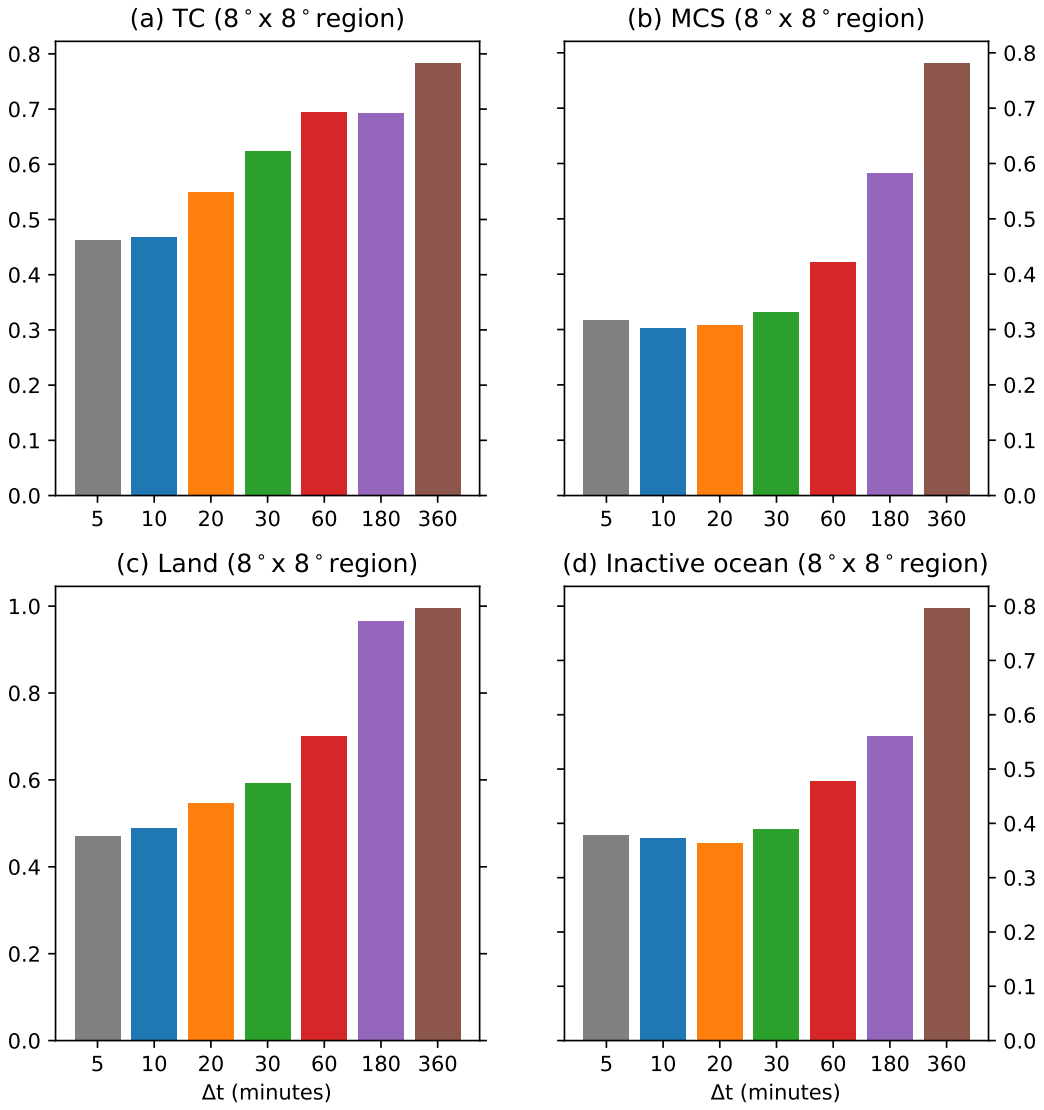

Figure 4.9: Mean of ratios of variance of residual (LHS-RHS) to variance of signal (RHS) for different Δt on the LHS, σ_r^2/σ_s^2, taken over the 12 time periods the circulation budget was calculated at. Circulation budget terms and circulation were calculated around the regions (a)–(d) shown in figure 4.2.

the profiles appear to follow the patterns set by the Δt=5 minutes case, albeit with increasingly weak amplitude. However, at time resolutions of Δt=1 hour or greater, often entire minima and maxima of the vertical profiles are missed; for example in (a) the entire fine structure of the lower half of the atmospheric profile is not visible in the signatures at 1 hour and is further smoothed out at lower time resolutions. Similarly in (b) the minimum at around 650 hPa is not reflected in the profiles of 1 hour and above at all.

To examine budget closure for different temporal resolutions systematically, σ_r^2/σ_s^2 is calculated again to quantify error introduced by different domain sizes and the inclusion of the friction term. For each Δt and at each time, the variance of the residual between the $\frac{\partial \Gamma}{\partial t}$ for a given Δt and the instantaneous budget terms was calculated as well as the variance of the circulation budget terms (the 'signal'). The ratio of the two variances was calculated, as in section 4.3, and the mean was taken over all times for each Δt, producing a summary of how the error increases with an increasing model output timestep shown in figure 4.9 for the four $8\times8^\circ$ regions. For (b) and (d), the error increase is negligible as Δt increases from 5 minutes to 30 minutes, but for all simulations there is at least a 30% increase in the variance ratio between Δt=5 minutes and Δt=1 hour.

Figure 4.9 confirms the suspicion that the errors between the circulation budget terms and the estimated circulation tendency is typically greater over land than over the ocean (comparing figure 4.9c to the other subfigures, noting the different scale). The TC case is an exception, and has nearly as great a magnitude of error as the land case for all Δt, which can perhaps be explained due to the fact that during the times investigated, the TC propagates into and most of the way out of the box. As it entered and left, the edges of the box would be colocated with the intense convection of a rapidly-intensifying TC which would have modulated the atmospheric profile away from the hydrostatic equilibrium approximation made in the estimation of ω, thus introducing errors into the circulation budget terms which are not present in the circulation tendency calculations which only use zonal and meridional wind.

4.7 Impact of Spatial Resolution

Another aspect of model configuration that may affect the circulation budget is the spatial resolution. Output data with high spatial resolution is not always available and it is of practical interest to see whether the circulation budget closure holds even when the spatial resolution

is reduced. For example, ERA5 reanalysis data (Hersbach et al. 2020) is commonly-used in analysis of atmospheric dynamics and is output at a horizontal resolution of 0.25 °. This section explores whether the circulation budget closure holds as well for these coarser grids up to the ERA5 resolution.

To simulate output on coarser model grids, output was regridded to spatial resolutions Δx of 0.1 °, 0.15 °, 0.2 °, and 0.25 ° and recalculated the instantaneous circulation budget terms and circulation tendency terms at each new grid spacing. The regridding was carried out using a linear regridding algorithm provided by xarray (Hoyer and Hamman 2017; Hoyer et al. 2022). The RHS of the circulation budget equations (sum of the instantaneous circulation budget terms) for the sample time of 01 UTC on 05 July 2016 (captured by figure 4.2) is shown in figure 4.10.

Variation of the circulation tendency profiles is inconsistent between the region; there is no clear trend in a positive, negative, or amplitude shift as spatial resolution changes. The inactive ocean region shown in figure 4.10d does not vary significantly between the different resolutions, perhaps as a result of the relatively weak circulation in the region. Meanwhile, there are very different signals present in the TC and land cases (figures 4.10a and c), where the fine structure of the native 4.4 km resolution appears to quickly be exaggerated as resolution decreases, and upon reaching 0.2 ° resolution, there are differences in the magnitude and sometimes the sign of the profile across various heights. Taken together, these results perhaps imply that missing fine structure in the circulation budget terms can lead to very different vertical profiles of circulation tendency, and thus may lead to differing interpretations of the physical processes represented by the circulation budget terms.

If one solely considers the question of circulation budget closure at different spatial resolutions, it does not necessarily matter whether the profiles themselves differ, so long as the difference between the LHS and RHS of the circulation budget equation is minimised. Figure 4.11 shows the mean σ_r^2/σ_s^2 for the 8×8 ° boxes over the full simulation period. For each spatial resolution, a corresponding circulation tendency is evaluated using $\Delta t = 5$ minutes. Generally, it appears that decreasing spatial resolution makes the closure of the circulation budget less close, a feature which is exaggerated for the regions with more activity (a, b, and c) relative to those with less (d). The inactive ocean region appears to have good closure which does not vary with spatial resolution.

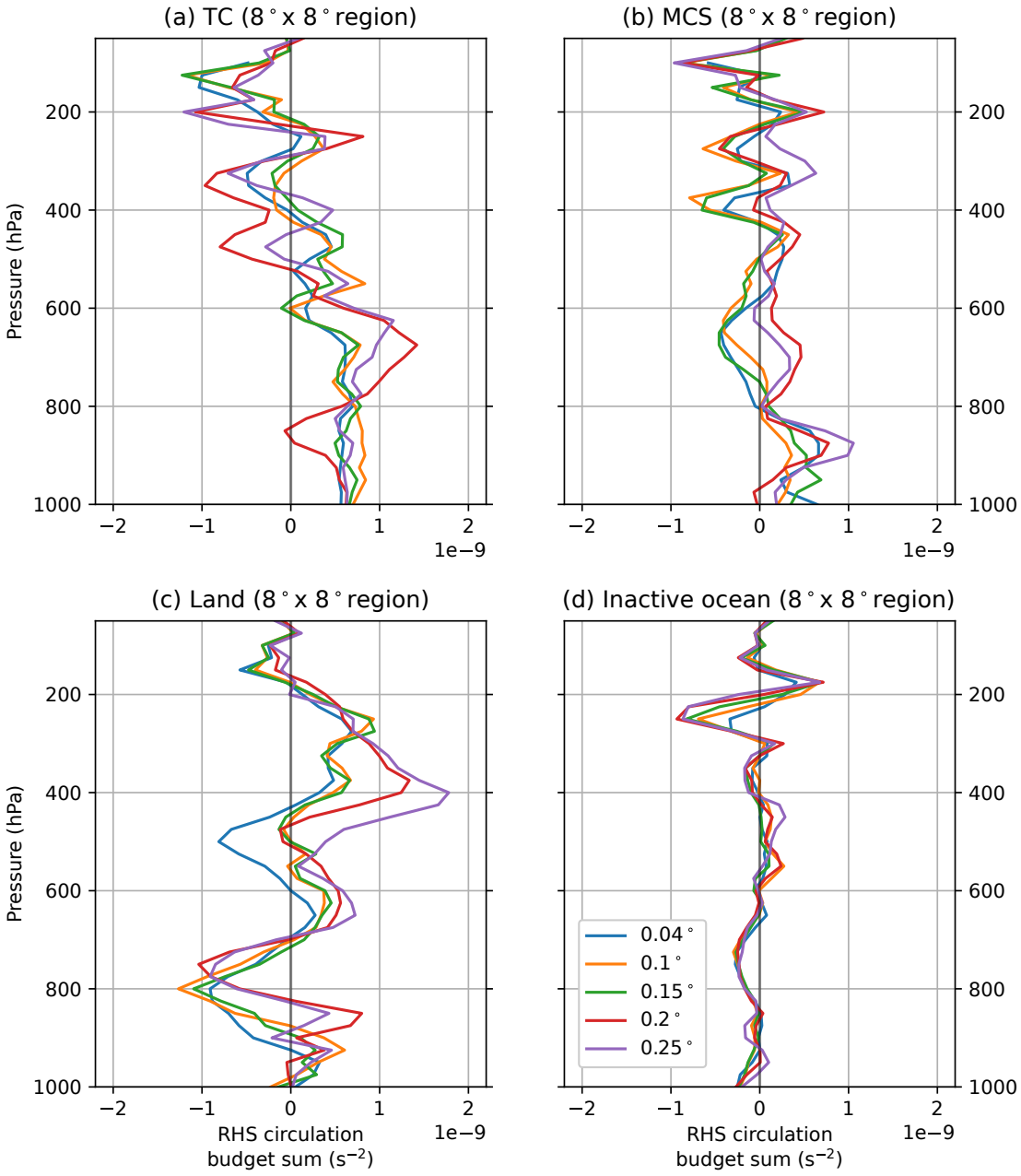

Figure 4.10: RHS of circulation budget profiles calculated for different spatial resolutions Δx, shown for the time snapshotted and regions a–d outlined in figure 4.2. The native grid resolution is the highest resolution shown, 0.04 °.

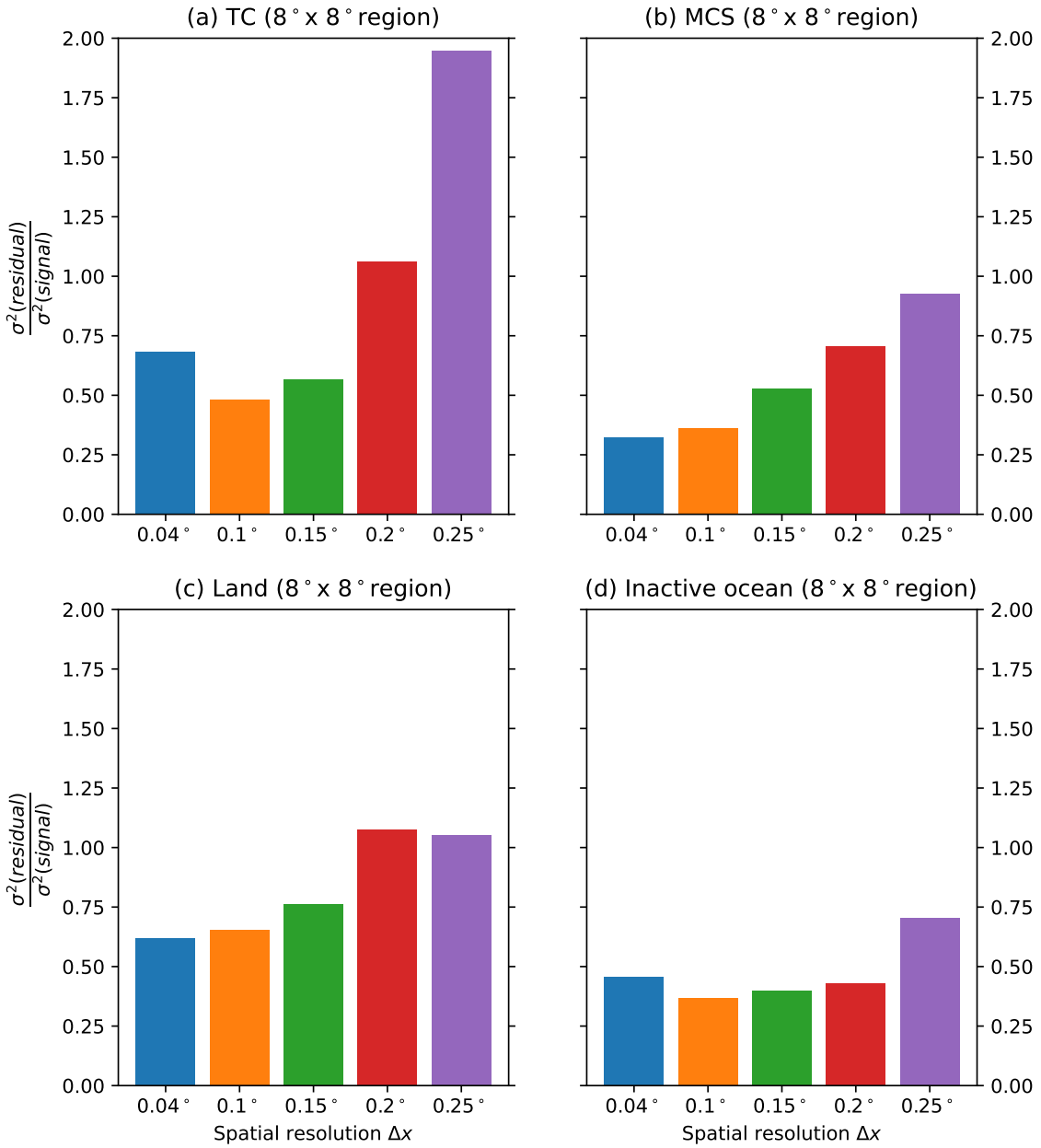

Figure 4.11: Mean of ratios of variance of residual (LHS-RHS) to variance of signal (RHS) for different Δx on the LHS, σ_r^2/σ_s^2, taken over the 12 time periods the circulation budget was calculated at. Circulation budget terms and circulation were calculated around the regions a–d shown in figure 4.2, at the respective grid resolutions Δx corresponding to each bar. The native grid resolution is the highest resolution shown, 0.04 °.

However, it is crucial to note that, should a methodology be using circulation budget terms to understand the contributions of different processes to circulation changes, a linear regridding as is carried out here may introduce errors into the profile by not sampling all grid points, and thus over- or under-representing small fluctuations which are crucial to modulating circulation. As a result, circulation tendencies as well as the budget terms may be calculated incorrectly. Instead, it would be wise to utilise an area-weighted regridding algorithm.

4.8 Impact of Varying Both Spatial and Temporal Resolution

Having evaluated the impact of varying both spatial and temporal resolution independently, it is of interest to see how varying both resolutions affects the closure of the circulation budget.

Figure 4.12 shows the mean ratio of variance of residual to variance of signal over the simulation times. The ratio increases as temporal and spatial resolution decrease, except in the case of the $\Delta x = 0.25\,^{\circ}$ spatial resolution, where the ratio has a minimum at a temporal resolution of around $\Delta t = 30$ minutes for all of the regions. A potential explanation for the latter phenomenon is that as the spatial and temporal resolutions decrease, they both reduce the variation in the vertical profile on the whole in the same way, and thus the LHS and RHS profiles are more similar, reducing the variance of the residual. Therefore, to obtain a closer closure in a low-resolution output it may be technically optimal to use a larger model output timestep, but it should be noted that the value that both the RHS and LHS approach may be further from the absolute truth. It is possible that instead, reducing both the temporal and spatial resolutions acts to damp out smaller-scale fluctuations in the budget in similar ways, resulting in the circulation budget terms providing less meaningful insight into the processes affecting the circulation tendency - especially of the small-scale processes that modulate large-scale motions in a cumulative sense.

Regardless, time output intervals of greater than one hour have significantly poorer closure over all spatial dimensions. Given that the majority of standard model output of dynamical fields is often output at hourly or even three-hourly intervals, circulation budget closure is likely to be poor for such models. Should an experiment require circulation budget analysis with good closure, it would be advisable to output data at 30-minute or higher resolution intervals, ideally on as high a resolution spatial grid as possible.

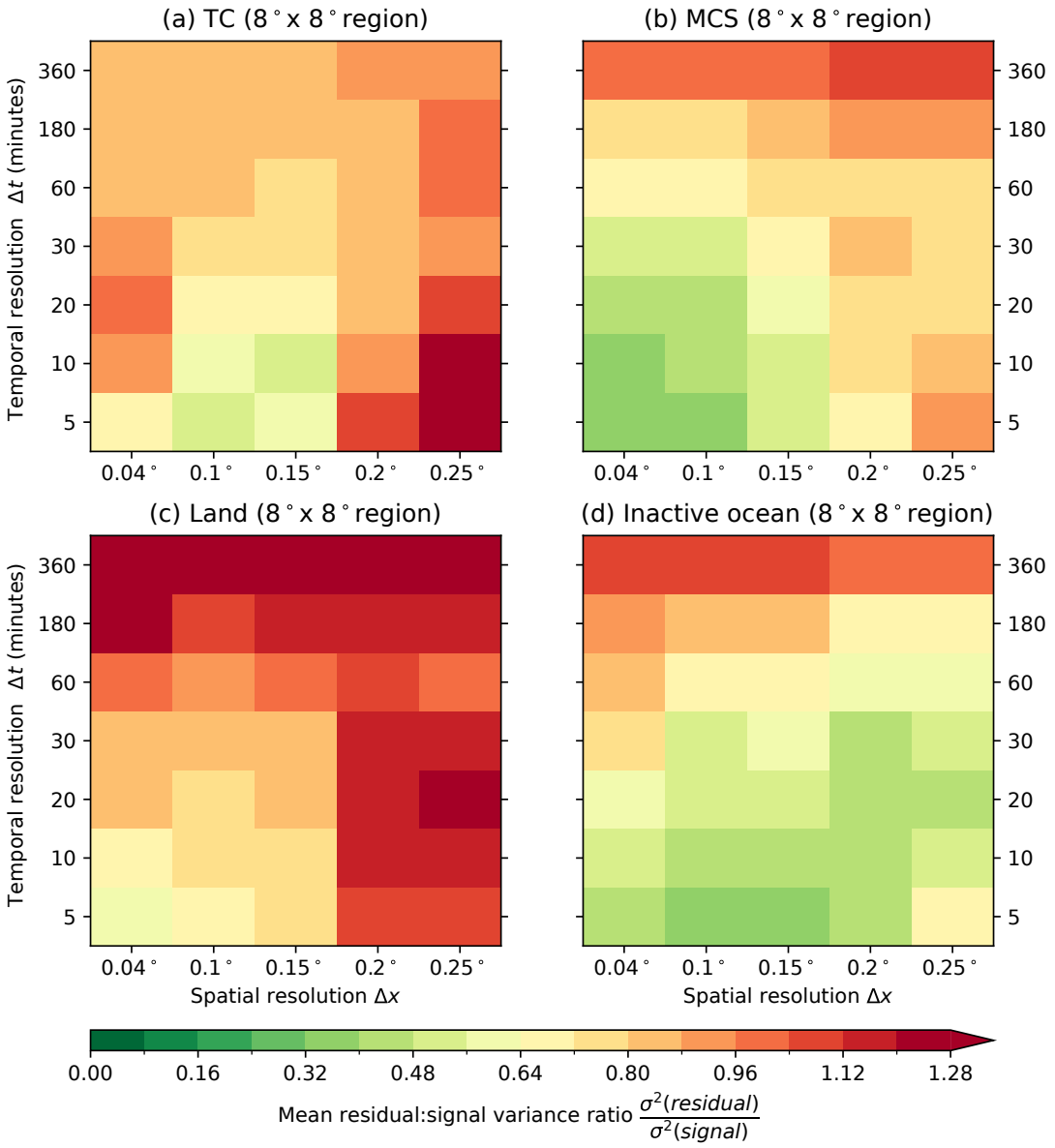

Figure 4.12: Mean of ratios of variance of residual (LHS-RHS) to variance of signal (RHS), σ_r^2/σ_s^2, for different Δx (x-axis) and Δt (y-axis), taken over the 12 time periods the circulation budget was calculated at, around the regions (a)–(d) shown in figure 4.2.

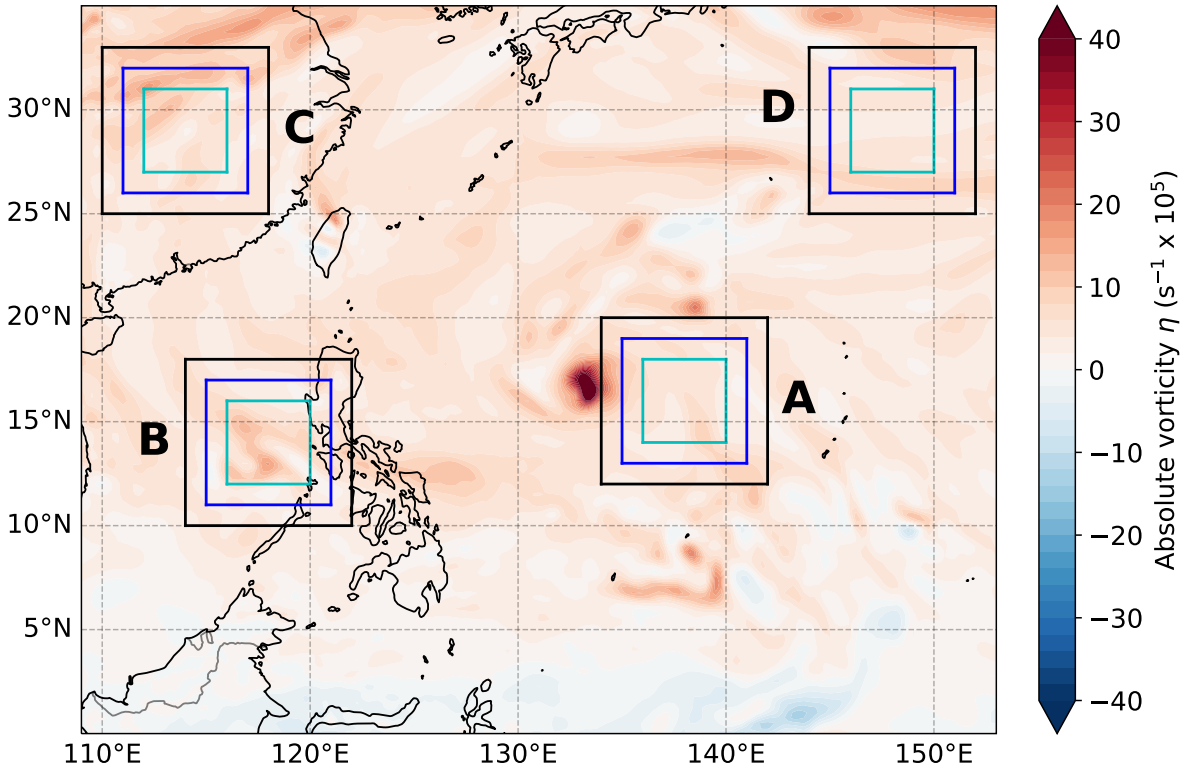

Figure 4.13: A snapshot of absolute vorticity (η, in $s^{-1} \times 10^5$) at 700 hPa, at 01 UTC on 05 July 2016, as calculated by ERA5 reanalysis. Case study regions are outlined by the black (8×8 °), blue (6×6 °), and cyan (4×4 °) boxes labelled A (Typhoon Nepartak), B (an oceanic MCS), C (an MCS over land), and D (oceanic region with least active convection).

4.9 Comparison to ERA5 Reanalysis

The previous section implies that the closure for ERA5 reanalysis data, output on a 0.25 ° grid at 1-hour intervals, would theoretically be significantly worse than closure at higher temporal and spatial resolutions. To test the hypothesis, ERA5 reanalysis data is examined on pressure levels from the same time period as the simulations, from 02 July 2016 until 06 July 2016. A snapshot of the absolute vorticity at 01 UTC on 05 July 2016 is shown in figure 4.13. The coarser resolution of the reanalysis does not provide anywhere near the fine details of vorticity structure observed in figure 4.2, and furthermore, the simulation shown in figure 4.2 is just one ensemble member run, which means that its simulated track of TC Nepartak is not perfectly aligned with observations. As a result, box (a) in figure 4.13 does not fully cover the tropical cyclone signature, which appears to exist to the west of the 8×8 ° box at this time (it passes through the box earlier in the simulation).

Figure 4.14 shows sample profiles from the time of the snapshot in figure 4.13 for the 8×8 °

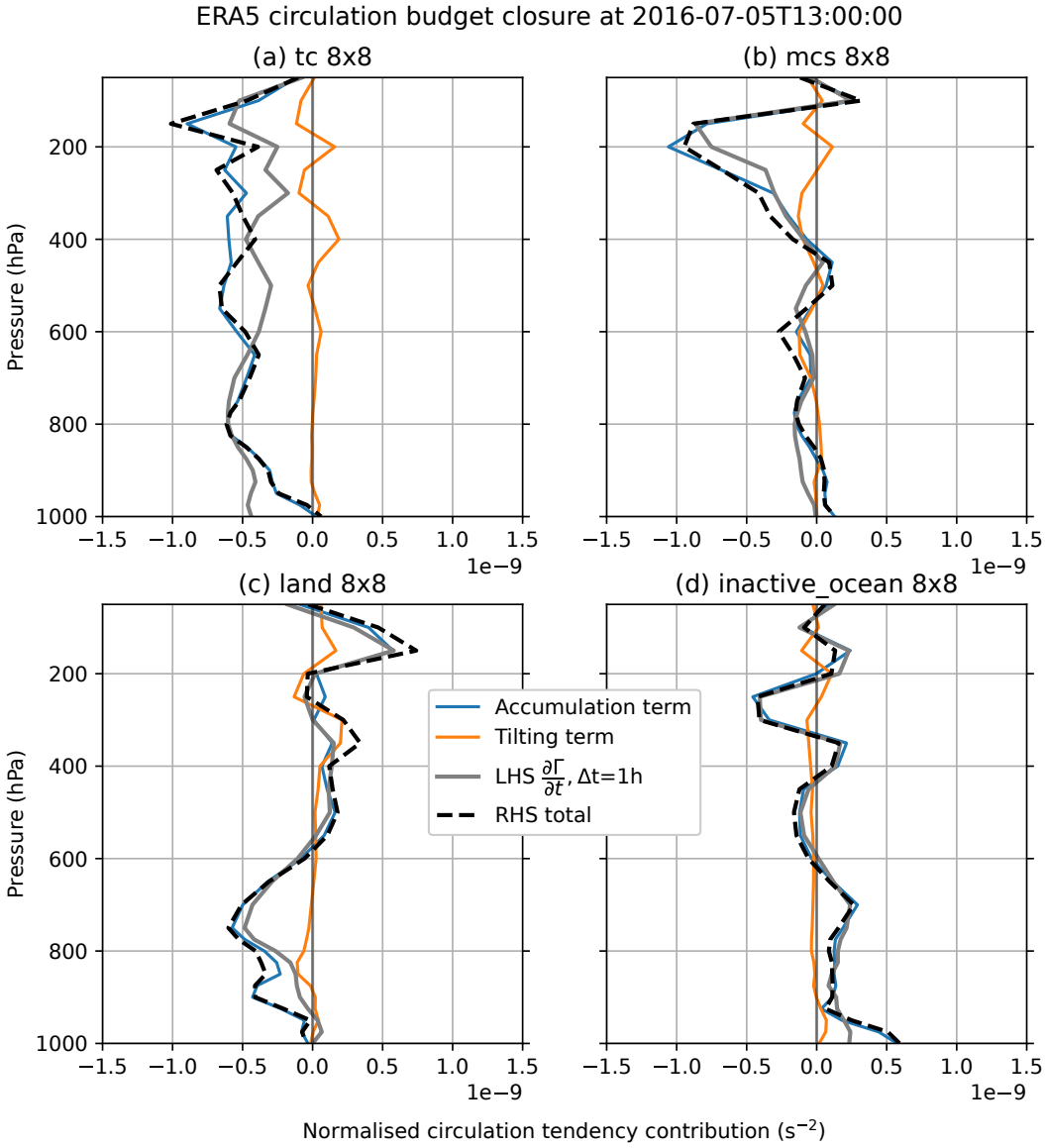

Figure 4.14: Similarly to figure 4.6, circulation budget terms from the ERA5 reanalysis, not including the friction term, calculated around the 8×8° black boxes labelled (a)–(d) in figure 4.13, at 01 UTC on 05 July in the simulation. The thinner coloured lines indicate the circulation budget terms calculated at each pressure level: the vorticity accumulation term (blue) and the tilting term (orange). The thick black line is the sum of the two terms. The thick grey line is the circulation tendency $\frac{\partial \Gamma}{\partial t}$ at the same time around the box.

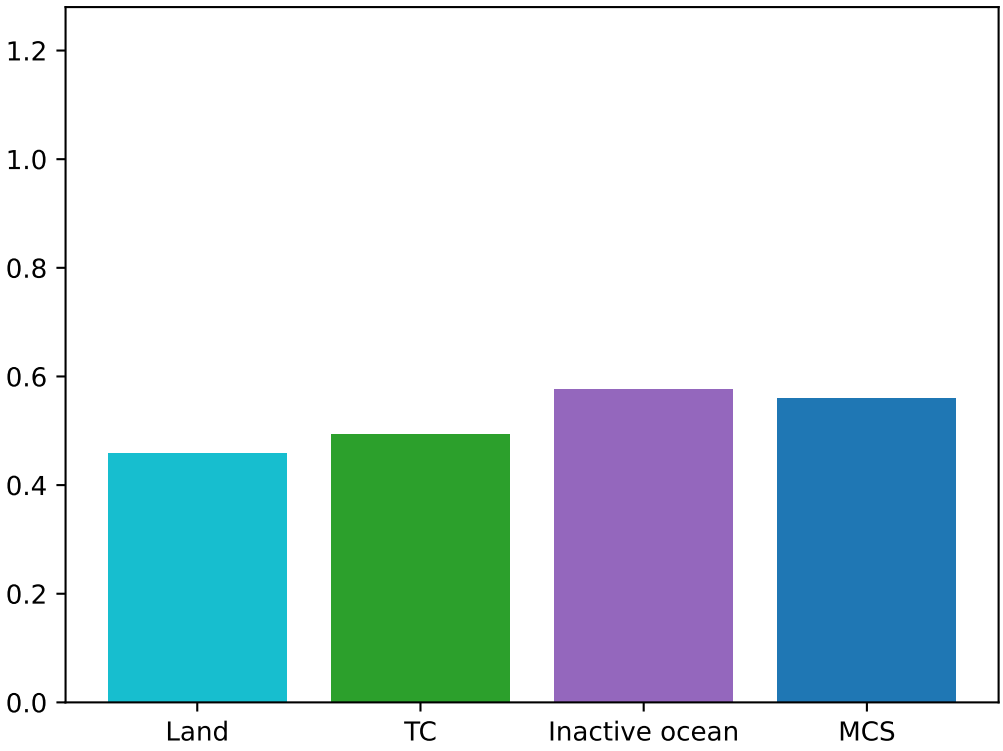

Figure 4.15: Mean of ratios of variance of residual (LHS-RHS) to variance of signal (RHS) σ_r^2/σ_s^2 in ERA5, taken over the 12 time periods the circulation budget was calculated at, around the regions (a)–(d) shown in figure 4.13.

domains around each of the regions (a)–(d). Due to a lack of pertinent variables in ERA5 reanalysis output, no attempt was made to calculate the friction term. As with the sample profiles for the simulation (shown in figure 4.6), the RHS sum of the circulation budget terms is largely dominated by the accumulation term (blue line) with the tilting term (orange) making a smaller contribution. The closure of the circulation budget appears relatively good, with the LHS grey line roughly following the black dashed RHS sum line in regions (b)–(c). There are more discrepancies in the TC case, but overall the profiles are relatively well-matched, with the largest residuals mostly appearing in the boundary layer, below 800 hPa.

In the same way as for the simulations, the σ_r^2/σ_s^2 was calculated over the twelve timesteps, 6 hours apart, over the study period, for each of the regions (a)–(d), shown in figure 4.15. The values of the ratio are smaller, overall, for ERA5 than they are for many spatial and temporal resolutions of the simulation, though they are higher than the native model output grid spacing and time intervals. For the ERA5 regions, the 'inactive ocean' region has the highest ratio,

implying a worse budget closure in the oceanic region, unlike the case in the MetUM simulation where the region had the closest closure overall. It is possible that the lower ratios for the other regions, indicating better closure, are related to the representation of convection in ERA5. Since the reanalysis uses a convection parameterisation, convective motions are not explicitly resolved. Therefore, small but noisy fluctuations associated with convection on the borders of circulation domains will not appear and as a result it is likely that the closure will be closer.

While the regridding of the simulated data implies that a model with the time output interval and grid resolution of ERA5 might have a more variable residual compared to its signal, the previous estimate may have been limited in accuracy due to the choice to use linear interpolation of the grids. With only a subset of the fine grid cells being sampled in the interpolation, small-scale fluctuations may be either missed entirely or amplified unnecessarily in the subsequent integration of the circulation budget terms, thus introducing errors in the RHS terms which lead to poor agreement with the LHS circulation tendency. ERA5, however, is being sampled here on its native grid, and no such errors through interpolation are introduced.

4.10 Evaluation and Conclusions

This chapter has evaluated the circulation budget as a technique for understanding how different processes affect circulation changes. In particular, the effect of different factors on the closure of the circulation budget have been investigated, including domain selection, time output resolution, and spatial grid resolution. The efforts result in some practical knowledge, relevant to the use of applying the circulation budget technique in future work.

Circulation budget closure is not perfect even for the highest time resolution available to us, and the chapter has discussed several reasons for the inexact outputs: within the model, inaccuracies are introduced through parameterised sub-grid scale processes and numerical truncation. Differences in algorithms for the calculation of derivatives and interpolation within the model and in post-processing will also introduce errors, and fundamentally the equation for the circulation budget approximates a shallow, hydrostatic atmosphere whereas the MetUM solves equations for non-hydrostatic, deep atmosphere.

Nonetheless, it is still useful to know how budget closure changes with the output time resolution. Often model outputs do not include direct fields which can be used to calculate the frictional

contribution to the circulation budget, so often the residual is employed as a means of calculating the frictional term. For Δt of under an hour, or spatial resolution Δx of $0.15\,^\circ$ or less, the residual may be small enough to produce a meaningful estimate of friction, but for lower spatiotemporal resolutions it would be unlikely to be accurate. Furthermore, when selecting a region to calculate a circulation budget around, if the aim is to be as accurate as possible to the circulation tendency term and achieve the best possible closure, it is wise to avoid sharply-fluctuating dynamics on the edges of the domain selected where possible. Ideally, the region should fully contain the convective activity. The relatively good closure in ERA5 further supports the idea that mesoscale convection limits closure accuracy, since ERA5 is unlikely to resolve mesoscale convection. However, if closure of the budget is not a concern, convection on the edges of a domain may still be of interest and indeed can contribute to the circulation tendency - meaning that the method could be an effective tool for exploring convection-circulation interactions.

It is worth noting that, even if the circulation budget cannot be closed since the time resolution is too low, that the instantaneous circulation budget terms remain as accurate for any timestep output so long as the fields are output as instantaneous values. Therefore, the circulation budget terms are still physically meaningful in themselves regardless of model output timestep. However, where models are resampled to lower spatial resolutions, particularly at $0.15\,^\circ$ or coarser and particularly in regions where there is active convection, the validity of the circulation budget terms is less certain as these instantaneous values on coarser grids can miss fine structure and fail to capture processes which are essential in modulating circulation.

Other factors affecting circulation budget closure to explore would be the options of using more sophisticated algorithms for the integration and differentiation used to calculate the instantaneous budget terms, as well as different regridding algorithms which serve to smooth out small-scale fluctuations, which appear to limit the accuracy of closure for coarser grid spacings. Furthermore it would be useful to evaluate the circulation budget where the model outputs directly onto pressure coordinates while maintaining the high time resolution, to avoid introducing errors in interpolating to pressure levels from MetUM hybrid height coordinates.

In summary, this chapter quantifies the closure of the circulation budget in a simulation over Southeast Asia by examining the circulation budget terms over several different regions. The chapter evaluates how the closure of the circulation budget changes when the time resolution limits the accuracy of the circulation tendency around a region. It would be of interest to

evaluate the circulation budget closure at even higher temporal output resolutions than 5-minute intervals, which was not possible in this instance due to constraints on data storage and available CPU time, but it appears that the majority of inaccuracies in the closure are a result of errors associated with estimating the friction term. An exploration of more sophisticated methods to estimate frictional contributions in both the boundary layer and at upper levels in unresolved processes was deemed beyond the scope of the thesis and this chapter.

However, regardless of the time resolution, and even without an accurate estimation of the friction term, the circulation budget terms provide an insightful tool for process-based analysis of synoptic circulation evolution. In the next chapter, the circulation budget technique will be applied over West Africa to interrogate synoptic-scale processes.

Chapter 5

Circulation Budget Analysis of Scale Interactions in West Africa

This chapter is based upon the paper 'How is synoptic-scale circulation modulated by mesoscale convection in West Africa?' in the Journal of Atmospheric Sciences, accepted March 2023.

In the previous chapter, examining different terms in the circulation budget was demonstrated to be a valid method for separating circulation changes associated with different processes. Applying the circulation budget technique, in this chapter, it is possible to explore one of the driving fundamental questions of the thesis: dynamically, what impact does mesoscale convection have on the synoptic circulation in tropical West Africa?

To gain insight into the nature of interacting mesoscale and synoptic diurnal processes in the West African Monsoon (WAM), the circulation budget terms is separated into mean and perturbed components in order to separate the contributions of mesoscale and synoptic-scale processes to circulation changes. Naturally, to understand the contribution of mesoscale convection to these processes, the dynamics of mesoscale convection should be characterised. To do so, dynamical fields are composited around precipitating features, discussing them in the framework of their circulation budget contribution and also from a momentum transport perspective. Composites are compared to measured properties of an observed organised precipitating system in West Africa from the JET2000 field campaign (see chapter 3).

Section 5.1 describes the mathematical division of scales across the circulation budget, and section 5.2 outlines the approach taken alongside the choice of dataset and analysis region. The

diurnal cycle of the circulation budget is explained in terms of processes in the WAM in section 5.3, and mesoscale contributions to the circulation budget are explained by analysing typical dynamics of mesoscale precipitation in section 5.4.

5.1 Scale Separation Using the Circulation Budget

In chapter 4, the circulation budget (equation 4.4) was calculated to demonstrate how circulation tendency can be decomposed into different physical processes: vorticity accumulation, vortex tilting, and friction. The method is based on a suggestion in Haynes and McIntyre (1987). However, Haynes and McIntyre (1987) also suggest splitting the velocity and vorticity elements into mean and perturbation elements for greater insight into processes at difference scales.

Let $\boldsymbol{u} = \bar{\boldsymbol{u}} + \boldsymbol{u'}$, $\eta = \bar{\eta} + \eta'$, and $\omega = \bar{\omega} + \omega'$, where the bars denote some mean quantity and dashed quantities are perturbations from said mean. The mean taken can be any mean, chosen to reflect the physical insights sought by using the technique. For the purposes of this chapter, the mean chosen is a spatiotemporal mean, over all points in the domain over all times at each given hour in the diurnal cycle. Taking the same mean over the entire equation:

$$\frac{\partial \bar{\Gamma}}{\partial t} = \oiint_S \nabla_{xy} \cdot \left(\bar{\boldsymbol{u}}\bar{\eta} + \boldsymbol{u'}\eta' - \bar{\omega}\hat{\boldsymbol{k}} \times \frac{\partial \bar{\boldsymbol{u}}}{\partial p} - \omega'\hat{\boldsymbol{k}} \times \frac{\partial \boldsymbol{u'}}{\partial p} + \hat{\boldsymbol{k}} \times \boldsymbol{F} \right) dS \tag{5.1}$$

$$\frac{\partial \bar{\Gamma}}{\partial t} = \oint_C \Bigg(\underbrace{\bar{\boldsymbol{u}}\bar{\eta}}_{\substack{\text{synoptic} \\ \text{accumulation}}} + \underbrace{\boldsymbol{u'}\eta'}_{\substack{\text{anomalous} \\ \text{accumulation}}} \underbrace{-\bar{\omega}\hat{\boldsymbol{k}} \times \frac{\partial \bar{\boldsymbol{u}}}{\partial p}}_{\substack{\text{synoptic} \\ \text{tilting}}} \underbrace{-\omega'\hat{\boldsymbol{k}} \times \frac{\partial \boldsymbol{u'}}{\partial p}}_{\substack{\text{anomalous} \\ \text{tilting}}} + \underbrace{\hat{\boldsymbol{k}} \times \boldsymbol{F}}_{\text{friction}} \Bigg) \cdot \hat{\boldsymbol{n}} dl. \tag{5.2}$$

Chapter 4 established that the circulation budget terms on the right-hand side (RHS) of the circulation budget equation (equation 5.2) are instantaneous. Therefore, the physical meaning of the terms is valid to evaluate how different processes modulate circulation, even if the circulation budget does not close. With the 3-hourly time output resolution of CP4's pressure level variables, it is unlikely to close accurately due to inaccuracies introduced by time derivatives. Therefore, in this chapter the aim is not to close the budget, but instead to simply examine diurnal variations of the RHS circulation budget terms. The separation of the circulation budget into the mean and perturbation components allows us to investigate elements of the circulation which are associated with synoptic (theoretically, the mean component) and mesoscale (theoretically the perturbation components) processes.

5.2 Data and Domain selection

The analysis uses three-hourly pressure-level dynamical and thermodynamic fields, and hourly precipitation data, from CP4 and R25 (see chapter 3). In particular, the analysis focused on July and August (season of peak WAM activity) in the current climate simulations. CP4 data was regridded to R25's resolution to minimise the impact of their different resolutions.

The region chosen was a box which has its southwestern corner at 10°W, 7.5°N, and its northeastern corner at 5°E, 15°N, illustrated in figures 5.1 and 5.1. The region was selected so that it was located entirely over land, not covering any major orographic features, and so that the box largely covers the zonal wind speed maximum of the AEJ (figure 5.2). The box covers the southern AEW track (Pytharoulis and Thorncroft 1999; Fink et al. 2017), which is strongly associated with Sahelian moist convection. A fixed region was analysed because the AEJ is geographically constrained by the moisture gradient between the Sahel and the Sahara (Schubert et al. 1991; Thorncroft and Blackburn 1999; Wu et al. 2009).

Dynamics have been analysed relative to the diurnal cycle (calculating the mean as the deviation from the average value across the domain at a given time in the diurnal cycle) because it is impossible to directly compare simulated events in free-running climate simulations. Furthermore, the processes that dominate West African weather systems are fundamentally diurnal in nature (Parker et al. 2005), especially over land. With a diurnal framework, processes can be separated according to time of day and understand the causes and impacts of diurnal activity, including convection.

Later in the chapter, composites of convection are compared to an observation of a storm from the JET2000 observational campaign (Thorncroft et al. 2003). Specifically, the measurements are taken from dropsondes launched from flight A781 which flew within the mesoscale circulation behind (to the east of) a decaying storm at around 11 UTC on 29 August 2000, passing behind the storm at roughly 11 ° N.

5.3 Circulation Budget Diurnal Cycle over West Africa

Figure 5.3 shows the mean diurnal circulation and circulation tendency around the box illustrated in figure 5.1. There are distinct diurnal patterns in circulation in both simulations, with the strongest variation at 1000–850 hPa, but there are several differences between the two sim-

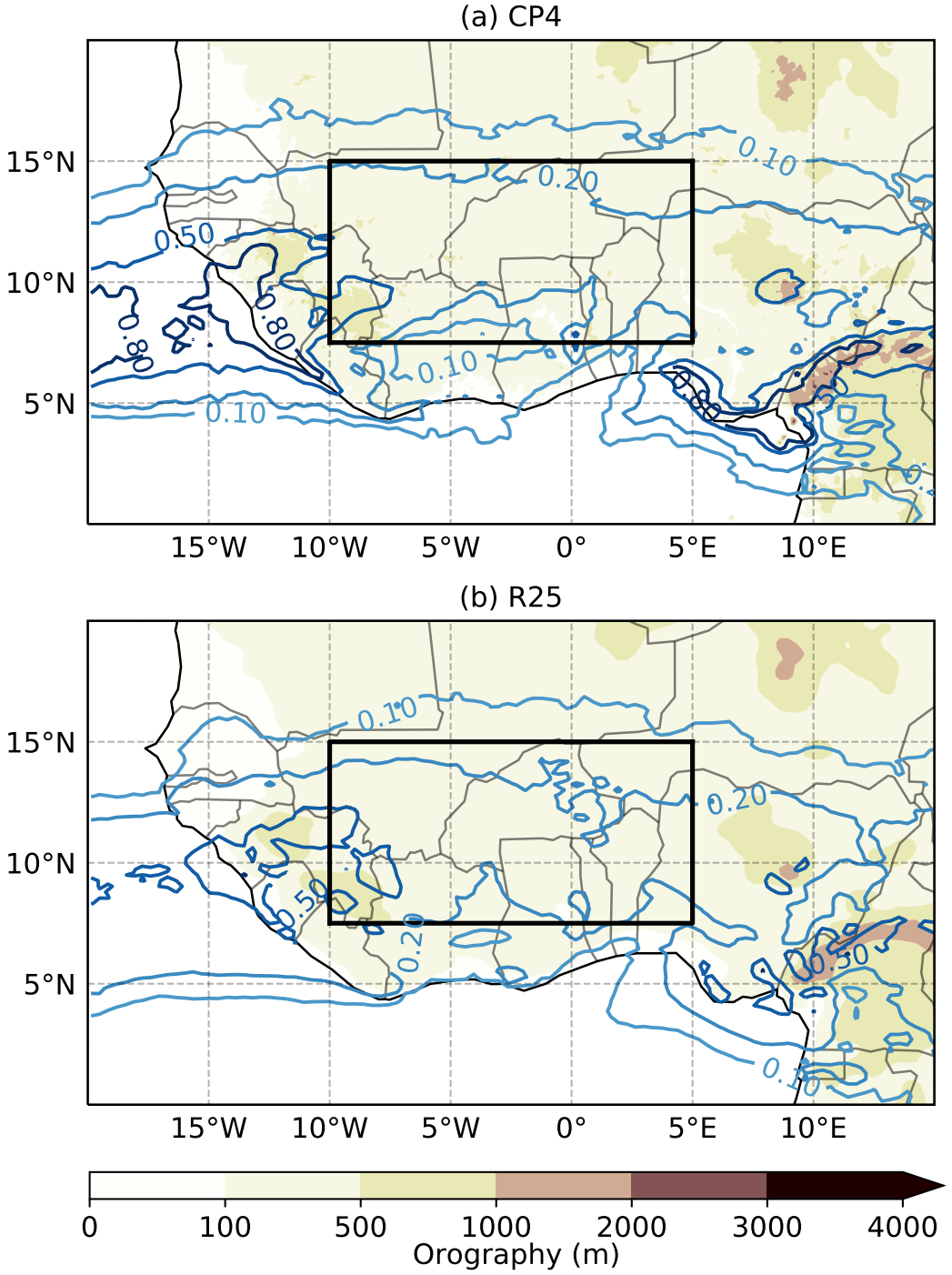

Figure 5.1: Orography (filled contours) and mean rainfall (line contours, labelled in mm h^{-1}) in July and August 1998-2006 for (a) CP4 and (b) R25. The region of interest analysed here is outlined by the black box.

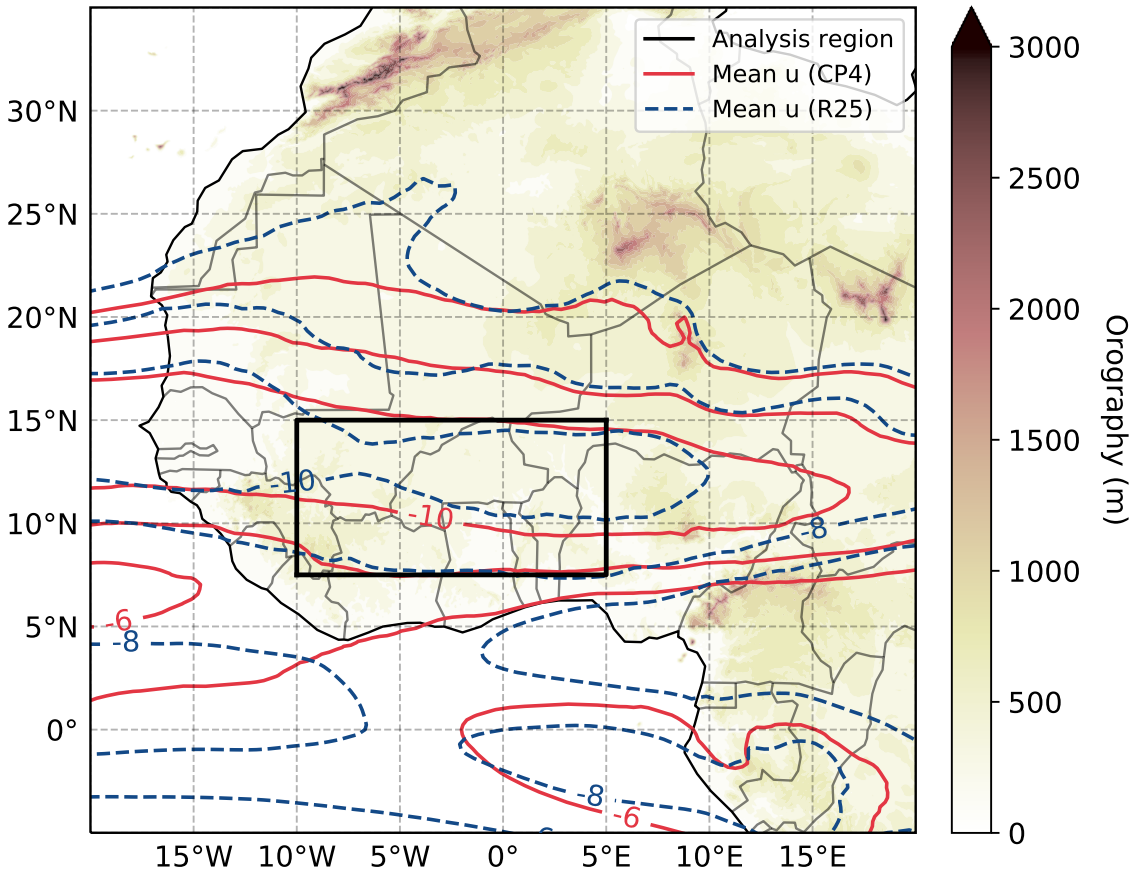

Figure 5.2: Orography (filled contours) and mean zonal wind (line contours, labelled in m s^{-1}) in July and August 1998-2006 for CP4 (red) and R25 (blue). The region of interest analysed here is outlined by the black box.

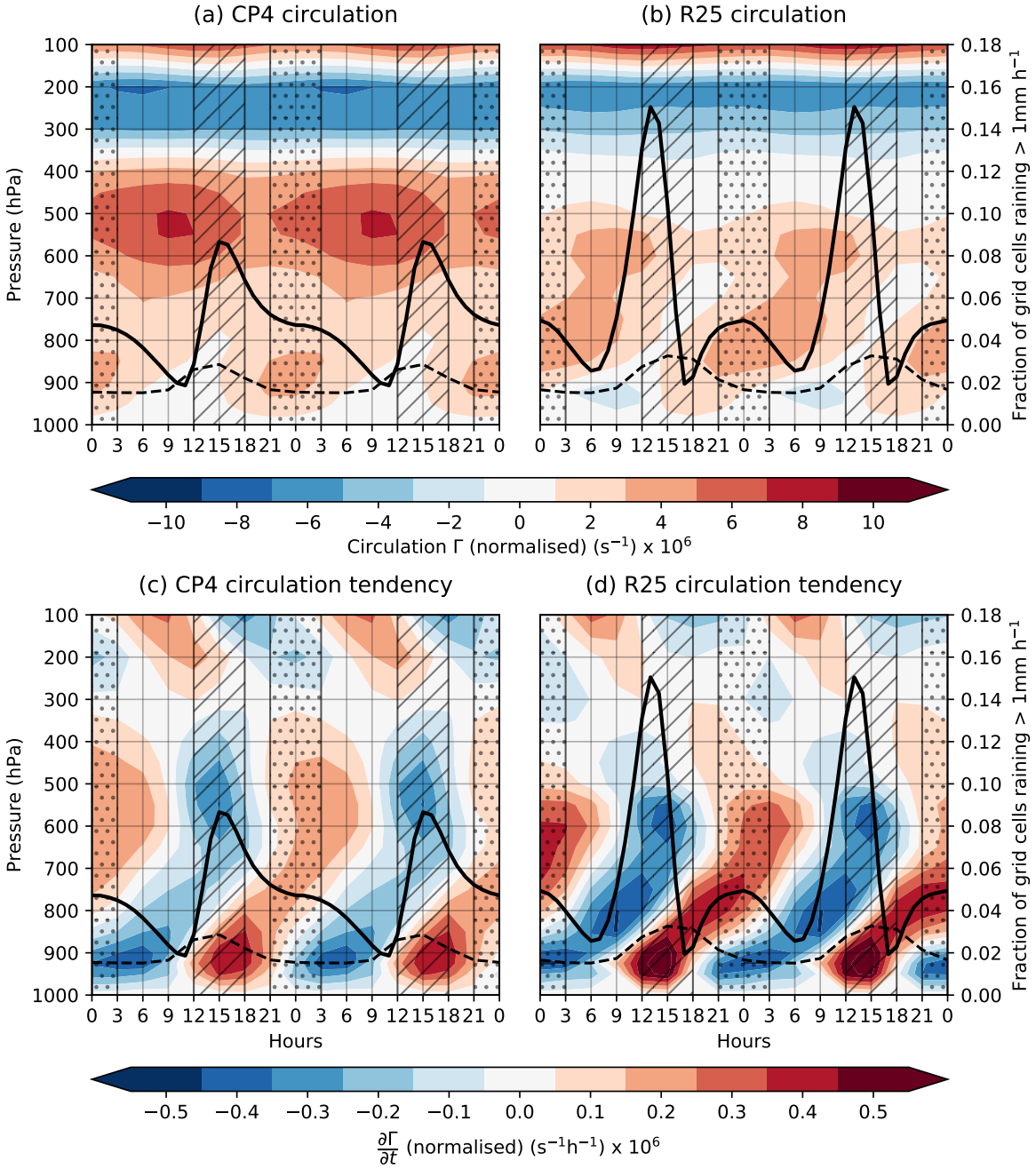

Figure 5.3: Mean diurnal cycle (repeated for two full days) of (a-b) circulation (normalised by area) Γ (s^{-1}; filled contours) and (c-d) normalised circulation tendency $\frac{\partial \Gamma}{\partial t}$ ($s^{-1}h^{-1}$; filled contours) around the synoptic region illustrated in figure 5.1. The mean is calculated over all points in the border of the selected synoptic region for each time in the diurnal cycle. Also shown is rainfall fraction (fraction of grid cells with a precipitation rate of 1mm h^{-1} or greater; black solid line) and estimated convective boundary layer height (dashed black line). (a) and (c) show these features in CP4, (b) and (d) in R25. The diagram also indicates the regions selected for "afternoon" (12–18 UTC) and "overnight" (21–3 UTC) convection in lined and dotted hashed regions respectively.

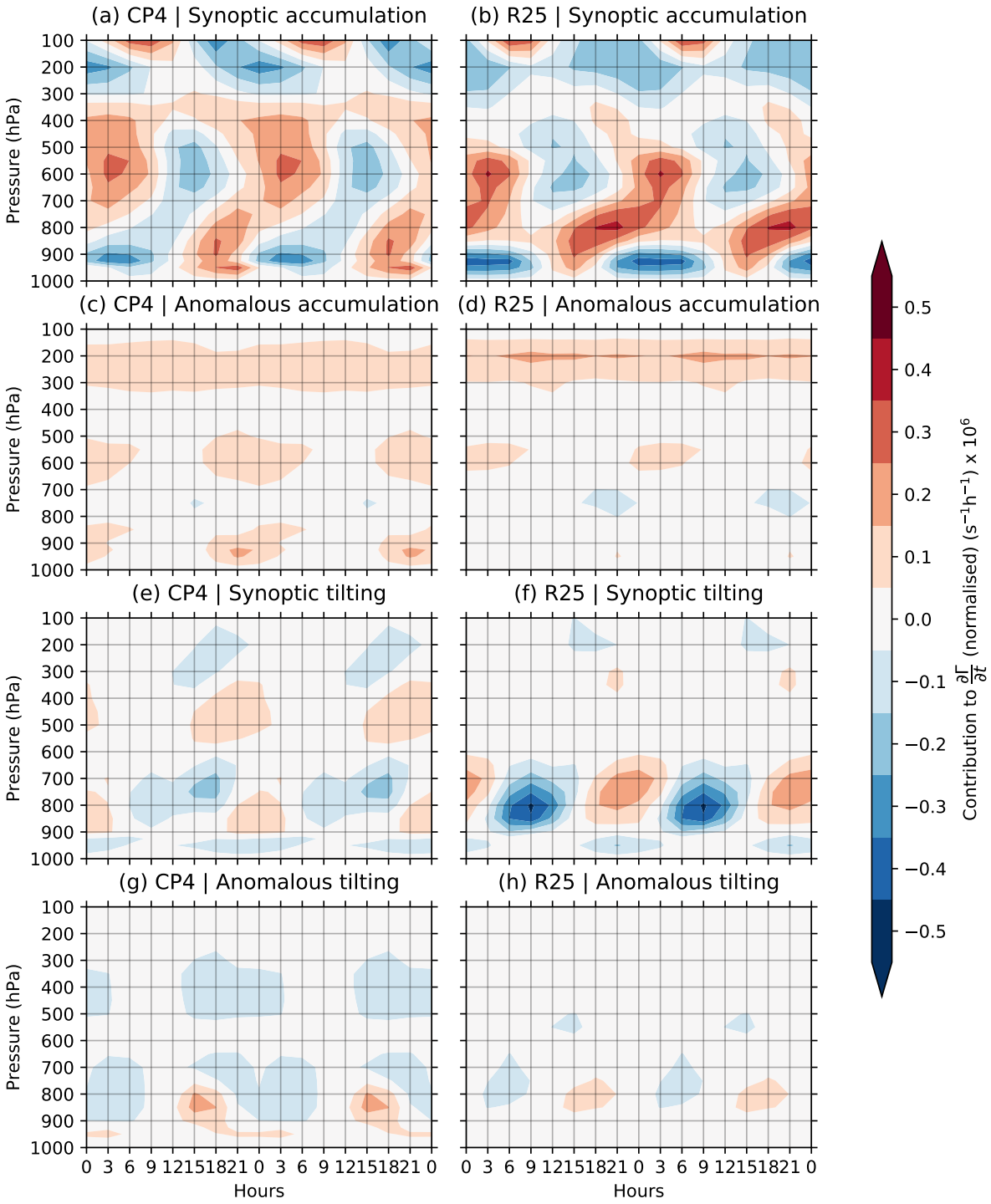

Figure 5.4: Mean diurnal cycle (repeated for two full days) of circulation budget terms. The mean is calculated over all points in the border of the selected synoptic region (black rectangle in figures 5.1 and 5.2) for each time in the diurnal cycle. The 'anomalous' terms are the integral of deviations from these mean values. (a-b) "Synoptic accumulation" term $-\oint_C \bar{\boldsymbol{u}}\bar{\eta} \cdot \hat{\boldsymbol{n}} dl$, (c-d) "Anomalous accumulation" $-\oint_C \boldsymbol{u'}\eta' \cdot \hat{\boldsymbol{n}}\boldsymbol{dl}$, (e-f) "Synoptic tilting" $\oint_C \bar{\omega}\hat{\boldsymbol{k}} \times \frac{\partial \bar{\boldsymbol{u}}}{\partial p} \cdot \hat{\boldsymbol{n}} dl$, (g-h) "Anomalous tilting" $\oint_C \omega'\hat{\boldsymbol{k}} \times \frac{\partial \boldsymbol{u'}}{\partial p} \cdot \hat{\boldsymbol{n}} dl$. The left column shows results for CP4 and the right column shows results for R25.

ulations. At 400–500 hPa, circulation is stronger and more strongly varying in CP4 than in R25. Generally, however, the circulation tendency in R25 has a greater magnitude, especially at around 800 hPa. Also, the patterns in CP4 lag those in R25 by around 3 hours. The lag corresponds with the difference in peak rainfall time shown by the solid black line in figure 5.3 which is at 15 UTC in CP4 and 12 UTC in R25, (Stratton et al. 2018; Berthou et al. 2019). To understand what processes cause the differences in circulation and circulation tendency, circulation budget terms described by equation 5.2 are calculated over a diurnal cycle (figure 5.4).

Anomalous and synoptic terms theoretically split the budget into contributions from diurnal synoptic motions and effects from individual storms, since one might assume that storms do not occur in the same place each day. However, the division is not precise since the mean value is taken relative to the diurnal cycle, and convection is a strongly diurnal process itself which is intrinsically linked to the synoptic diurnal weather systems such as the WAM. Therefore, some effects of convection on the circulation budget will be contained within the synoptic circulation budget terms rather than the anomalous terms.

The patterns in the synoptic terms in figures 5.4a–b and e–f can be explained in the context of the WAM. Firstly, note that the background absolute vorticity of the region is general positive due to planetary vorticity f, and the background vorticity contributed by the wind shear associated with the AEJ. In the morning, over land in West Africa, solar radiation causes surface heating, leading to ascent in dry convection in the North of the region over the Sahara from low-to-mid levels, associated with the negative tendency in the synoptic tilting term which peaks at 9 UTC in R25, and a little later in CP4 (figure 5.4e–f). The convection disrupts the southerly monsoon flow which has developed overnight (see Parker et al. 2005), especially in the north, causing convergence within the box. The positive background vorticity leads to low-to-mid level synoptic-scale accumulation as convection begins in both simulations. CP4 (figure 5.4a) has smaller and later synoptic accumulation than R25 during hours of afternoon convection because of the delay in the daily onset of convection, and because CP4's monsoon flow extends further north (Jackson et al. 2022), so there is less synoptic convergence in the box. It is for the same reason that CP4's tilting tendency is weaker than R25: the ascent over the Sahara is further north and the northern edge of the box behaves more similarly to its southern edge than in R25. Jackson et al. (2022) also note that CP4's ascent tends to be deeper and more

intense, which may account for the greater vertical extent of CP4's circulation tendencies.

Above the monsoon flow, there is a northerly return flow at midlevels. Since the northern edge of the monsoon flow has been disrupted, the return flow now only exists in the southern edge of the box, causing an overall divergence signature at 600 hPa as convection initiates, in both simulations, associated with the negative synoptic accumulation anomaly. By contrast, the synoptic accumulation at 200 hPa remains negative for almost the entire diurnal cycle in both simulations. Winds at 200 hPa are dominated by the behaviour of the tropical easterly jet which peaks at 8° N, near the southern edge of the box. In CP4, there is lower positive absolute vorticity during the hours of active convection, perhaps due to the deeper convection in CP4 and associated upper-level negative vorticity anomalies (see section 5.4.2), reducing the negative anomaly in synoptic accumulation compared to R25 in the early afternoon.

Overnight, diurnal convection dies down, beginning with the north of the region and leading to subsidence on the northern edge of the box, while some convection remains active to the south of the box. The meridional variance in ascent is associated with the positive tilting term anomalies in the early evening at 850 hPa. Around 0–3 UTC, the convection on the southern edge also begins to wane, leading to southern subsidence which reverses the tilting signature and results in the negative tilting term in the early hours of the morning.

As convection diminishes, surface monsoon flow resumes and reaches its full extent beyond the north of the box. The flow advects positive planetary vorticity northwards, replacing vorticity in the region with lower-magnitude vorticity from the South, where f is smaller, and resulting in a low-level negative accumulation term overnight from 0–9 UTC. The anomaly is larger in R25 than CP4 because the monsoon flow in R25 is stronger (Jackson et al. 2022). Again, there is a northerly return flow at midlevels with the opposite effect at the same time, causing positive accumulation from 800–600 hPa (up to 400 hPa in CP4).

From the data available, it was not possible to estimate the frictional term adequately. The residual between the total circulation tendency and the known terms was calculated (not shown), which would include the effects of friction. One might expect friction to have maximum intensity at low levels in the convective boundary layer (CBL) during peak hours of convection. As a proxy CBL height (dashed black line in figure 5.3) is estimated using profiles of virtual potential temperature θ_v averaged through the region, defining CBL height as the first vertical pressure level where θ_v has decreased by 1 K from its value at 950 hPa. The estimated residual does

peak in the expected periods of high turbulence, but is not negligible at upper levels, where it cannot be attributed to friction. The discrepancy is caused by the low (3-hour) time resolution, leading to non-instantaneous and imprecise derivatives, as explained in chapter 4.

CBL height peaks during the hours of active afternoon convection and drops to a minimum in the early hours of the morning. R25's afternoon boundary layer is slightly deeper than CP4's, and in it there is a strong positive circulation tendency anomaly which is delayed and less intense in CP4, perhaps due to CP4's blended boundary layer scheme (see chapter 3). Since the positive anomaly is not accounted for in the other terms in the circulation budget (figure 5.4), it is likely to be a result of the friction term.

5.4 Dynamics of Mesoscale Precipitating Features

To investigate whether the contributions to the circulation budget may be attributed to MCSs, in this section, the dynamics of precipitating features on the mesoscale are calculated.

Features are composited around 500-km boxes centred on grid cells precipitating at a rate greater than 1mm h^{-1} (considered the threshold for rainfall to significantly affect soil moisture). The composites are taken for all grid cells precipitating above these thresholds during the afternoon (12–18 UTC) and overnight (21–3 UTC). During the selected period, in CP4 127,443 precipitating grid cells were identified during the afternoon regime and 100,324 overnight. R25 had 178,839 and 95,158 precipitating grid cells in the afternoon and overnight regimes respectively (consistent with the fraction of precipitating grid cells in figure 5.3).

In the following subsections, composites are linked to processes that control synoptic circulation by plotting the dynamical features which relate to the accumulation ($-\oint_C \boldsymbol{u}\eta \cdot \hat{\boldsymbol{n}}\boldsymbol{dl}$) and tilting ($-\oint_C \omega\hat{\boldsymbol{k}} \times \frac{\partial \boldsymbol{u}}{\partial p} \cdot \hat{\boldsymbol{n}} dl$) terms in the circulation budget. The tilting term, which generates the characteristic North-South relative vorticity dipole, is addressed first, followed by the vorticity accumulation term.

5.4.1 Vortex Tilting by Precipitating Features on the Mesoscale

One of the key features that the tilting term creates, as convective updraughts interact with background zonal wind shear, is the characteristic pattern of North-South oriented dipoles of positive and negative relative vorticity. Figure 4.1 illustrates how, for a given vortex tube,

Table 5.1: Number of grid cells precipitating at a rate of 1mm h^{-1} or greater along each edge of the synoptic box for the two regimes of convection.

# precipitating cells in CP4 along	South border	East border	North border	West border
Afternoon (12–18 UTC)	3004	2545	3499	3831
Overnight (21–3 UTC)	1886	2097	2306	4715
# precipitating cells in R25 along	South border	East border	North border	West border
Afternoon (12–18 UTC)	5515	4038	4614	5479
Overnight (21–3 UTC)	3124	1702	872	5726

the vorticity may be tilted from its horizontal orientation into a vertical dipole. For the zonal wind profile characteristic of West Africa, an updraught results in a dipole with a positive relative vorticity anomaly to the north and a negative anomaly to the south. In this section, the cumulative effects of the tilting term on the circulation budget are examined, as well as the relationship between the tilting term and convective momentum transport.

Composites of the tilting term integrand

To understand how mesoscale precipitating features modulate the tilting term, the integrand of the tilting term, $\left(\omega\hat{\boldsymbol{k}} \times \frac{\partial \boldsymbol{u}}{\partial p}\right)$ is composited along 500-km cross-sections centred on grid cells precipitating at a rate greater than 1mm h^{-1}. The direct contributions to the circulation budget are from the components of $\omega\frac{\partial \boldsymbol{u}}{\partial p}$ facing outwards along each side of the box. For the northern and southern edges the integrands are $\omega\frac{\partial u}{\partial p}$ and $-\omega\frac{\partial u}{\partial p}$ respectively, and for the east and west borders, $-\omega\frac{\partial v}{\partial p}$ and $\omega\frac{\partial v}{\partial p}$ respectively. Both meridional (north-south) composites of $\omega\frac{\partial v}{\partial p}$ and zonal (east-west) composites of $\omega\frac{\partial u}{\partial p}$ are examined.

The net contribution of precipitating systems to the tilting term over the whole synoptic region is proportional to the difference between the number of precipitating pixels, and the corresponding integrand term. The number of precipitating grid cells on each edge of the box for the afternoon and overnight phases of convection are shown in table 5.1, the consistent, during the afternoon, with the climatological rainfall distribution (figure 5.1). There is a greater difference in precipitating grid cells between the eastern and western (meridional) edges than the difference between the northern and southern (zonal) edges, so the tilting term integrand along the West edge should contribute most strongly to the circulation budget.

In CP4, the meridional composites of $\omega\frac{\partial v}{\partial p}$ show a tripole, with a negative anomaly up to around 700 hPa, which then becomes a positive anomaly until around 400 hPa and negative again up to

300 hPa (figure 5.5). (Note that the quantities shown in the composites are multiplied by 10^5 so that the legend has a reasonable scale.) R25 similarly has a low-level negative anomaly with a mid-level positive anomaly, but has a greater meridional extent. The overnight convection composites (figures 5.5c–d) look more similar between the two models, with stronger low-level negative anomalies and positive anomalies extended from around 650 hPa to upper levels.

The zonal composites of $\omega\dfrac{\partial u}{\partial p}$ (figure 5.6) have anomalies up to around five times more intense than the meridional composites (figure 5.5) in afternoon convection, and almost twice as intense in overnight convection. While there is a greater difference in the number of precipitating grid cells between the eastern and western borders, the differences between the northern and southern borders may contribute just as strongly as the meridional composites to the total tilting term due to their greater intensity. Since there is more rainfall along the northern (southern) edge in CP4 (R25), the zonal composite signatures would contribute positively (negatively) to the total tilting term in the circulation budget. Note the difference in rainfall, attributable to the more northern position of the WAM system in CP4 (Jackson et al. 2022). The zonal composites' tripole signature is very localised to the centre of the precipitation. R25's signature is limited to a negative anomaly at 900–500 hPa, slightly more intense and extended in the overnight composite than the afternoon.

One could think of the signatures in figure 5.6 as being a reflection of the updraught being projected onto the shear anomalies associated with the convection. In both cases, the zonal wind shear between the surface and the AEJ is reduced since the AEJ is typically decelerated by MCSs, which results in a negative $\dfrac{\partial u}{\partial p}$ anomaly up to around 700 hPa, with a strong updraught (negative ω) resulting in an overall negative $-\omega\dfrac{\partial u}{\partial p}$ anomaly. Above this, in the CP simulation, the shear anomaly becomes positive, especially to the east of the composite, because of the overturning updraught to the rear of the storm (illustrated in figure 5.7 as a pink arrow), which results in a positive $-\omega\dfrac{\partial u}{\partial p}$ anomaly. Finally, at upper levels, in CP4, there is another positive shear anomaly induced by strong divergence at the top of the updraught, which results in a negative $-\omega\dfrac{\partial u}{\partial p}$ anomaly again, thus creating a vertical tripole structure.

The structures in the tilting integrand composites are somewhat reflected in the CP4 synoptic tilting term (figure 5.4e), where the tripole structure appears during the hours of active afternoon convection. Both the western (figure 5.5) and northern (figure 5.6 edge contribute a negative anomaly at low levels, a positive anomaly at midlevels, and a negative anomaly at

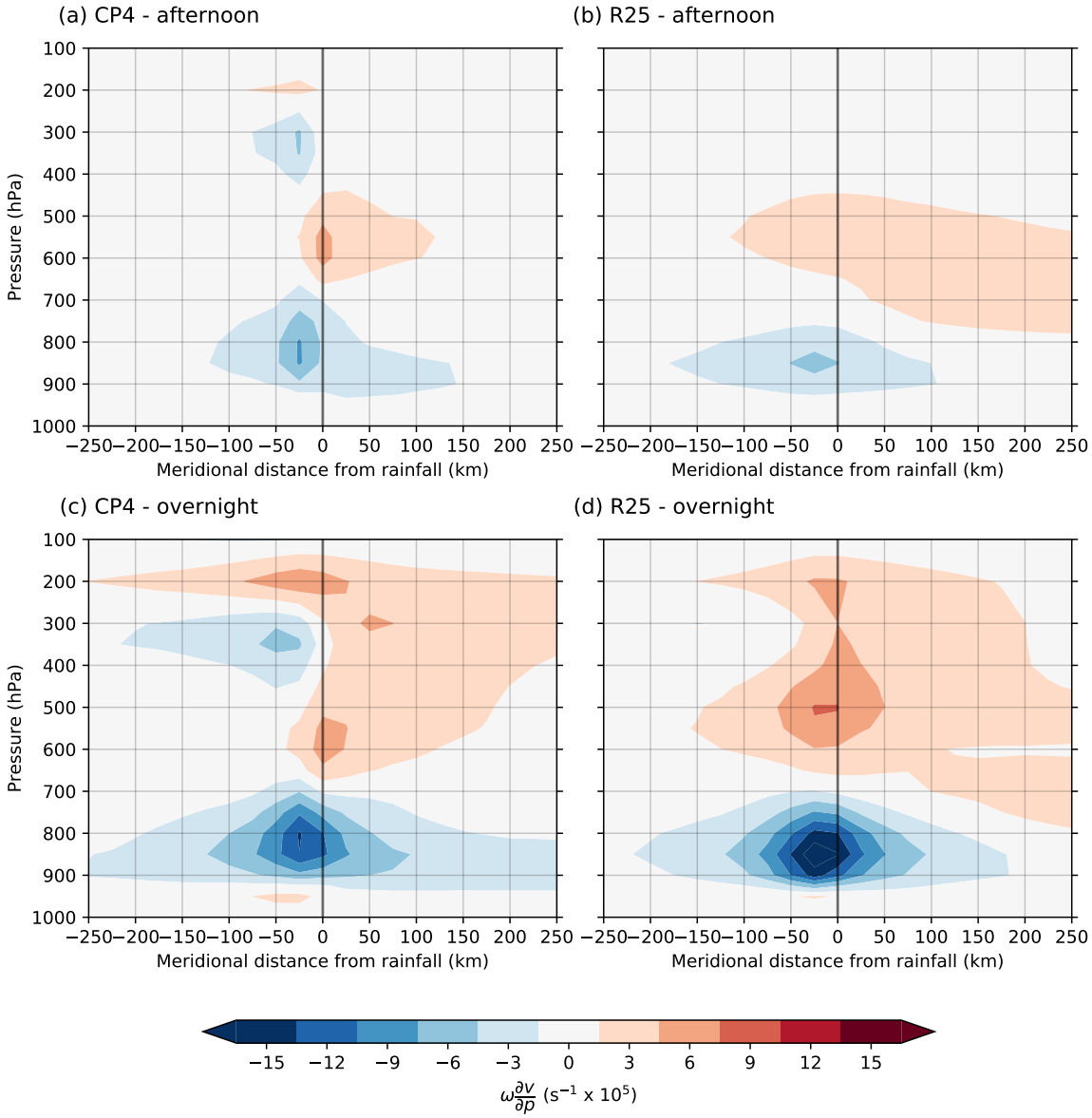

Figure 5.5: Composites of tilting term integrand $\left(\omega\dfrac{\partial v}{\partial p}\right)$ anomaly across a meridional (north-south) cross-section of 500 km centred on grid cells precipitating at a rate of 1mm h^{-1} or greater. The composited integrands contribute to the tilting integral through the eastern and western edges of the box.

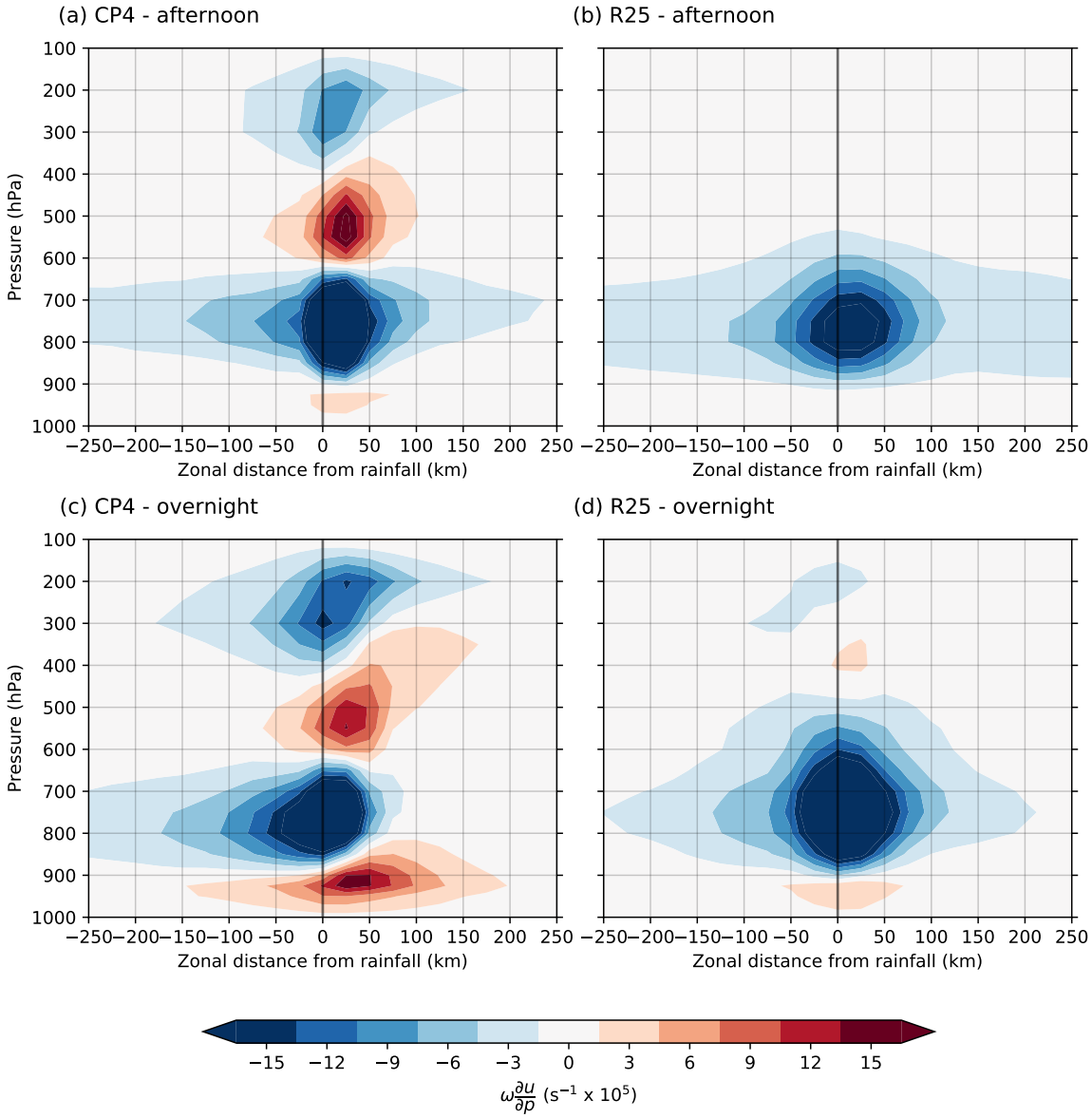

Figure 5.6: Composites of tilting term integrand $\left(\omega\dfrac{\partial u}{\partial p}\right)$ anomaly across a zonal (east-west) cross-section of 500 km centred on grid cells precipitating at a rate of 1mm h^{-1} or greater. The composited integrands contribute to the tilting integral through the northern and southern edges of the box.

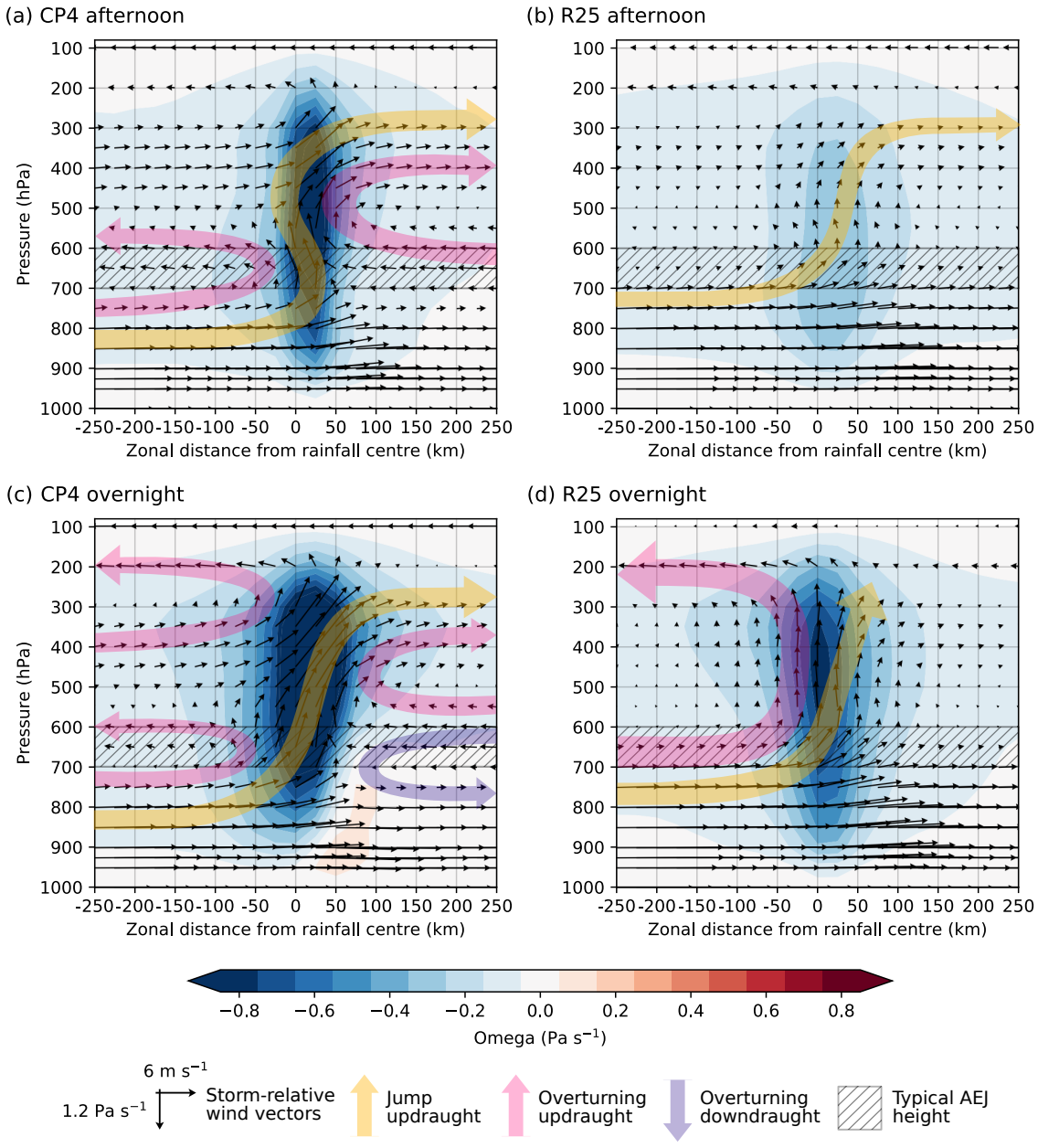

Figure 5.7: Composite of mean fields in a zonal cross-section extending 250 km to the west and east around grid cells precipitating at a rate of 1mm h^{-1} or greater, as averaged through afternoon convection 12–18 UTC (top row) and overnight convection 21–3 UTC (bottom row), for CP4 (left column) and R25 (right column). Vertical velocity in Pa s^{-1} is shown by filled contours. Vector arrows show storm-relative wind speeds such that the zonal and vertical components are on the same scale in the plane of the cross section. The thick overlaid arrows are schematic illustrations of the jump updraughts (yellow), overturning updraughts (pink) and overturning downdraughts (purple), with the hatched region showing the approximate height of the AEJ.

upper levels to the tilting integrand. The tilting term signature associated with convection is superimposed over the synoptic tilting associated with monsoon ascent and subsidence discussed previously. R25 does not have a similar tripole signature in the synoptic term. Again, the effect of these MCSs is not necessarily a synoptic process: when anomalies around non-precipitating grid cells are plotted (not shown) there is no signal at all, so the anomalies in the tilting integrand composites are robustly associated with precipitation. The diurnal convection is simply projected onto the synoptic tilting term. The signature of the anomalous tilting term, while small in magnitude, tends to roughly mirror the sign of the synoptic tilting term, likely from storms on the opposite sides of the box to where rain dominates.

Convective Momentum Transport and the Tilting Term

The differences in CP4 and R25's zonal tilting integrand composites is linked to the behaviour of the storm-relative winds around precipitating points, so figure 5.7 shows composites of storm-relative u and ω through a zonal (East-West) cross-section of the storm. An approximate storm propagation speed is calculated by taking the mean of the zonal velocity u across all points in the composite from 700 hPa and above. Storm-relative winds are calculated by subtracting this single value from all individual points in the composite. These propagating speeds are not likely to be precisely the mean of tracked MCSs in the domain, but they were of appropriate magnitude and agree with the literature which suggests that storms in CP4 move more slowly than storms in R25 (Crook et al. 2019).

Figures 5.7a and 5.7c show an intense updraught centred on the grid cell, with a stronger, wider, and slightly more elevated signature during overnight compared to afternoon convection. Both figures also illustrate a jump updraught moving from lower levels at the front of the storm to upper levels at the rear of the storm (yellow arrow). However, the signature differs from the archetypal profile shown in figure 2.3a (beyond the fact that here, pressure coordinates are used, replacing w with ω). There appear to be multiple overturning circulations (pink arrows) in both 5.7a and 5.7c: two to the front of the storm and an elevated overturning updraught to the rear of the storm. The pattern appears to disrupt the jump updraught somewhat in figure 5.7a. Figure 5.7c, however, does have an overturning downdraught (purple arrow) present at low levels to the rear of the storm, which matches the archetypal triple-branch circulation.

Because these composites are averaged over the entire storm, flows through the system can be

treated as three-dimensional, and can intersect. The double overturning updraught that appears to be present could simply be an impact of the AEJ intersecting a single overturning circulation, but perhaps the multiple-updraught signature is due to the reversal of the background shear profile at midlevels, where the mean background wind slows between the height of the AEJ and tropical easterly jet (TEJ). Whether it is the AEJ intersecting a single circulation or a double circulation, the momentum transport features implied by the composites still reflect the mean impact of storm systems in the region on momentum.

Figures 5.7b and 5.7d show the wind profiles in the R25 simulation for afternoon and overnight time periods respectively. The storm-relative patterns are less distinct than in CP4, with a slight jump updraught signature in figure 5.7b and weaker winds around the precipitating grid cell. In figure 5.7d there is a stronger updraught than in figure 5.7b, with a weak signature of an overturning updraught ahead of the storm but a less distinct jump updraught flow from front to rear. R25's composites are approximately symmetrical along a longitude (except for the easterly winds at upper levels comprising the TEJ, and the strong westerly storm-relative flow at low levels) which could be because its simulated squall lines do not travel in consistent directions.

In figure 5.8, the vertical profile of the products of mean storm-relative zonal velocity u_m and vertical velocity ω_m at each pressure level are calculated. The product $u_m\omega_m$ is effectively the convective momentum flux. The mean is taken across all u_m and ω_m values at each pressure level within the composites in figure 5.7. In Moncrieff (1992), the mean is taken for all points where the system has modulated the background wind field, while here it is taken between the edges of the composites since the size of a storm and its influence over the local wind profile is highly variable. The magnitude will be different since the values have not been normalised using inflow velocity (because the background motion of each precipitating grid point is difficult to calculate) and because pressure rather than height coordinates are used, one would expect the shape of the profile to be similar to the profile in figure 2.3b except negative.

However, in figure 5.8 there are two negative momentum peaks instead of one, at around 850 hPa and 400 hPa respectively. The pattern here makes sense in the context of the double overturning updraughts shown in figure 5.7. Each peak is associated with one of those updraughts, and the positive peak at around 600 hPa in CP4 is associated with the overturning updraught behind the storm in the other direction. The lower-level peak in overnight CP4 is less intense than

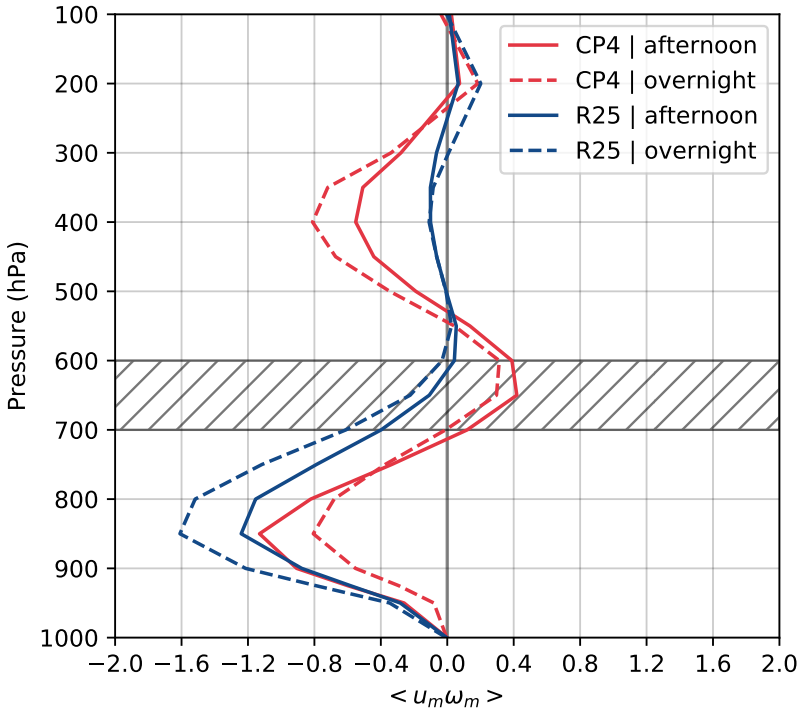

Figure 5.8: Vertical profiles of the mean product of composited storm-relative zonal velocity u_m and vertical velocity ω_m for CP4 (red lines) and R25 (blue lines) through afternoon convection 12–18 UTC (solid lines) and overnight convection 21–3 UTC (dashed lines). The mean values are calculated at each pressure level for the entire width of the zonal composites in figures 5.9–5.7. The hatched region represents the typical height of the AEJ.

the corresponding afternoon peak, which is consistent with figure 2.3b in that the presence of a downdraught significantly dampens the momentum transport signature. R25 is reasonably similar to these patterns although it does not exhibit as strong a negative circulation tendency, which may seem unexpected since the storm-relative wind profiles in figure 5.7 are quite different to CP4's. However, the background wind shear is similar between the two models which would cause the two different peaks in momentum transport due to two areas where wind speed increases with height. The similarity between momentum transport signatures is particularly noticeable during the afternoon period where the wind profiles of average precipitating features in CP4 and R25 are more similar. Overnight, there are more differences between the profiles of momentum transport in figure 5.8, perhaps because overnight precipitation is dominated by organised convective systems which CP4 represents differently to R25 (Crook et al. 2019).

The tilting integrand is connected in some respects to the convective momentum transport, $\langle \rho u_m \omega_m \rangle$. To understand the link between the tilting term and the momentum flux, consider the flux-form of the momentum equation:

$$\frac{\partial \boldsymbol{u}}{\partial t} + \nabla \cdot (\boldsymbol{uu}) = -f\hat{\boldsymbol{k}} \times \boldsymbol{u} - \frac{\nabla p}{\rho} - g\hat{\boldsymbol{k}}. \tag{5.3}$$

$\boldsymbol{uu}$ is the momentum flux tensor, a tensor product of $\boldsymbol{u}$ with itself, which can be explicitly written as

$$\boldsymbol{uu} = \begin{pmatrix} uu & uv & u\omega \\ uv & vv & v\omega \\ u\omega & v\omega & \omega\omega \end{pmatrix} \tag{5.4}$$

The momentum flux Λ described in Moncrieff (1992) is proportional to uw (or, in pressure coordinates, $u\omega$) which is one of the components of the momentum flux tensor (bottom row of the matrix). Considering the $u\omega$ component only, its pressure derivative can be calculated, $\frac{\partial \boldsymbol{u}\omega}{\partial p}$, which is one of the terms of the divergence of the momentum flux tensor $\nabla \cdot (\boldsymbol{uu})$ and is proportional to momentum change $\frac{\partial \boldsymbol{u}}{\partial t}$. Since

$$\frac{\partial}{\partial p}(\boldsymbol{u}\omega) = \boldsymbol{u}\frac{\partial \omega}{\partial p} + \omega\frac{\partial \boldsymbol{u}}{\partial p}, \tag{5.5}$$

the variation of the momentum flux Λ is indeed controlled to some extent by the "tilting" term, $\omega\frac{\partial \boldsymbol{u}}{\partial p}$.

Because of the relationship between the tilting term integrand and convective momentum transport, it is of interest to compare figures 5.5 and 5.6 to figure 5.8. The tilting term pattern (figure 5.6) is similar to the pressure derivative of the patterns shown by the convective momentum transport estimated in figure 5.8. Therefore, it is likely that the representation of convective momentum transport in storms leads to impacts on the circulation budget through the tilting term.

While the direct impacts of convective momentum transport on the tilting term are on the edges of the box, there are also indirect impacts. By modulating the wind field around the storm, the momentum transport may lead to changes in the vorticity accumulation patterns on the mesoscale and upscale. Of course, if a perfect vorticity dipole is contained within the circulation then it will have no net impact on the circulation, but dipoles associated with convection are rarely symmetrical (see figure 5.9, so the vorticity accumulation may be modulated. Also, the momentum transport could modulate the overall zonal wind field within the box, impacting the synoptic winds beyond that which can be measured by circulation. Understanding these effects would require further momentum budget analysis, which is beyond the scope of this chapter.

5.4.2 Vorticity Accumulation by Precipitating Features on the Mesoscale

Since accumulation is the flux of vorticity into the region, the anomalies (relative to the mean at a given point at a given time in the diurnal cycle) of absolute vorticity and divergence associated with precipitating grid cells were composited (figure 5.9). Meridional (North-South) composites in both CP4 and R25 show meridional dipoles of relative vorticity, with low-level convergence and upper-level divergence implying the existence of an updraught between the two. Overnight, composites exhibit midlevel convergence up to around 450 hPa (figures 5.9c and d). Composites around grid cells with rainfall under 1mm h^{-1} have negligible vorticity and divergence signatures (not shown), suggesting that the convective dynamics in figure 5.9 are robustly associated with precipitation.

CP4 has a narrower, more intense vorticity dipole than R25 with a greater vertical extent, from about 850 hPa up to over 200 hPa in the afternoon. In R25, the dipole exists at around 800–700 hPa in the afternoon and is around five times weaker. The dipole is consistent with lifting of vortex tubes (caused by the climatological vertical background shear) by vertical velocity associated with convection (e.g Holton and Hakim 2013a), and most simulations of squall lines

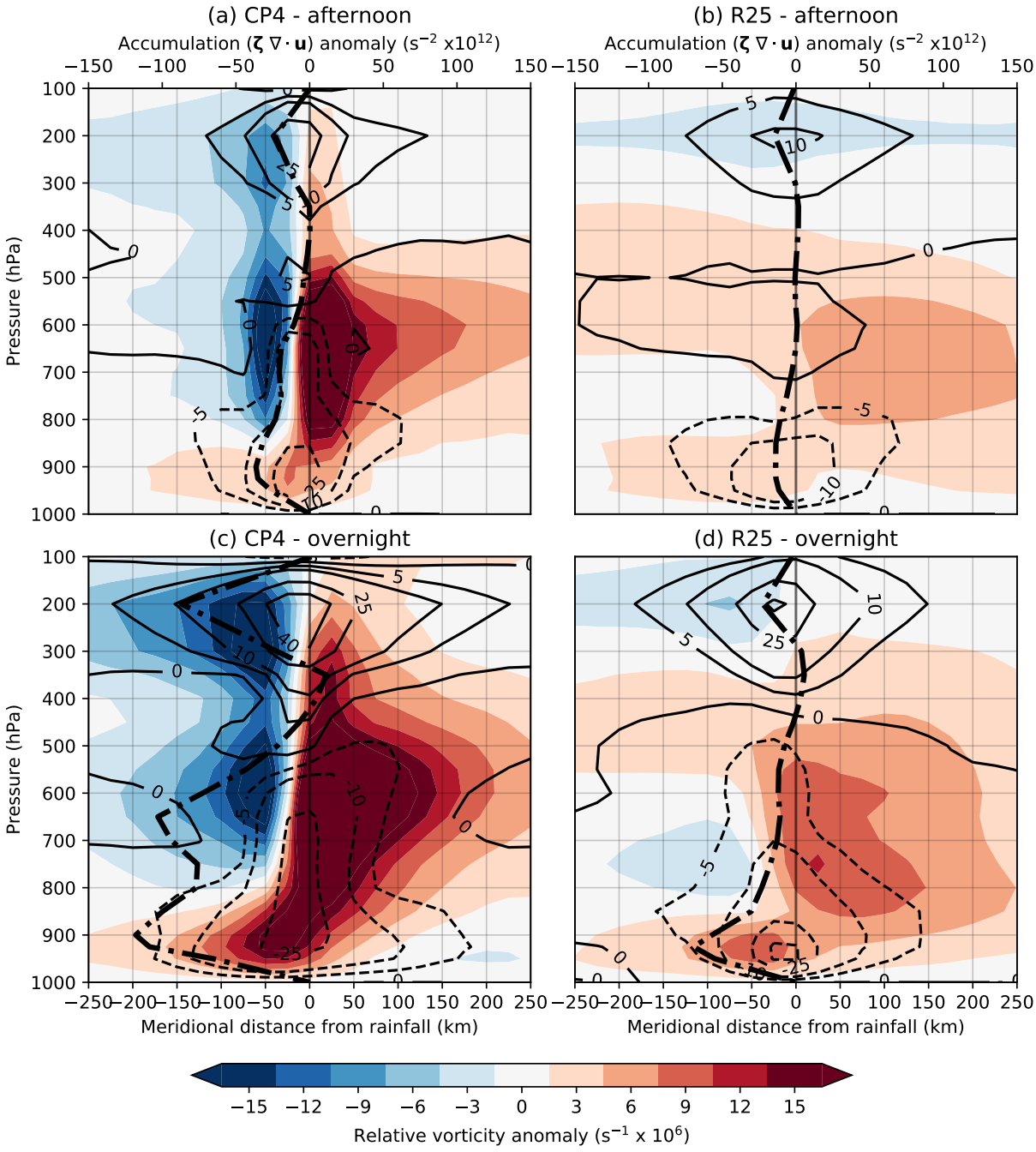

Figure 5.9: Composites of relative vorticity anomaly (filled contours) and divergence anomaly (line contours) across a meridional (north-south) cross-section of 500 km around grid cells precipitating at a rate of 1 mm h^{-1} or greater. Divergence anomaly is labelled in s^{-1} $\times 10^6$; dashed lines represent negative values (convergence). Thick black dot-dash line shows the product of the divergence and vorticity anomalies, averaged meridionally across the composite.

in West Africa (Rotunno et al. 1988), although case studies of some examples have a reversed North-South orientation (Diongue et al. 2002). The positive anomalies are more pronounced and extensive than the negative, due to the positive background planetary and relative vorticity (induced to the south of the AEJ due to the AEJ's zonal shear profile) being intensified by vortex stretching.

Both simulations have low-level convergence (negative divergence field) and upper-level divergence within around 150 km of the central precipitating point in the afternoon convection and expanding to around 200 km overnight. The convergence in CP4 is more sustained towards midlevels compared to R25. In both simulations, the vorticity and divergence signatures intensify overnight, where typically a larger fraction of convection is organised, and in CP4 the signatures widen and are elevated. Storms in R25 do not travel in such a uniform direction as those in CP4, which may impact the vorticity intensity, alongside the parameterisation being associated with a weaker updraught. The parameterisation may also not be reliably representing midlevel convection during the afternoon hours.

The product of vorticity and divergence approximately corresponds to the negative of the accumulation term's integrand. It is negative for almost the entire column, with intensity peaking at around 900 hPa and 200 hPa. Therefore, particularly at lower and upper levels, precipitating systems contribute positively to the circulation budget through accumulation (see equation 4.4) associated with storm-induced convergence pulling positive absolute vorticity into the region, increasing circulation. The same process may occur at midlevels where there is elevated convection. At upper levels, storm-induced divergence pushes negative vorticity anomalies associated with storms out of the box, which similarly contributes positively to the circulation tendency. The process of mesoscale convection therefore reinforces cyclonic circulation on the synoptic scale at lower and upper levels as reflected in figure 5.4c–d, and at midlevels in CP4, implying there is more elevated convection, or a greater updraught and convergence profile depth. The more intense positive low-level anomalous accumulation in CP4 can be explained by the stronger vorticity and divergence signatures than R25.

As discussed in section 5.3, precipitating convection may still be reflected in the synoptic accumulation term. For example, the height of the vorticity dipoles in CP4's composites can explain why the vertical signature of synoptic accumulation is more elongated in CP4 than R25, and the stronger negative vorticity anomalies at upper levels reduce the overall positive

absolute vorticity and thus decrease the negative synoptic accumulation tendency at 200 hPa when convection is active.

5.4.3 Comparison to Observations

The composited precipitation features are compared to an observed storm in August 2000, with measurements taken by dropsondes from a plane flying through the decaying storm at around 11 UTC. The east leg of flight A781 is along a constant longitude of approximately 2.2 ° E from 8 ° N to 18 ° N before turning around and passing behind the storm located at roughly 11 ° N. The storm can be identified in figure 5.10a by the reduced zonal velocity at around 600 hPa, where the winds induced by the storm have caused the jet to decelerate, and corresponding acceleration of easterlies in at lower levels, associated with the rear-inflow jet (Lafore and Moncrieff 1989). The deceleration signature coincides with convergence in the meridional wind field at 600 hPa and divergence at around 800 hPa (figure 5.10b).

Since the plane flew along a single latitude the measurements are not instantaneous nor can they provide a complete calculation of vorticity, but the component of vertical vorticity from the variation of zonal velocity along latitude ($-\frac{\partial u}{\partial y}$) as the plane flew by is estimated (figure 5.11a). There is a dipole structure present just below 600 hPa. The horizontal resolution is limited by the distance between sondes dropped (0.5 degrees, or around 55 km), so the precise scale of the dipole is unclear, but it is almost certainly constrained within 100 km either side of its centre. Below 800 hPa, a reversed dipole structure signature exists, forming a quadrupole which extends to around 200 km either side of the storm's centre. Figure 5.11 also shows the $\frac{\partial v}{\partial y}$ component of divergence. There is a divergence signature from around 900 to 750 hPa within around 100 km of the storm, with smaller regions of convergence 100–200 km from the centre of the storm between 850 and 750 hPa. Above 700 hPa, there is convergence at the centre of the vorticity dipole up to 500 hPa.

Few studies provide detailed observations of the internal structure of Sahelian storms. One of the few examples is a squall line observed on 22 June 1981 as part of the COPT81 project, analysed in Chong et al. (1987), Roux (1988) and Chalon et al. (1988). These papers show AEJ deceleration after the squall line passes, consistent with the observed vorticity structure (figure 5.11a) and descending rear inflow jet (figure 5.10) in this case.

Figures 5.11b and 5.11c, plotted following figure 5.9, are composites of relative vorticity and

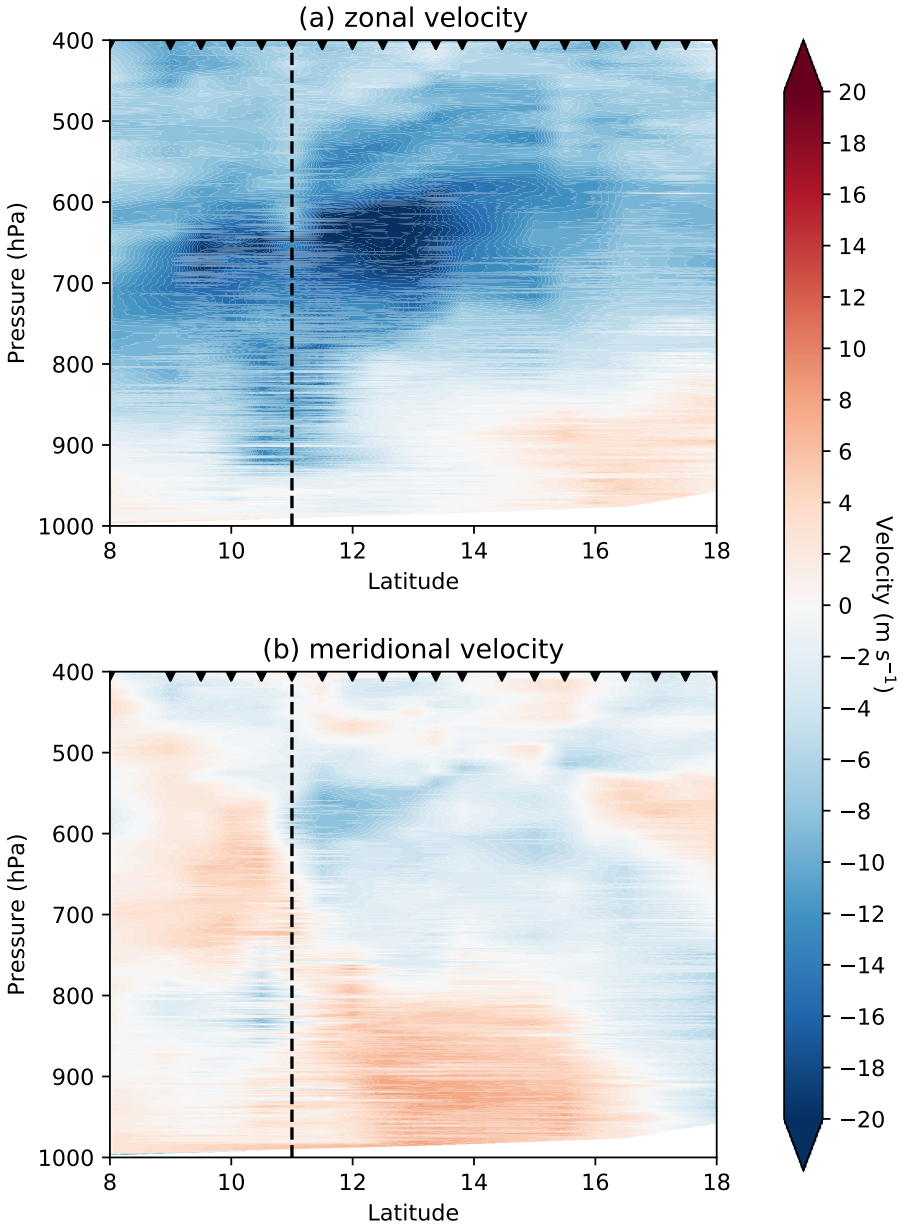

Figure 5.10: Cross-section of dropsonde profiles of (a) zonal and (b) meridional velocity (m s^{-1}) for flight A781 on the JET2000 campaign. The position of the storm that the flight travelled behind is marked at 11° N with a black dashed line. The positions at which dropsondes were dropped are shown by the black pips at the top.

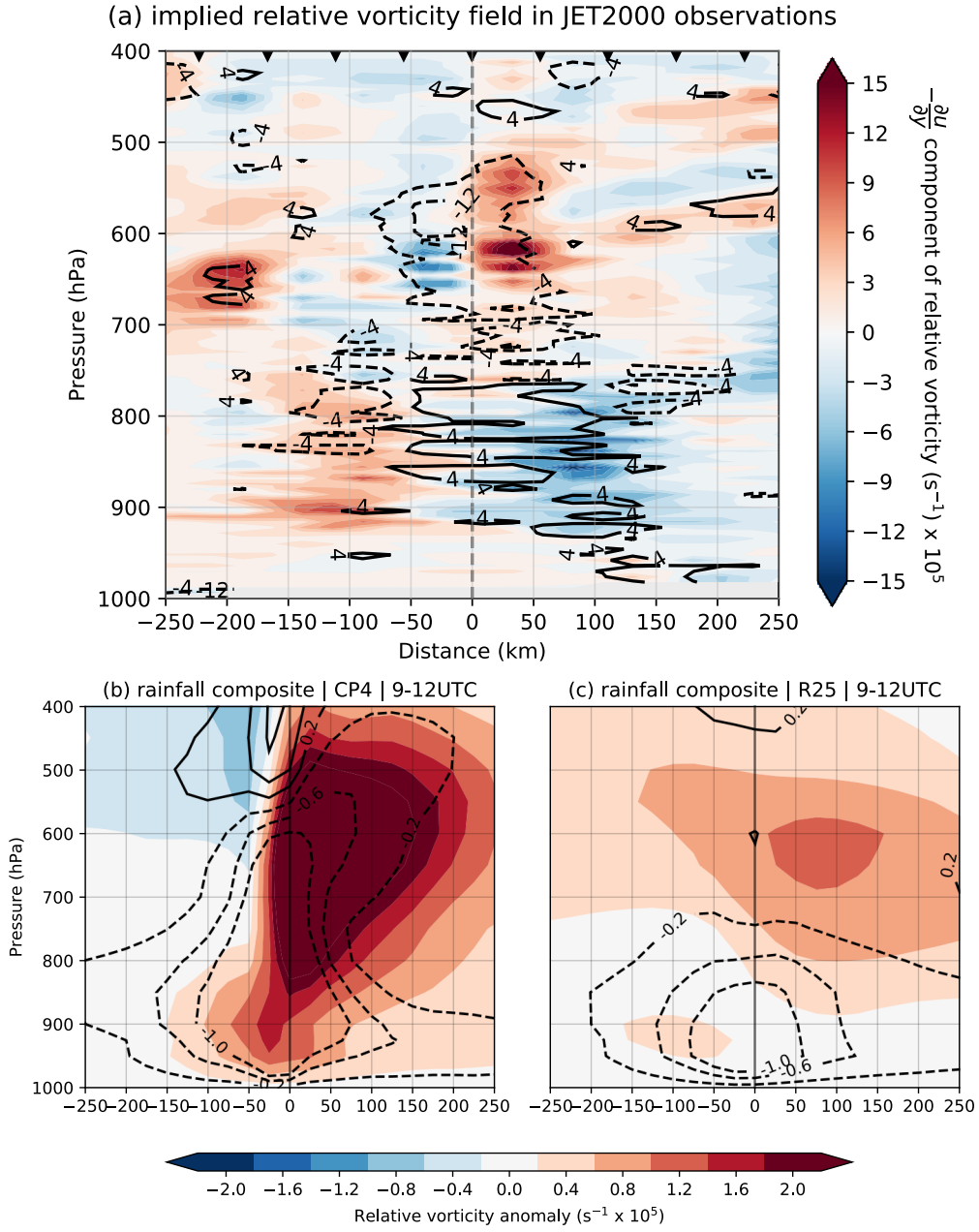

Figure 5.11: (a) Meridional cross-section of the relative vorticity term contributed by latitudinal change in zonal velocity, $-\frac{\partial u}{\partial y}$ (shading), and the horizontal divergence from meridional velocity variation $\frac{\partial v}{\partial y}$ (line contours, labelled in s^{-1} $\times 10^6$), spanning 500 km centred on the storm at 11 ° N (black dashed line). (b) Meridional cross-section of relative vorticity and divergence anomaly in composites around grid cells precipitating at a rate > 1mm h^{-1} in CP4 at 9–12 UTC over the same pressure range as (a). (c) As in (b) but for R25.

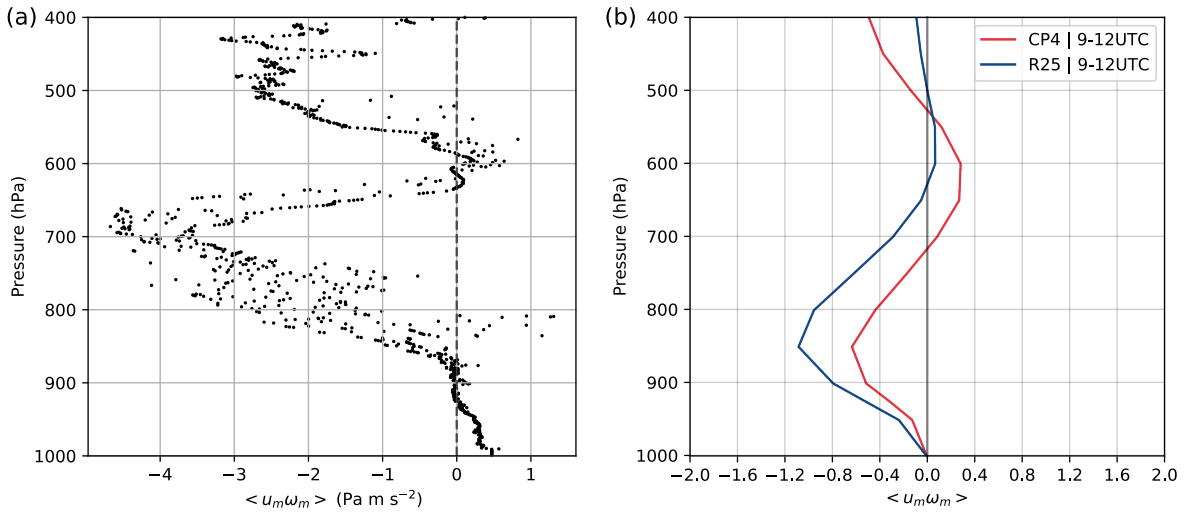

Figure 5.12: (a) Vertical profile of convective momentum flux $< u_m\omega_m >$ measured by the dropsondes in the JET2000 campaign at 11 ° N. (b) Vertical profile of convective momentum flux $< u_m\omega_m >$ calculated using storm-relative winds from composites around grid cells precipitating at a rate of 1mm h^{-1} or greater at 9–12 UTC in CP4 (red line) and R25 (blue line).

divergence anomalies around precipitating grid cells in CP4 and R25 respectively, over the same height range as the observations in figure 5.11a, taken over all July and August days at 9 and 12 UTC to approximately match the observation time on the observation flight. (In CP4, 36,630 grid cells are included in the period, and in R25 there are 126,772.) Note that the scales are different for observed (5.11a) and modelled (5.11b and 5.11c) plots since composited fields are a mean representation of many events, so it is difficult to compare the intensity of the vorticity signatures. Above 800 hPa, the shape of the observed signature is closer to the dipole structure in CP4 than the single positive vorticity anomaly in R25. Below 800 hPa, the observed reversed vorticity dipole is not present in either simulation. The reversed dipole may be a feature of decaying storms specifically, or perhaps is located only in the stratiform region which is not uniquely sampled by the compositing method. There is evidence for the latter: while not present in figures 5.11b and c, composites centred two grid cells to the west of precipitating grid cells (not shown) show low level divergence that matches the observations.

The dropsonde observations were also used to calculate an approximation of convective momentum flux $< u_m\omega_m >$ up to 400 hPa, shown in figure 5.12a. Measurements of zonal wind were used to calculate u_m at 11 ° N. ω_m was calculated by integrating $\frac{\partial\omega}{\partial p} = -\frac{\partial u}{\partial x} - \frac{\partial v}{\partial y}$ with respect to pressure. No data was available to calculate $\frac{\partial u}{\partial x}$, but a descending easterly rear inflow jet would contribute a negative $\frac{\partial u}{\partial x}$ at midlevels and above in the stratiform region of the storm behind

the convective line. The $\frac{\partial \omega}{\partial p}$ term may, therefore, be more positive than the estimated value, which would lead to a quicker decrease in omega with height, thus a shortened downdraught, and hence a more pronounced positive omega anomaly at 600 hPa.

Figure 5.12a shows a similar vertical structure to modelled profiles of $< u_m \omega_m >$ in 5.12b, with a stronger negative anomaly at lower levels and a weaker positive anomaly which peaks at around 650 hPa, and the correction discussed in the previous paragraph would bring the structure closer to the modelled ratio of peaks in CP4. The positive anomaly occurs in the region where the vertical velocity has become an updraught but the AEJ still causes a negative zonal velocity anomaly, leading to a positive product. Physically the anomaly corresponds to the upwards transport of easterly momentum from the jet.

The maximum negative momentum transport is smaller in both simulations' composites than in the observed storm, which may again be the dilution effect of composites. The peak momentum transport is also at a lower height in the simulations than the observations, perhaps because MCSs tend to have a descending rear inflow jet and, since the observations are taken towards the rear of the storm, the rear inflow jet is higher than it might be as it approaches the storm's leading edge. Therefore, the zonal wind profile of the observation will be elevated and as such so will the convective momentum signature. While a comparison to a single observation is not a robust validation, CP4 does reflect convective momentum transport more similarly to the observed case.

5.5 Summary and Conclusions

In this chapter, connections between processes on meso- and synoptic scales are considered in a specific focus area (figure 5.1) using two regional current-climate simulations: one with a deep convection parameterisation and one without. Following Haynes and McIntyre (1987), a synoptic circulation budget is calculated, with terms split by separating both vorticity and velocity into their diurnal mean ("synoptic") and perturbation ("anomalous") components. Using composites of dynamical quantities corresponding to the accumulation and tilting terms in the circulation budget around precipitating grid cells, picture of the dynamics of a typical MCS is constructed, and the processes are linked to the circulation tendencies in the region.

The contributions of convection-related processes in the four circulation budget terms consid-

ered, and their differences between the two simulations, are outlined in the schematic shown in figure 5.13. The circulation budget is dominated by the "synoptic accumulation" term (figure 5.13a), which is reasonably similar between the two simulations except for a slight difference in diurnal timing which corresponds to a lag in rainfall peak, and vertical extent. A process-based analysis explains that the WAM largely drives synoptic accumulation, but convective systems play a role in reinforcing and disrupting the WAM's diurnal variation. Storms contained entirely within a circulation will cause convergence of positive vorticity anomalies at lower levels, and at midlevels where there is substantial elevated convection, resulting in positive accumulation anomalies which move upwards as convection becomes more elevated overnight. At upper levels, storms cause divergence of positive background vorticity, resulting in negative accumulation anomalies on the synoptic scale. In CP4, since convection is deeper, negative vorticity anomalies are generated at upper levels, which lower the overall mean positive vorticity, reducing the magnitude of negative synoptic accumulation term at upper levels. The greater vertical extent in CP4 may be linked to the tendency of convection-permitting models to overestimate updraught speed and extent (Kendon et al. 2021). It is reassuring that the dominant term in the circulation budget, which appears to rely on convergence (and hence heating) profiles of convection, is similar in both simulations. It is not a new argument that the heating profile a parameterisation produces is crucial for simulating the wider impacts of convective dynamics, but the work carried out in this chapter supports the existing literature.

The representation of convection also affects the anomalous accumulation term, with the positive anomalies overnight representing the impacts of individual MCSs that do not occur in the same place regularly, but when they do initiate, their profile of vorticity accumulation is almost entirely positive. The anomalous MCSs act to reinforce cyclonic circulation around them (figure 5.13c).

The greatest differences between the two simulations' circulation budgets are in the synoptic tilting term. It appears that diurnal convection projects onto the synoptic tilting term, and is the most likely explanation of the difference in the term between simulations at mid- to upper levels. The tilting term is linked to convective momentum transport, a relationship detailed in subsection 5.4.1. Both simulations indicate an intense negative anomaly at low levels in composites of the integrand of the tilting term, so storms on the eastern (western) or northern (southern) edges of a cyclonic circulation will accelerate (decelerate) cyclonic circulation between

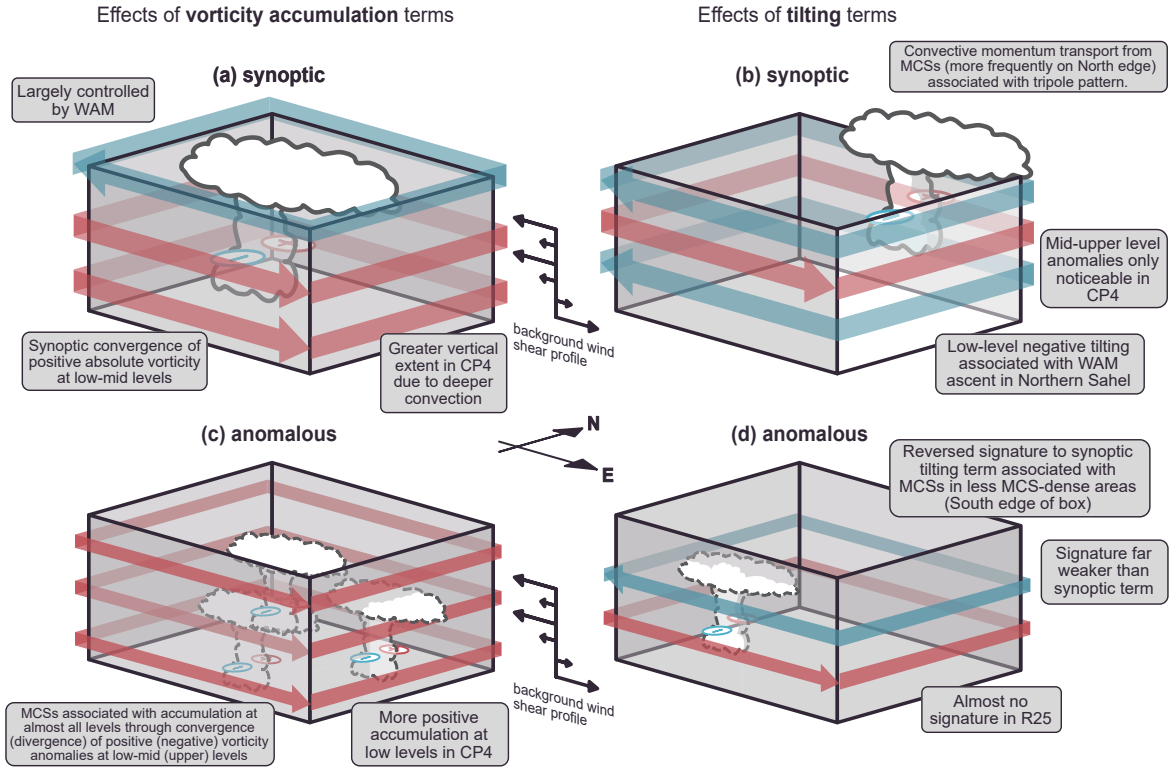

Figure 5.13: Schematic illustrating the effects of vorticity accumulation and vortex tilting linked to convection on the circulation budget. Top row shows synoptic (diurnal mean) effects and bottom row shows anomalous effects. Storms are illustrated in the location in the box where they impact each term. Red (blue) arrows indicate reinforcement of (anti)cyclonic circulation. Objects, and illustrative arrows, are not to scale.

around 900 and 600 hPa. In CP4, there is an opposite effect at 600–400 hPa, and returns to the original pattern above 400 hPa. The synoptic tilting term in CP4 shows a corresponding pattern, indicating that storms can modulate circulation on a large scale in resolved convection (figure 5.13b). Anomalous tilting shows a signature with opposing signs, indicating that some storms contribute an opposing circulation tendency to the diurnal pattern of rainfall: these are the less frequent storms on the southern (northern) side of the box in CP4 (R25) (figure 5.13d).

The analysis focuses on a fixed region, but understanding could be applied to specific case studies of circulations such as AEWs. There is a consensus in the literature that convection often is located to the west of an AEW trough axis, reinforcing the AEW circulation (see chapter 2). The results indicate that the momentum transport on the southern edge of a vortex serves to reinforce it, despite literature suggesting that weaker (non-developing) AEWs have convection to their south. However, convection on the western edge of a trough would reinforce the low-level cyclonic circulation associated with an AEW: that is, ahead (to the west of) an AEW trough, consistent with the literature.

The chapter goes on to use the circulation budget to examine interactions between mesoscale convection and synoptic circulation over the diurnal cycle in West Africa. The latter investigation reaffirms the importance of simulating realistic heating profiles in convective parameterisations. It further discusses the less crucial but still relevant role of considering convective momentum transport in MCSs in the context of the circulation budget tilting term, which in this particular case was distinctly different between simulations with and without a deep convection parameterisation. Convective momentum transport is therefore an important factor to consider in developing parameterisations in the future.

Having examined how the representation of precipitating convection affects nearby synoptic-scale circulations, the first part of research question 2 has been addressed. The second part of question 2 refers to the downstream impacts of the differing representation of convection, in the form of tropical cyclogenesis over the Atlantic, which will be explored in the next chapter.

Chapter 6

North Atlantic vortex populations in CP models

Having discussed the dynamics of precipitating convection over land in West Africa and how such dynamics influence the synoptic-scale circulation in the region, this chapter addresses another form of mesoscale organised convection which can originate over West Africa: tropical cyclones (TCs).

Convection-permitting (CP) models have demonstrated potential for improved representation of TCs in simulations. Chapter 2 presents a summary of literature about TC genesis, and work so far indicates that considerable value is added by the use of CP models to simulate populations of TCs in global climate models (GCMs). A consensus in the literature suggests that African Easterly Waves (AEWs) are a key precursor to Atlantic cyclogenesis, with up to 70% of Atlantic TCs originating from AEW disturbances (Russell et al. 2017). Since it is also established that the representation of convection is crucial to accurately simulating AEWs, and that AEWs are better-represented in CP models, it follows that a potential source of skill in the representation of TCs in CP models may be as a result of TC genesis associated with convective clusters that originate over West Africa. However, the hypothesis is the subject of debate, with some studies arguing that the link between AEWs and TCs is overstated (Patricola et al. 2018; Danso et al. 2022).

In this chapter, the statistics vortices generated over land and over the ocean in CP4 are quantified and compared to those in R25 to evaluate the impact of a convection parameterisation

on the vortex populations. The work reinforces the link between vortices and the representation of convection in the simulations, as examined in the composites in chapter 5, and explores the thermodynamics of the vortices generated in both simulations. Finally, there is a discussion of the implications of the vortex characteristics for the generation of tropical depressions and TCs in CP models, and the motivation for the development of CP GCMs.

6.1 Data and methodology

6.1.1 Data

To quantify the value of CP models, compared to models with deep convective parameterisations, for representing vortex structures that may undergo tropical cyclogenesis, a CP climate simulation is compared to a similar simulation with a convective parameterisation. As in chapter 5, the simulations used are CP4-Africa (CP4) and its corresponding parameterised simulation (R25). The model configurations are described in detail in chapter 3. The simulations were selected because CP4 has demonstrably improved convective characteristics relative to R25, but they are comparable experiments which cover West Africa and part of the Eastern Atlantic, with a long timescale over which to calculate statistics of vortex populations.

There are limitations to using CP4 and R25: firstly, they are free-running 10-year simulations, so it is not possible to directly compare case study events. Furthermore, the resolution of the two models is different. Regridding the data to the same resolution counteracts the resolution difference somewhat, but a finer grid will inherently improve dynamical representation of smaller features. Thirdly, the investigation region is limited by the model boundaries, which only extend to 24.5° W. Therefore, the full lifetime of tropical cyclogenesis cannot observed within the domain, and boundary effects near the edge of the domain must be accounted for. The analysis is therefore limited to the very first steps of tropical cyclogenesis: the generation of vortex populations with dynamical and thermodynamic properties such that they may be suitable candidates to develop into tropical depressions.

Finally, it should be noted that CP4 and R25 are not ocean-coupled simulations. Models with atmosphere-ocean coupling are preferred for the simulation of TCs, since the intensification and maintenance of TCs depends significantly on interactions with the upper-level ocean, the state of which can in turn be modulated by a TC's dynamics and precipitation. CP4 and

R25's oceans are prescribed fixed sea surface temperatures (SSTs) on a daily basis, derived from a climatology of the region during the simulated years of 1997–2006 (Stratton et al. 2018), effectively acting as an unmediated energy source to drive rainfall, potentially resulting in the noticeable wet biases over the ocean in CP4.

However, despite these limitations, a study of the potential for vortex formation in a CP simulation compared to a simulation with a deep convective parameterisation, over a region where TC seeds are known to form, should serve as an evaluation of the added value of CP models for representing tropical cyclogenesis. The investigation could potentially illustrate the pitfalls of using simulations with convective parameterisations in the Atlantic Basin to examine the genesis of TCs.

6.1.2 Vortex Identification

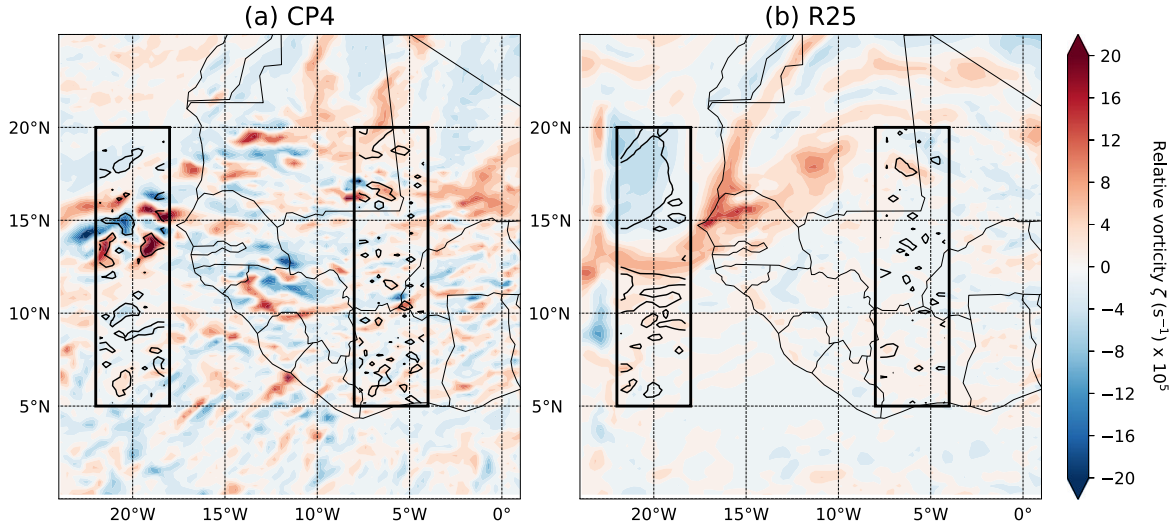

Figure 6.1: Snapshot of 850 hPa relative vorticity on 5th September 2006 at 15 UTC (filled contours) in (a) CP4 and (b) R25. (Note that the plot does not correspond to the actual date since the simulations are free-running climate models). Vortices identified with kinematic vorticity number $W_k > 1$ are outlined in black contours. Thick black outline indicates regions of interest over land and sea.

Vortices are identified in both simulations during August and September, the most active months of the North Atlantic TC season. Two regions were selected, illustrated in figure 6.1, extending from 5° N to 20° N, one over land (4° W to 8° W) and one over ocean (18° W to 22° W), and statistics of the vortices within each were compared for all timesteps. The ocean region is as wide as possible without starting to interact with edge effects due to proximity to the model domain boundary. The land region is as long as possible while constrained to be entirely over

land. These dimensions were matched for both regions.

Vortices which exist for multiple timesteps are counted multiple times, which is accounted for in the analysis. If any vortices cross the boundary of the selected regions, only the area of the vortex within the region is analysed when calculating its properties, so the maximum vortex area is limited. Vortices are identified at 850 hPa, a height often used to track AEWs (Bain et al. 2014) since it is close to the vertical level where the background zonal wind is zero. As a result, forecasters often diagnose pre-convective mesoscale vortices at 850 hPa (Cornforth et al. 2017).

To identify the vortices, objects are thresholded using the kinematic vorticity number, W_k, a dimensionless parameter which quantifies the rotation-strain ratio in a fluid. W_k is defined by Schielicke et al. (2019) as

$$W_k = \frac{||\mathbf{\Omega}||}{||\mathbf{S}||}, \tag{6.1}$$

where $||\mathbf{\Omega}||$ is the tensor norm of the skew-symmetric rotational component of the velocity gradient tensor, $\nabla\mathbf{u}$, and $||\mathbf{S}||$ is the tensor norm of the symmetric strain-rate non-rotational component. W_k is used rather than simply relative vorticity contours because W_k identifies vortices of cyclonic and anticyclonic rotation, and also specifically selects region of rotation rather than regions of shear vorticity, which is especially important in a region as strongly dominated by background wind shear as West Africa. Vortices are defined by contours of $W_k > 1$, identified using Python package scikit-image (Van Der Walt et al. 2014).

6.1.3 Thermodynamic Metrics

The thermodynamic metrics of cyclone phase space defined in Hart (2003), $-|V_U^T|$ and $-|V_L^T|$, were calculated centred on the centroids of identified vortices. The metrics were developed to characterise the process of extratropical transition of tropical disturbances as they decayed after making landfall, but in this case it can be used to characterise the thermodynamics of vortices over land in West Africa and over the North Atlantic Ocean. AEWs typically have cold-core structures at lower levels (Kiladis et al. 2006), with convection colocated with the edges of AEW troughs rather than directly at the centre. As they move over the ocean, a subset of the AEWs may turn into warm-core vortices which are potential candidates for tropical cyclogenesis.

Quantities $-|V_U^T|$ and $-|V_L^T|$ are defined as

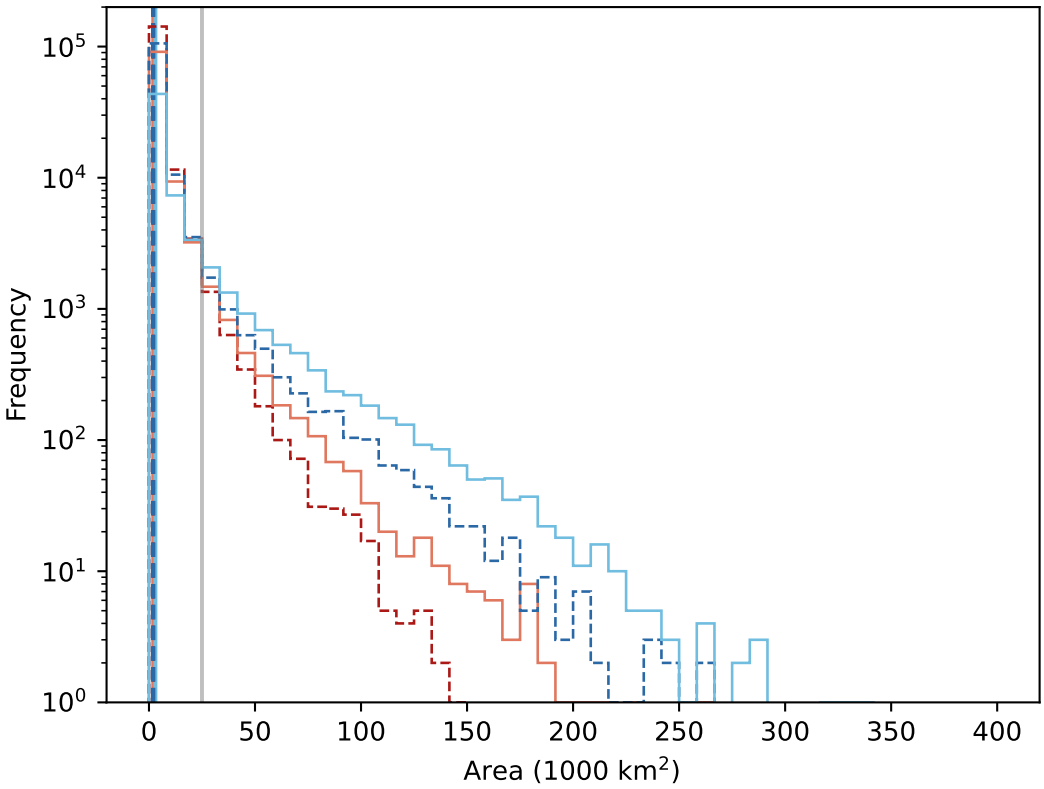

Figure 6.2: Histogram showing frequency of vortices, on a logarithmic scale, with different values of area. Median values for each model and region are shown by the vertical lines. Dashed darker lines represent CP4 and the lighter, solid lines represent R25. Sea region is shown in blue and land in red. Grey line indicates an area of 25,000 km^2.

$$-|V_L^T| = \frac{\partial(\Delta Z)}{\partial \ln p}\Big|_{600\,\mathrm{hPa}}^{900\,\mathrm{hPa}} \quad \text{and} - |V_U^T| = \frac{\partial(\Delta Z)}{\partial \ln p}\Big|_{300\,\mathrm{hPa}}^{600\,\mathrm{hPa}}, \tag{6.2}$$

where ΔZ is the difference between the minimum and maximum values of geopotential in a radius of 500 km around the centroid of the structure, and p is pressure. A warm-core structure is indicated by positive values of $-|V_U^T|$ and $-|V_L^T|$.

6.2 Vortex Statistics

6.2.1 Vortex Frequency and Intensity

Vortices with $W_k > 1$ were identified in the two regions illustrated in figure 6.1, and their area, intensity (mean relative vorticity), and mean moisture within each vortex (specific humidity and total column water) was calculated. Low-level cyclonic vorticity (at, for example, 850 hPa)

is often associated with disturbances that may become TCs, as is low-to-mid-level moisture. There are more vortices in total in CP4 compared to R25, over both land and sea, which can be seen in figure 6.2. Figure 6.2 indicates that in both simulations, the vortex population is dominated by very small vortices over both land and sea. The larger number of small vortices in CP4 than R25 may be a byproduct of their differing resolutions, but in both cases there are far more vortices with large areas over the ocean than over land.

Since the algorithm identifies even single grid-cell features with a $W_k > 1$, it is important to remove features which are far too small to be properly resolved in the simulations. At best, simulations resolve features which are at least 4–5 grid cells across (Inness and Dorling 2013), meaning a radius of at least 50–75 km assuming approximately circular features on grid with 25-km spacing. For the purposes of this chapter, the most relevant vortices are those which are suitable candidates to become tropical cyclone precursors. While small-scale vortices may merge later on in their lifetimes, to ensure only vortices that might feasibly become tropical depressions are selected, the population is narrowed down to those with larger areas. TCs in the North Atlantic Basin typically form with radii of 400 km or greater, but most TC precursors that originate over land will be smaller. Taking the balance between sufficiently resolved features and vortices that are somewhat smaller than the baseline radii of TCs, vortices of areas greater than 25,000 km^2 are selected from all the identified features (illustrated by the grey line in figure 6.2), corresponding to a radius of around 90 km.

Figure 6.3 shows the effect of limiting the vortices to only those of sufficient area on the distributions of three key measurements: the mean relative vorticity within each vortex at the height at which they are identified (850 hPa, left column), the mean specific humidity at the same height (middle column), and the mean total column water in each vortex (right column). The top row shows the distributions of properties for all vortices and the bottom row shows the impact of limiting the vortex populations to only those with area > 25,000 km^2. Perhaps due to the smaller sample size, the difference in the medians of the different distributions (indicated by the vertical lines) is greater for the population restricted to larger vortices, particularly for the moisture characteristics. Figures 6.3e shows that for both simulations, the 850 hPa specific humidity within vortices decreases, on average, over the ocean relative to the vortices over land. However, in terms of total column water, the median value stays similar for the land and ocean populations in R25, but is higher over the ocean than over the land in CP4. The

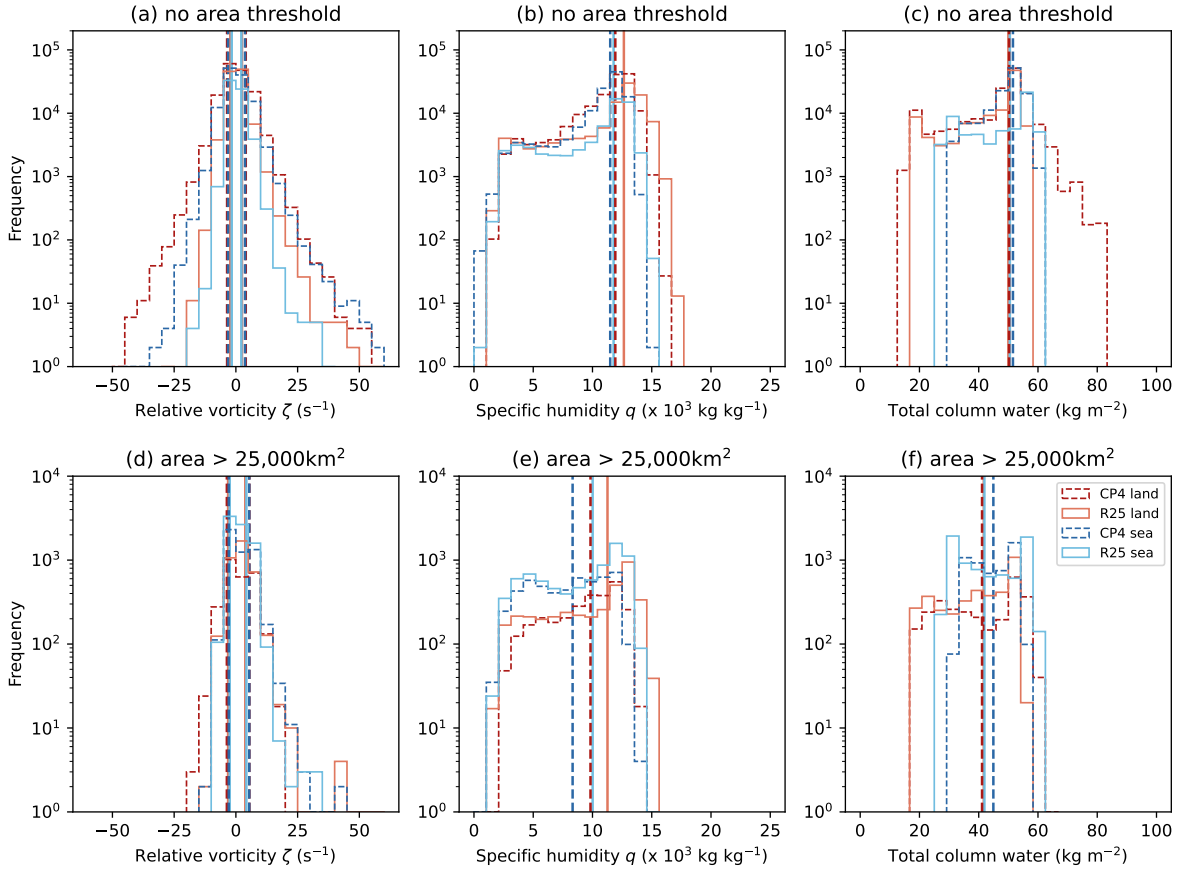

Figure 6.3: Histogram showing frequency of vortices, on a logarithmic scale, with different values of mean relative vorticity at 850 hPa (left column), mean specific humidity at 850 hPa (middle column), and mean total column water (TCW; right column). Dashed darker lines represent CP4 and the lighter, solid lines represent R25. Sea region is shown in blue and land in red. The vertical lines indicate the respective medians of each distribution (for relative vorticity, medians are calculated for both positive and negative vortices). The top row indicates statistics for all vortices, and the bottom row limits the population to vortices with an area of 25,000 km^2 or greater.

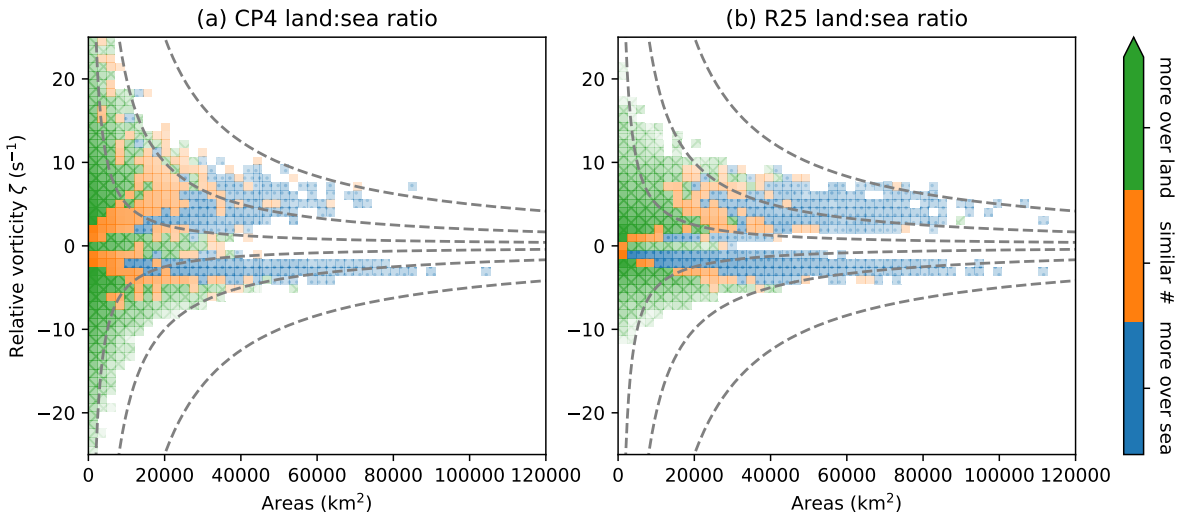

Figure 6.4: 2-D histogram showing the ratio of number vortices in the land region to number of vortices in the sea region in given bins of area (x-axis) and mean relative vorticity (y-axis), for (a) CP4 and (b) R25. Colours indicate whether the ratio is greater than 1.2 (more vortices over land, green), between 0.8 and 1.2 (around the same number of vortices over land and ocean, orange), or less than 0.8 (more vortices over sea, blue). The opacity of each box is proportional to the total frequency of vortices in each box in both simulations. Bins are only shown if there are at least 10 total vortices over land and sea in the given bin. The grey dashed lines illustrate levels of constant circulation.

increase in total column moisture implies that vortices over the ocean in CP4 are wetter, which ties in with known wet over-ocean biases in the simulation. A discrepancy in lower-atmosphere humidity implies that there are differences in either vertical transport, convective efficiency, or the representation of monsoon winds.

There are subtle differences in the mean relative vorticity distributions between the two simulations. There are fewer negative vortices with relative vorticity < 0 in R25 than in CP4, especially over the ocean. However, when limited to only large vortices with areas $> 25{,}000\,\mathrm{km}^2$, the negative vortex populations are similar. The distribution of negative vortices is not as directly relevant for the formation of TC precursors since that depends on cyclonic vorticity, but the values of positive vorticity are also slightly higher in vortices over the ocean in CP4 than in R25, suggesting that on average the CP4 population of ocean vortices are more likely to undergo cyclogenesis.

Mean relative vorticity and area are both relevant when considering the potential for cyclogenesis in a vortex, so the distributions of area and relative vorticity are presented in conjunction in a two-dimensional histogram in figure 6.4. Both CP4 and R25 produce smaller and more intense vortices more frequently over land, with larger and less intense vortices over the ocean. In

CP4, there are more bins with similar numbers of vortices in both regions, shown by the larger orange area, and the distribution of vortices skews smaller and more intense (likely an effect of the finer resolution). For both simulations, there are more vortices over 25,000 km^2 in area over the ocean than over land.

The larger vortex sizes in R25 result in a greater ratio of vortices with higher circulations compared to those in CP4, but these vortices may be more diffuse and too weak to become TC precursors. In both simulations, vortices with higher circulations tend to be more prevalent over the ocean than over land. CP4 has more vortices over the land with higher circulations, due to their higher values of vorticity. However, over the ocean, following figure 6.3d, there appear to be similar frequencies of large vortices over the ocean.

The difference between the number of intense vortices over the land and over the ocean is much higher in R25 than it is in CP4; in fact, for vortices over 25,000 km^2 in CP4, there is a higher frequency of more intense vortices over the ocean. There are two possible reasons for the difference: for a given number of vortices that are generated over land, either (i) the way in which vortices are transported from over land to over the ocean is different between the two simulations, (ii) the way in which ocean vortices are generated varies between the two simulations, or some combination of both effects.

To investigate the advection of vortices from land to ocean, vorticity signatures are composited around the centroids of positive vortices over land for both the time at which the vortex was identified and the following timesteps for 48 hours (figure 6.5). The vorticity signatures in figure 6.5 are not truly a reflection of the average transportation of a vortex; as composites they will account for the dissipation of vortices and will merge the effects of vortices travelling in directions other than directly westwards, and at speeds which are both faster and slower than the observed "translation speed" in these plots. It is likely the effect of averaging over various trajectories which dominates the apparent decrease in the amplitude of vorticity at later times.

Regardless of the direct interpretation of the patterns observed in the composites, CP4 and R25 both seem to have rather similar signatures in terms of the favoured direction of translation and the amplitude (perhaps implying a similar distribution of vortices which travel in different directions). As a result, the figure suggests that the mean advection associated with vortices in the two simulations are very similar. Therefore, reason (i) is not a likely cause of the disparity in differences in vortex numbers.

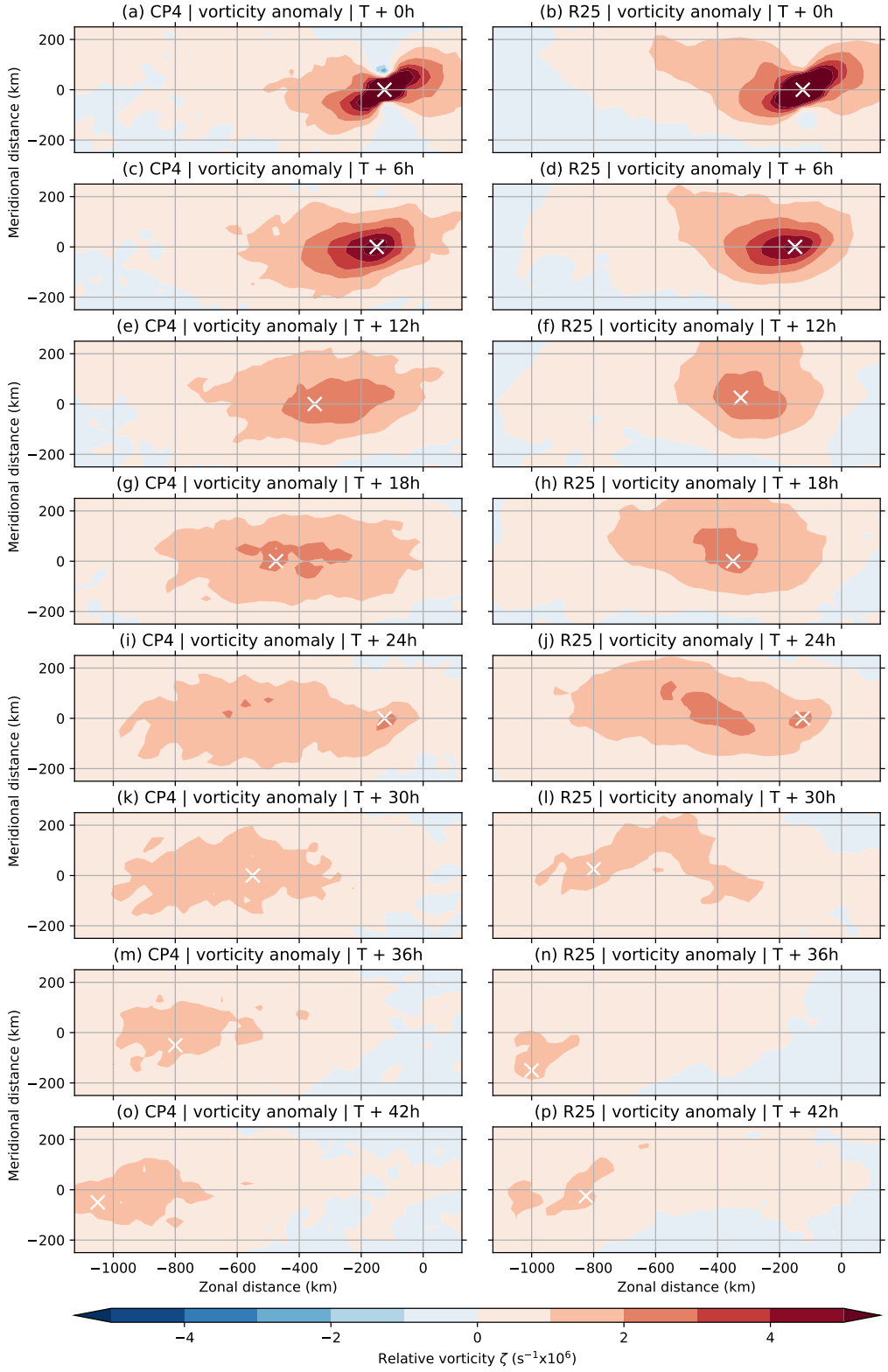

Figure 6.5: Composites of the relative vorticity anomaly (filled contours, s^{-1}) around centres of positive vortices at the time that the vortices identified using the $W_k > 1$ threshold over land, and composited around the same location as time goes on, thus showing the average vorticity field evolution around a given identified vortex. The centroid of the identified vortex is at coordinate (0,0). Vortices in CP4 are shown in the left column and R25 are shown in the right column.

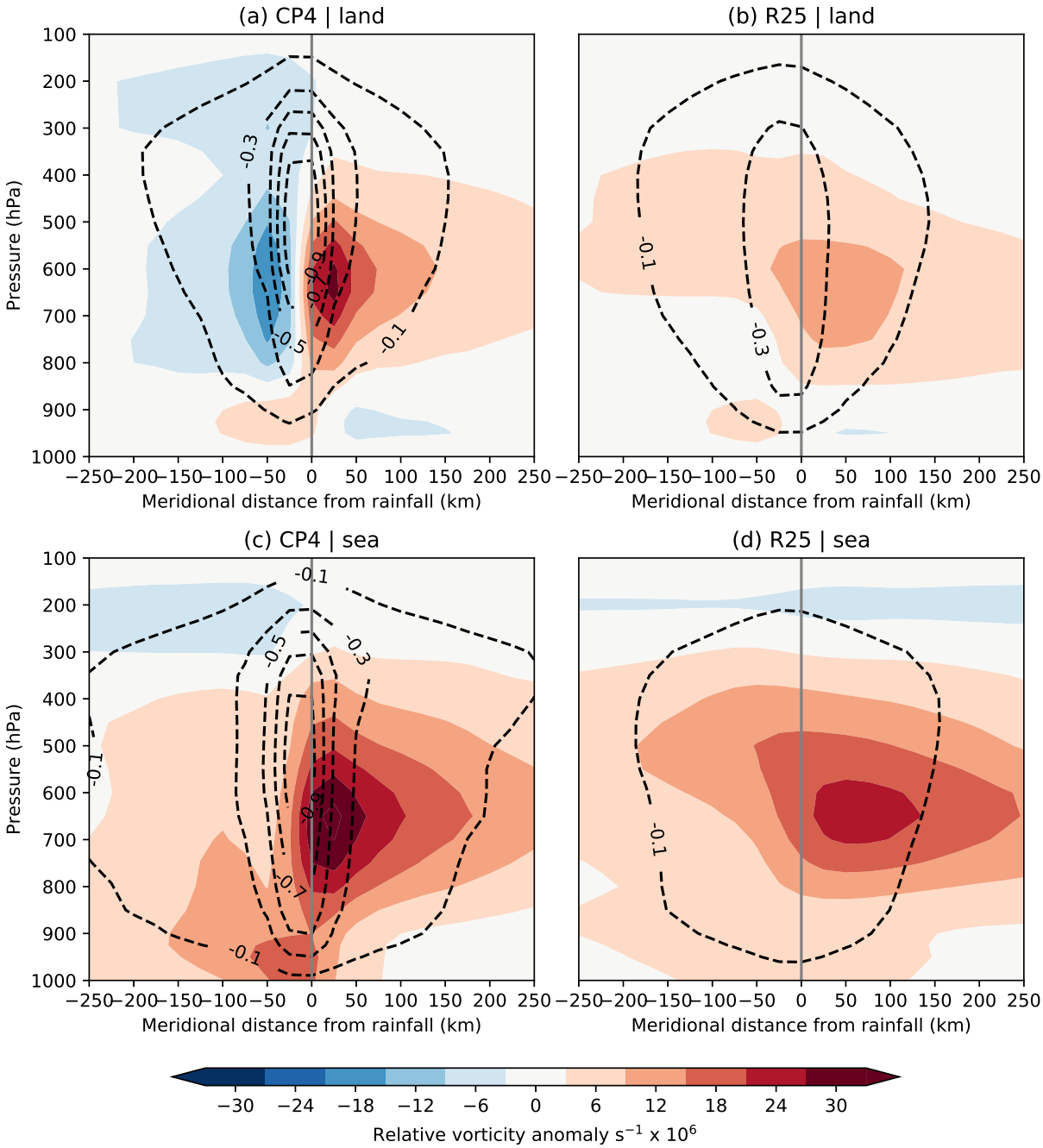

Figure 6.6: Composites of the relative vorticity anomaly (filled contours, s^{-1}) and vertical velocity (line contours; Pa s^{-1}) in a 500-km north-south (meridional) cross-section centred around grid cells where the rainfall rate exceeds 1 mm h^{-1}.

Another potential cause of the large drop-off in number of vortices over the ocean could be due to differences in oceanic convection in both simulations. To examine the differences between the dynamics associated with convection, the vorticity field is composited along a 500-km meridional cross-section around grid cells precipitating at a rate of $1\,\mathrm{mm\,h^{-1}}$ in figure 6.6, in a similar way as is computed in chapter 5. Vorticity anomalies around precipitating grid cells, as well as the updraught, are more intense and narrower in CP4 than in R25, which corroborates with the well-established behaviour of CP models (Kendon et al. 2021). Because of the strong colocation of vorticity with rainfall, it is possible that the large number of vortices observed in CP4 over the ocean are linked to the wet bias in the region (Stratton et al. 2018).

6.2.2 Vortex Thermodynamics

The thermodynamic properties of vortices also vary for those over land and over the ocean. Calculating the values of $-|V_L^T|$ and $-|V_U^T|$ for each vortex in each region produces distributions shown in figure 6.7 for all vortices and for exclusively large vortices. Observations and reanalysis indicate that AEWs often have cold-core structures below 700 hPa, but increase in temperature above the jet level (e.g. Kiladis et al. 2006), which is reflected in the lower average value of $-|V_L^T|$ and higher average value of $-|V_U^T|$ for larger vortices in CP4 over land (dark red dashed line in figures 6.7c and d).

The variation in warm- and cold-core structures over the land suggests, therefore, that there are vortex structures which are both within and outside of AEWs. In both simulations, there is a distinct shift of the modal value of $-|V_L^T|$ from less to more positive between land and ocean, indicating that vortices over the ocean have warmer-core structures between 900 hPa and 600 hPa than vortices over land, regardless of vortex size. The change in the median between the land and ocean is of a similar magnitude in both simulations, suggesting that the transition of vortices from cold-core to warm-core structures at low levels is similar in CP4 and R25. It should also be noted that since the vortices are identified using dynamics at 850 hPa, any tilt in the vortices may result in the thermodynamics at 600 hPa and above being decoupled from a deeper vortex structure that tilts.

By contrast, the median value of $-|V_U^T|$ decreases moving from land to ocean in CP4, becoming negative over the ocean (figure 6.7b and d). It appears that $-|V_U^T|$ and $-|V_L^T|$ are somewhat negatively correlated over land, which can be seen in the two-dimensional histograms in figure

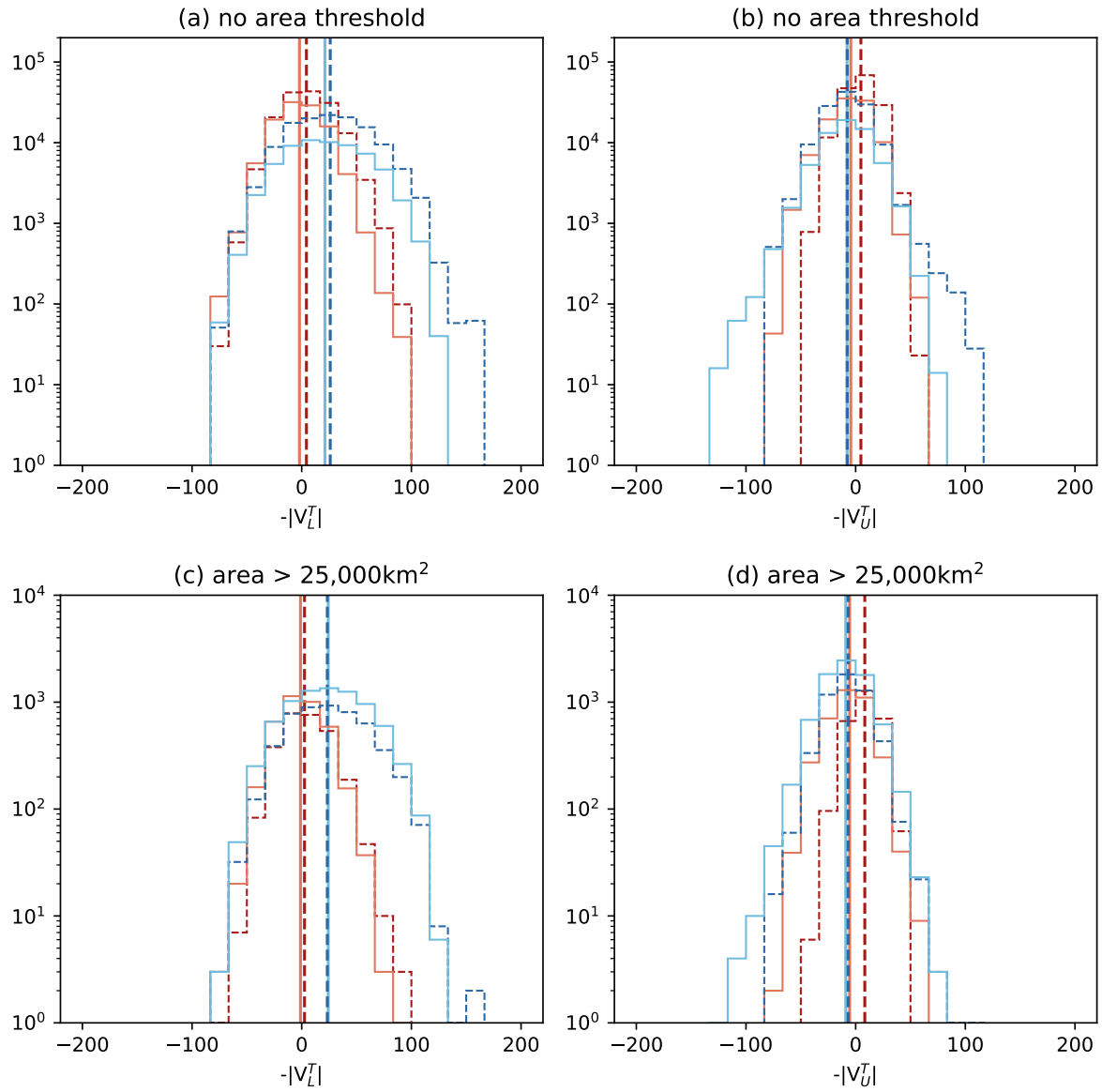

Figure 6.7: Histograms showing the frequency of vortices with different values of $-|V_L^T|$ (left column) and $-|V_U^T|$ (right column) for all vortices (top row) and only vortices with area > 25,000 km^2. The dashed darker lines indicate vortex populations in CP4 and the lighter, solid lines indicate vortex populations in R25. Sea region is shown in blue and land in red. The vertical lines indicate the medians of corresponding distributions.

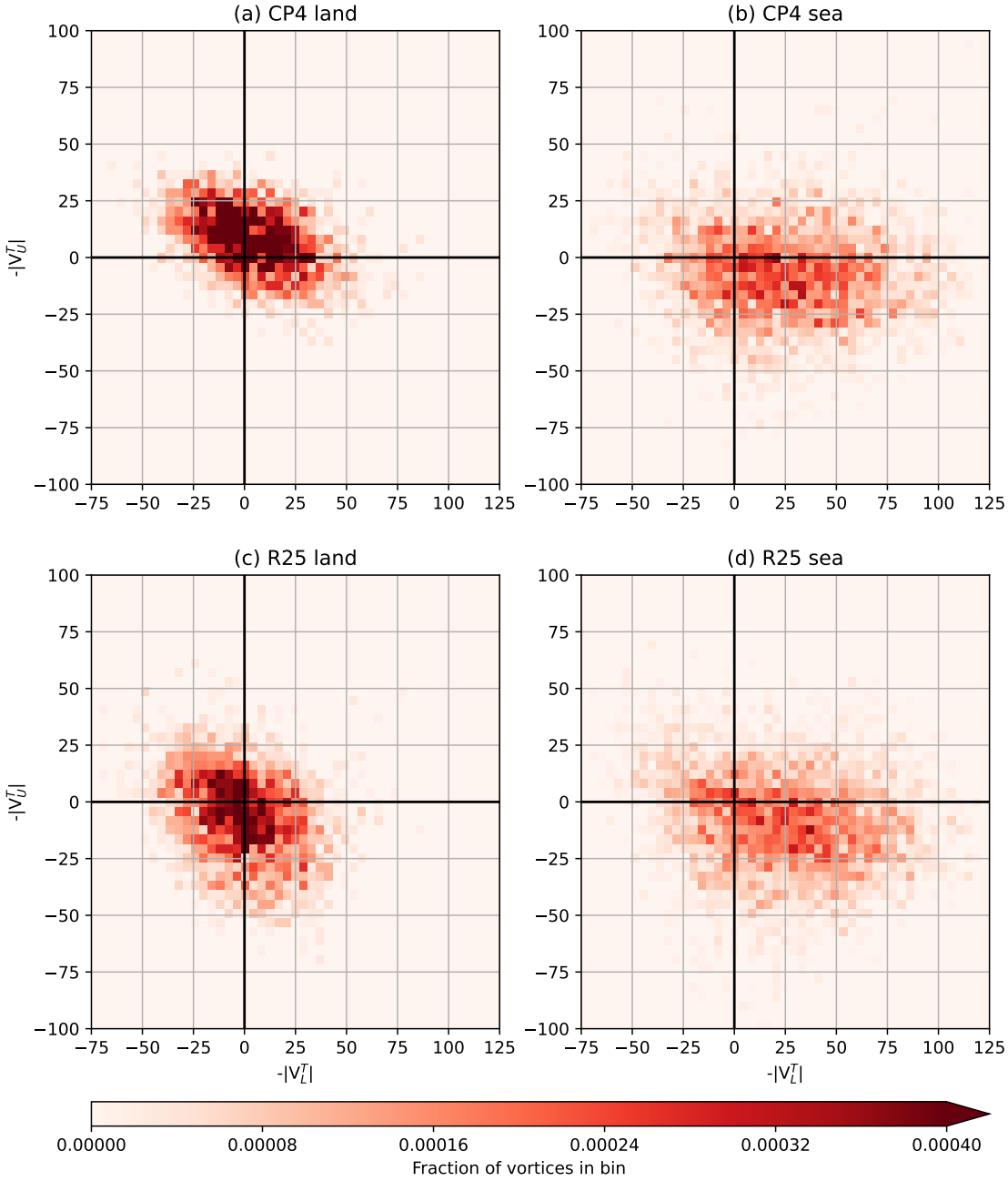

Figure 6.8: Two-dimensional histograms with $-|V_L^T|$ on the x-axis and $-|V_U^T|$ on the y-axis, for the vortices with area $> 25{,}000\,\mathrm{km}^2$ identified over the land (left column) and sea (right column) in CP4 (top row) and R25 (bottom row). The fill colour of each box represents fraction of the vortices which lie in each box of the histogram on the colorbar.

6.8. While there is a fraction of vortices which are positive in both $-|V_U^T|$ and $-|V_L^T|$ over land in both simulations, the mean value of $-|V_U^T|$ shifts to a less positive value over the ocean compared to the distributions over the land, although the decrease is less pronounced in R25 where $-|V_U^T|$ is lower over land anyway, which may reflect the shallower heating profiles associated with convective parameterisations. Figure 6.6 shows that the peak of the updraught of precipitating convection in CP4 is more elevated and more intense, which could result in more latent heating at levels above 600 hPa, and thus increase the value of $-|V_U^T|$ relative to the weaker heating in R25. Where the two simulations produce a more similar depth of structure, over the ocean (figures 6.6c–d), the distributions of $-|V_U^T|$ are more similar.

However, when comparing CP4 and R25, there is a slightly greater fraction of all vortices which meet the warm-core criteria (both positive $-|V_L^T|$ and $-|V_U^T|$) than in R25. Not all of these vortices are close in size to the 500-km radius measurement that Hart (2003) uses, so it is possible that environmental thermodynamics unrelated to the vortices is being captured in these distributions. There are few vortices identified in the study regions with sufficient area to cover the entire 500-km radius ($\gtrsim$80,000 km^2; figure 6.4 shows that there are only tens of vortices of such size).

6.3 Conclusions and Future Outlook

In this chapter, two 10-year climate simulations are compared to investigate the differences in representation of vortex populations over the ocean between CP and parameterised models. The CP model used shows a higher frequency of vortices overall, over both land and the ocean, compared to the parameterised simulation. There are more intense vortices in the CP model over both land and sea, especially more intense negative vortices. The distribution is a result of stronger vortex structures associated with oceanic convection and a greater frequency of storms generated both over land and the ocean, since the transport of vortices is similar in both simulations.

Section 6.2.2 examines the thermodynamics of the storms by considering the warm-core metrics introduced in Hart (2003) for the vortices. There is a demonstrable increase in the lower cyclone phase space thermodynamic metric, $-|V_L^T|$, indicating overall a shift towards more warm-core structures between 900 and 600 hPa over the ocean, which is similar in both simulations. However, the corresponding upper-level metric, $-|V_U^T|$, decreases for vortices over the

ocean relative to vortices over the land in CP4. One hypothesis is that the differing upper-level thermodynamics is linked to the depth of convection being markedly different between the land and ocean in CP4, leading to higher values of $-|V_U^T|$ over land where the convection is deeper, and perhaps a more accurate reflection of AEW thermodynamics with a lower cold core and warm anomaly aloft. However, $-|V_U^T|$ is somewhat similar between the land and the oceans in R25. Taking the two metrics together, CP4 shows a higher proportion of vortices with positive values of both $-|V_L^T|$ and $-|V_U^T|$, thus suggesting that a higher proportion of its oceanic vortex population could have warm-core structures throughout the vortex height, making them more likely candidates to undergo tropical cyclogenesis.

It cannot be assumed that the number of vortices off the coast of West Africa will directly impact the number of TCs. However, CP4 creates many more vortices with characteristics that may be important for such vortices to undergo cyclogenesis, as seen in the example (figure 6.1) and the statistics (figures 6.3, 6.4, and 6.7). Research into CP models indicates that they predict more TCs than models with a deep convection parameterisation (Judt et al. 2021), and having a greater number of candidate vortices in the Atlantic Basin could be a factor determining the future changes to TC populations under warming.

One key limiting factor of this study is the lack of ocean-atmosphere coupling in CP4, which leads to wet biases over the ocean. The lack of coupling could lead to an overestimation of the frequency of convective cells over the ocean, leading to larger vortex populations than may be realistic. The study of tropical cyclogenesis in convective-scale simulations will be limited until atmosphere-ocean coupling can be integrated into CP simulations.

Further investigation of how an altered population of vortices impacts the eventual development of TCs or their intensity would be beneficial to connect this work to the impacts of TCs. The work in this chapter suggests that there is merit in further investigation of TC evolution across their lifetime from genesis to extratropical transition within CP models, with a view to eventually improve seasonal and subseasonal TC forecasting, as well as developing understanding of cyclogenesis mechanisms. In order for the full lifetimes of TCs to be simulated, CP simulations would need to be global or cover the entire Atlantic as well as most of Northern Africa (to capture genesis of AEWs), which is at present still a costly demand, especially to perform similar statistics to those shown in this chapter because a long timescale would need to be simulated at high resolution and large area. An alternative would be to run NWP operational simulations

at convective scales over the region for a single season or even part of a season. With a larger domain, it would then be worth tracking TCs from their development backwards to their initiation over Africa, either as AEWs or vortices embedded within organised convection. Since an appropriate simulation is not currently available, a full investigation is left as future work.

While it is not possible to determine whether they eventually become TCs with the available data, it is, however, possible to track MCSs in the existing CP4 simulation using outgoing longwave radiation (OLR) signatures. Combining such a dataset of MCS tracks with modelled dynamical fields allow us to understand how the MCSs modulate the local area in different parts of their lifetime, and the environments that they form in, which is the basis for the investigations that continue in chapter 7.

Chapter 7

Initiation and dissipation environments of MCSs in CP4-Africa

Chapters of this thesis have so far focused on the upscale impacts of organised mesoscale convection, but to fully understand their scale interactions it is also of interest to understand the impacts of synoptic-scale environments on the initiation and intensification of organised convective systems. This chapter uses a dataset of tracked mesoscale convective systems (MCSs) in CP4-Africa and its corresponding parameterised simulation, R25, described in chapter 3, to examine what features are characteristic of environments of MCSs at initiation and throughout their lifespan.

Since in-situ measurements of organised convection, especially from its very initiation, are rare in West Africa, a convection-permitting (CP) model provides value as an opportunity to explore the structure around MCS initiations and over their lifetime from a 3-dimensional perspective. Furthermore, by contrasting such observations to a model with a deep convection parameterisation, one can examine the differences in conditions that are associated with initiation and intensification of convection, and thus provide an overview of weaknesses of the convection scheme in representing responses to certain features compared to simulations with explicit convection. It is possible that doing so may have practical implications for the implementation of convection schemes and the validity of their triggering conditions. While the same simulations

examine dynamics of precipitating convection by compositing around precipitating grid cells in chapter 5, the work in this chapter will go further to analyse dynamics specific to certain parts of MCS lifetimes: their initiation, and the features they leave behind once they have dissipated.

To understand the response of MCS initiation to local- and synoptic-scale features, in this chapter, statistics of the dataset of tracked MCSs generated in Crook et al. (2019) are examined, filtering the storms to only examine the behaviour of coherent, long-lived systems and identifying the points at which the storms initiate and dissipate. To establish features of the environments which are conducive to MCS initiation in the two simulations, composites are generated centred on the centroids of storm initiations, and statistics of key environmental properties local to the initiation point are summarised. The dataset of tracked MCSs allows for an opportunity to examine the environments of dissipating storms at the final points in each MCS track, in order to understand what MCSs leave behind once the precipitation or anvil cloud has dissipated. As a result, it is possible to draw conclusions about how the impact of MCSs on their environment can modulate the initiation of subsequent MCSs.

7.1 MCS Populations in CP4 and R25

The MCS dataset used in this chapter is taken from the dataset generated by Crook et al. (2019) and described in more detail in section 3.3.2. The analysis focuses on MCSs that are initiated in the months of June–September (JJAS) from 1997 to 2007 in the current-climate configurations of CP4 and R25 between 20 ° W and 20 ° E and 0 ° N and 30 ° N, covering most of northwest Africa. The domain is the area shown in figure 7.1. The JJAS season covers the onset and peak of the West African Monsoon (WAM) where there are most frequent MCSs climatologically.

The analysis that follows uses storms identified by their outgoing longwave radiation (OLR) signature, limited to storms which have a maximum area exceeding 5,000 km^2 and a lifetime of 6 hours or longer. In CP4, there are 20,135 storms that fit these criteria, and in R25 there are 21,061. While CP4 typically has more precipitating features than in R25 (see chapter 5), the lower resolution of R25 means that more of the features are likely to reach what is technically a larger size, because in order to register as an identifiable object in at least one grid cell, they must be inherently larger. For the purposes of examining spontaneous storm initiations, storms which have split from existing MCS structures are also excluded, since such storms will likely have structures that are characteristic of mature systems. These further restrictions limit the

number of storms to 8,142 in CP4 and 2,263 in R25.

Figure 7.1 shows the density of initiations for (a) CP4 and (b) R25, as well as the orography on their respective model grids. Mountains and other high orographic features provide orographic lift that drives the formations of storms, particularly over the Guinea Highlands and the mountains of Cameroon. The density of storm tracks themselves (figures 7.1c and d for CP4 and R25 respectively) reflects the location of initiation, with similar hotspots near the major mountainous features in the Sahel region. The band of storm initiations is largely limited to the 5–15 ° N latitude range, where the WAM provides sufficient moisture for convective initiation and where southern-track African Easterly Waves (AEWs) couple to convective systems. Key differences between the simulations are that there are, overall, more frequent storms initiating in CP4 and they especially are more common over the ocean, which corresponds to the over-ocean wet bias documented in CP4 (Kendon et al. 2019).

The density of storm dissipations is shown in figures 7.1e–f. The dissipation distribution is almost identical to the track density plot in the row above, perhaps with a slightly higher proportion of dissipations over the ocean at about 18 ° W than track density proportion in the same location. The similarity between the distribution of storm tracks and storm dissipations suggests that the dissipation of storms is unlikely to be modulated strongly by permanent geographical or climatological conditions.

7.2 Initiation Environments of MCSs in CP4 and R25

7.2.1 Composites Illustrating Mean Initiation Environments

By compositing around initiation locations of the filtered storms, it is possible to characterise the archetypal environment that a storm is likely to form in within each of the simulations. Figure 7.2 shows an example of such a composite at the initiation location, showing the associated specific humidity anomaly (filled contours) and horizontal divergence anomaly (line contours) fields over a 500-km zonal cross-section centred on the storm's centroid at initiation in figures 7.2a and c. Anomalies are calculated relative to the mean values of each field at each point across all times in the June–September period of the 10 years of simulations.

To compare to the wider background state at the time of initiation, composites are also generated centred on random grid cells within the domain, at the same time as the initiations of each

filtered MCS (subject to the conditions described in the previous subsection), providing an illustration of an average cross-section through any given point in the region (figures 7.2b and d). These 'random' composites serve to prove that signals observed in the composites around initiations are robustly linked to the MCS initiation, and not simply a reflection of the background state at the typical time of day of storm initiations, or during the season altogether.

One subtlety that should be noted before exploring the results of compositing around 'initiation points' is that, while the time of initiation is defined as the first time that a storm which, at some point, reached appropriate size and lifetime thresholds, was first identified by the algorithm. However, storm-like structures could start evolving before the algorithm has identified an appropriate cloud cluster, so it may be that at 'initiation', the storm already has a developed updraught and associated dynamical features of a more mature system. Regardless, because the algorithm tracks storms through advected-overlapping (see section 3.2), it does still capture differing dynamics through a storm's lifetime and therefore captures uniquely early-lifetime storm dynamics compared to fully mature storm features. Furthermore, composites are also produced at the initiation centroid of the storm for the 3–6 hours before this 'initiation' has been identified by the algorithm, thus capturing dynamics that precede storm initiation as fully as possible with the available time output resolution of the simulation.

Figure 7.2 shows that MCS initiation characteristically has an enhanced low-level moisture signal relative to the background moisture patterns, particularly in CP4. There is also a signal of low-level convergence and upper-level divergence in CP4, which emerge as a result of continuity as an updraught is generated. The divergence patterns are extremely localised and strong, especially compared to R25 where any convergence is weaker and more diffuse, with a smaller vertical extent. A narrower and more intense updraught associated with convective features is typical of CP models (Kendon et al. 2021).

Figures 7.3 and 7.4 show zonal and meridional cross-sections through MCS initiations respectively, as well as the 3 and 6 hours before the initiation at the same location. These composites show vectors of wind anomaly and relative vorticity anomaly through the cross-section. Signals in the corresponding 'random' composites are negligible, so figure 7.3 show an enhancement in wind shear characteristic of the region in the 3–6 hours before the MCS initiates, with enhanced westerlies below 850 hPa and enhanced easterlies at 800–600 hPa. The signals are small (most of the wind anomalies are less than 1 $\mathrm{m\,s^{-1}}$) but may have become diffuse due to the large number

of storms that are averaged in the composites. R25 shows smaller signals of enhanced shear than CP4, and does not, unlike CP4, show any indication of a developing updraught 3 hours before the initiation. In CP4, however, 3 hours before the initiation there is evidence of some ascent at low levels, which starts to form a low-amplitude vorticity dipole (in figure 7.4b) due to the lifting of the vortex tube formed by the background shear. By initiation of the storms, an intense, coherent updraught has formed which is associated with a strong north-south dipole of relative vorticity, consistent with theory (see chapter 2) and with the precipitation composites generated in chapter 5.

The composites show some evidence of a distinct vortex existing at midlevels before there is an updraught that can generate vortices independently; the anomalies visible in the T-6 composites are about 2–3 times larger in magnitude than anomalies seen in random test composites (not shown). Therefore, while it is unlikely that all storms form from existing vortex structures, it is possible that some storms reinvigorate existing vortices.

Fitzpatrick et al. (2020) suggest that, contrary to observations, there is not a strong response between environmental shear and precipitating systems in CP4. Results from the composites in this chapter suggest otherwise, with an evident shear signal in composites around the initiation points of MCSs. It is possible that this discrepancy emerges due to a difference in the definition of the systems; Fitzpatrick uses precipitating grid cells whereas here the MCSs are defined by OLR thresholds.

Another element of the local- and synoptic-scale environments which can modulate the initiation of storms is the land surface temperature (LST) and soil moisture (e.g. Taylor et al. 2012, see chapter 2). Figures 7.5 and 7.6 show the anomalies of soil moisture and LST respectively leading up to MCS initiation. In figure 7.5, there is a distinct soil moisture signature, and corresponding random test composites (not shown) show a very weak signal. CP4 corroborates evidence that MCSs are often formed on boundaries between drier and wetter soil or over dry patches of soil. By contrast, R25 appears to have storms forming over wetter soil, a bias that has been revealed by previous modelling studies (Taylor et al. 2013).

Figure 7.6 looks remarkably similar to its corresponding test composites, shown in figure 7.7, suggesting that the cooling of LSTs as MCSs start forming is not a local effect, but at least exists on the synoptic scale of the full region. The pattern of MCS formation occurring over a negative LST anomaly which follows positive LST anomalies could be associated with the diurnal cycle,

since MCSs tend to form in the early hours of the evening as the surface temperature starts to fall after its peak in the early–mid afternoon.

7.2.2 Statistics Describing Initiation Environments

While the composites are useful for determining which properties characterise MCS initiation, it is important to acknowledge that they are simply an average over thousands of storms and they do not account for the variability of MCS initiation environments. Various properties are calculated around each MCS initiation, in order to examine the full range of properties from a statistical perspective. For example, figure 7.8 shows the distribution of the values of maximum relative vorticity anomaly in the 500-km boxes centred on the centroid of each MCS at initiation, as well as 3 and 6 hours before, indicated by the opacity of lines shown in the legend. The figure demonstrates that for all pre-initiation environments, R25 has far weaker maximum vorticity anomalies than CP4, which in itself is not particularly revolutionary since this is a natural result of CP4's more intense updraughts and higher resolution grid, but it does reinforce the conclusions associated with figures 7.3 and 7.4: that CP4 has stronger vorticity anomalies throughout.

Figure 7.8 also reflects the fact that there is no noticeable change in the distributions of maximum vorticity anomaly in the hours leading up to the initiation of MCSs. It is also reasonably similar to its respective distribution for random points (not shown), which indicates that there is no particular tendency for MCS initiations to have the presence of a strong vortex near its initiation.

The distribution of variance in soil moisture anomaly around the initiation points of storms is shown in figure 7.9a, with figure 7.9b showing the equivalent distribution for random points. CP4 has a higher variance in soil moisture patterns overall, but soil moisture variance is particularly enhanced in the regions where MCSs form, indicating that higher variance in soil moisture (for example, on sharp gradients of soil moisture anomalies) is associated with the initiation of MCSs. However, R25 also has more variance in soil moisture associated with MCS initiation compared to its background soil moisture variance, even if it is not as variable, implying some sort of response in the convection scheme to variation in soil moisture anomaly.

7.3 Dissipation Environments of MCSs

As well as understanding what environments MCSs form in, in order to understand their influence on the subsequent initiation of other MCSs, it is important to understand how they modulate their environments. One obvious way in which MCSs modulate their environment is through producing precipitation throughout their lifetimes, dampening soil on local scales and producing sharp gradients where soil has previously been dry. Other such influences are the results of the production of vortices. Mesoscale convective vortices (MCVs) are often produced as midlevel positive vortices in the stratiform regions of MCSs, in addition to the strong vortex dipoles which occur around updraughts. Figure 7.10 shows that even after the storm itself has dissipated, signatures of vortices continue to exist. The persistence of vortices is true for both simulations, although it is more distinct in CP4 simply because the vortices are stronger to begin with. In CP4 the vortices also have a more distinct tendency to propagate westward, perhaps because the MCS populations in CP4 more reliably propagate in that direction, in line with observed MCSs (Crook et al. 2019). Not only may the initiation of new MCSs be associated with the pre-existence of vortex structures, as discussed in the previous subsection, but MCSs can generate of vortices which continue to propagate beyond the storm's lifetime. These vortices could serve to reinforce synoptic structures such as AEWs, and go on to undergo tropical cyclogenesis if they were to propagate over the Atlantic.

Another way in which MCSs modulate the atmosphere is through moisture transport. In a direct contrast to figure 7.2, figure 7.11 shows that there is, in CP4, a much lower specific humidity anomaly at the dissipation point of a storm compared to its initiation or even to the background (random composite, figure 7.2b). The updraught in the storm has, over its lifetime, transported the low-level moisture that fuels the moist convection to higher levels, leading to positive specific humidity anomalies at 600–400 hPa, which persist for up to 6 hours after the storm has dissipated. By this point, the low-level moisture has been restored, so the reduction in low-level humidity is not a long-term effect. The effect is similar if less pronounced in R25.

7.4 Conclusions and MCS Feedbacks

Elements of MCS initiation that are illustrated by the composites in this chapter are the presence of low-level moisture to supply the moist convection, slightly enhanced background zonal wind shear, and the existence of dry patches in the soil moisture signature. The most distinct

signatures of MCS initiation are in the moisture fields.

It is also possible to composite, around each initiation centroid, the density of other MCS tracks which had passed through a 500-km square in the 24 hours before the storm is initiated. Such a composite would illustrate the feedbacks that MCSs have on one another's initiation. The results, as well as test composites of storm tracks in a given 24 hours around random points at the same times as the storm is initiated, are shown in figure 7.12. As previously, the test composites can be treated as a 'background' field.

Track density anomaly was computed rather than raw track density to counteract the effect of particular geographic 'hotspots' of storm density associated with orography (see figure 7.1) leading to overwhelmingly positive track density signatures. Since the compositing removes a single storm track from each composite relative to the background by ignoring the storm it is compositing around in each iteration of the compositing algorithm, all the values are negative anomalies.

It is possible that the track of the intiating storm is the cause of the signal seen in figure 7.12a, since storms in CP4 tend to consistently propagate in a southwesterly direction, leading to a negative track anomaly where these patterns have been removed. The signal also indicates a tendency of storms to not follow the same tracks as storms that have recently propagated through the region. A potential mechanism for the minimisation of storm tracks in the track of a propagating storm from the initiating position is the effect of soil moisture. If a storm has already propagated down a track, the ground will be wet due to the storm's precipitation, reducing the sensible heat flux and thus dampening the potential for strong updraughts to intensify future storms. Thus, it appears that there is a negative feedback of MCSs on future MCS initiation at their specific track locations; they produce enough rainfall to suppress future MCS initiation. A similar albeit far weaker pattern exists in the R25 simulations (around 30 times weaker; note that figure 7.12c uses a different colorbar to the top row).

Furthermore, since low-level moisture is lifted by storms over their lifetime (compare figure 7.2 to figure 7.11), which is a persistent feature after their dissipation, the existence of a storm means there is reduced low-level moisture. Since low-level moisture seems to be a necessity for the MCS to draw on in order to initiate and develop (figure 7.2), it would generate a negative feedback between MCS initiations at the same point. However, as shown in figure 7.11, the low-level humidity is largely replenished within 6 hours of storm dissipation, so it is unlikely that

the low-level moisture feedbacks have as long-term an effect as soil moisture, which is typically a longer-lived signature.

The persistence of vortices from previous MCS tracks leading to regeneration of new MCSs would probably result in an enhanced signature to the northeast of the initiation centroid, at least in CP4 where the overwhelming majority of storms propagate in a southwesterly direction. The track density anomaly is less negative in the east of the track density composite of figure 7.12, which does imply that MCSs which may have dissipated to the east of an initiation point could be leaving behind westward-propagating vortices which help to spin up the newly-initiated MCS. Figure 7.10 shows the vorticity maximum travelling 100–200 km over the course of six hours, so it may be that the 500-km composite in 7.12 is too small for the a signature of vortex propagation from an MCS which has existed in the past 24 hours to be observed.

Overall, it appears that the patterns in MCS initiation and dissipation relative to other MCSs is representative of the fact that, typically, in West Africa, thunderstorms do not strike twice: storm tracks do not typically have the exact same centroids across timescales of a few days, which is consistent with literature which highlights the unusual temporal incoherence of precipitation in West Africa at a given location (Roehrig et al. 2013). This chapter proposes that soil moisture patterns are a key mechanism for such feedbacks since MCSs appear to initiate consistently on soil moisture anomaly gradients, thus meaning that MCSs do have a positive feedback on the generation of future MCSs, but not at the same location.

Using observational data would serve to validate the results presented in this chapter, but reliable estimates of wind profiles around MCSs, and thus the signatures of vorticity and wind shear associated with their initiation and dissipation, would be challenging to obtain. Some satellite data detailing wind profiles exist, but these are polar-orbiting satellites which do not capture large scales of motion around mesoscale systems and are unlikely to track a single system over its lifetime due to their orbit. Standard reanalysis products are also unsuitable for the evaluation carried out in this chapter since they use deep convection parameterisations and do not explicitly resolve convective dynamics. However, as more comprehensive reanalysis at higher resolutions is produced, or more convective-scale observational data is obtained, the statistics here could be reproduced using the observational or reanalysis data to validate CP models of organised convection and improve its model representation, even at convective scale.

From existing observations and theory of MCSs in other regions, it does appear that CP4 offers

added value over a parameterised model in representing the environments associated with the initiation and dissipation of MCSs. The evidence of structure in the patterns of MCS tracks around initiation points implies feedback mechanisms which are represented in the CP model. So far in the thesis, the effects of convection have been diagnosed by comparing CP simulations to simulations with parameterisations. In order to continue exploring the convective feedbacks at play between MCSs, the next chapter examines simulations with different initial conditions at convective scales, allowing for two similar synoptic scenarios to evolve with and without the influence of convection. The approach allows us to diagnose the impacts of convection on the larger-scale features, and more easily understand the feedbacks through which these impacts propagate.

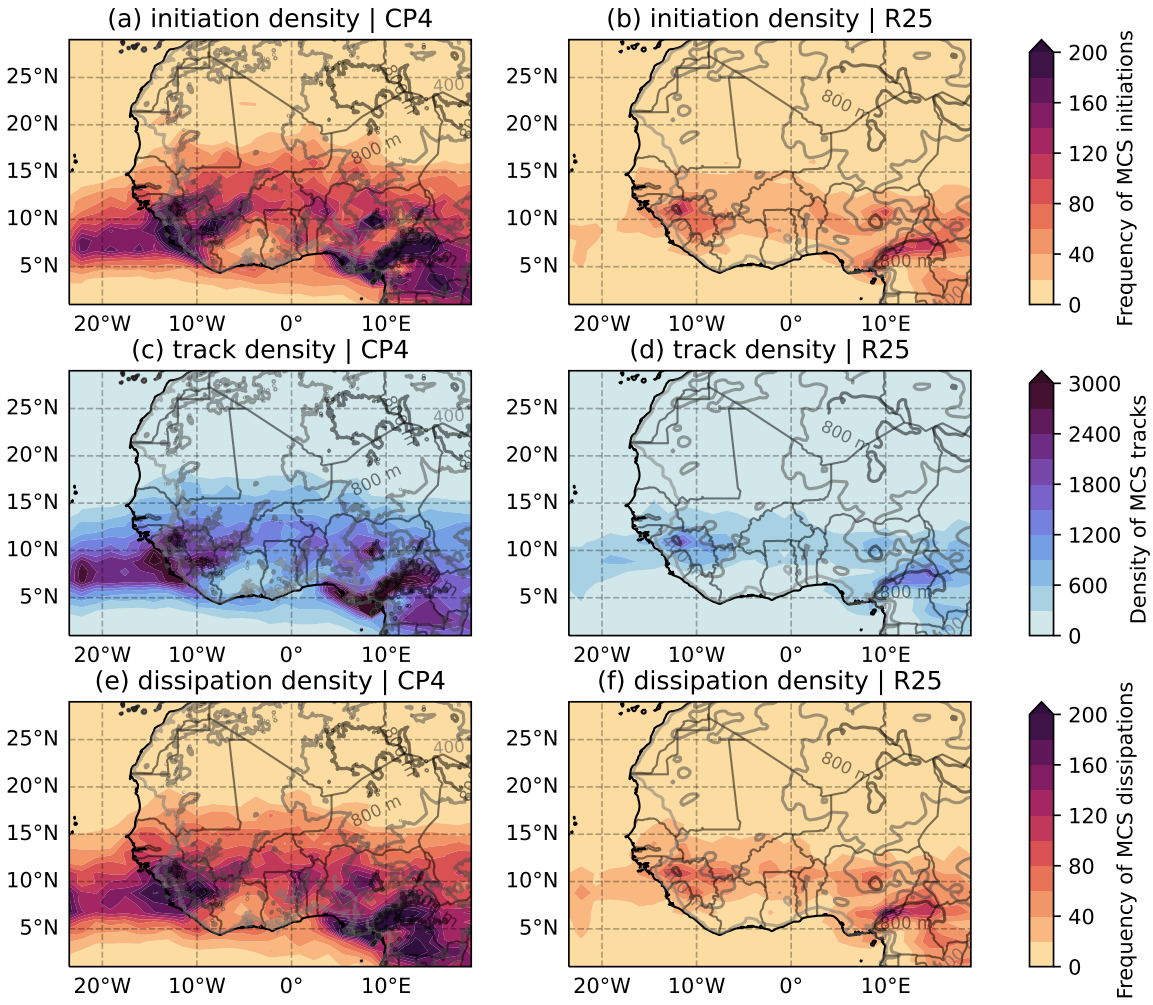

Figure 7.1: Density of initiations (top row) and tracks (bottom row) of MCSs in CP4 (left column) and R25 (right column), indicated by filled contours. The grid orography for each simulation is shown in labelled line contours.

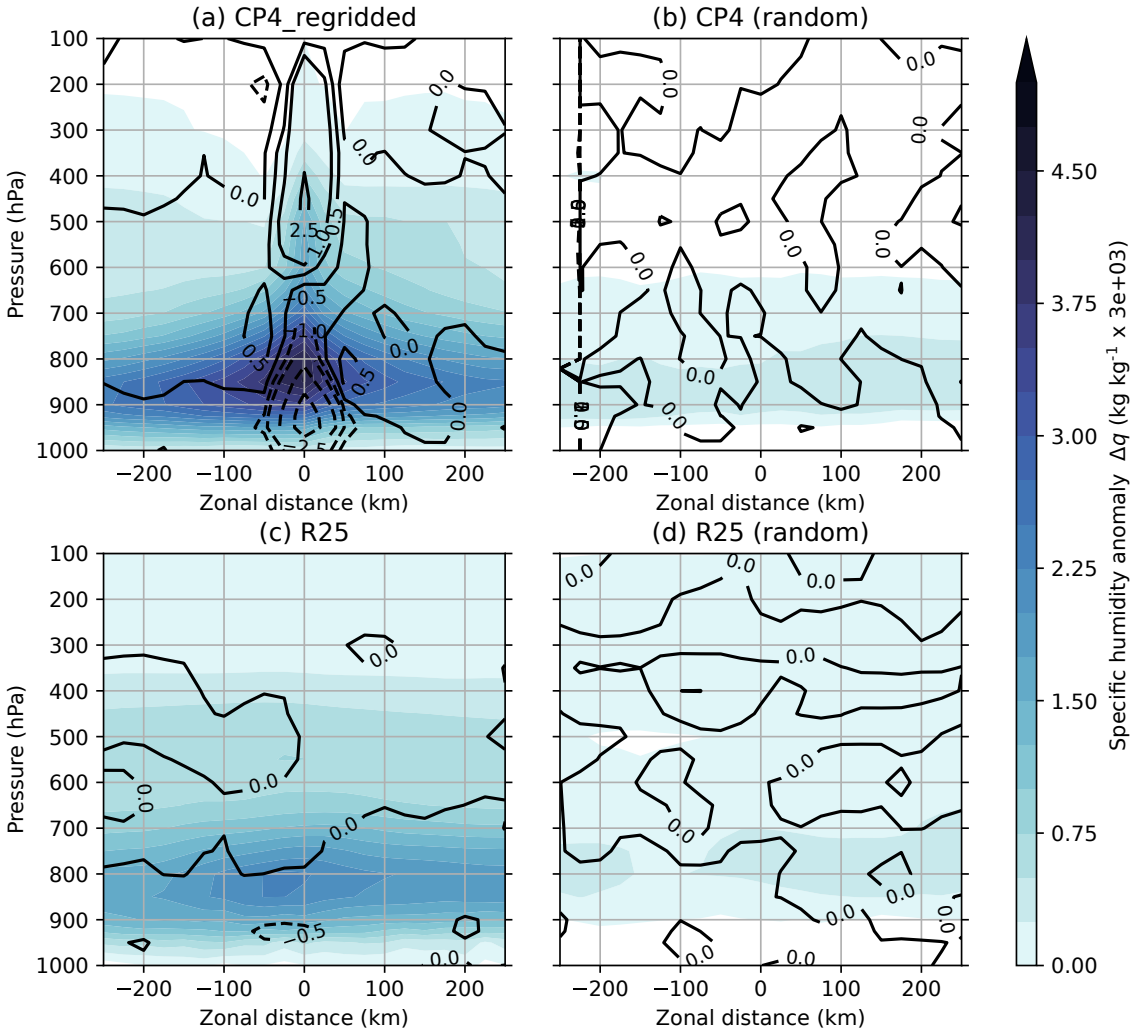

Figure 7.2: Left column shows composites of specific humidity anomaly (filled contours) and horizontal divergence anomaly (line contours, labelled in units of $s^{-1} \times 10^5$) along zonal (east-west) cross-sections through MCS centroids at initiation in CP4 (top row) and R25 (bottom row). Right column shows, instead of initiation centroids, composites around random points at the times of initiations of storms.

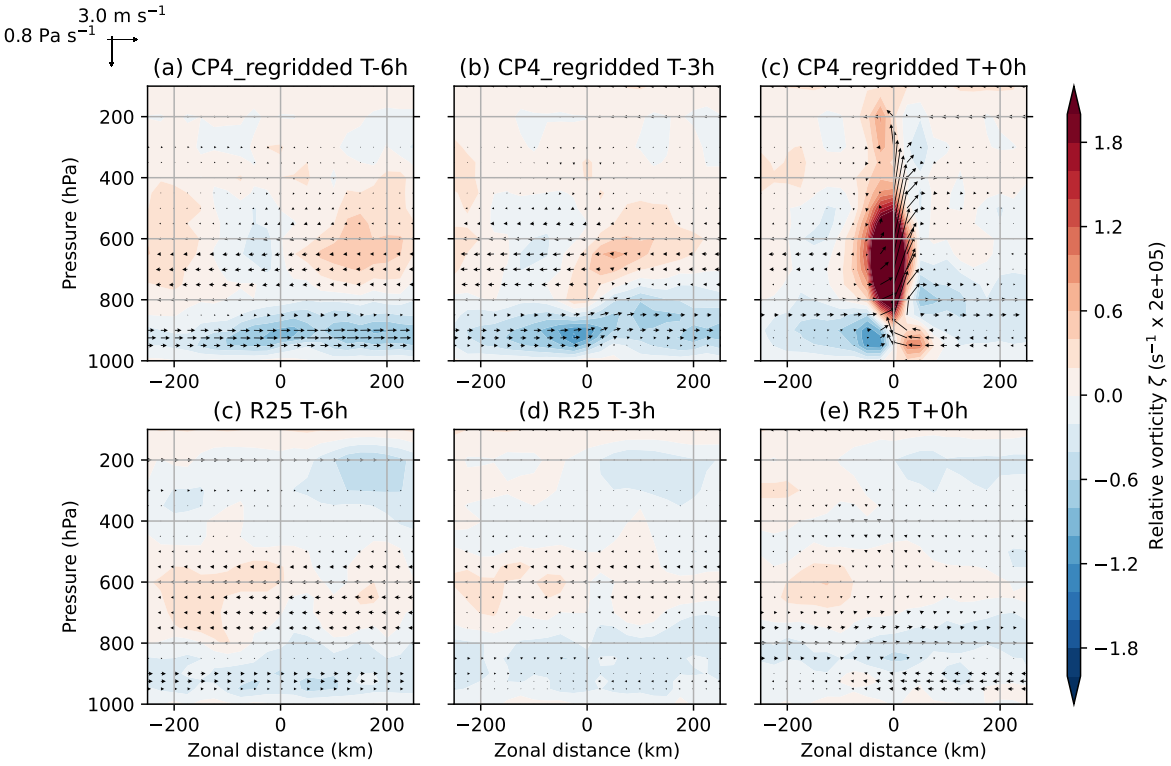

Figure 7.3: Composites of relative vorticity anomaly (filled contours) and wind anomaly (vectors) along zonal (east-west) cross-sections through MCS centroids at and leading up to time of initiation in CP4 (top row) and R25 (bottom row).

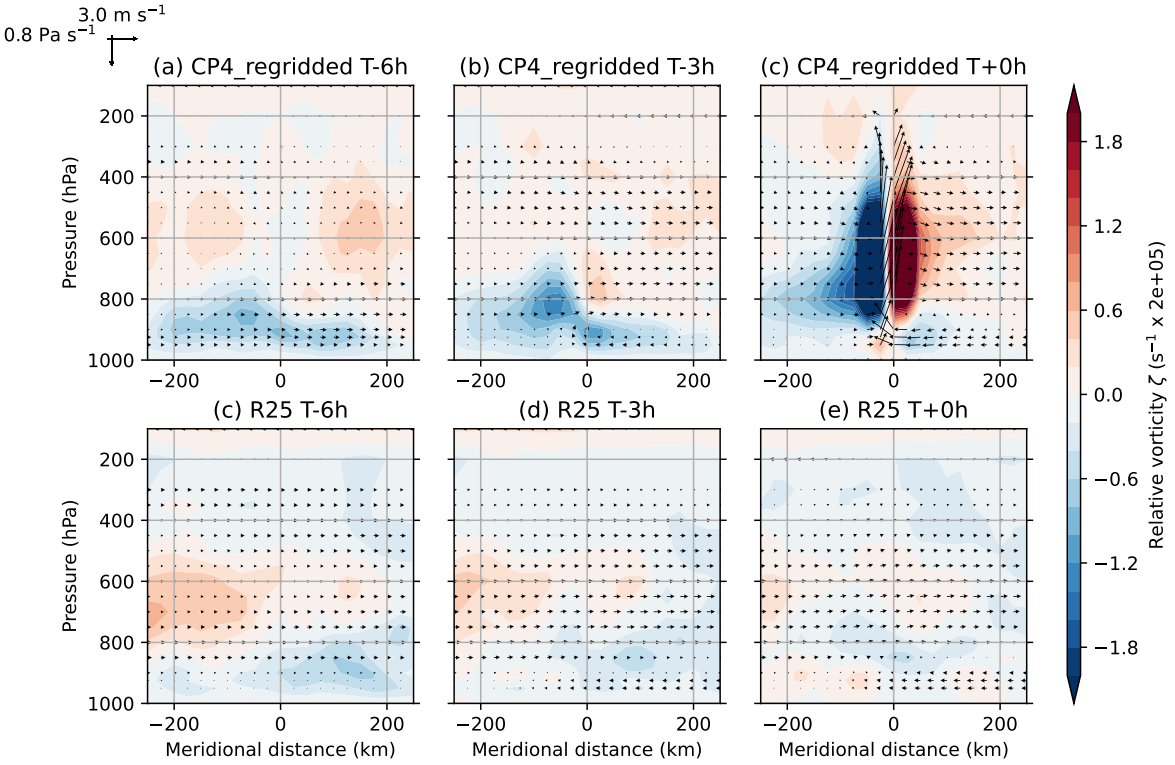

Figure 7.4: Composites of relative vorticity anomaly (filled contours) and wind anomaly (vectors) along meridional (north-south) cross-sections through MCS centroids at and leading up to time of initiation in CP4 (top row) and R25 (bottom row).

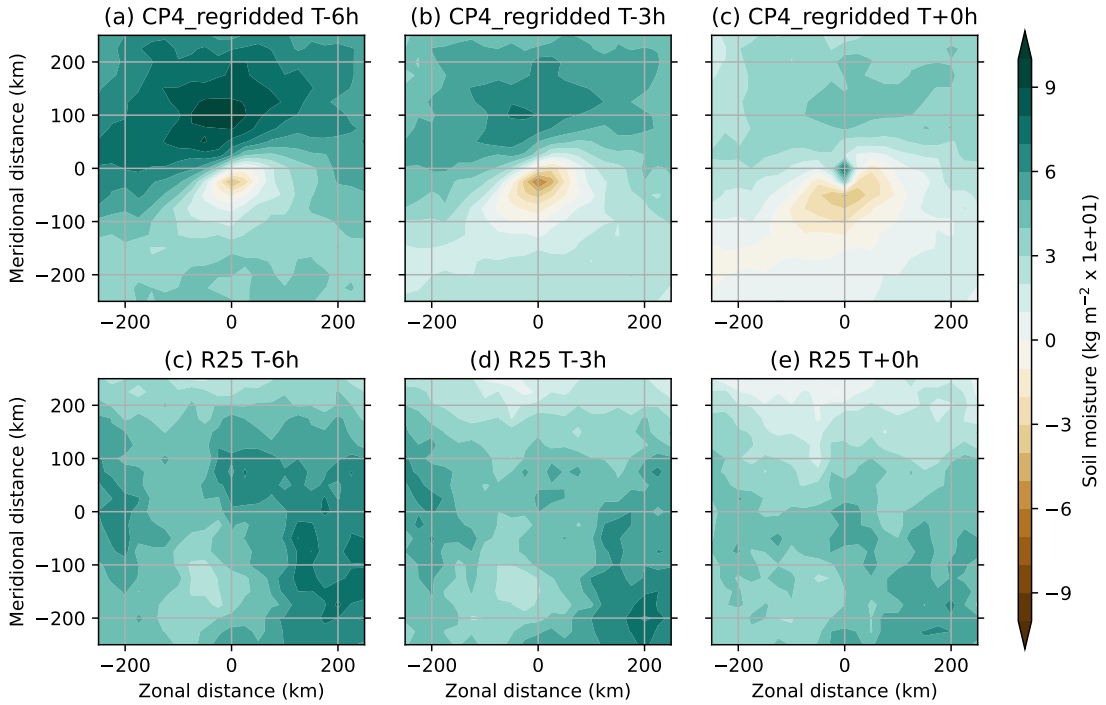

Figure 7.5: Composites of soil moisture anomaly (filled contours) in 500-km squares centred on MCS centroids at and leading up to time of initiation in CP4 (top row) and R25 (bottom row).

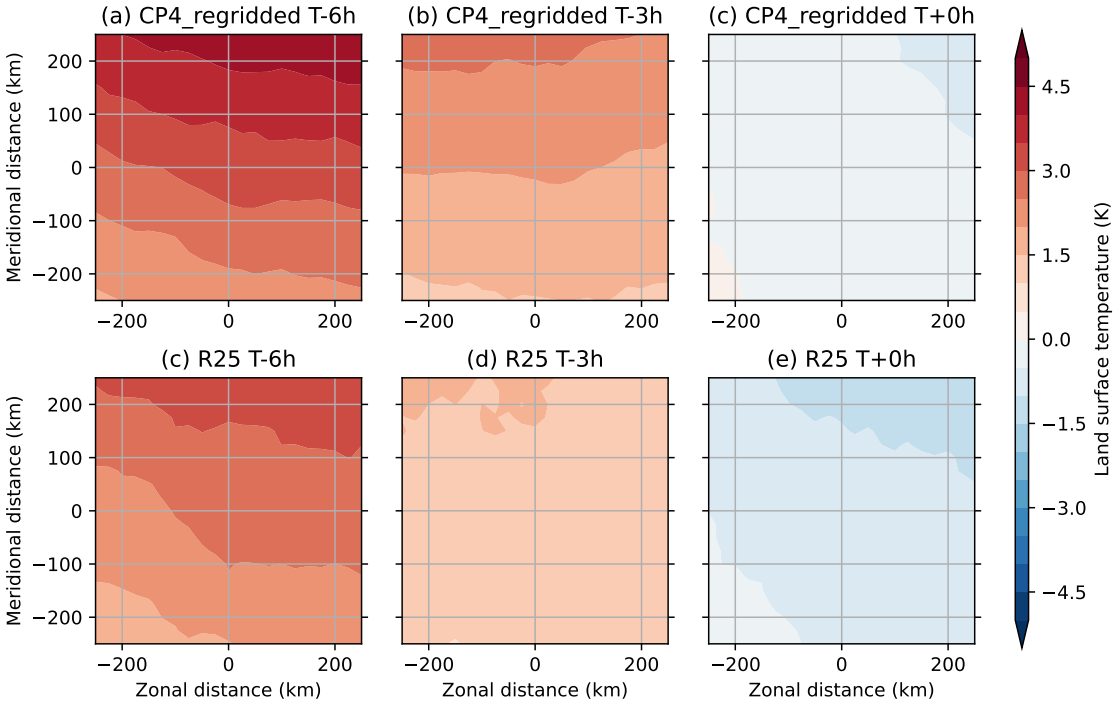

Figure 7.6: Composites of land surface temperature (LST; filled contours) in 500-km squares centred on MCS centroids at and leading up to time of initiation in CP4 (top row) and R25 (bottom row).

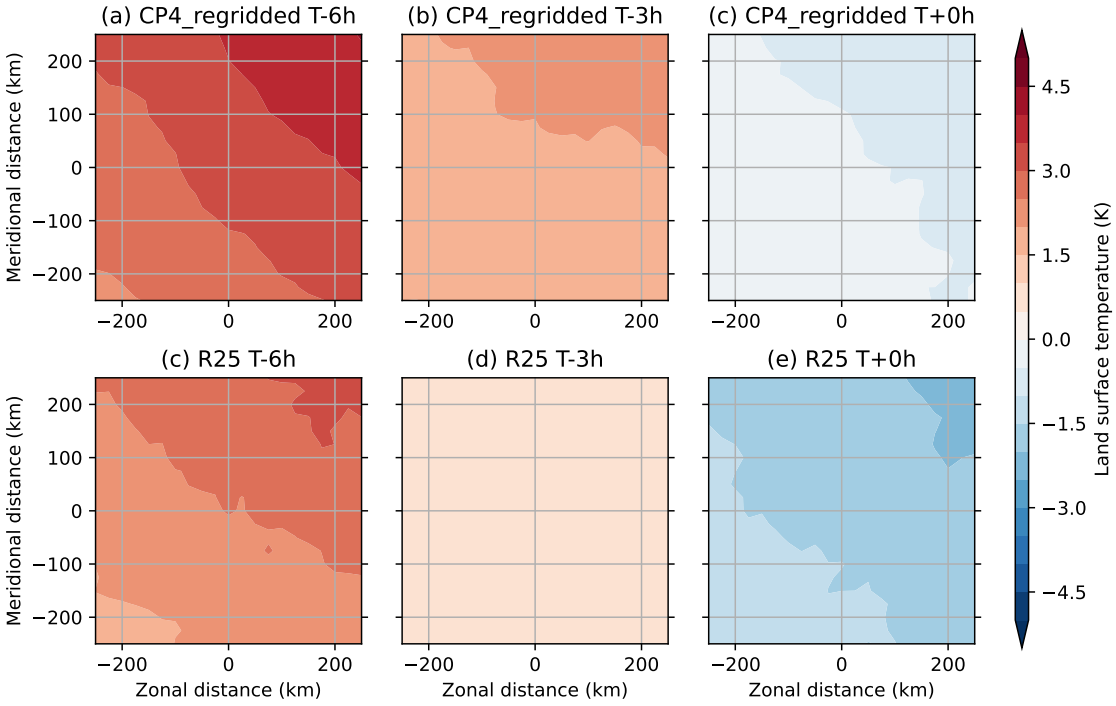

Figure 7.7: Composites of land surface temperature (LST; filled contours) in 500-km squares centred on random points at and leading up to time of each MCS initiation in CP4 (top row) and R25 (bottom row).

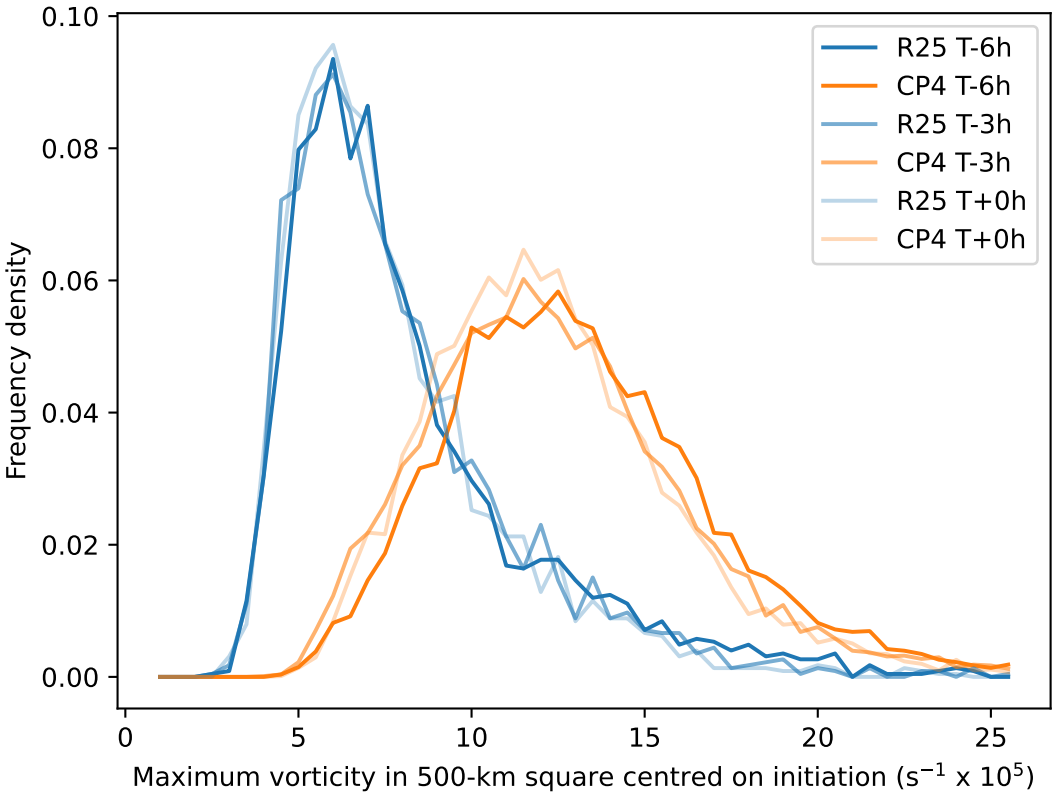

Figure 7.8: Maximum value of relative vorticity anomaly ($\zeta \times 10^5$) in 500-km squares centred on centroid of MCS at its initiation leading up to time of each MCS initiation in CP4 (orange lines) and R25 (blue lines).

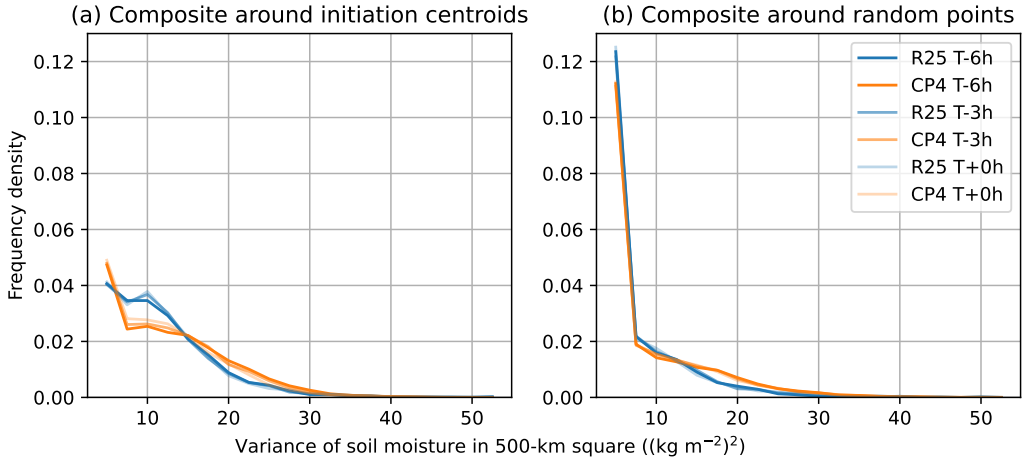

Figure 7.9: Variance of soil moisture anomaly in 500-km squares centred on centroid of MCS at its initiation leading up to time of each MCS initiation in CP4 (orange lines) and R25 (blue lines).

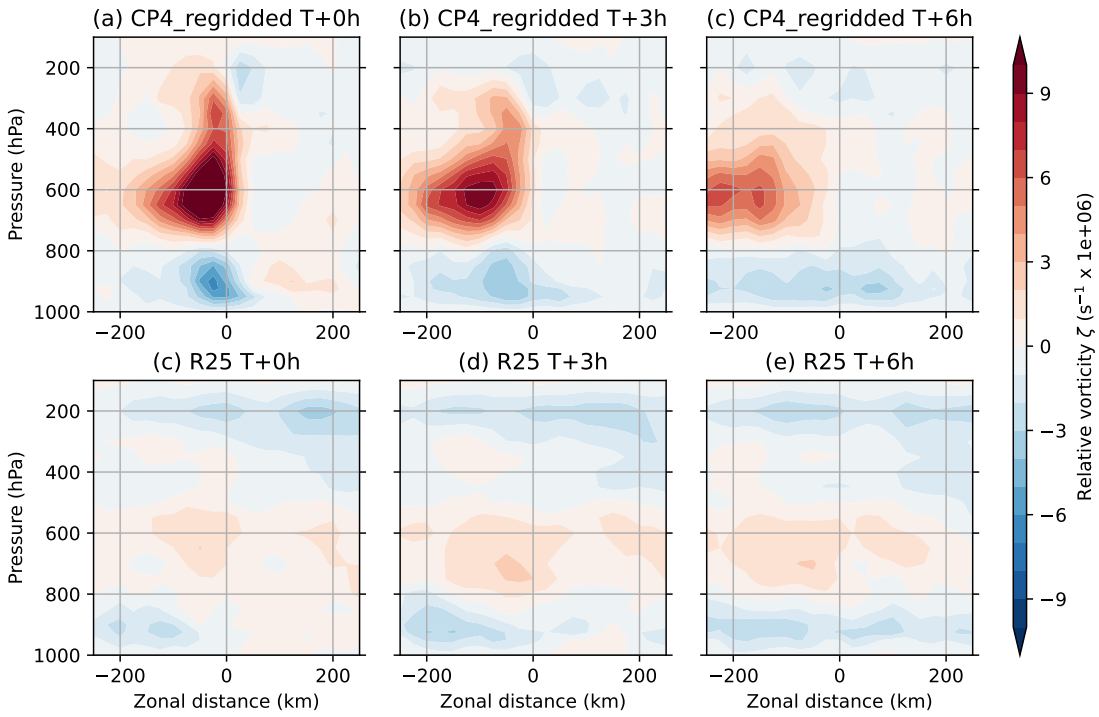

Figure 7.10: Composites of relative vorticity anomaly (filled contours) and wind anomaly (vectors) along zonal (east-west) cross-sections through the centroid of MCS at dissipation and for 3 and 6 hours after dissipation at the same point, in CP4 (top row) and R25 (bottom row).

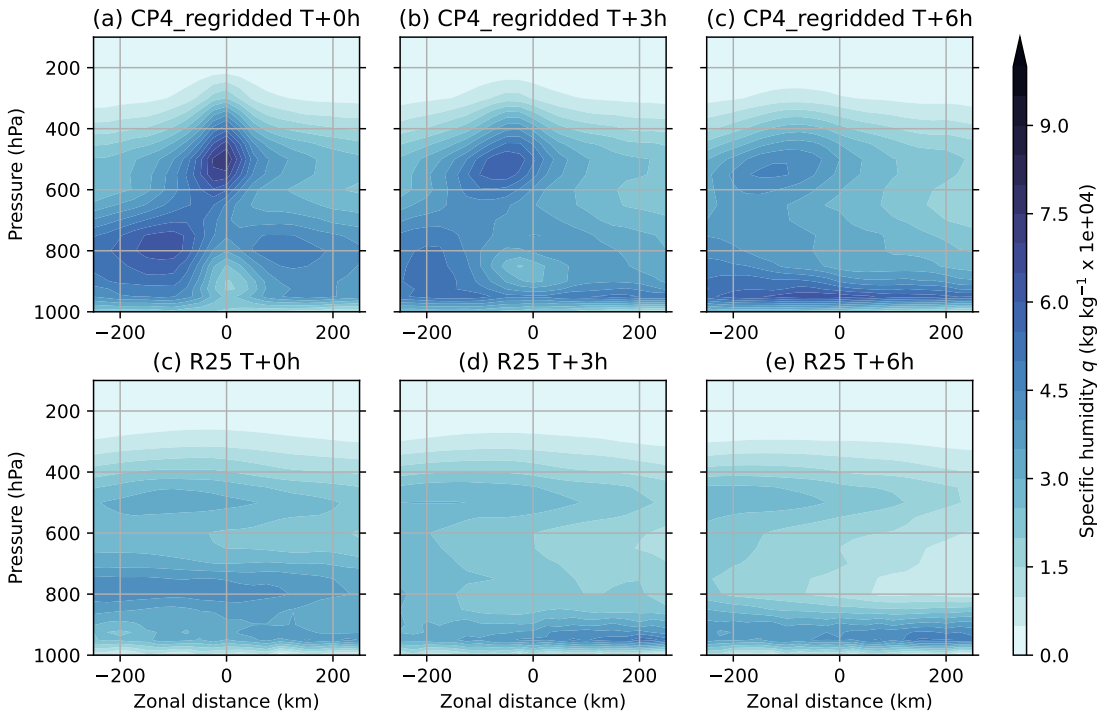

Figure 7.11: Composites of specific humidity anomaly (filled contours) and wind anomaly (vectors) along zonal (east-west) cross-sections through the centroid of MCS at dissipation and for 3 and 6 hours after dissipation at the same point, in CP4 (top row) and R25 (bottom row).

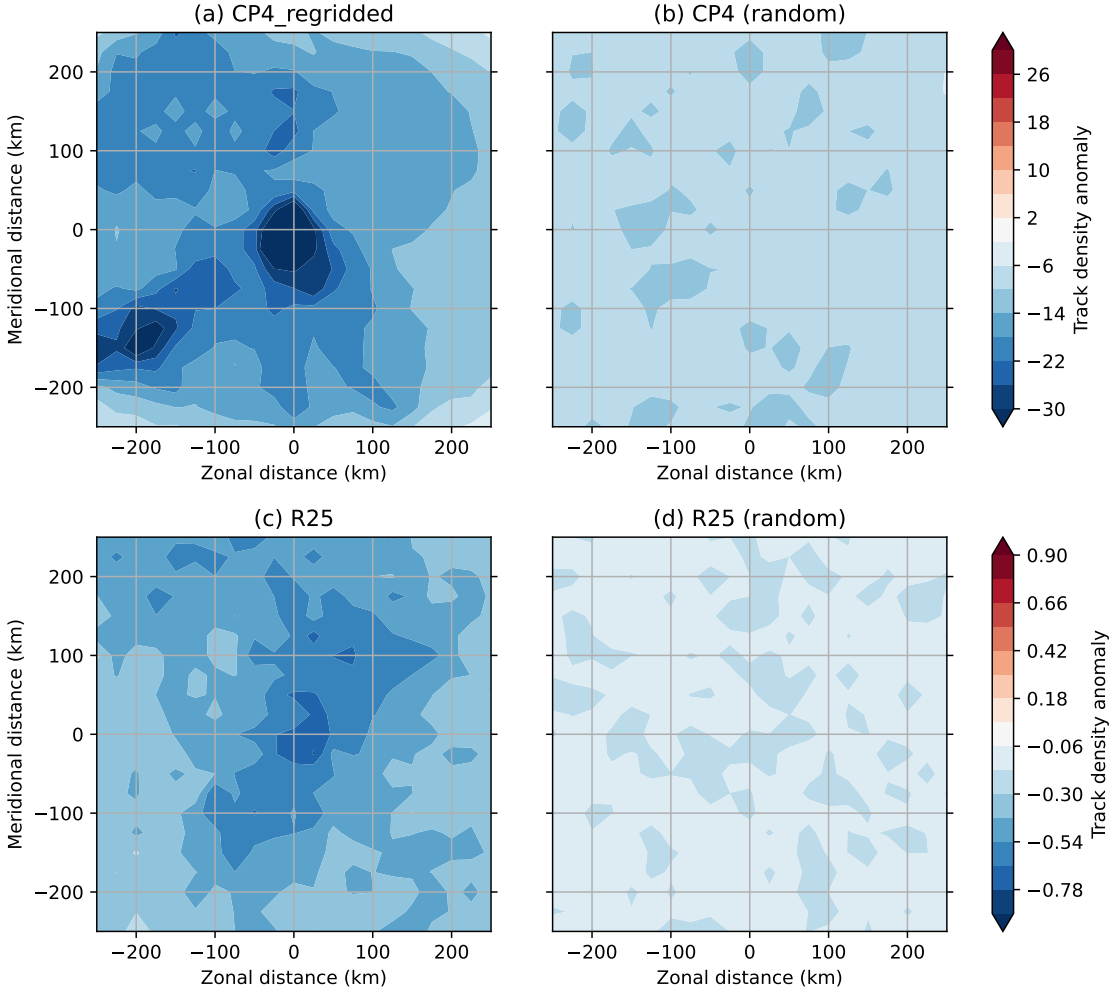

Figure 7.12: Composites of anomalous MCS track density within the 24 hours before initiation around centroids at MCS initiation (left column) and random points at the time of MCS initiations (right column) in CP4 (top row) and R25 (bottom row). The composite excludes centroids of storms as they are being composited around.

Chapter 8

Practical Implications of Convective Feedbacks in an NWP Model

The previous chapters have presented descriptions of organised convective systems and suggested some ways in which they might affect synoptic circulation in free-running climate models and comparing the simulations to observations. The exploration of such mechanisms attempts to address one of the major gaps in contemporary understanding of climate modelling: the feedbacks between mesoscale convective processes and synoptic-scale atmospheric circulation, including both the upscale (chapter 5), downstream (chapter 6), and downscale (chapter 7) impacts.

So far, the explorations of the feedbacks associated with convection have largely been based on the assumption that convection-permitting (CP) simulations can be taken as a 'truth' or at least have a more accurate representation of convective dynamics. Indeed, many studies treat the use of CP simulations as synonymous with an improvement in convection relative to a parameterised simulation (e.g. Finney et al. 2019), and while CP models have shown demonstrable improvements in the diurnal cycle, precipitation intensity, and convective organisation compared to models with a deep convection parameterisation (outlined in more detail in chapter 2), the comparison between the two does not constitute a comparison between similar synoptic scenarios with and without convection, particularly for the case of comparing free-running climate models.

In order to interrogate the impacts of convection, it is of interest to consider the synoptic circulations in the same case, except for conditions with and without convective structures. The

described scenario is difficult to recreate. One could remove mesoscale features by reconstructing streamfunctions (as in, e.g., Oertel and Schemm 2021), or considering different parameterisations (as above), but these and other such methods are a somewhat artificial means of creating such scenarios. It is also possible to consider similar but not identical case study scenarios where convection does and does not develop, but in these situations it is difficult to unpick the effects of convection from the larger-scale conditions which prevent convection from forming, and indeed accurate observations or simulations of both cases are required.

This chapter utilises analogues to operational numerical weather prediction (NWP) simulations with different initialisation techniques: the 'warm-started' and 'cold-started' simulations based on the Tropical Africa Model (TAM) described in section 3.1.3 of chapter 3. The driving global model used to force the lateral boundary conditions (LBCs) of the regional models is also used as a point of reference. Because the warm-started simulations are initialised with a blend of smaller-scale structure from the previous run of the regional forecast, and large-scale structure from the current global reanalysis, they combine a similar synoptic situation with different convective conditions at initialisation in a more organic way than artificially inducing or suppressing convection. These simulations care used to evaluate how the evolution of meso- and synoptic-scale weather systems is affected by convection or the lack thereof at the start of the forecast. If the existence of convection has significant upscale impacts later in the forecast, it provides a strong argument for further simulations at convective scales on large regional and even global domains, since it demonstrates that there are consequences of representing convection explicitly on larger scales than that of the convection itself.

First in this chapter an in-depth case study is presented of the warm- and cold-started initialisations at 18 UTC on 17 June 2020, alongside an explanation of how and why the two simulations differ in their representation of precipitation. The description and explanation is followed by an exploration of the impacts of the differences in mesoscale convective structure on the synoptic scale features. The first case study (Case Study 1) is then compared to an alternative initialisation of the forecast where there are far fewer differences in convective and synoptic-scale structures: Case Study 2, a forecast initialised at 18 UTC on 7 August 2020, later in the season. Finally, general diagnostics are evaluated for the entire experiment to provide an overall insight into the impacts of the initialisation techniques on the later forecast qualities, and the implications for the feedbacks between synoptic circulation and mesoscale convection

are discussed.

8.1 Case Study 1: Forecast Initialised at 18 UTC on 17 June 2020

The 2020 boreal summer was a season of anomalously high rainfall in West Africa, with an enhanced WAM (Blunden and Boyer 2021). Multiple devastating floods impacted the region throughout the season (Echendu 2022; Mendes and Fragoso 2023). On June 17–18 2020, heavy rain fell over the continent as part of multiple organised systems which propagated westward across the region.

Figure 8.1, reproduced based on figure 1 in Warner et al. (2023), shows the mean rainfall rate in the three hours centred on forecast hours T+0, T+12, T+24, T+36, and T+48 following the initialisation at 18 UTC on 17 June 2020. Overall both simulations produce rainfall which is too scattered and intense relative to the Global Precipitation Measurement (GPM) observations. However, the warm-started simulation (figures 8.1b and e) captures far more rainfall in the early stages of the forecast than the cold-started simulation (figures 8.1c and f), with some form of organised convective system emerging by T+12 in the warm-started forecast. This system is not quite in the right place, being too far to the southwest of the observed system in the GPM observations and too small (see figures 8.1d and g). However, the system is not generated at all in the cold-started simulation. The operational forecast, therefore, initialised using the standard method, would have completely missed the prediction of an intense, long-lived convective system which crossed several countries and hundreds of kilometres raining at rates of over $8\,\mathrm{mm\,h^{-1}}$ en route.

The smoothness of the small-scale prognostic fields at the initialisation of the cold-started forecast meant that convection did not develop quickly. The small convective elements present in the initialisation of the warm-started forecast evidently were able to collectively aggregate over the next twelve hours into an MCS, and without these elements the model was unable to spin-up the convection required to formulate the system. In this case, it is likely because as the simulation is initialised at 18 UTC, the solar radiation incident on the region is well past its peak for the day and thus there is nothing to generate the convective available potential energy (CAPE) required to trigger such convection.

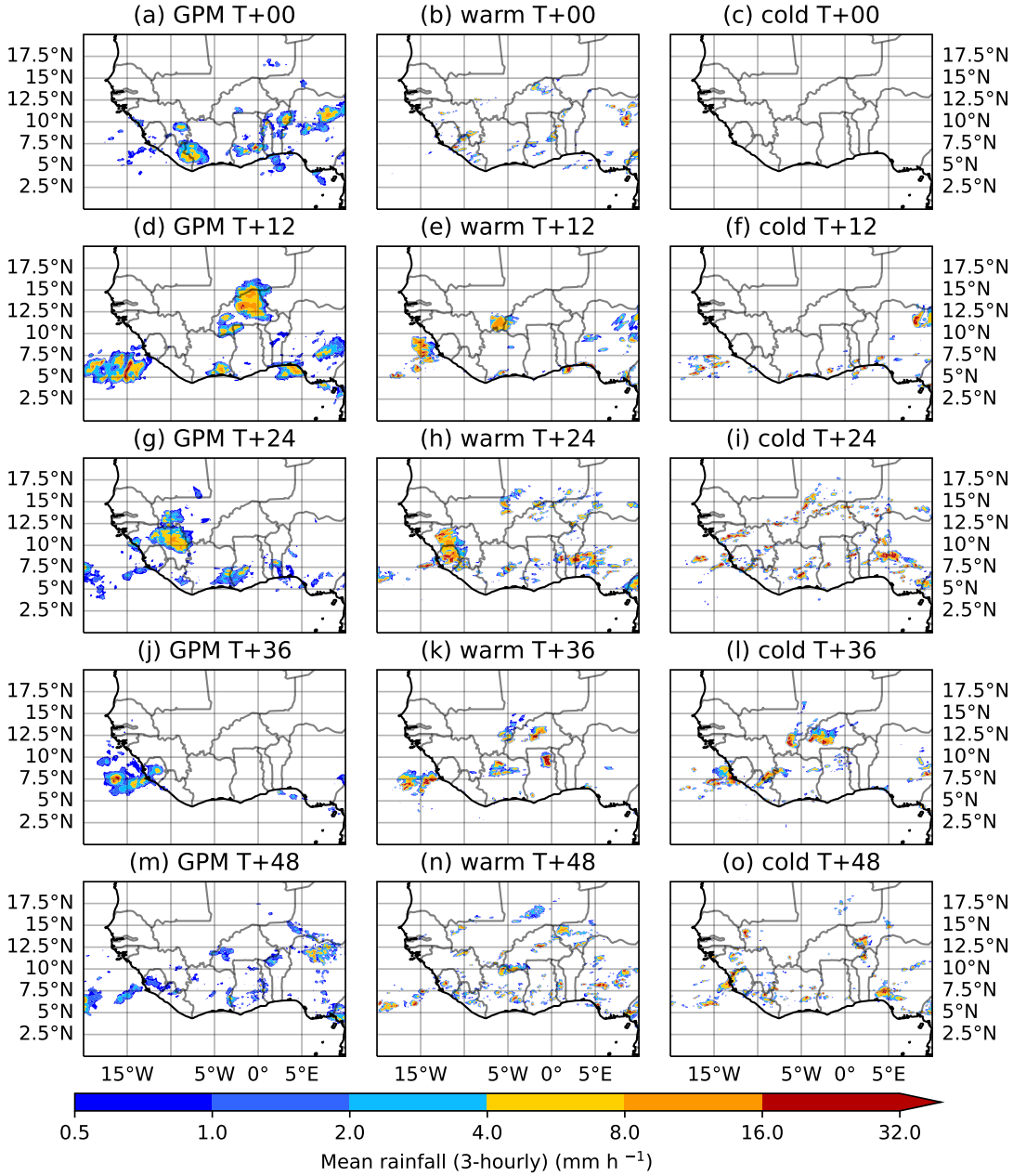

Figure 8.1: Three-hourly averages of precipitation rate at 12-hour intervals (represented by each row) from 18 UTC on 17 June 2020 onwards. The left column shows the Global Precipitation Measurement (GPM) final-run gridded product. The middle and right columns show the precipitation in the warm- and cold-started simulations respectively, both regridded to the same resolution as GPM.

However, even beyond the initial lack of forecast for this storm, there are further incorrect elements in the cold-started forecast. In fact, both the warm- and cold-started forecasts produce convection over Mali and northern Niger which begins to initiate at T+24, then develops into a second organised storm by T+36. However, in the GPM observations, no such precipitation exists. Nonetheless, in the warm-started simulation, the system is far less organised by T+36 as it has started to dissipate already, which is closer to the 'storm-less' reality than the coherent strong system that exists in the cold-started simulation at the same time. Supporting the conclusions of Warner et al. (2023), there is evidence in this case study that the existence of small-scale convective structure at model initialisation has effects on forecasts for not only the spin-up period but also beyond.

The following subsections attempt to, firstly, explain why there are differences in the forecasts after the initial spin-up period, and secondly, to quantify what these differences are, in order to understand the mechanisms behind and impacts of convective feedbacks.

8.1.1 Explaining Differences Between Warm-Started and Cold-Started Forecasts

In the example considered here, an organised convective system emerges from precipitation that exists at initiation. After it propagates across the continent, another organised system begins to generate at T+24h after initialisation, but in the warm-started simulation it does not organise as strongly as it does in the cold-started simulation. The subsequent analysis explores why the original system is generated in one simulation and not the other, and whether it caused the suppression of organisation in the second storm formed in its wake.

Figure 8.2 shows the relative vorticity at 700 hPa (filled contours) along with the $0.5\,\mathrm{mm\,h^{-1}}$ rainfall line contour in black for the first few hours of the forecast. Studies have shown that it is possible for the mesoscale convective vortex (MCV) generated in the stratiform region of a squall line to go on to initiate further convection (e.g. Davis and Galarneau 2009, see section 2.3.1). Certainly, at the beginning of the forecast there are stronger and more abundant vorticity anomalies in the warm-started forecast compared to the cold-started forecast, as a result of the small-scale structure being retained in the prognostic fields of horizontal wind, which are either associated with dry convection over the Sahara, or strongly colocated with rainfall. In all precipitation features, there are associated vorticity anomalies, which makes sense

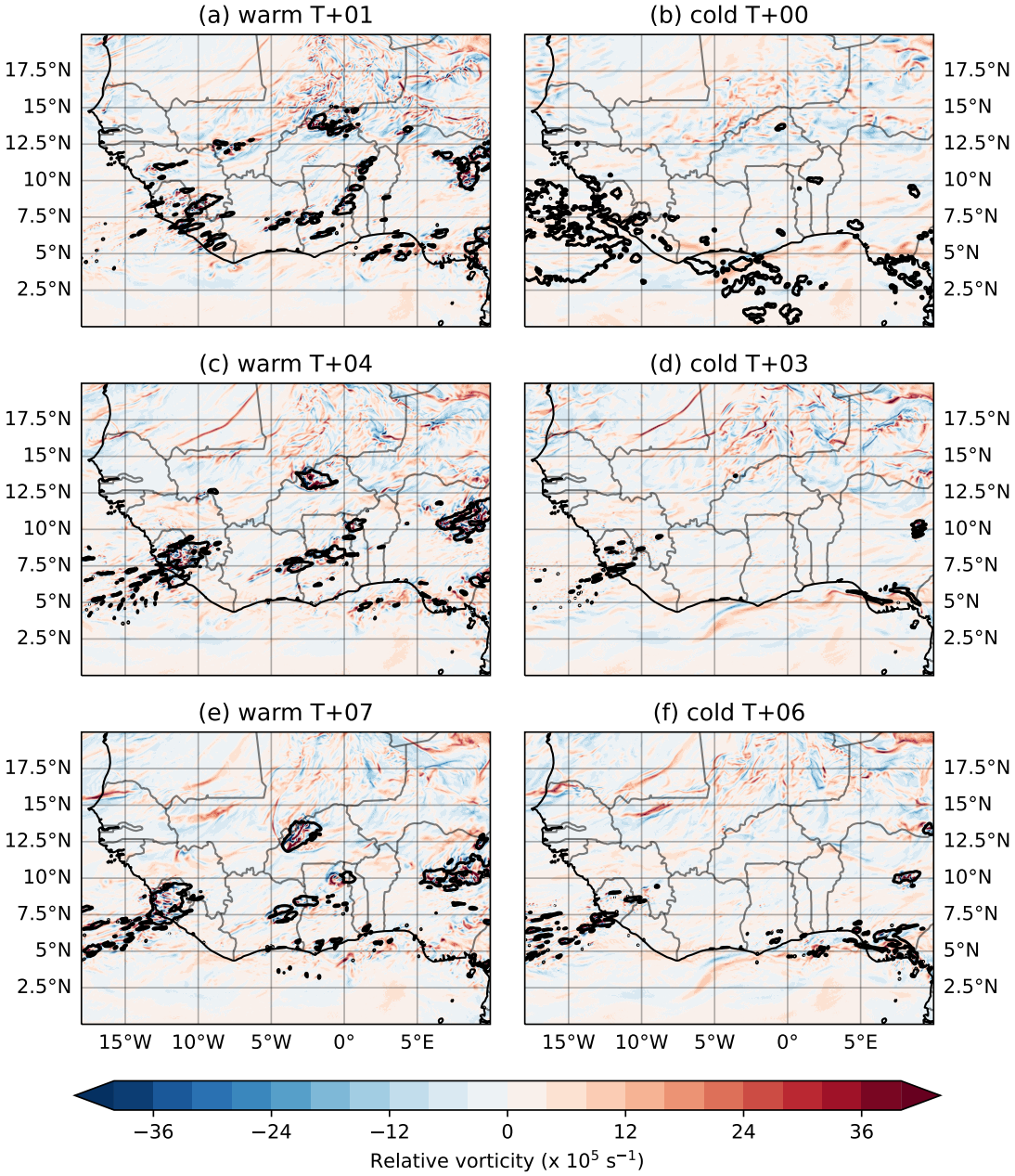

Figure 8.2: Relative vorticity ζ at 700 hPa at forecast hours T+0 (top row), T+3 (middle row), and T+6 (bottom row), for the cold-start simulation (right column) and closest approximations for warm-started output (left column), after initialisation at 18 UTC on 17 June 2020. Rainfall contours at 0.5 mm h^{-1} are shown by the black line contour.

since there is robust evidence from theory and modelling that convective cells are associated with vorticity dipoles (see section 2.3.1, chapter 5, and chapter 7). At times beyond T+6 hours, maps show similar colocation of rainfall and relative vorticity dipoles. However, it is difficult to diagnose whether the precipitation or the vortices (and their associated updraughts) emerge first. Therefore, it is difficult to draw concrete conclusions about the role of vorticity in convective memory or initiation of new MCSs from the simulations used in this chapter.

Organised convection can also generate mesoscale circulation over the depth of the troposphere which can modulate the wider environment and thus affect the wind conditions that are associated with convective initiation. For example, figure 8.3 shows the 925 hPa winds for T+18–24 hours in the forecast. Typically, low-level southwesterly monsoon winds strengthen overnight, advecting cool moist air over the land from the Gulf of Guinea, but in this case the winds are disrupted by the rear-inflow jet (RIJ) of the MCS in figure 8.3a, seen where there is a line of reduced wind speed extending northwest from the back of the storm. In addition, there is evidence of a cold pool pushing ahead of the storm as it moves forwards, further disrupting the monsoon flow.

It is possible that the disruption of winds from the RIJ leads to reduced low-level convergence in the following timesteps, and thus affects the formation of precipitating features in figures 8.3c and e compared to the system that forms in 8.3d and f. The rainfall in figures 8.3c and e seem to comprise two smaller coherent regions of rainfall on either side of Niger's northeastern border, compared to a more coherent single larger system along the border in the cold-started simulation. Arguably the latter could be considered 'more organised'.

In the region near the RIJ of the system in figure 8.3a, relative humidity is lower than at the same position in figure 8.3b. Perhaps the RIJ has reduced the flow of moist cool air as part of the monsoon, or the moisture in the atmosphere has been converted into cloud and lifted out of the boundary layer. Regardless, the region where the second system forms in the warm-started simulation is noticeably drier than its cold-started counterpart. Again, it is difficult to diagnose whether the suppressed convection is a direct result of interrupted low-level flow, since by the time the system is forming at the following timestep there are already updraughts which necessitate convergence by continuity. Nonetheless, it is of note that the reduced southwesterly monsoon winds, disrupted by the MCS's RIJ, extends along the northwestern border of Niger, which is where two mesoscale systems are separated in figure 8.3e, but in figure 8.3f they exist

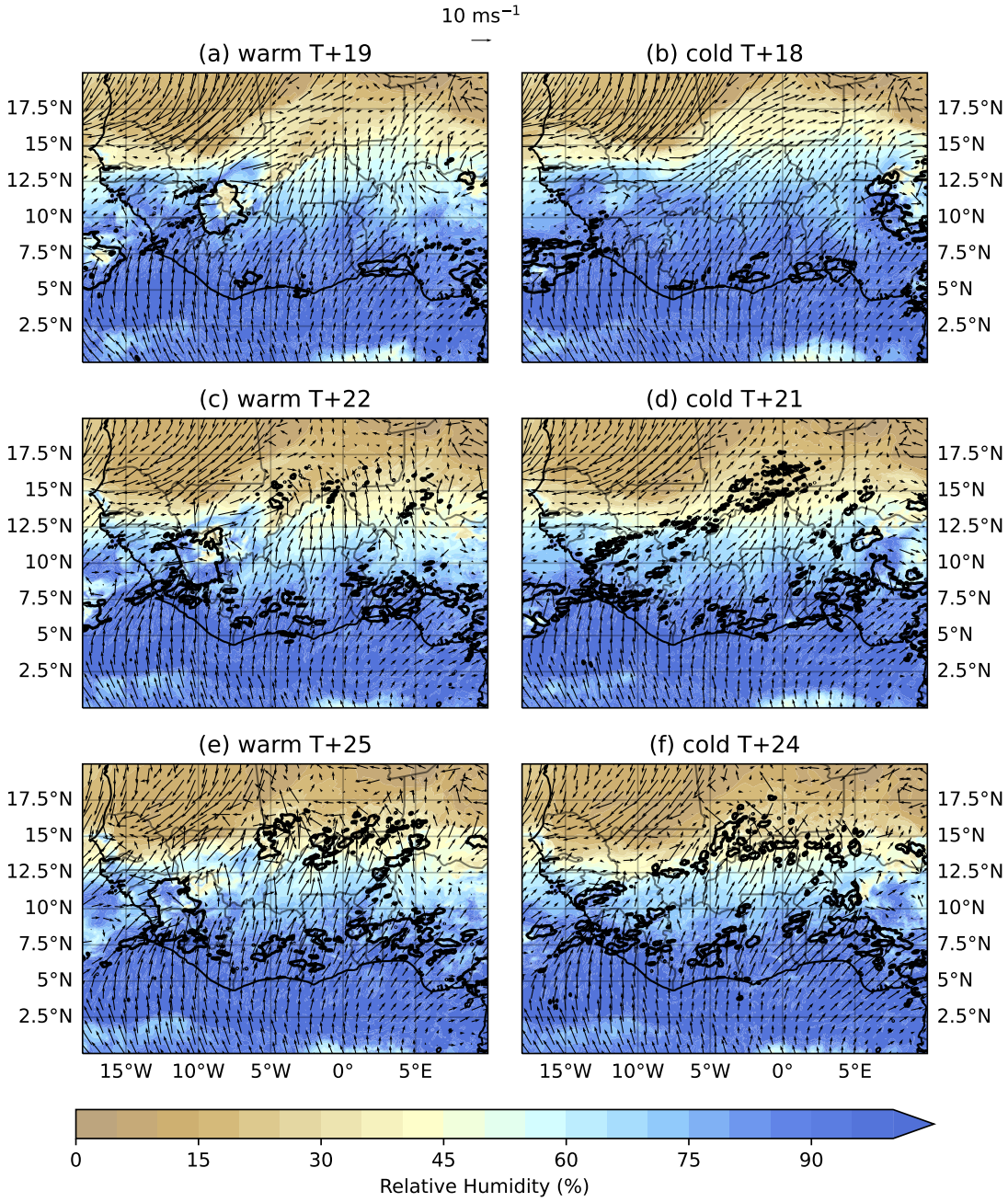

Figure 8.3: Wind at 925 hPa (shown by black vectors) and relative humidity at 925 hPa at T+18 (top row), T+21 (middle row), and T+27 (bottom row), for the cold-start simulation (right column) and closest approximations for warm-started output (left column) after initialisation at 18 UTC on 17 June 2020. Rainfall contours at 0.5 mm h^{-1} are shown by the black line contour.

as part of a single larger system.

Another potential mechanism for convective feedbacks is the effect of precipitation on the land surface. Heavy rainfall will result in the moistening of the soil beneath it, which is evident in figure 8.4a by the moist anomaly behind the track of the MCS. Since no such storm existed in the cold-started simulation, no such moist anomaly is present in figure 8.4b. Soil moisture, however, can affect how convective storms initiate and intensify as described in section 2.3.1, and the positive soil moisture anomaly is a persistent feature which still exists 12 hours later, when more convective cells begin forming at 18 UTC on 18 June 2020. More cells appear to form in the cold-started simulation in figure 8.4d than in the warm-started simulation (8.4c), and by the time it reaches T+36, the cells in the cold-started simulation have organised into a coherent system (figure 8.4f) whereas in the warm-started simulation they have dissipated and become parts of smaller systems (figure 8.4e). It is possible that because in the cold-started simulation, the soil was drier as a result of the first MCS not forming, which intensified the second MCS, allowing it to organise and become stronger compared to the system in the warm-start which was limited due to the damp soil.

Overall it appears that in this case study, the existence of the first storm impacted the potential of the second storm in its formation and intensification. GPM observations indicate that the second set of organised convection over Niger at T+36 (seen in figure 8.1k–l) did not, in fact, exist (figure 8.1j). Since the warm-started simulation has a more dispersed and less coherent storm than the cold-started simulation, it can be regarded as a closer depiction of reality, though it is still incorrect. However, the mechanisms of the formation of the second MCS suggest that the impact of the first MCS on the low-level winds (reducing the moisture flux and low-level convergence in the area where the convective cells were generated) and soil moisture (dampening the soil which meant that the convection did not intensify as strongly) were responsible for the suppression of the initiation and organisation of the second MCS. Perhaps the second storm exists in the warm-start simulation because the first storm was too small and too far westward even in the warm-started simulation relative to observations (figure 8.1d–e), meaning that the impact of its RIJ and the modulation of the land surface was reduced relative to reality, where they may have acted to fully suppress the second storm.

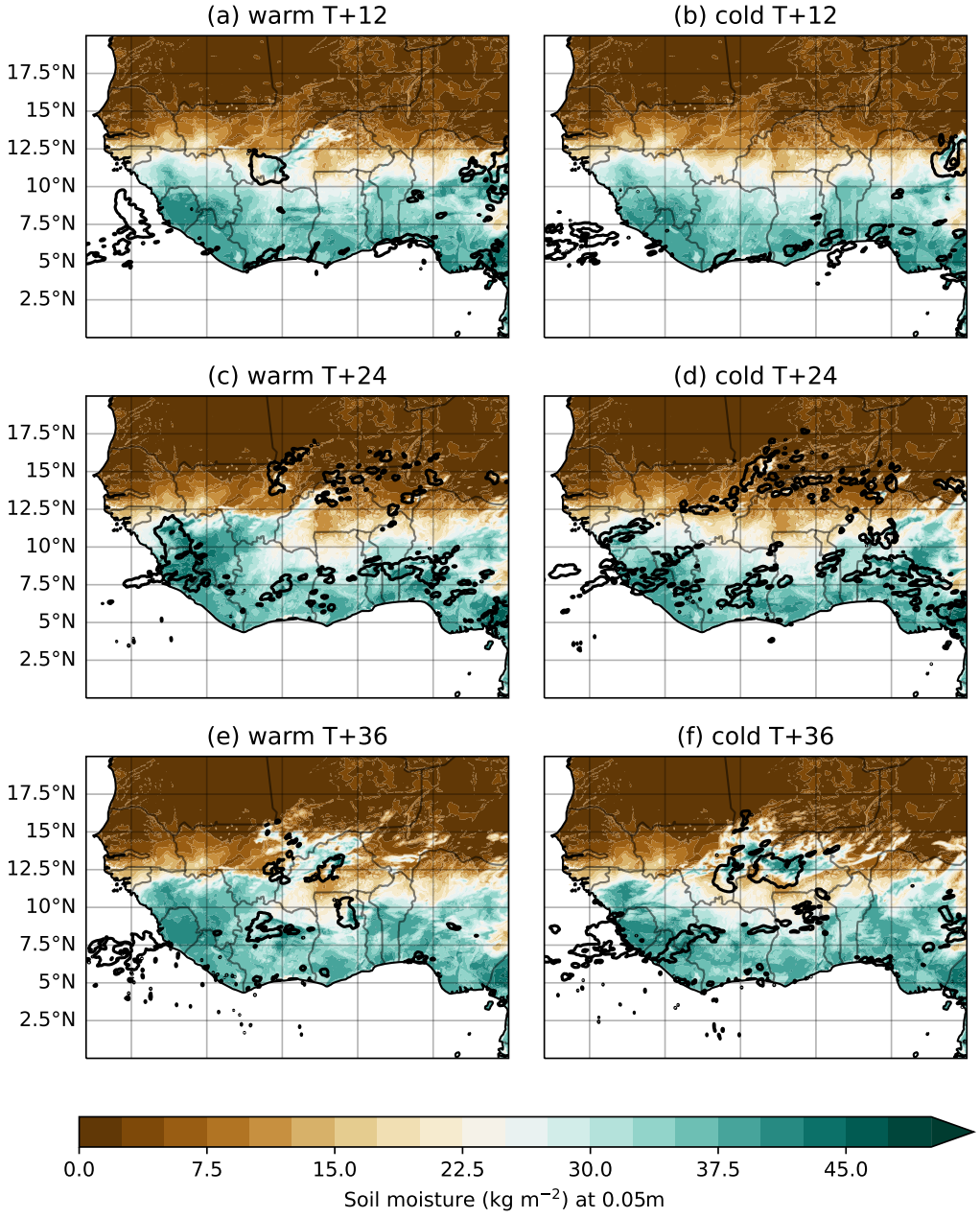

Figure 8.4: Soil moisture at 0.05 m below the surface at T+12 (top row), T+24 (middle row), and T+36 (bottom row), for the cold-started (right column) and warm-started (left column) simulations after initialisation at 18 UTC on 17 June 2020. Rainfall contours at 0.5 mm h^{-1} are shown by the black line contour.

8.1.2 Upscale Impacts of Forecast Differences

Having established what the impact of the mesoscale differences in the forecast make on other mesoscale features, it is now of interest to examine how the mesoscale differences make changes in the forecast on synoptic scales. The first tool one could use to examine the impact of mesoscale differences is by taking the difference between wind vectors at the same time between the two simulations (within an hour of accuracy due to the lack of synchronisation between model outputs) to understand how the winds at different heights are behaving differently based on the two initialisations.

Figure 8.5 shows the differences between the simulations at 700 and 200 hPa. Evidently, over the course of the forecast, the different MCS structures are generated have induced different circulations across scales. For example, figures 8.5a and c show evidence of midlevel inflow entering the rear of the first MCS at 700 hPa, and as it moves off the coast in figure 8.5e it generates a cyclonic circulation relative to the cold-started simulation, even though there is still a precipitation feature at approximately the same time and location in the cold-started simulation (see figure 8.1l). The feature in the warm-started simulation is larger and further to the west. It is more mature, having emerged from an existing system which has a developed circulation.

However, the most remarkable changes in the circulation occur at upper levels, shown in the right-hand column of figure 8.5. The first MCS causes distinct upper-level divergence anomalies of around $15\,\mathrm{m\,s^{-1}}$, which enable an anticyclonic circulation to form that drives a considerable northwesterly wind across the continent (seen in figure 8.5d and f). Such a modulation of wind could disrupt the tropical easterly jet (TEJ) and affect the wind shear profile which serves to organise MCSs in the region.

Another synoptic-scale impact of the differences in convection is the modulation of African Easterly Waves (AEWs). Following the tracking methodology in Bain et al. (2014), Hovmöller plots were produced to track the northern and southern AEWs using curvature vorticity, shown in figure 8.6. The black lines highlight local coherent curvature vorticity maxima propagating in an easterly direction overall. The southern-track AEWs (figures 8.6c–d) look relatively similar in qualities between the two simulations, but the vorticity signatures are significantly weaker and the strong wave signal starting at 5 ° W and hour 7 in the warm-started simulation does not emerge in the cold-started simulation. Furthermore, the warm-started simulation generates

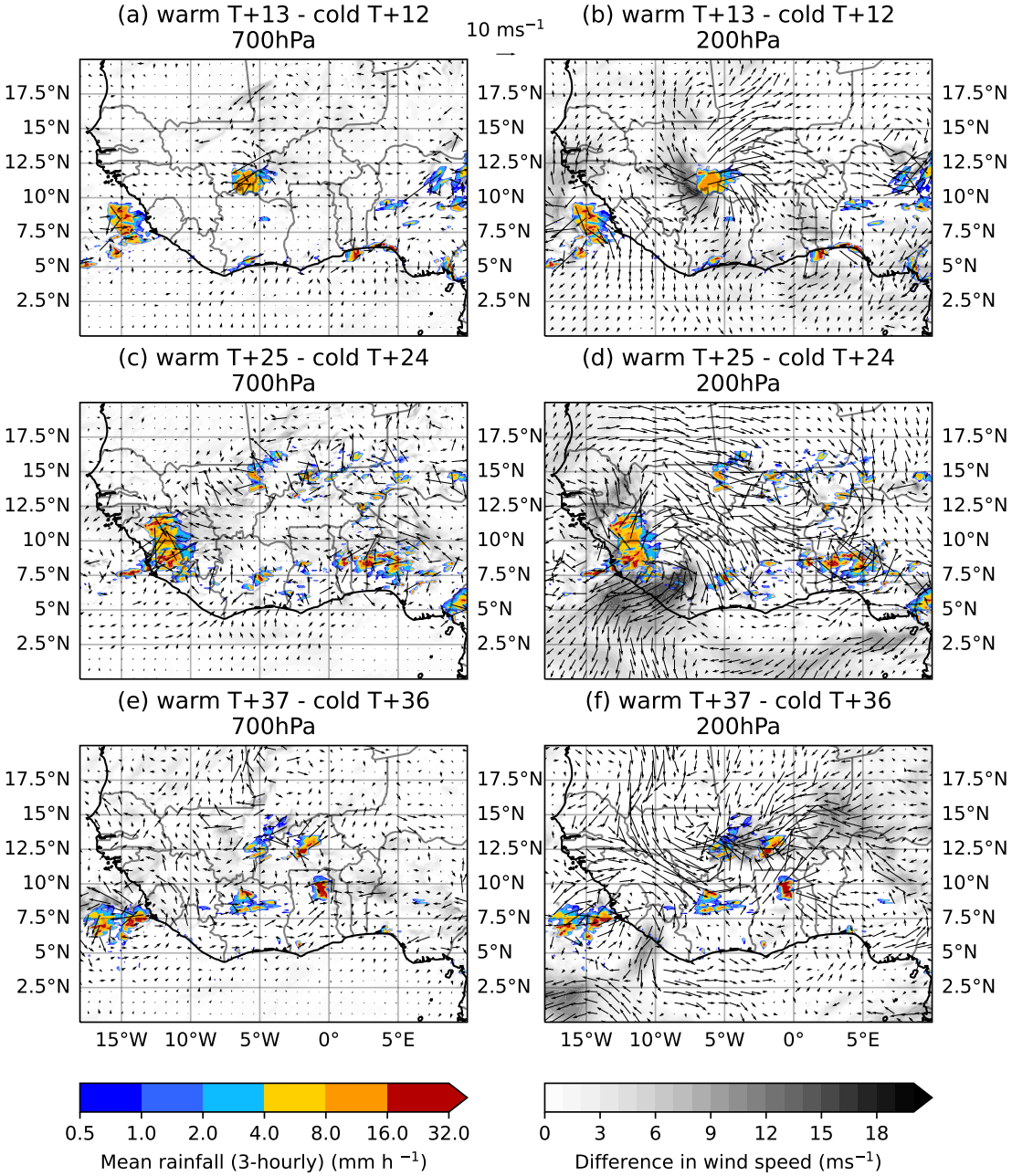

Figure 8.5: Wind vectors (black vectors and greyscale shading) representing the difference between the warm- and cold-started simulations at T+13 (top row), T+25 (middle row), and T+37 (bottom row) after initialisation at 18 UTC on 17 June 2020 for 700 hPa and 200 hPa (right column). The warm-started simulation's 3-hourly mean rainfall rate is shown by the coloured contours.

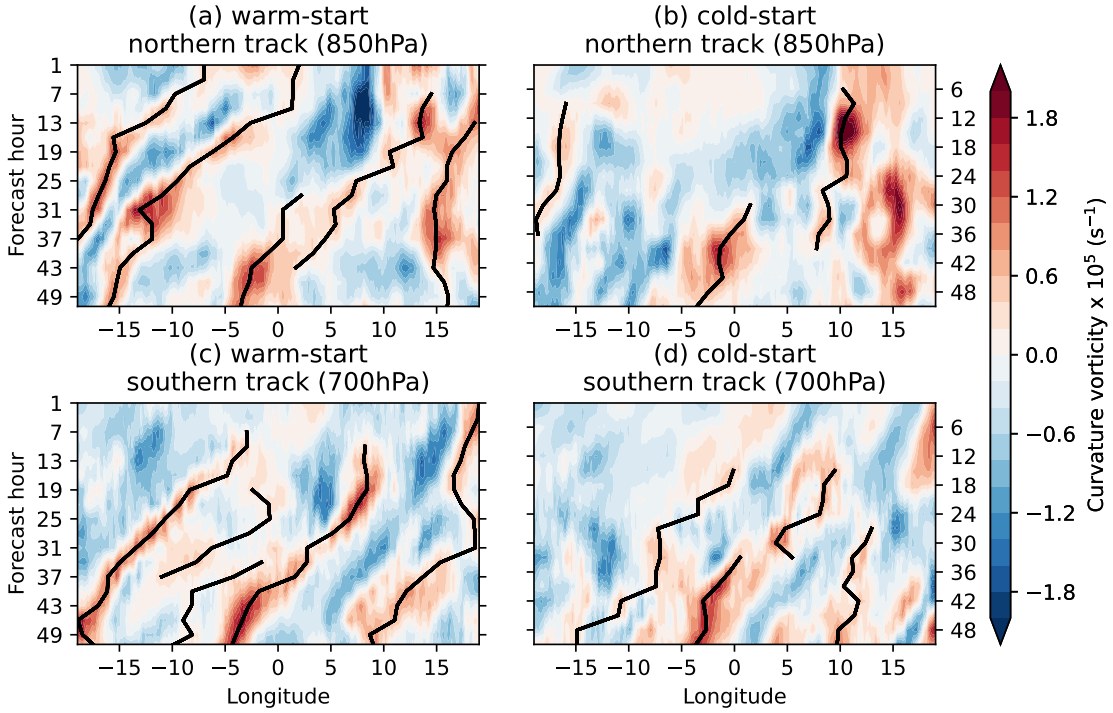

Figure 8.6: Hovmöller plots of curvature vorticity (filled contours) averaged over (a–b) 15–22.5 ° N at 850 hPa and (c–d) 5–12.5 ° N at 700 hPa, plotted for each longitude against forecast hour, for the warm-started simulations (left column) and cold-started simulations (right column). The location of AEWs in longitude and time are plotted by black lines.

an AEW-like signature in the northern track which does not appear whatsoever in the cold-started simulation. The AEW structure in the warm-started simulation seems to originate from positive vorticity anomalies at 0 ° E above 15 ° N, which exist at the very start of the forecast, and are stronger in the warm-started simulation than in the cold-start due to the retention of small-scale structure from previous runs (see figures 8.2a–b). The key period of intensification that the vortex signature undergoes in the warm-started simulation which does not occur in the cold-started simulation is between 12 and 20 hours, which corresponds to 06–14 UTC on 18 June 2020.

While some of these vorticity anomalies do not appear to directly couple to convection during the simulation (as they exist on the dry northern AEW track over the Sahara), it appears that it is an upscale impact of a nearby MCS which reinforces cyclonic circulation and intensifies the AEW. Where the cold-started simulation has not generated an MCS, the wave signature is weaker and barely exists. It is very important for downstream forecasting that the warm-start vorticity anomalies collectively assimilate and grow into a coherent propagating wave signal whereas those in the cold-started simulation do not, since AEWs can trigger further convection

and even undergo tropical cyclogenesis once they propagate over the Atlantic (see chapter 6).

Another perspective for understanding the scales of energy involved in both forecasts is to examine the spectral energy density at various pressure levels. Figure 8.7 shows energy spectra for various pressure levels over the first 9–10 hours of the cold- and warm-started forecasts, as well as for the global driving model at the same valid times as the warm-started simulation. The closest possible output times are compared, which have the warm-started and global outputs leading the cold-started outputs by one hour due to output inconsistencies. The spectra are calculated in the region defined by 20 ° W–20 ° E, 5 ° S–25 ° N (note that this region is larger than the domains shown in previous figures).

To begin with, in the forecasts, it is possible to see the impact of the initialisation techniques in the difference in the energy spectra in figures 8.7a–b, where below 10^5 m (100 km), the cold-start has noticeably less energy per wavenumber than in the warm-start, showing the impact of including small-scale structures from the previous model run which are not present in the global reanalysis. The global model shows consistently lower energy per wavenumber at smaller wavelengths but it should be noted that it has been scaled down to the regional grid, creating some resonances at smaller wavelengths, so its values at wavelengths below 33 km (its native resolution, at 33,000 m $\approx 10^{4.5}$ m) are not meaningful.

The gap between the cold- and warm-started energy spectra at these smaller wavelengths is most distinct at 850 hPa, noticeable at 700 hPa, and is barely distinct at 200 hPa (perhaps since there tend to be fewer mesoscale or smaller-scale structures at upper levels). However, over the subsequent hours, the spectra observed in both simulations become closer together, with the cold-started simulation having slightly lower energy at larger ($>10^{5.5}$ m) scales at 850 hPa by T+10 (figure 8.7). The difference here may not be significant due to the hour-long lag of the cold-start behind the warm-start simulation. Nonetheless, both simulations, particularly at 850 and 700 hPa, seem to shift somewhat the amplitude of energy and the angle of the spectrum over the forecast, perhaps indicating the existence of a diurnal cycle in the spatial kinetic energy distribution.

To understand these changes in the energy spectra across forecast times, after smoothing the signals, the time derivative of the energy spectra $\left(\frac{\partial \log E_k}{\partial t}\right)$ was calculated (effectively taking the gradient over time across the plots shown in figure 8.7 and for further times in the simulation). Figure 8.8 shows Hövmoller-style plots of the $\frac{\partial \log E_k}{\partial t}$ signal varying with forecast

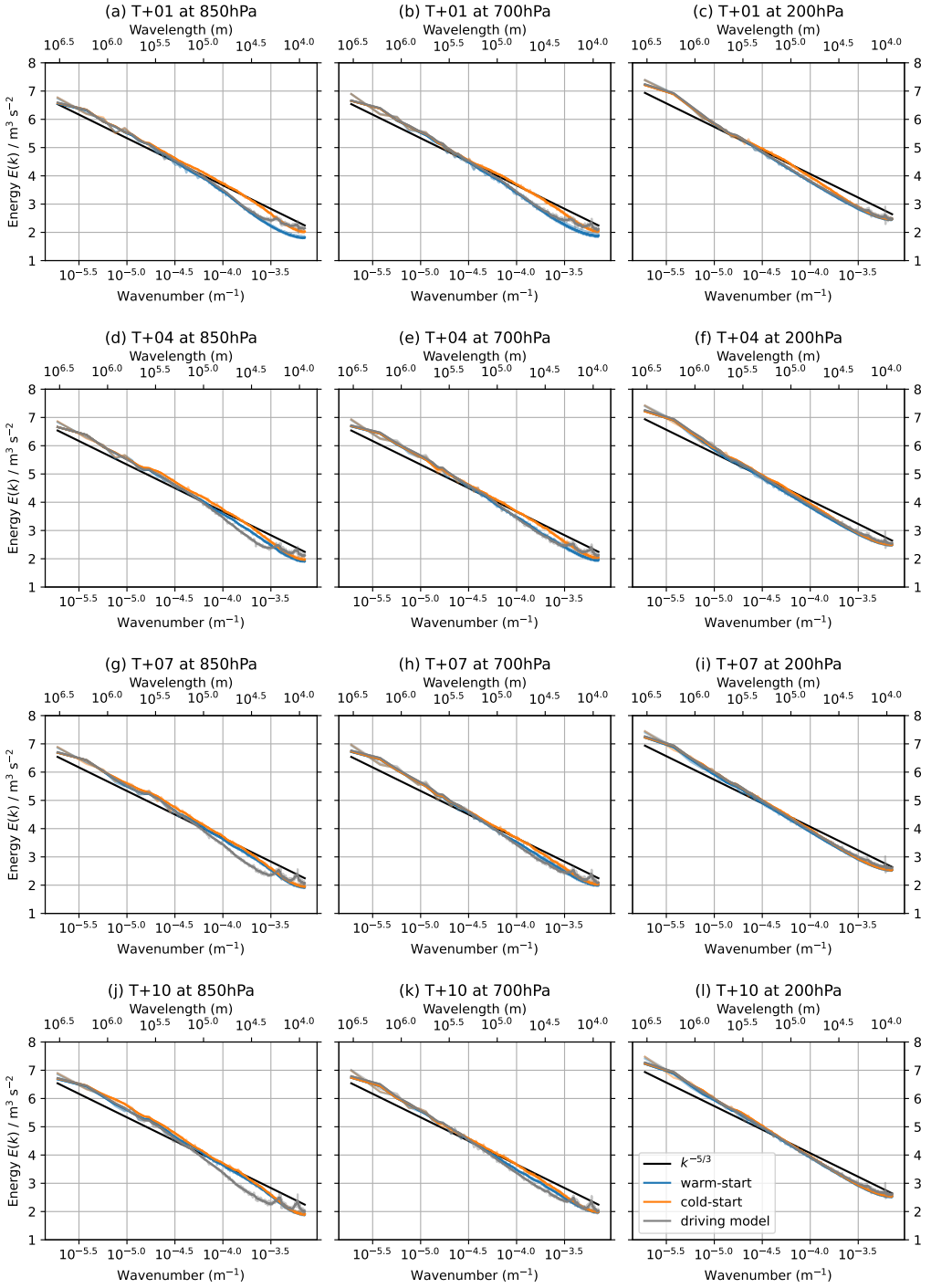

Figure 8.7: Spectral energy density plotted against wavenumber on a log-log plot, for the first four forecast hours (indicated by row; T+1, 4, 7, and 10 for the warm-started simulation and T+0, 3, 6, and 9 for the cold-started simulation) after initiation of the simulation at 18 UTC on 17 June 2020. Spectra are shown at three different pressure levels (indicated by column; 850 hPa, 700 hPa, and 200 hPa), for the warm-started and cold-started initialisations (orange and blue lines respectively) as well as forecasts at the same time from the closest driving global model initialisation (grey lines). The spectra are smoothed using a variable-size uniform filter along their length to limit noise (raw signals are shown in faded colours behind the lines). Reference lines showing the archetypal $E(k) \sim k^{-\frac{5}{3}}$ relationship (with arbitrary scalings to approximate observed amplitudes in the plots) are in black.

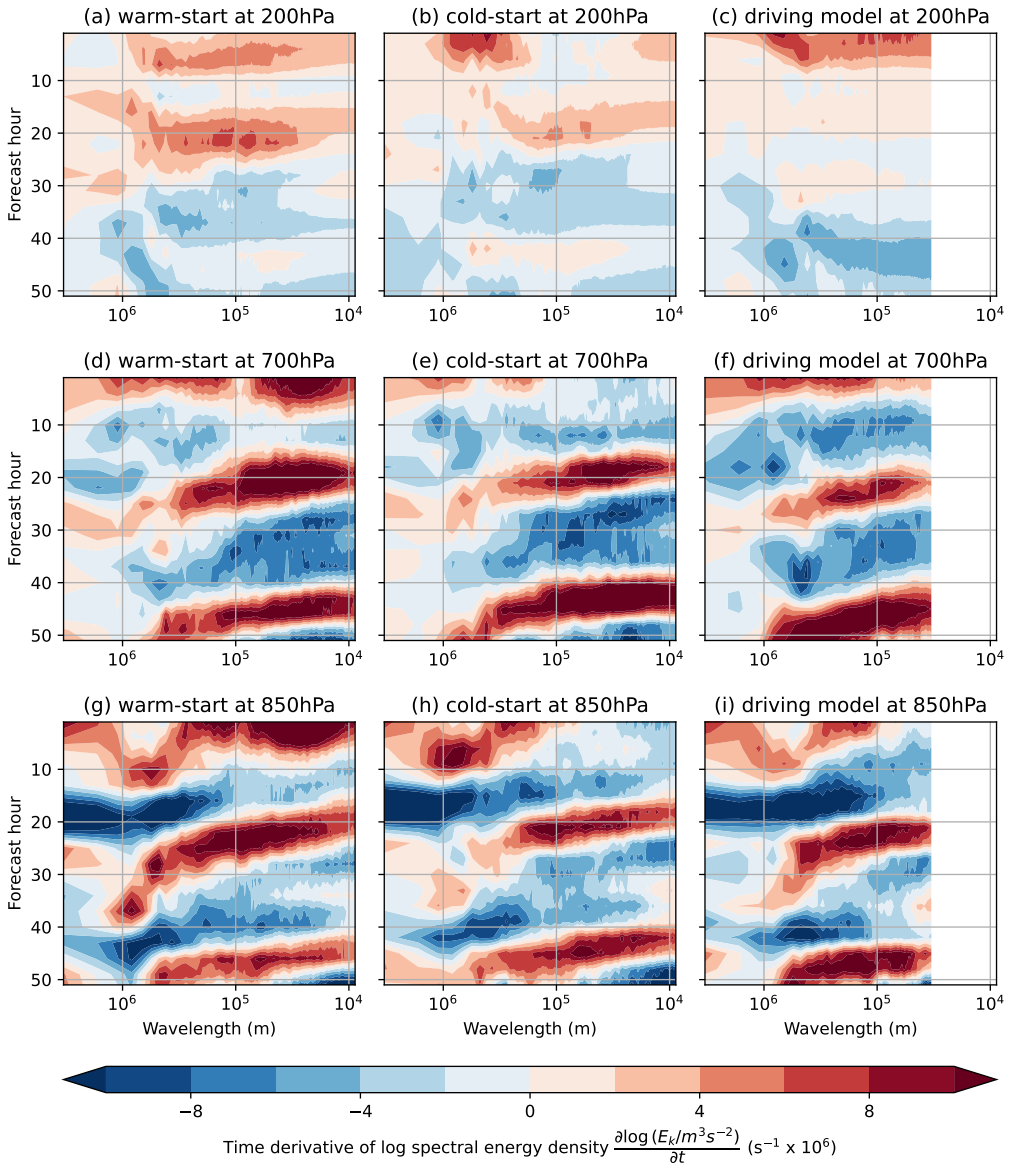

Figure 8.8: Rate of change of the logarithm of spectral energy density (filled contours) plotted against log(wavelength) on the x-axis and forecast hour on the y-axis for the forecast initialised at 18 UTC on 17 June 2020, with the warm-started regional forecast (left column), cold-started regional forecast (middle column), and global model (right column). Global model spectra are only shown above the model's native grid spacing (≈33 km).

hour on the y-axis and wavelength on the x-axis. Note that the values below $\lambda \approx 10^{4.5}$ m have been removed for the driving simulation. The initial part of the forecast is where the most obvious differences are, with an increase for the first ten hours of the warm-started forecast in the features below 100 km or less at all levels, though stronger at lower levels, while the energy decreases at these scales in the cold-start simulation until the afternoon the next day.

As the forecast time increases there is a 24-hour cycle of decreasing smaller-scale energy features in the early hours of the morning (T+9 to T+18) which then increases in the afternoon the next day (T+18 to T+24). Energy appears to be generated at smaller scales beginning in the early afternoon, then as the afternoon progresses, the scale where energy is increasing most rapidly becomes larger, such that by T+36 hours (06 UTC on 19 June 2020), energy on scales of up to 10^6 m is increasing, at 850 hPa in the warm-started simulation (figure 8.8g). The cycle of energy corresponds to the generation of convection through diurnal heating in the early afternoon, which then clusters into more organised systems with mesoscale circulations in the late afternoon and early evening, and then appear to feed back on synoptic-scale systems of scale $\geq$ 1000 km (10^6 m).

At 200 hPa (figures 8.8a–c), the variation in energy across all three simulations is smaller in magnitude and does not have a prominent diurnal cycle in the same way as the lower-level energy spectra. However, it is at this level where the forecasts seem to have the most differences in how the energy evolves at different scales. For example, across all scales at T+21–24 hours, there is a maximum in the warm-started simulation which likely corresponds to the strong upper-level response to deep convection in the form of the warm-started simulation's storm (see figure 8.5). The maximum is stronger than in the cold-started simulation and is barely present in the global simulation, which, as the discussion of the upper-level impacts of the presence of the storm suggests, further supports the idea that the presence of deep convection has discernible impacts on the upper-level meso- and synoptic-scale circulations.

At 850 hPa and 700 hPa, the signatures of $\dfrac{\partial \log E_k}{\partial t}$ seem to be relatively similar, although the afternoon diurnal upscale energy transfer appears to be delayed by 2–3 hours in the driving model compared to the cold- and warm-started simulations. However, a key differences arises in the upscale energy rate of change at approximately T+36 (mostly at 850 hPa, but a small signature exists at 700 hPa) where the warm-started simulation shows a strong positive anomaly which is not reflected as distinctly in the cold-started or global simulations. Since the essential

difference between the cold- and warm-started simulations is the initial convective conditions, and the global simulation uses a convective parameterisation with limited representation of organised moist convection, the difference implies that it is the moist convection that forces the upscale transfer of energy that causes differences in the synoptic-scale features.

The case study makes a convincing argument that moist convection has an impact on atmospheric evolution at larger scales, even days into a forecast. However, in order to validate the conclusions drawn from the case study, it is worth investigating a case where convection is not represented so differently in the early stages of the forecast.

8.2 Case Study 2: Forecast Initialised at 18 UTC on 7 August 2020

The second case study is intended to provide a contrasting scenario. Figure 8.9 shows a comparison with GPM observations for the two simulations over the course of the forecasts. In this case, although there is extensive convective structure present at the initialisation of the warm-started forecast that is absent from the cold-started initialisation (figures 8.9a–c), the simulations evolve to have very similar precipitation fields over the rest of the forecasts. The initial convection present in the warm-started simulation has a similar shape to the observed GPM precipitation, but is too spatially incoherent, and shortly dissipates. Twelve hours after initialisation, the cold-start has generated a similar structure to the warm-started precipitation, which is also similar to the observed structures but with a smaller spatial extent. Over the rest of the forecast, the convective features evolve to look very similar, with some spurious scattered convection across the region at T+24 which is not observed leading to another organised system at T+36 which is not present in observations (on the Mali-Senegal border; see figures 8.9j–l).

The similarity in the precipitation structures is echoed in the synoptic-scale dynamics in the region. Figures 8.10 and 8.11 indicate that the AEW tracks and energy spectra changes respectively look very similar between the simulations. The curvature vorticity signature in figure 8.10 look very similar, with only very minor differences, such as a small positive vorticity signature in the cold-started simulation in the northern-track at 15 ° W (figure 8.10b) which extends slightly further into the forecast than it does in the warm-started simulation (figure 8.10a).

Furthermore, figure 8.11 shows that the rate of change of energy spectra for the warm- and

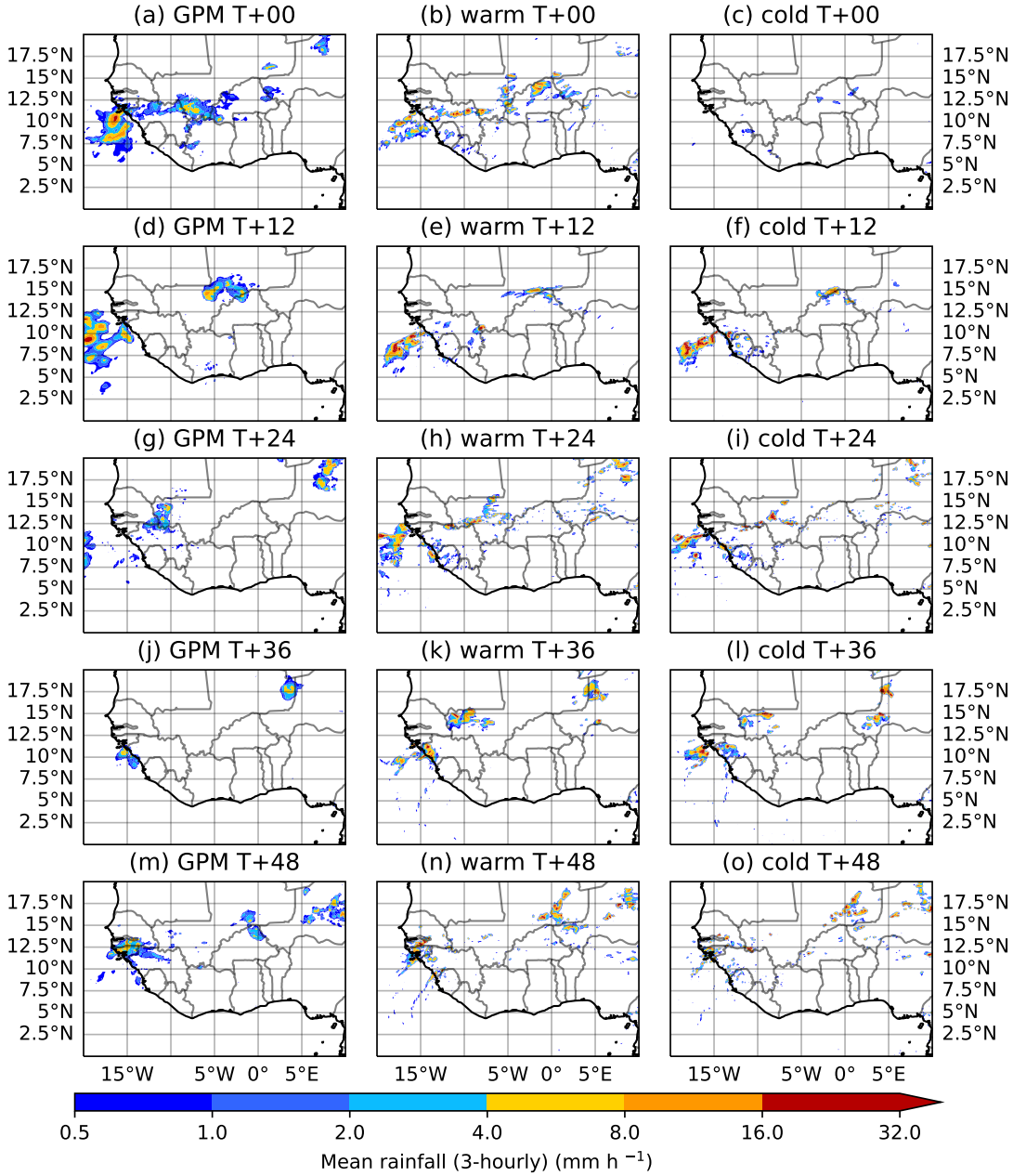

Figure 8.9: Three-hourly averages of precipitation rate at 12-hour intervals (represented by each row) from 18 UTC on 7 August 2020 onwards. The left column shows the Global Precipitation Measurement (GPM) final-run gridded product. The middle and right columns show the precipitation in the warm- and cold-started simulations respectively, both regridded to the same resolution as GPM.

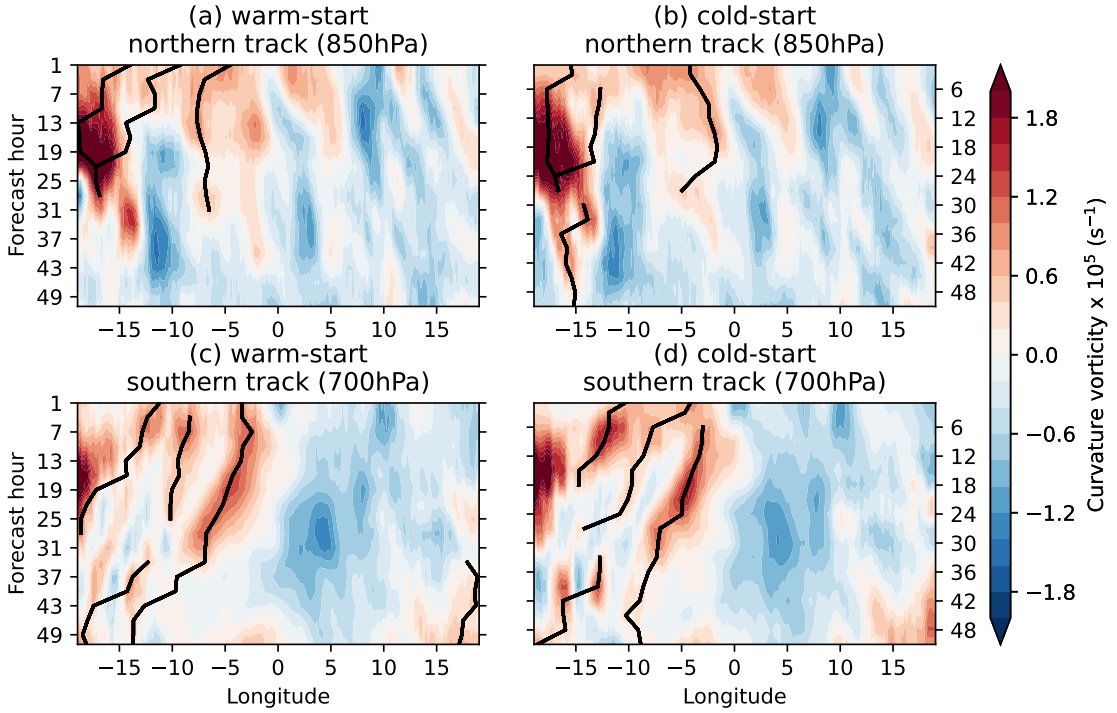

Figure 8.10: Hovmöller plots of curvature vorticity (filled contours) averaged over (a–b) 15–22.5 ° N at 850 hPa and (c–d) 5–12.5 ° N at 700 hPa, plotted for each longitude against forecast hour since initialisation at 18 UTC , for the warm-started simulations (left column) and cold-started simulations (right column). The location of African Easterly Waves (AEWs) in longitude and time are plotted by black lines.

cold-started initialisations look very similar at all levels with the exception of the first 10 hours at scales below around 2×10^5 m, which is to be expected given the nature of the initialisation. Afterwards, the cold-started simulation quickly recovers to recreate a near-identical diurnal cycle. There are more differences between the driving simulation and the regional simulations, where the diurnal cycle is again delayed and truncated at around 10^4 m at 700 hPa. Since the convection is similar in both the warm- and cold-started simulation beyond forecast times of T+10 hours, it makes sense that the limited convection in the driving global simulation is the reason behind the differences (which are again, most pronounced at 200 hPa).

Figures 8.10 and 8.11 explore the same feedback mechanisms as for Case Study 1, aiming to diagnose why the forecasts produce similar precipitation and thus moist convective structures. The figures show similar synoptic-scale structures, perhaps as a direct result of the similar initialisation conditions and evolution.

Figure 8.12 shows the 925 hPa wind vectors and relative humidity for the the first 9–10 hours after the initialisation at 18 UTC on 7 August. The humidity is overall much higher than

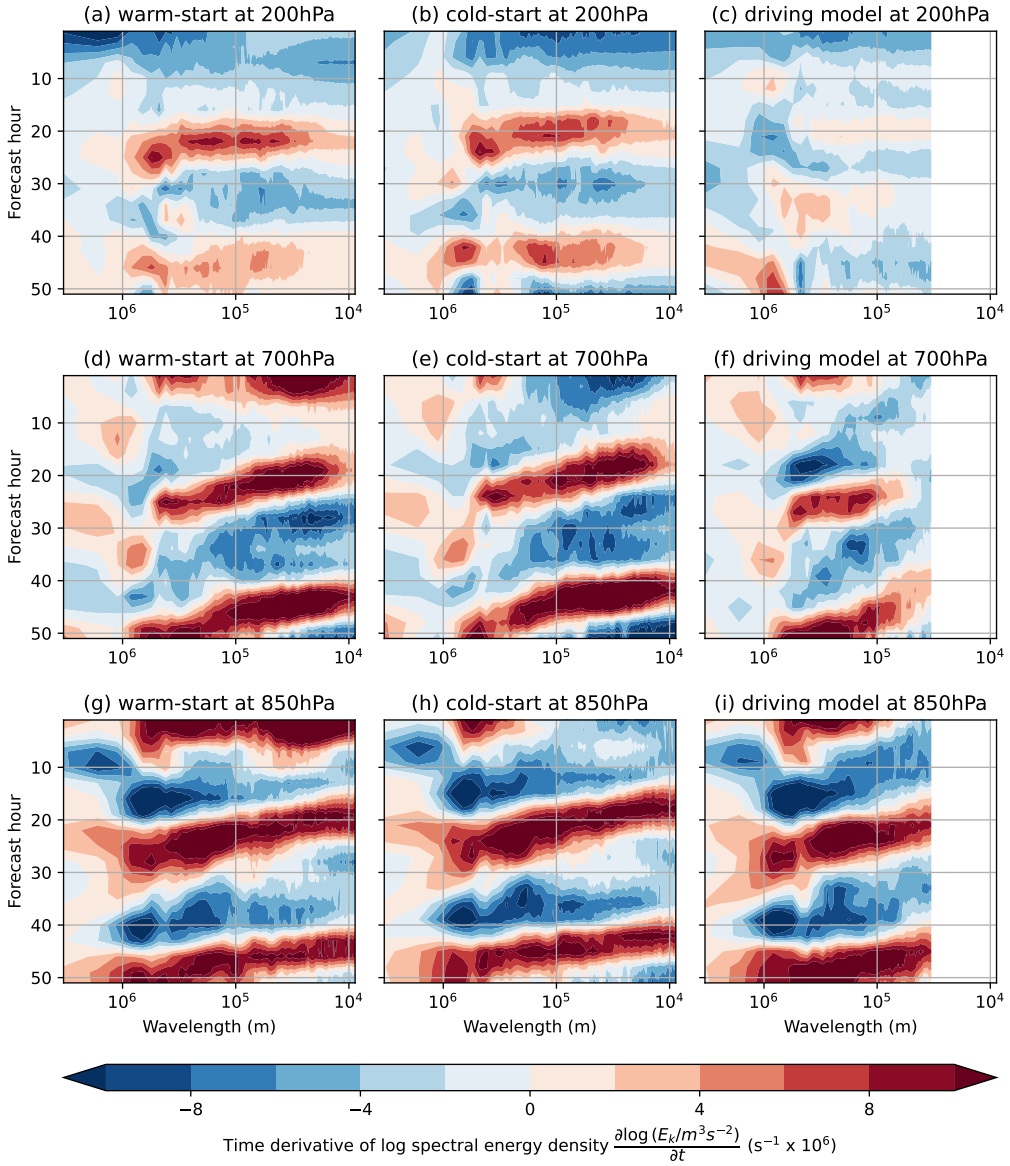

Figure 8.11: Rate of change of the logarithm of spectral energy density (filled contours) plotted against log(wavelength) on the x-axis and forecast hour on the y-axis for the forecast initialised at 18 UTC on 7 August 2020, with the warm-started regional forecast (left column), cold-started regional forecast (middle column), and global model (right column). Global model spectra are only shown above the model's native grid spacing (≈33 km).

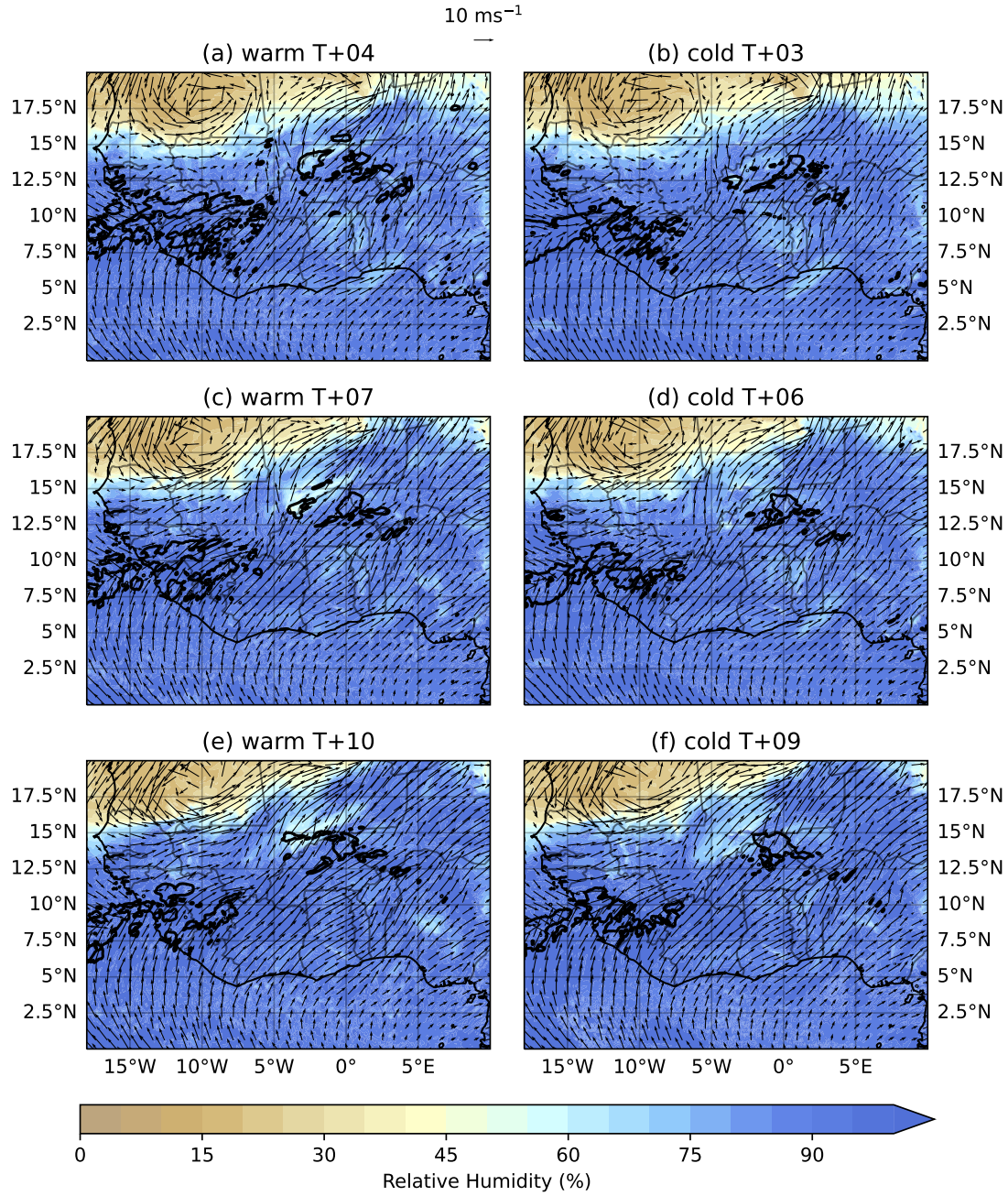

Figure 8.12: As for figure 8.3, for the initialisation at 18 UTC on 7 August 2020. Wind vectors at 925 hPa (shown by black vectors) and relative humidity at 925 hPa at T+3 (top row), T+6 (middle row), and T+9 (bottom row), for the cold-start simulation (right column) and closest approximations for warm-started output (left column). Rainfall contours at 0.5 mm h^{-1} are shown by the black line contour.

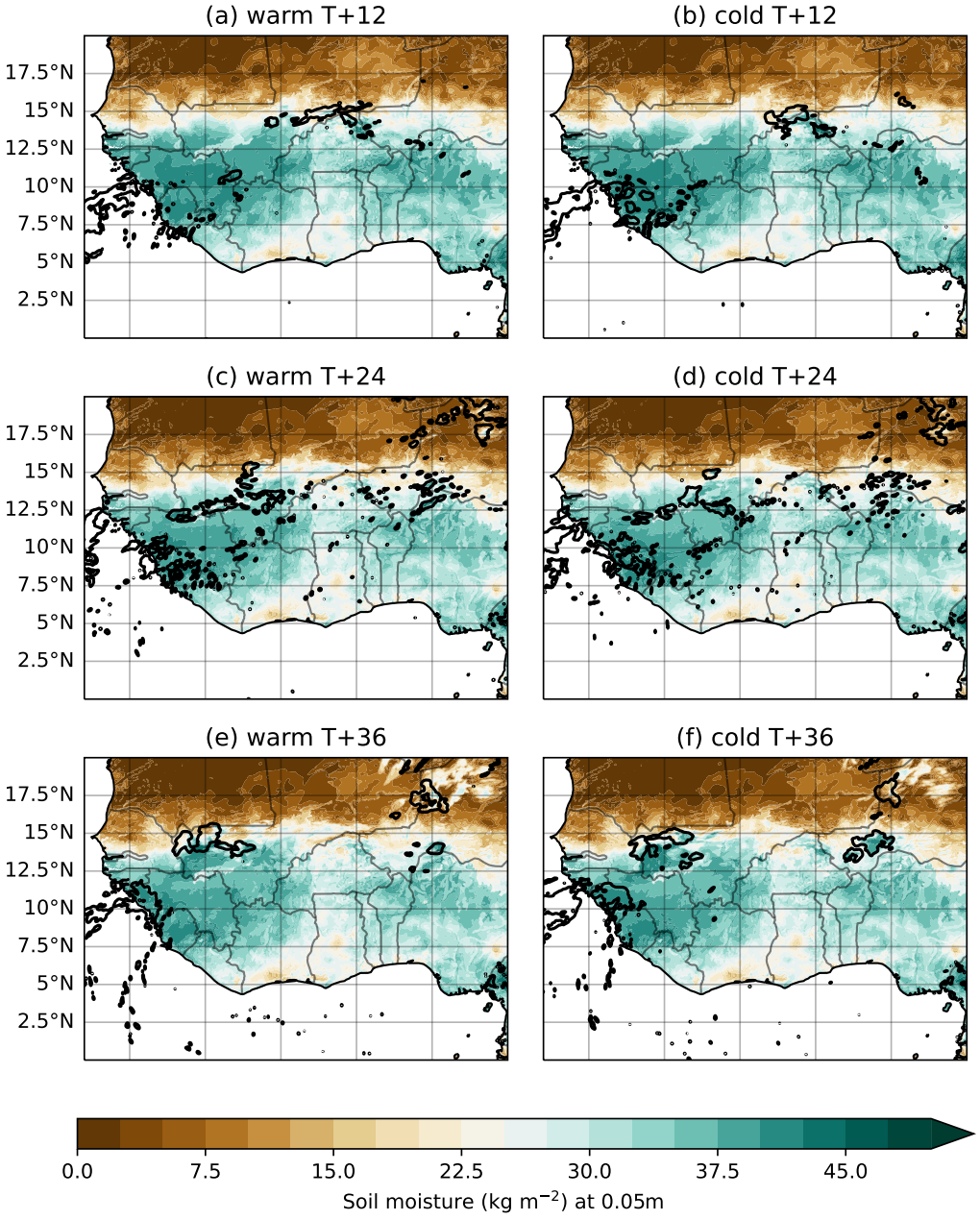

Figure 8.13: Soil moisture at 0.05 m below the surface at T+12 (top row), T+24 (middle row), and T+36 (bottom row), for the cold-started (right column) and warm-started (left column) simulations after initialisation at 18 UTC on 17 June 2020. Rainfall contours at 0.5 mm h^{-1} are shown by the black line contour.

the 17 June case (figure 8.3) because it is later in the monsoon season. Climatologically, the moisture has penetrated further north through the Sahel up to around 15 ° N, with much less distinct variation in the moisture field. Convective precipitation seems to spin up relatively quickly in the cold-started forecast, with structures already existing at T+3 which are very similar to those that exist at the same time in the warm-started simulation, perhaps due to the plentiful moisture creating a favourable environment for convective initiation. As a result, the low-level moisture and wind fields is altered in much the same way in the first 12 hours of both forecasts, which means that the subsequent convection is not modulated differently between the two simulations.

Figure 8.13 tells a similar story. Again, the moist soil signature extends further north since it is later in the season, and as a result of the convection evolving similarly in the early hours of the forecast, the soil moisture signature is extremely similar between the two forecasts. Chapter 7 establishes that soil moisture patterns are robustly associated with MCS initiation, a relationship that is supported in section 8.1 where figure 8.4 illustrates that storm systems tend to develop over sharp gradients in soil moisture, and intensify over dry soils. Therefore, similar soil moisture patterns are likely to lead to a similar generation and evolution of precipitation structures in both simulations.

The similarities between the convective structures as well as the soil moisture and low-level atmospheric moisture transport suggests that these factors are crucial for forecasting the initiation and maintenance of convection. In conjunction with the stark differences in convective structures that appear to be linked to differences in soil and low-level moisture in Case Study 1, it seems that accurately representing small fluctuations in these values caused by the existence of previous storms is crucial for continued skill in forecasting.

8.3 Overall Impact of Convective Feedbacks on Forecasts

Over the entire three-month experiment, generalised diagnostics were calculated based on elements of the two case studies in order to evaluate whether the existence of convection at initiation has a consistent impact on the synoptic-scale response. Total energy spectra for all dates in the three-month experiment were calculated, for each forecast hour output following 18 UTC initialisations (to remove the impact of the diurnal cycle). These were compared for the warm- and cold-started regional simulations as well as for the driving global model.

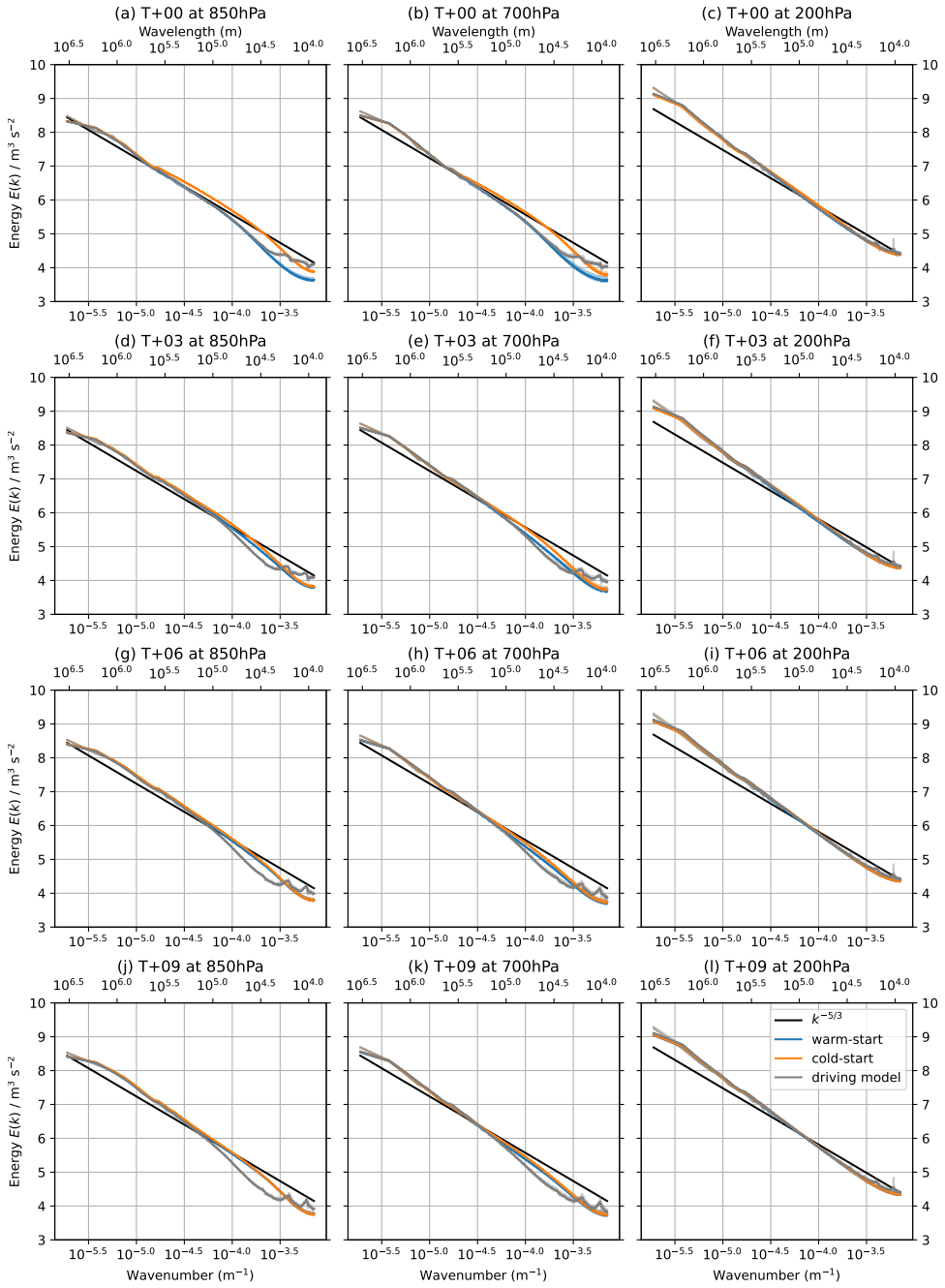

Figure 8.14: Plotted as in figure 8.7 energy density plotted against wavenumber on a log-log plot over the full three-month experiment, for the first four forecast hours (indicated by row; T+1, 4, 7, and 10 for the warm-started simulation and T+0, 3, 6, and 9 for the cold-started simulation) at three different pressure levels (indicated by column; 850 hPa, 700 hPa, and 200 hPa), for the warm-started and cold-started initialisations (orange and blue lines respectively) as well as forecasts at the same time from the closest driving global model initialisation (grey lines). The spectra are smoothed using a variable-size uniform filter along their length to limit noise (raw signals are shown in faded colours behind the lines). Reference lines showing the archetypal $E(k) \sim k^{-\frac{5}{3}}$ relationship (with arbitrary scalings to approximate observed amplitudes in the plots) are in black.

Figure 8.14 shows the spectra for the first 9–10 hours of the forecast, and they bear a strong resemblance to the spectra for the first case study (figure 8.7): at first there is a distinct lack of energy on scales below 100 km in the cold-started simulation relative to the warm-started simulation, but the gap quickly closes and the two simulations look similar by T+10 after initialisation. Again, as for the first case study, the driving model simulation has a distinct dip in energy below wavelengths of 100 km throughout due to its coarser horizontal resolution, and resonances appear due to regridding of the simulations. The difference between the regional and global simulations is reduced at 200 hPa, however, where the energy spectra appear to closely match between simulations across scales.

Examining the full length of all the 18 UTC warm- and cold-started forecasts reveals that there is a prominent diurnal pattern in the scales of energy that emerge, which is not unique to the case studies selected previously but exists across the full experiment for both initialisations and in the drving model. It appears that the injection of energy on the scale of tens of kilometres by convection at midday–early afternoon robustly develops into larger-scale kinetic structures. The pattern occurs at all heights in the atmosphere but is strongest at low–mid heights. Overnight the structures dissipate, starting with the smaller structures and then the larger ones. Since there is no further increase in smaller-scale energy before the next diurnal cycle begins, it does not appear that the larger structures routinely break down into smaller ones before dissipating; perhaps instead they weaken in intensity but do not shrink in size.

While there is a distinct difference in the evolution of kinetic energy spectra in the first 10 hours or so between the warm- and cold-started forecasts (left and right columns of figure 8.15 respectively), the effects on upscale differences are somewhat limited as, particularly at lower levels (figures 8.15c–f), the evolution of the spectra look very similar. There is a slight increase in the horizontal extent of the positive $\frac{\partial \log E_k}{\partial t}$ anomaly as it reaches the T+30 forecast hour in the warm-started simulations relative to the cold-started simulations. Nonetheless, at 200hPa the positive $\frac{\partial \log E_k}{\partial t}$ anomaly at T+21 is noticeably stronger in the warm-started simulation than the cold-started simulation. The increase in the kinetic energy in the 200 hPa spectrum at scales of approximately 100 km is consistent with the major shifts seen in the first case study of the 200 hPa wind because of the presence of large organised systems generating strong divergent upper-level wind anomalies.

While it appears that the diurnal cycle dominates the changes in the energy spectra, there

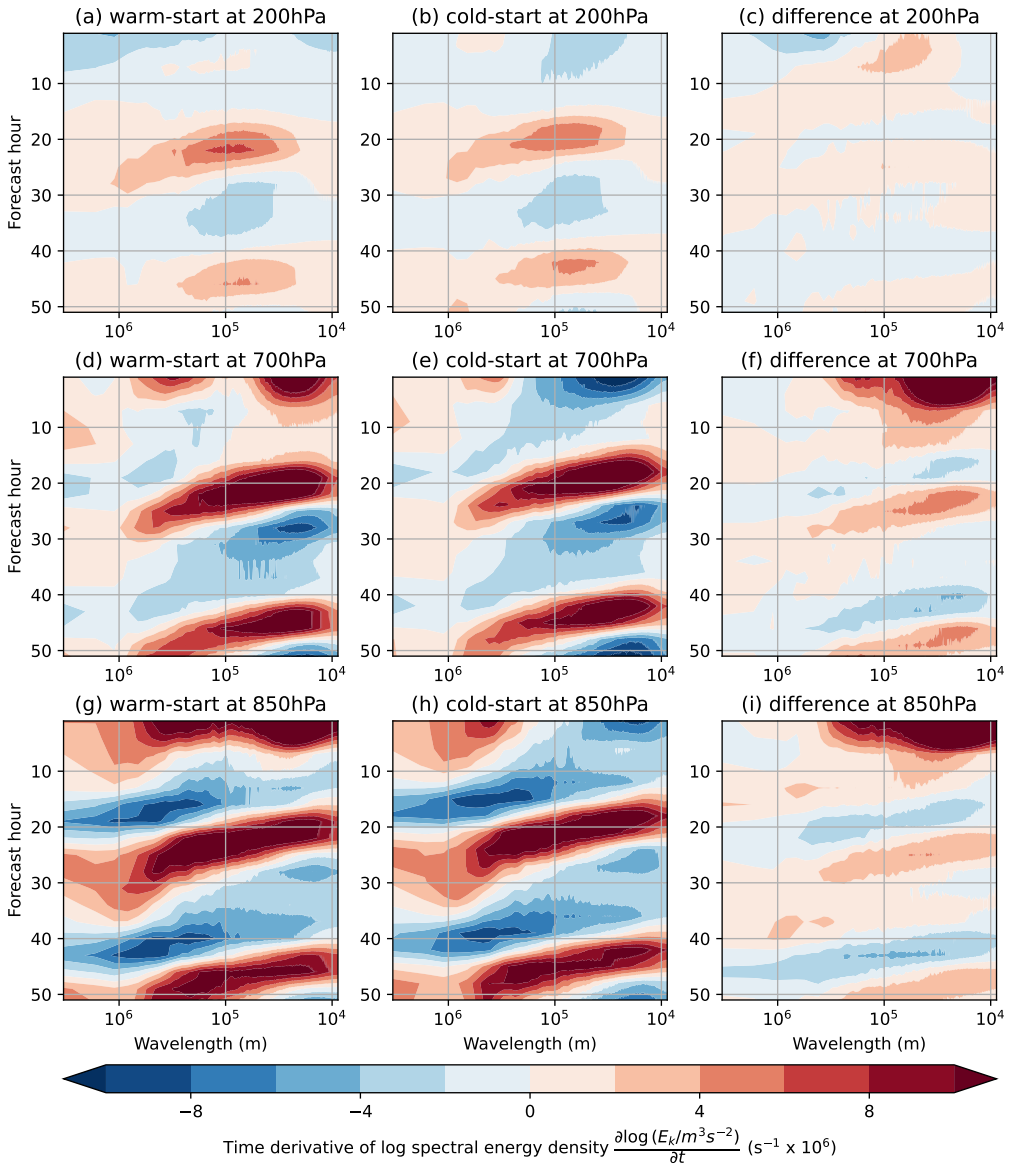

Figure 8.15: Rate of change of the logarithm of total spectral energy density across all initialisations at 18 UTC (filled contours) plotted against log(wavelength) on the x-axis and forecast hour on the y-axis for warm-started (left column) and cold-started (central column) initialisation, with the difference between the two in the right column

are noticeable differences overall between the simulations which start with and without small-scale convective structure later in the forecasts, with maximum impact in the upper levels of the atmosphere. The particular enhancement of patterns at upper levels is consistent with the findings in Warner et al. (2023), who show that there is reduced root mean square error (relative to ERA5 reanalysis) in the warm-started simulation compared to the cold-started simulation at 200 hPa even up to 48 hours into the forecast.

Further results can be established by examining the differences between the regional simulations and the driving simulation in order to determine the effects of explicit convection on the energy spectra changes over the course of a forecast. Figure 8.16 shows the differences between the warm- and cold-started simulations and the driving simulations in the two right hand columns, with the spectra for all three simulations shown as a reference. There are marked differences between the regional convective-scale simulations and driving simulations, which at low levels appear to be related to the delay in when the energy at smaller scales begins to increase in the diurnal cycle, as noted in the discussion of figure 8.8. The delay may be associated with the dry bias over West Africa in the Global Atmosphere (GA) 6.1 configuration used in the driving simulation (see chapter 3). Similarly, the lack of precipitation due to insufficient convection could explain the weaker diurnal signatures present in the 200 hPa driving model energy spectrum relative to both the warm- and cold-started simulations.

The differences between the changes in energy spectra throughout the forecasts may seem subtle, but the simulations suggest a distinct upscale energy transfer is present at lower and mid-levels in the atmosphere in regional simulations, which has implications on a case-by-case basis for synoptic-scale energy distributions. Therefore, if convection is not adequately represented, the impacts are likely to extend to at least synoptic scales, and particularly can influence atmospheric motions at upper levels.

8.4 Summary and discussion

This chapter utilises the output of an experiment testing novel initialisation techniques, designed to decrease spin-up time after initialisation, for CP NWP simulations. The upscale differences between the very similar simulations, differing only by the scales of structures existing at initialisation, are examined. From this, mechanisms through which the existence of moist convection might modulate the larger-scale differences. Results from the regional convective-

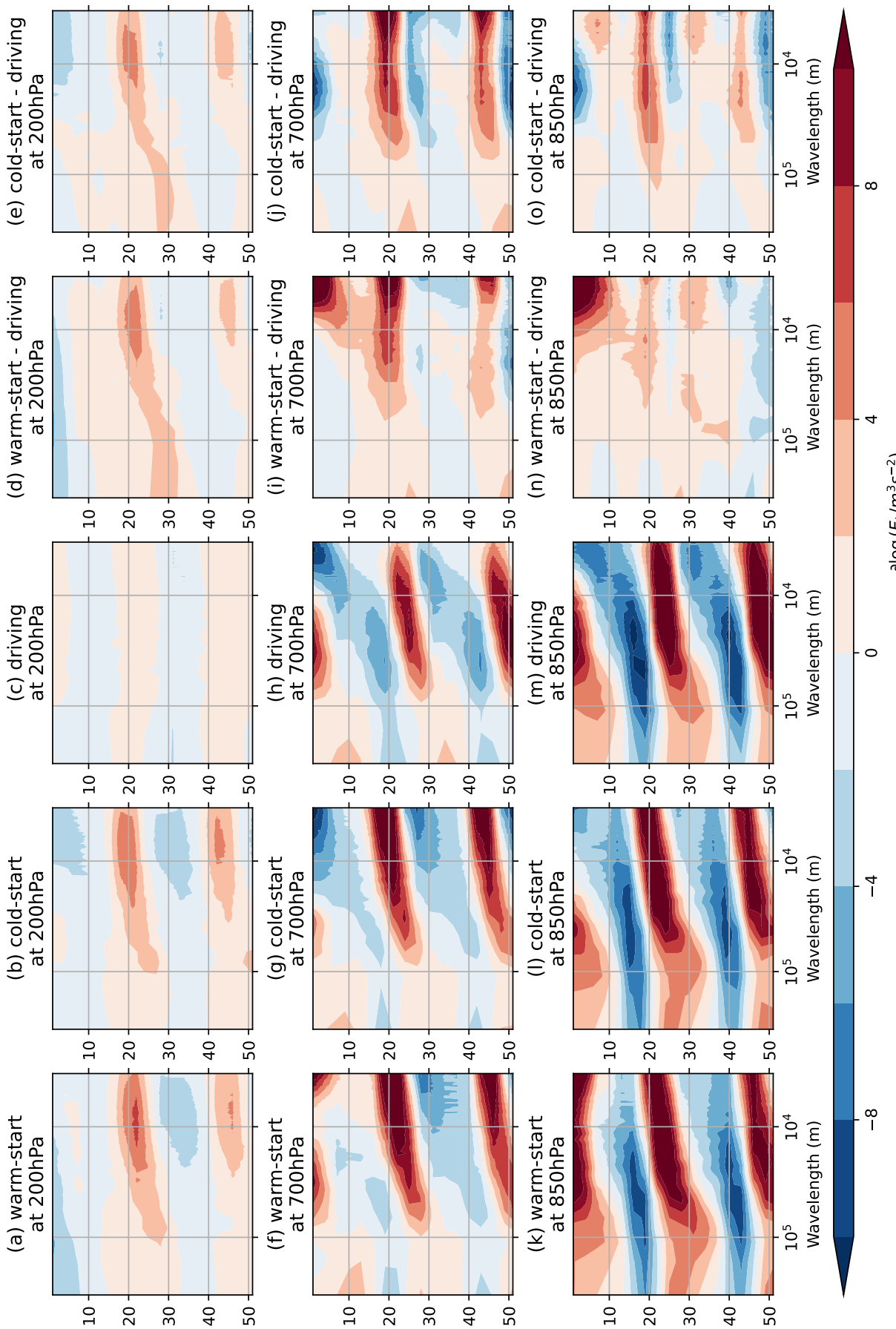

Figure 8.16: Rate of change of the logarithm of total spectral energy density across all initialisations at 18 UTC (filled contours) plotted against log(wavelength) on the x-axis and forecast hour on the y-axis for warm-started and cold-started CP simulations, driving model simulations, and the difference between the warm-started and cold-started simulations and the driving simulation (right two columns). Spectra only shown above native resolution of driving simulation ($\approx 33\,\text{km} \approx 10^{4.5}$ m).

scale simulations are contrasted with results for their driving model which uses a convection parameterisation, in order to further highlight the role of deep convection and its impacts.

Crucially, this chapter illustrates that low-level moisture transport and soil moisture patterns are mechanisms for the modulation of MCS activity through case studies, highlighting the importance of accurately observing, assimilating, and forecasting soil moisture patterns and low-level moisture anomalies. The selected case studies were chosen due to having some of the most different precipitation conditions at the start of their initialisations. However, the processes that they represent (effects of soil moisture and low-level moisture) are reflected by dynamics which are present throughout the simulations and indeed in other simulations (see chapter 7). Since variation in soil moisture patterns is more pronounced during the early days of boreal summer, it is more challenging to forecast MCSs since the soil and low-level moisture feedbacks will be more variable. (The early monsoon season, where onset occurs, is also the time period when forecasting MCS activity is most important for agricultural purposes, as it affects choices of crop planting dates.) Single systems can modulate the conditions that lead to suppression (where the ground has been moistened by precipitation, or where low-level moisture has been converted into precipitation by a storm) or stimulation (on wet-dry boundaries, or drier patches of land) of MCS initiation and intensification over the following days. As a result, accurately representing the feedbacks of MCSs is likely to be important for prediction of monsoon onset on subseasonal scales; where MCSs and their initiations are represented less accurately (such as in parameterised simulation), storms may be forecasted to form in what are actually unrealistic conditions, leading to incorrect onset predictions.

The chapter also supports conventional understanding that interactions with MCSs and their effects on the local area can lead to the intensification of AEWs. An example of AEW-convection interaction can be seen in Case Study 1 where a positive curvature vorticity anomaly, which exists across the northern and southern AEW track regions at the start of both forecasts, dissipates in the cold-started simulation but strengthens and propagates in the warm-start simulation. By contrast, a second case where organised convection is similar between the two initialisations shows similar AEW signatures. The cases highlight how differences in mesoscale features can result in very different synoptic-scale patterns, which emphasises the role of upscale energy transfer in driving AEWs.

It also shown in this chapter that there is a diurnal upscale transfer of energy as convective activ-

ity injects smaller-scale energy into the atmosphere during the day, which then propagates into larger-scale energetic features overnight. Such an illustration evidences the benefit of the use of convection-permitting simulations, since the results indicate that the presence of mesoscale convection drives the upscale growth of energetic structures in the atmosphere up to scales of thousands of kilometres and potentially beyond. The differences in the energy spectra, alongside further analysis of the differences between the simulations, also underlines the fact that the representation of convection has a strong impact on circulation in the upper troposphere, which can in turn drive weather systems, which strongly suggests that there are circulation-convection feedbacks and scale interactions. Evidence is presented to suggest that CP simulations represent the upscale impacts of convection, particularly at upper levels, differently to GCMs with convection parameterisations.

Future work could involve running suites of idealised simulations with prescribed soil moisture or low-level atmospheric moisture patterns to investigate whether it is the soil moisture or the low-level moisture which plays a more significant role in the generation of different convective structures. Furthermore, the original experiment did not include a spatial filtering of soil moisture patterns prescribed by the previous run of the regional model (see chapter 3), as it had not yet become clear what a crucial element soil moisture played in convective feedbacks. Including soil moisture in the spatial filtering in the warm-started initialisation may contribute to improving spin-up time in such simulations.

Finally, analysis in this chapter is limited to the use of a regional CP simulation to calculate energy spectra, so the results cannot clearly show an upper limit of the scales where upscale energy transfer can be linked to convective activity. Exploring similar diagnostics to those presented in this chapter would be of great interest to examine whether the upscale propagation of energy extends even further than the limited domain analysed in this chapter can show. As larger CP simulations become available in the coming years, these methods could be applied to them.

Chapter 9

Discussion and Conclusions

Organised convection is a key element of tropical West African climate. Variation in frequency of mesoscale convective systems (MCSs) is a major factor in the interannual variability of the region's precipitation. Not only are MCSs high-impact weather (HIW) events, but their self-sustaining circulations act to modulate the synoptic-scale atmospheric motions in their vicinity, which in turn modulate the intensity and formation likelihood of MCSs, resulting in feedbacks between mesoscale convection and synoptic-scale circulations.

Since numerical weather prediction (NWP) models struggle to represent mesoscale convection using convection parameterisations, researchers have turned to using higher-resolution models which have sufficient resolution to explicitly resolve some dynamics of mesoscale convection, leading to more realistic simulations of convective systems and their effects on the environment. While many research institutions are dedicating vast proportions of their computational resources to running large-domain and even global-scale convection-permitting (CP) models, there is some debate as to whether the extensive carbon cost of running such models can be justified, especially since CP models still have noticeable biases. Downloading data and running simulations has computational (and therefore carbon) cost, which can be reduced by running it at lower spatial resolution or using parameterisations. While CP models may demonstrate some improvements, it is virtually impossible to generate a perfect model, which can represent all processes explicitly: there will always be a 'grey zone' where some processes are unresolved. It is therefore crucial that the value of convective-scale models for climate and NWP modelling is critically evaluated. The work in this thesis suggests that CP models are indeed a useful tool to diagnose the impacts of mesoscale convection on synoptic-scale circulation, and can rep-

resent upscale effects that the current generation of deep convection parameterisations cannot replicate.

The purpose of this thesis was to improve contemporary understanding of the scale interactions between organised convection and synoptic circulation in West Africa. More specifically, the questions asked at the start of the thesis were:

1. How can the modulation of synoptic-scale atmospheric dynamics by organised mesoscale convection be measured?
2. How does organised convection in West Africa modulate synoptic-scale dynamics both locally (e.g. AEJ, AEWs, monsoon wind) and downstream into the Atlantic Ocean (e.g. modulating tropical cyclogenesis)?
3. Which environmental conditions, on the mesoscale and on larger scales, affect the initiation and development of MCSs in West Africa?
4. How do MCSs in West Africa interact with each other across temporal and spatial scales?

In this chapter, the extent to which the thesis has addressed the above questions will be evaluated in turn. Afterwards, a synthesis of the key findings of the thesis will be provided, followed by suggestions for work which could build on the results of this thesis in the future.

9.1 Answering the Research Questions

The subject of the first research question is the use of various methods for measuring the perturbation of synoptic-scale dynamics by organised mesoscale convection. Throughout the thesis, several methods are utilised to examine the impacts of mesoscale convection on larger-scale dynamics, including compositing around precipitating features (chapter 5) and storm initiations and dissipations (chapter 7) to understand their impacts on the surroundings, and Fourier analysis of the energy spectra in the region over diurnal cycles (chapter 8). The use of the kinetic energy spectrum to analyse the scales of atmospheric motions is not uncommon in contemporary literature, but its evolution over forecasts as they spin up, and with respect to the diurnal cycle, has not been explored in such detail and provides some insight into how mesoscale convection interacts with larger-scale features on a diurnal basis.

Another method examined is the use of the scale-separated circulation budget, explored in

chapters 4 and 5. The circulation budget is a form of the vorticity equation, integrated over a pressure surface, which separates contributions to circulation tendency into contributions from vorticity accumulation (vortex stretching, and horizontal advection of vorticity), vortex tilting (the tilting of horizontal vorticity into the vertical through vertical winds), and frictional effects, described in Haynes and McIntyre (1987).

In chapter 4, the closure (how closely two sides of the equation match) of the circulation budget is evaluated for a high-resolution CP model over Southeast Asia for a range of temporal model output intervals and interpolated grid spacings. The model was selected for its high-resolution time output interval of 5 minutes, and at this output interval the closure is reasonably accurate. The closure remains reasonably accurate up to output intervals of 30 minutes. The reason the closure is explored is because in many model outputs, values that can be used to calculate the frictional contribution directly are not present and as a result, some might assume that the residual between the circulation tendency (a time derivative of the circulation) and the other directly-calculated circulation budget terms can be taken as equivalent to the absent frictional term. However, at time resolutions of 1 hour or greater, doing so would lead to largely inaccurate estimates of the frictional contribution to the circulation budget. Furthermore, when regridding fine grid resolutions to coarser horizontal scales, the closure worsens, perhaps due to a loss of information associated with the resampling to lower resolutions. Closure is consistently worsened also by convective activity or small-scale variations on the borders of the enclosing region.

Nonetheless, the chapter concludes that the calculation of individual budget terms can still be meaningful when output at larger time output intervals, because their values are instantaneous. Since at high time resolutions, the budget terms very closely match the circulation tendency, particularly when on the native grid of a simulation, the chapter indicates that the calculations of the terms are accurate in the context of the model. Care should be taken when regridding simulations to coarser horizontal grids, however, since doing so introduces substantial deviations from the values of circulation budget terms calculated on their native grid. Chapter 4 acts as the first published evaluation of the accuracy of the closure of the circulation budget, and its variation with differences spatial and temporal resolution.

In chapter 5, the circulation budget method evaluated by chapter 4 is utilised to measure the effects of mesoscale features on synoptic-scale circulation. The circulation budget terms are split

into mean and anomalous components over a diurnal cycle. Calculating the circulation tendency around a synoptic-scale region over land in West Africa allows for an interrogation of the diurnal monsoon processes, and by comparing the fields of circulation budget term integrands around precipitating convection to the synoptic-scale values, the analysis estimates which contributions were associated with convective processes. The fact that chapter 5 was able to draw conclusions from the circulation budget method provides a reasonable argument for its utility in diagnosing mesoscale contributions to synoptic-scale circulation. The circulation budget has not been applied before in West Africa, and has typically only been applied in cases of TC genesis (see Raymond et al. 2014) or for MCVs (Evans et al. 2014) rather than for synoptic-scale atmospheric motions.

The conclusions of chapter 5 provide some insight into the local modulation of synoptic-scale dynamics by organised convection, which contributes to answering the second research question. Ultimately, the convergence profiles that are required by convective updraughts - low-level convergence to feed the updraught and upper-level divergence as it reaches the tropopause - dominate the effect of mesoscale convection on the circulation budget. The effect manifests as a diurnal mean tendency (as opposed to an anomalous tendency) in the circulation budget due to the strong diurnal cycle of convection. There is also a smaller contribution from the tilting term of precipitating convection, which is a result of the convective momentum transport associated with updraughts, theoretically described by Moncrieff (1992). The analysis also reveals some key differences between the representation of convection in CP simulations compared to simulations with parameterisations: parameterised simulations fail to capture the convective momentum transport in mesoscale convection that contributes to the tilting term in the circulation budget.

While chapter 5 explores the effects of convection in a fixed box across the domain, its outcomes can be applied to how organised convection might modulate other pertinent circulations in the region such as African Easterly Waves (AEWs). For a storm contained within an AEW's cyclonic circulation (an AEW trough), the vorticity accumulation that results from the low-level convergence in precipitating convection can serve to strengthen and intensify the AEW's vorticity signature. When storms are on the western edge of such a circulation, the effects of vortex tilting also reinforce circulation, which is consistent with literature that identifies strong AEWs as having organised convective systems not only within but to the leading edge of the wave trough (Semunegus et al. 2017).

Chapter 8 also shows how the existence of organised convection modulates AEWs by comparing NWP simulations with two different initialisation techniques: one initialised from a lower-resolution global reanalysis ('cold-start'), and another blended with information from a previous run of the high-resolution convective-scale forecast ('warm-start'), described in Warner et al. (2023). The results in the chapter are based on a very novel technique and it is the first time that warm-starting or scale-blending techniques have been used to to diagnose convective feedbacks, rather than simply to improve forecasting by metric of comparison to observations and reanalysis.

The chapter examines two case studies, the first of which is initialised on 17 June 2020 at 18 UTC. In the 17 June case study, an MCS develops in the warm-started simulation which is not present in the cold-started simulation. Meanwhile, a low-magnitude positive curvature vorticity signal in the northern AEW track, present at the start of both simulations, is amplified considerably in the warm-started simulation whereas it dissipates in the cold-started simulation. The MCS appears to have amplified the weak AEW signature in the early hours of the warm-started forecast, allowing the AEW to strengthen and propagate, whereas the absence of an MCS in the cold-started simulation led to its dissipation. Meanwhile, where precipitation signatures are very similar in the second case study (7 August initialisation), the AEW signatures were also similar. Taken together, the results indicate that differences in the distribution and intensity of organised mesoscale convection leads to discernible differences between AEW tracks and intensities. In particular, the lack of AEW signature in the 17 June cold-start simulation in chapter 8 is a clear and novel example of the direct role that organised convection plays in intensifying AEWs, as suggested by such works as Hsieh and Cook (2005). Chapter 8 also illustrates the strong impacts at upper levels in the atmosphere associated with the existence of MCSs generating divergent circulations, indicating that one of the key mechanisms for convective impact on synoptic-scale circulations is through modulating upper-level winds.

The second research question also asks about the to downscale impacts of organised mesoscale convection. Chapter 6 addresses the question by examining the vortex populations associated with mesoscale precipitation in a CP and parameterised simulation, and their potential to undergo tropical cyclogenesis downstream. The CP model has more frequent and more intense vortices than its parameterised counterpart, but the difference could be a result of overestimation of oceanic convection due to the lack of ocean-atmosphere coupling in the simulation leading to

a wet bias over the ocean (Kendon et al. 2019). However, a larger proportion of the population of vortices over the ocean in CP4 have positive warm-core metrics at both upper and lower levels compared to R25, suggesting that a higher fraction of the vortices that exist over the ocean could be candidates for cyclogenesis. This chapter is among the first work done to explore the earliest stages of tropical cyclogenesis through statistics of longer-term CP simulations, and its results hints at potential for CP models to add value to the simulation of tropical cyclogenesis. Understanding the early stages of TC initiation could help explain why there is a tendency towards a greater frequency of TCs in trials of global CP simulations (e.g. Judt et al. 2021).

Furthermore, in chapter 7, composites around dissipations of the centroids of tracks of identified MCSs suggest that remnants of vortices characteristic of a mature MCS structure continue to exist and propagate even after the storms have dissipated for at least 6 hours. The phenomenon is observed in both CP and parameterised simulations, but since CP models have far more intense vortex signatures in MCS structures, their remnant vortices may be more persistent and have greater downstream impacts. Such mesoscale convective vortices (MCVs) may be a source for reinitiation of MCSs, since in composites of the environments preceding spontaneous MCS initiation, signatures of midlevel vortices exist. Therefore a further downstream effect of organised convection is potentially the further reinitiation of organised convective systems by persistent MCVs, which has been observed in the midlatitudes (e.g. Schumacher and Johnson 2008), but has yet to be explored in the tropics.

Chapter 7 also provides conclusions that are relevant to the third research question, which asks what environmental conditions affect the initiation and development of MCSs. The CP model reveals that, in some cases, a vortex is present before MCS initiation, which may help to generate updraughts. Other characteristics of the pre-MCS environment are in the soil moisture, where dry patches of soil seem to be associated with MCS initiation, consistent with observations in the literature (Klein and Taylor 2020), and low-level atmospheric moisture is consistently enhanced in regions of MCS initiation. Chapter 8 also highlights low-level atmospheric moisture and soil moisture gradients as a key element of MCS initiation environments in discussing the feedbacks of existing MCSs on the generation of future MCSs, which leads into the fourth research question, examining the spatiotemporal interactions between MCSs.

To examine feedbacks between existing MCSs and MCS initiation downstream, chapter 7 reveals that there is some structure in the locations of MCSs that pass by the tracks of existing

storms through comparing composites of various fields around MCS initiations to composites around random points taken at the same time. It appears that an MCS is less likely to form if another system's track has propagated through a region in the previous 24 hours. The finding is consistent with observational literature that MCSs tend intensify over drier land surfaces (Klein and Taylor 2020), which are unlikely to have been rained on in the past day. Furthermore, since the chapter shows that MCSs generally lift moisture upwards over their lifetime, they remove low-level moisture which is also shown to be a crucial element for MCS initiation. The combination of low-level moisture and soil moisture feedbacks ultimately implies a negative feedback, on the timescale of a day, between MCSs occurring over the same tracks. Chapter 7 is one of the first chapters to utilise composites around the dissipations of MCSs to understand how they modulate the atmosphere around them.

Chapter 8 provides further evidence for soil moisture and low-level atmospheric moisture feedbacks through comparing the T+24–T+48 forecast hours of the case studies. Earlier in the monsoon season in the 17 June case study, the MCS which exists in the warm-started but not the cold-started simulation creates a noticeable soil moisture anomaly, over which later systems weaken and dissipate, whereas in the cold-started simulation a strong system develops over the dry soil which has not been rained on by the first system. However, in the second case study, initialised at 18 UTC on 7 August 2020, the monsoon season has progressed. The impact of rainfall on soil moisture gradients is reduced due to climatologically higher soil moisture over the entire region, and as a result, similar convection evolves later in the forecasts for both the cold- and warm-started simulations, despite very different convective conditions at initialisation.

9.2 Summary of Key Results and Implications

Throughout the thesis, conclusions have sought to provide answers to the four research questions stated above, and overall have made steps towards addressing them. Resolving these questions provides convincing evidence for the value of accurately representing the dynamics of mesoscale convection in simulations, thus justifying further research using high-resolution convective-scale simulations. The work also suggests some viable metrics for the evaluation of upscale effects of mesoscale convection, and recommendations for improvements to deep convection parameterisations. It also reinforces existing understanding of the interactions between organised convection and AEWs from a dynamical perspective, and MCS feedbacks through low-level atmospheric

and soil moisture.

The circulation budget is shown to be a viable method for assessing the effect of different processes on changes to circulation tendency, and chapter 4 also provides recommendations for when its usage is most appropriate; for example, its closure is good enough to estimate frictional contributions from residuals at models with high resolution output time intervals of 30 minutes or below, but for one hour intervals or greater, the estimates are likely to be inaccurate. However, instantaneous circulation budget terms are valid for use to diagnose the effects that different processes have on circulation tendency even if the budget does not close accurately. The recommendations here may be helpful in future work exploring the effects of organised convection on synoptic-scale circulation.

Chapter 5 and chapter 8 support prior evidence that MCSs reinforce and intensify AEW signatures, which serves to further underline the importance of representing the effects of moist convection on synoptic-scale circulation. Chapter 5 also illustrates key differences between CP and parameterised simulations in terms of mesoscale convective dynamics, highlighting the relevance of convective momentum transport for inclusion in organised convective parameterisations.

From chapters 7 and 8, there is strong evidence that soil moisture is a key feedback for MCS initiation, with distinct anomalies associated with their initiation in CP simulations, further highlighting an advantage in representation of convection in CP simulations compared to those with deep convection parameterisations. The importance of soil moisture motivates the further development of land-surface and hydrology models to accurately replicate real behaviour of soil moisture patterns in the region. Work in chapter 8 also implies that soil moisture feedbacks are of particular importance for MCS prediction in the early weeks of boreal summer, before and during monsoon onset, which means that it could be of significance for predicting the monsoon onset.

Finally, chapter 8 provides insight into the upscale impacts of moist convection, illustrating that its most noticeable impacts are felt in the upper troposphere. Chapter 8 also reveals a diurnal cycle in kinetic energy spectra. The kinetic energy spectrum in the model has a strong diurnal variation, with mesoscale perturbations increasing the energy spectra on the order of tens of kilometres during the early to mid-afternoon of each day, and increases in energy at larger scales as the day progresses, with the smaller-scale energy decreasing in amplitude as diurnal convection ceases in the late evening. During the first 9–12 hours of the cold-started simulation,

where there is little to no small-scale precipitation, there is a negative anomaly of small-scale kinetic energy relative to the warm-started simulation. Later in the case study forecasts, there are distinct differences not only at small scales in the energy spectra, but also at large scales in the warm- and cold-started simulations, and also differences compared to the driving global model which has parameterised convection. Taken together, the differences in energy spectra across the scales and forecast times imply the existence of an upscale energy cascade driven by injection of energy into the atmosphere through mesoscale convection in the afternoon, strongly suggesting that mesoscale convection directly modulates synoptic-scale structures.

9.3 Limitations and Future Outlook

While meaningful suggestions for the evaluation of convective impacts, as well as implications that convective-scale forcing can noticeably impact synoptic and even larger-scale circulations, have been provided by this thesis, almost all of its studies have used output from models on regional domains, forced by lower-resolution global models with one-way nesting. To fully understand the impacts of mesoscale convection on larger scales, it would be of great benefit to apply some of the techniques tested in this thesis to CP simulations on larger regional domains, or even on global CP simulations. In the current research climate, significant efforts are being put towards running large-domain or global CP simulations, with lengthy timescales, and as a result, in the near future more datasets of CP simulations will be available and require examination to evaluate their quality and the value they add to short- and long-term forecasts. Many of the techniques applied in this thesis could be applied to these datasets to more robustly diagnose the impact of resolving mesoscale convection, such as the circulation budget analysis or the time derivatives of the global kinetic energy spectra over a diurnal cycle. Applying these analysis techniques can serve as further justification as to whether it is worth continuing to run such high-resolution large-domain simulations.

The analysis in chapter 6 could particularly be developed by having access to larger domains which cover both tropical Africa and the Atlantic Ocean, through to the Caribbean and North America so that TCs could be tracked over their full lifetimes, from their initiation as AEWs or MCSs in West Africa to their landfall in the Americas. The statistical influence of vortex populations over land in West Africa could then be linked to the eventual TC population within the season, and the thermodynamic development of vortices over their lifetimes could be

explored in more detail. Investigation of tropical cyclogenesis in high-resolution simulations will also benefit from the integration of atmosphere-ocean coupling into CP models, which will reduce wet biases and allow for more realistic simulation of oceanic convection. New simulations will be quick to emerge in the coming months and years, and rapid developments in understanding the downstream impacts of mesoscale convection in the context of tropical cyclogenesis could follow, perhaps using the metrics and tools trialled in chapter 6.

The thesis has also highlighted the importance of soil and low-level atmospheric moisture for the feedbacks of convective systems, particularly in the early monsoon season. Future work on monsoon onset prediction should carefully consider the effects of soil moisture feedbacks at the start of the season. The results in the thesis also motivate further work to develop accurate hydrological land surface models which should be included in any simulations which aim to accurately represent organised convective systems on either NWP or climate timescales.

While this thesis has largely taken CP simulations as something of a 'truth', and indeed has shown that they improve on the representation of mesoscale convective dynamics relative to simulations with deep convection parameterisations, CP models still have biases and flaws, and still require significant development. In recent years there have been more field campaigns taking measurements over or near West Africa (e.g. the 'Convective Processes Experiment Cabo Verde' CPEX-CV field campaign, described in Nowottnick et al. 2023), and plans exist for more sophisticated remote observations that can quantify convective updraughts and momentum transport (such as the 'Investigation into Convective Updrafts' INCUS mission; see Prasanth et al. 2023). Such observations could be used to constrain CP simulations with unprecedented high-resolution measurements, working to resolve CP model biases or validate the simulated values of convective momentum transport in MCSs over West Africa.

In addition, chapter 8's evaluation of the results of the warm-starting experiment not only reinforces the value of the warm-starting technique for initialising simulations but also provides some explanation as to why it is so effective. It would be of great interest to reproduce the warm-starting technique over more regions, such as South America or South East Asia, to see whether the benefits of the technique apply in other locations and, if so, whether the feedback mechanisms are similar.

In summary, the field of convective-scale modelling is a rapidly-growing area of meteorological research with vast potential for improving the representation of synoptic- and even planetary-

scale features through their scale interactions with mesoscale convection. In the coming years, high-resolution convective-scale modelling is likely to dominate computational resource in meteorological and climate science research, and the work done in this thesis motivates such developments. This thesis has demonstrated, through a range of techniques, the value of CP models for exploring scale interactions between convection and tropical circulation. Novel applications of techniques for analysing high-resolution simulations have been outlined, as well as some results highlighting key feedbacks of organised convection on itself in West Africa. Ultimately, the work highlights the importance of mesoscale convective dynamics in the context of accurately representing motions across scales in the tropical atmosphere.

References

Alfaro, D. A. 2017. Low-Tropospheric Shear in the Structure of Squall Lines: Impacts on Latent Heating under Layer-Lifting Ascent. *Journal of the Atmospheric Sciences* **74**(1), pp. 229–248.

Arakawa, A. and V. R. Lamb. 1977. Computational Design of the Basic Dynamical Processes of the UCLA General Circulation Model. *Methods in Computational Physics: Advances in Research and Applications*. **17**. Elsevier, pp. 173–265.

Ashley, W. S., A. M. Haberlie, and J. Strohm. 2019. A Climatology of Quasi-Linear Convective Systems and Their Hazards in the United States. *Weather and Forecasting* **34**(6), pp. 1605–1631.

Badlan, R. L., T. P. Lane, M. W. Moncrieff, and C. Jakob. 2017. Insights into convective momentum transport and its parametrization from idealized simulations of organized convection. *Quarterly Journal of the Royal Meteorological Society* **143**(708), pp. 2687–2702.

Baidu, M., J. Schwendike, J. H. Marsham, and C. Bain. 2022. Effects of vertical wind shear on intensities of mesoscale convective systems over West and Central Africa. *Atmospheric Science Letters* **23**(8).

Bain, C. L., K. D. Williams, S. F. Milton, and J. T. Heming. 2014. Objective tracking of African Easterly Waves in Met Office models: Objective Tracking of African Easterly Waves. *Quarterly Journal of the Royal Meteorological Society* **140**(678), pp. 47–57.

Barrett, A. I., C. Wellmann, A. Seifert, C. Hoose, B. Vogel, and M. Kunz. 2019. One Step at a Time: How Model Time Step Significantly Affects Convection-Permitting Simulations. *Journal of Advances in Modeling Earth Systems* **11**(3), pp. 641–658.

Bartels, D. L. and R. A. Maddox. 1991. Midlevel Cyclonic Vortices Generated by Mesoseale Convective Systems. *Monthly Weather Review* **119**(1), pp. 104–118.

Bauer, P., A. Thorpe, and G. Brunet. 2015. The quiet revolution of numerical weather prediction. *Nature* **525**(7567), pp. 47–55.

Bechtold, P. 2019. Challenges in Tropical Numerical Weather Prediction at ECMWF. *Current Trends in the Representation of Physical Processes in Weather and Climate Models*. Ed. by D. A. Randall, J. Srinivasan, R. S. Nanjundiah, and P. Mukhopadhyay. Springer Singapore, pp. 29–50.

Berry, G. J. and C. Thorncroft. 2005. Case Study of an Intense African Easterly Wave. *Monthly Weather Review* **133**(4), pp. 752–766.

Berry, G. J. and C. D. Thorncroft. 2012. African Easterly Wave Dynamics in a Mesoscale Numerical Model: The Upscale Role of Convection. *Journal of the Atmospheric Sciences* **69**(4), pp. 1267–1283.

Berthou, S., D. P. Rowell, E. J. Kendon, M. J. Roberts, R. A. Stratton, J. A. Crook, and C. Wilcox. 2019. Improved climatological precipitation characteristics over West Africa at convection-permitting scales. *Climate Dynamics* **53**(3-4), pp. 1991–2011.

Best, M. J., M. Pryor, D. B. Clark, G. G. Rooney, R. . H. Essery, C. B. Ménard, J. M. Edwards, M. A. Hendry, A. Porson, N. Gedney, L. M. Mercado, S. Sitch, E. Blyth, O. Boucher, P. M. Cox, C. S. B. Grimmond, and R. J. Harding. 2011. The Joint UK Land Environment Simulator (JULES), model description – Part 1: Energy and water fluxes. *Geoscientific Model Development* **4**(3), pp. 677–699.

Bickle, M., J. H. Marsham, S. D. Griffiths, A. N. Ross, and J. Crook. 2022. The Influence of the Diurnal Cycle in Wind Shear and Thermodynamics on Squall Lines in the West African Monsoon. *Journal of the Atmospheric Sciences* **79**(8), pp. 2125–2143.

Birch, C. E., D. J. Parker, A. O'Leary, J. H. Marsham, C. M. Taylor, P. P. Harris, and G. M. S. Lister. 2013. Impact of soil moisture and convectively generated waves on the initiation of a West African mesoscale convective system: Impact of Soil Moisture and Waves on MCS Initiation. *Quarterly Journal of the Royal Meteorological Society* **139**(676), pp. 1712–1730.

Birch, C. E., J. H. Marsham, D. J. Parker, and C. M. Taylor. 2014a. The scale dependence and structure of convergence fields preceding the initiation of deep convection. *Geophysical Research Letters* **41**(13), pp. 4769–4776.

Birch, C. E., D. J. Parker, J. H. Marsham, D. Copsey, and L. Garcia-Carreras. 2014b. A seamless assessment of the role of convection in the water cycle of the West African Monsoon. *Journal of Geophysical Research: Atmospheres* **119**(6), pp. 2890–2912.

Birch, C. E., M. J. Roberts, L. Garcia-Carreras, D. Ackerley, M. J. Reeder, A. P. Lock, and R. Schiemann. 2015. Sea-Breeze Dynamics and Convection Initiation: The Influence of Con-

vective Parameterization in Weather and Climate Model Biases. *Journal of Climate* **28**(20), pp. 8093–8108.

Bishop, C. H., B. J. Etherton, and S. J. Majumdar. 2001. Adaptive Sampling with the Ensemble Transform Kalman Filter. Part I: Theoretical Aspects. *Monthly Weather Review* **129**(3), pp. 420–436.

Bloom, S. C., L. L. Takacs, A. M. Da Silva, and D. Ledvina. 1996. Data Assimilation Using Incremental Analysis Updates. *Monthly Weather Review* **124**(6), pp. 1256–1271.

Blunden, J. and T. Boyer. 2021. State of the Climate in 2020. *Bulletin of the American Meteorological Society* **102**(8), S1–S475.

Böing, S. J., H. J. J. Jonker, A. P. Siebesma, and W. W. Grabowski. 2012. Influence of the Subcloud Layer on the Development of a Deep Convective Ensemble. *Journal of the Atmospheric Sciences* **69**(9), pp. 2682–2698.

Bony, S., B. Stevens, D. M. W. Frierson, C. Jakob, M. Kageyama, R. Pincus, T. G. Shepherd, S. C. Sherwood, A. P. Siebesma, A. H. Sobel, M. Watanabe, and M. J. Webb. 2015. Clouds, circulation and climate sensitivity. *Nature Geoscience* **8**(4), pp. 261–268.

Boutle, I. A., J. E. J. Eyre, and A. P. Lock. 2014. Seamless Stratocumulus Simulation across the Turbulent Gray Zone. *Monthly Weather Review* **142**(4), pp. 1655–1668.

Bowler, N. E., A. Arribas, K. R. Mylne, K. B. Robertson, and S. E. Beare. 2008. The MOGREPS short-range ensemble prediction system. *Quarterly Journal of the Royal Meteorological Society* **134**(632), pp. 703–722.

Brannan, A. L. and E. R. Martin. 2019. Future characteristics of African Easterly Wave tracks. *Climate Dynamics* **52**(9-10), pp. 5567–5584.

Brown, A., S. Milton, M. Cullen, B. Golding, J. Mitchell, and A. Shelly. 2012. Unified Modeling and Prediction of Weather and Climate: A 25-Year Journey. *Bulletin of the American Meteorological Society* **93**(12), pp. 1865–1877.

Bush, M., T. Allen, C. Bain, I. Boutle, J. Edwards, A. Finnenkoetter, C. Franklin, K. Hanley, H. Lean, A. Lock, J. Manners, M. Mittermaier, C. Morcrette, R. North, J. Petch, C. Short, S. Vosper, D. Walters, S. Webster, M. Weeks, J. Wilkinson, N. Wood, and M. Zerroukat. 2020. The first Met Office Unified Model–JULES Regional Atmosphere and Land configuration, RAL1. *Geoscientific Model Development* **13**(4), pp. 1999–2029.

Bush, M., I. Boutle, J. Edwards, A. Finnenkoetter, C. Franklin, K. Hanley, A. Jayakumar, H. Lewis, A. Lock, M. Mittermaier, S. Mohandas, R. North, A. Porson, B. Roux, S. Webster,

and M. Weeks. 2023. The second Met Office Unified Model–JULES Regional Atmosphere and Land configuration, RAL2. *Geoscientific Model Development* **16**(6), pp. 1713–1734.

Cangialosi, J. P., E. Blake, M. DeMaria, A. Penny, A. Latto, E. Rappaport, and V. Tallapragada. 2020. Recent Progress in Tropical Cyclone Intensity Forecasting at the National Hurricane Center. *Weather and Forecasting* **35**(5), pp. 1913–1922.

Chagnon, J. M. and S. L. Gray. 2009. Horizontal potential vorticity dipoles on the convective storm scale. *Quarterly Journal of the Royal Meteorological Society* **135**(643), pp. 1392–1408.

Chalon, J. P., G. Jaubert, J. P. Lafore, and F. Roux. 1988. The West African Squall Line Observed on 23 June 1981 during COPT 81: Mesoscale Structure and Transports. *Journal of the Atmospheric Sciences* **45**(19), pp. 2744–2763.

Charney, J. G. and N. A. Phillips. 1953. Numerical Integration of the Quasi-Geostrophic Equations for Barotropic and Simple Baroclinic Flows. *Journal of Meteorology* **10**(2), pp. 71–99.

Cheng, Y.-M., J. Dias, G. Kiladis, Z. Feng, and L. R. Leung. 2023. Mesoscale Convective Systems Modulated by Convectively Coupled Equatorial Waves. *Geophysical Research Letters* **50**(10), e2023GL103335.

Chong, M., P. Amayenc, G. Scialom, and J. Testud. 1987. A Tropical Squall Line Observed during the COPT 81 Experiment in West Africa. Part 1: Kinematic Structure Inferred from Dual-Doppler Radar Data. *Monthly Weather Review* **115**(3), pp. 670–694.

Christensen, H. M. and O. G. A. Driver. 2021. The Fractal Nature of Clouds in Global Storm-Resolving Models. *Geophysical Research Letters* **48**(23).

Clark, D. B., L. M. Mercado, S. Sitch, C. D. Jones, N. Gedney, M. J. Best, M. Pryor, G. G. Rooney, R. L. H. Essery, E. Blyth, O. Boucher, R. J. Harding, C. Huntingford, and P. M. Cox. 2011. The Joint UK Land Environment Simulator (JULES), model description – Part 2: Carbon fluxes and vegetation dynamics. *Geoscientific Model Development* **4**(3), pp. 701–722.

Cornforth, R., Z. Mumba, D. J. Parker, G. Berry, N. Chapelon, K. Diakaria, M. Diop-Kane, V. Ermert, A. H. Fink, P. Knippertz, J. P. Lafore, A. Laing, S. Lepape, R. Maidment, J. Methven, B. Orji, D. Osika, E. Poan, R. Roca, S. Rowell, R. Smith, T. Spengler, C. M. Taylor, C. Thorncroft, J.-C. Vincendon, C. Yorke, and C. Thorncroft. 2017. Synoptic Systems. *Meteorology of Tropical West Africa*. Ed. by D. J. Parker and M. Diop-Kane. Chichester, UK: John Wiley & Sons, Ltd, pp. 40–89.

Crook, J., C. Klein, S. Folwell, C. M. Taylor, D. J. Parker, R. Stratton, and T. Stein. 2019. Assessment of the Representation of West African Storm Lifecycles in Convection-Permitting Simulations. *Earth and Space Science*, 2018EA000491.

Danso, D. K., C. M. Patricola, and E. Bercos-Hickey. 2022. Influence of African Easterly Wave Suppression on Atlantic Tropical Cyclone Activity in a Convection-Permitting Model. *Geophysical Research Letters* **49**(22).

Davies, H. C. 1976. A lateral boundary formulation for multi-level prediction models. *Quarterly Journal of the Royal Meteorological Society* **102**(432), pp. 405–418.

Davis, C. A. and T. J. Galarneau. 2009. The Vertical Structure of Mesoscale Convective Vortices. *Journal of the Atmospheric Sciences* **66**(3), pp. 686–704.

DeMaria, M., C. R. Sampson, J. A. Knaff, and K. D. Musgrave. 2014. Is Tropical Cyclone Intensity Guidance Improving? *Bulletin of the American Meteorological Society* **95**(3), pp. 387–398.

Diedhiou, A., S. Janicot, A. Viltard, and P. de Felice. 1998. Evidence of two regimes of easterly waves over West Africa and the tropical Atlantic. *Geophysical Research Letters* **25**(15), pp. 2805–2808.

Diongue, A., J.-P. Lafore, J.-L. Redelsperger, and R. Roca. 2002. Numerical study of a Sahelian synoptic weather system: Initiation and mature stages of convection and its interactions with the large-scale dynamics. *Quarterly Journal of the Royal Meteorological Society* **128**(584), pp. 1899–1927.

Douville, H., K. Raghavan, J. Renwick, R. Allan, P. Arias, M. Barlow, R. Cerezo-Mota, A. Cherchi, T. Gan, J. Gergis, D. Jiang, A. Khan, W. Pokam Mba, D. Rosenfeld, J. Tierney, and O. Zolina. 2021. Water Cycle Changes. *Climate Change 2021: The Physical Science Basis. Contribution of Working Group I to the Sixth Assessment Report of the Intergovernmental Panel on Climate Change*. Ed. by V. Masson-Delmotte, P. Zhai, A. Pirani, S. Connors, C. Péan, S. Berger, N. Caud, Y. Chen, L. Goldfarb, M. Gomis, M. Huang, K. Leitzell, E. Lonnoy, J. Matthews, T. Maycock, T. Waterfield, O. Yelekçi, R. Yu, and B. Zhou. Type: Book Section. Cambridge, United Kingdom and New York, NY, USA: Cambridge University Press, pp. 1055–1210.

Dunning, C. M., E. Black, and R. P. Allan. 2018. Later Wet Seasons with More Intense Rainfall over Africa under Future Climate Change. *Journal of Climate* **31**(23), pp. 9719–9738.

Echendu, A. J. 2022. Flooding in Nigeria and Ghana: opportunities for partnerships in disaster-risk reduction. *Sustainability: Science, Practice and Policy* **18**(1), pp. 1–15.

Elless, T. J. and R. D. Torn. 2019. Investigating the Factors That Contribute to African Easterly Wave Intensity Forecast Uncertainty in the ECMWF Ensemble Prediction System. *Monthly Weather Review* **147**(5), pp. 1679–1698.

Emanuel, K. 2003. Tropical Cyclones. *Annual Review of Earth and Planetary Sciences* **31**(1), pp. 75–104.

Engel, T., A. H. Fink, P. Knippertz, G. Pante, and J. Bliefernicht. 2017. Extreme Precipitation in the West African Cities of Dakar and Ouagadougou: Atmospheric Dynamics and Implications for Flood Risk Assessments. *Journal of Hydrometeorology* **18**(11), pp. 2937–2957.

Enyew, B. D. and A. Mekonnen. 2021. The Interaction between African Easterly Waves and Different Types of Deep Convection and Its Influence on Atlantic Tropical Cyclones. *Atmosphere* **13**(1), p. 5.

Evans, C., M. L. Weisman, and L. F. Bosart. 2014. Development of an Intense, Warm-Core Mesoscale Vortex Associated with the 8 May 2009 "Super Derecho" Convective Event*. *Journal of the Atmospheric Sciences* **71**(3), pp. 1218–1240.

Feng, Z., L. R. Leung, R. A. Houze, S. Hagos, J. Hardin, Q. Yang, B. Han, and J. Fan. 2018. Structure and Evolution of Mesoscale Convective Systems: Sensitivity to Cloud Microphysics in Convection-Permitting Simulations Over the United States. *Journal of Advances in Modeling Earth Systems* **10**(7), pp. 1470–1494.

Feng, Z., L. R. Leung, N. Liu, J. Wang, R. A. Houze, J. Li, J. C. Hardin, D. Chen, and J. Guo. 2021. A Global High-Resolution Mesoscale Convective System Database Using Satellite-Derived Cloud Tops, Surface Precipitation, and Tracking. *Journal of Geophysical Research: Atmospheres* **126**(8).

Ferrett, S., G.-Y. Yang, S. J. Woolnough, J. Methven, K. Hodges, and C. E. Holloway. 2020. Linking extreme precipitation in Southeast Asia to equatorial waves. *Quarterly Journal of the Royal Meteorological Society* **146**(727), pp. 665–684.

Fink, A. H. 2003. Spatiotemporal variability of the relation between African Easterly Waves and West African Squall Lines in 1998 and 1999. *Journal of Geophysical Research* **108**(D11), p. 4332.

Fink, A. H., A. Agustí-Panareda, D. J. Parker, J.-P. Lafore, J.-B. Ngamini, E. Afiesimama, A. Beljaars, O. Bock, M. Christoph, F. Didé, C. Faccani, N. Fourrié, F. Karbou, J. Polcher,

Z. Mumba, M. Nuret, S. Pohle, F. Rabier, A. M. Tompkins, and G. Wilson. 2011. Operational meteorology in West Africa: observational networks, weather analysis and forecasting. *Atmospheric Science Letters* **12**(1), pp. 135–141.

Fink, A. H., T. Engel, V. Ermert, R. van der Linden, M. Schneidewind, R. Redl, E. Afiesimama, W. M. Thiaw, C. Yorke, M. Evans, and S. Janicot. 2017. Mean Climate and Seasonal Cycle. *Meteorology of Tropical West Africa*. Ed. by D. J. Parker and M. Diop-Kane. Chichester, UK: John Wiley & Sons, Ltd, pp. 1–39.

Finney, D. L., J. H. Marsham, L. S. Jackson, E. J. Kendon, D. P. Rowell, P. M. Boorman, R. J. Keane, R. A. Stratton, and C. A. Senior. 2019. Implications of Improved Representation of Convection for the East Africa Water Budget Using a Convection-Permitting Model. *Journal of Climate* **32**(7), pp. 2109–2129.

Fitzpatrick, R. G. J., D. J. Parker, J. H. Marsham, D. P. Rowell, L. S. Jackson, D. Finney, C. Deva, S. Tucker, and R. Stratton. 2020. How a typical West African day in the future-climate compares with current-climate conditions in a convection-permitting and parameterised convection climate model. *Climatic Change* **163**(1), pp. 267–296.

Forster, P., T. Storelvmo, K. Armour, W. Collins, J.-L. Dufresne, D. Frame, D. Lunt, T. Mauritsen, M. Palmer, M. Watanabe, M. Wild, and H. Zhang. 2021. The Earth's Energy Budget, Climate Feedbacks, and Climate Sensitivity. *Climate Change 2021: The Physical Science Basis. Contribution of Working Group I to the Sixth Assessment Report of the Intergovernmental Panel on Climate Change*. Ed. by V. Masson-Delmotte, P. Zhai, A. Pirani, S. Connors, C. Péan, S. Berger, N. Caud, Y. Chen, L. Goldfarb, M. Gomis, M. Huang, K. Leitzell, E. Lonnoy, J. Matthews, T. Maycock, T. Waterfield, O. Yelekçi, R. Yu, and B. Zhou. Type: Book Section. Cambridge, United Kingdom and New York, NY, USA: Cambridge University Press, pp. 923–1054.

Galvin, J. 2016. An introduction to the meteorology and climate of the tropics. Chichester, West Sussex: John Wiley & Sons, Inc.

Geen, R., S. Bordoni, D. S. Battisti, and K. Hui. 2020. Monsoons, ITCZs, and the Concept of the Global Monsoon. *Reviews of Geophysics* **58**(4).

Gustafsson, N., T. Janjić, C. Schraff, D. Leuenberger, M. Weissmann, H. Reich, P. Brousseau, T. Montmerle, E. Wattrelot, A. Bučánek, M. Mile, R. Hamdi, M. Lindskog, J. Barkmeijer, M. Dahlbom, B. Macpherson, S. Ballard, G. Inverarity, J. Carley, C. Alexander, D. Dowell, S. Liu, Y. Ikuta, and T. Fujita. 2018. Survey of data assimilation methods for convective-

scale numerical weather prediction at operational centres. *Quarterly Journal of the Royal Meteorological Society* **144**(713), pp. 1218–1256.

Hakim, G. J. and J. Patoux. 2021. Weather: A Concise Introduction. 2nd ed. Cambridge University Press.

Hamilton, H. L., G. S. Young, J. L. Evans, J. D. Fuentes, and K. M. Núñez Ocasio. 2017. The relationship between the Guinea Highlands and the West African offshore rainfall maximum. *Geophysical Research Letters* **44**(2), pp. 1158–1166.

Hanley, K. E., J. S. R. Pirret, C. L. Bain, A. J. Hartley, H. W. Lean, S. Webster, and B. J. Woodhams. 2021. Assessment of convection-permitting versions of the Unified Model over the Lake Victoria basin region. *Quarterly Journal of the Royal Meteorological Society* **147**(736), pp. 1642–1660.

Hardy, S., J. Schwendike, R. K. Smith, C. J. Short, M. J. Reeder, and C. E. Birch. 2021. Fluctuations in Inner-Core Structure during the Rapid Intensification of Super Typhoon Nepartak (2016). *Monthly Weather Review* **149**(1), pp. 221–243.

Hart, R. E. 2003. A Cyclone Phase Space Derived from Thermal Wind and Thermal Asymmetry. *Monthly Weather Review* **131**(4), pp. 585–616.

Haynes, P. H. and M. E. McIntyre. 1987. On the Evolution of Vorticity and Potential Vorticity in the Presence of Diabatic Heating and Frictional or Other Forces. *Journal of the Atmospheric Sciences* **44**(5), pp. 828–841.

Hersbach, H., B. Bell, P. Berrisford, S. Hirahara, A. Horányi, J. Muñoz-Sabater, J. Nicolas, C. Peubey, R. Radu, D. Schepers, A. Simmons, C. Soci, S. Abdalla, X. Abellan, G. Balsamo, P. Bechtold, G. Biavati, J. Bidlot, M. Bonavita, G. Chiara, P. Dahlgren, D. Dee, M. Diamantakis, R. Dragani, J. Flemming, R. Forbes, M. Fuentes, A. Geer, L. Haimberger, S. Healy, R. J. Hogan, E. Hólm, M. Janisková, S. Keeley, P. Laloyaux, P. Lopez, C. Lupu, G. Radnoti, P. Rosnay, I. Rozum, F. Vamborg, S. Villaume, and J.-N. Thépaut. 2020. The ERA5 global reanalysis. *Quarterly Journal of the Royal Meteorological Society* **146**(730), pp. 1999–2049.

Hill, S. A., Y. Ming, I. M. Held, and M. Zhao. 2017. A Moist Static Energy Budget–Based Analysis of the Sahel Rainfall Response to Uniform Oceanic Warming. *Journal of Climate* **30**(15), pp. 5637–5660.

Holloway, C. E., A. A. Wing, S. Bony, C. Muller, H. Masunaga, T. S. L'Ecuyer, D. D. Turner, and P. Zuidema. 2017. Observing Convective Aggregation. *Surveys in Geophysics* **38**(6), pp. 1199–1236.

Holton, J. R. and G. J. Hakim. 2013a. Mesoscale Circulations. *An Introduction to Dynamic Meteorology*. Elsevier, pp. 377–411.

Holton, J. R. and G. J. Hakim. 2013b. Synoptic-scale motions I: Quasi-Geostrophic analysis. *An Introduction to Dynamic Meteorology*. Elsevier, pp. 377–411.

Holton, J. R. and G. J. Hakim. 2013c. Tropical Dynamics. *An Introduction to Dynamic Meteorology*. Elsevier, pp. 377–411.

Hou, A. Y., R. K. Kakar, S. Neeck, A. A. Azarbarzin, C. D. Kummerow, M. Kojima, R. Oki, K. Nakamura, and T. Iguchi. 2014. The Global Precipitation Measurement Mission. *Bulletin of the American Meteorological Society* **95**(5), pp. 701–722.

Houze, R. A. 2004. Mesoscale convective systems. *Reviews of Geophysics* **42**(4).

Houze, R. A. 2012. Orographic effects on precipitating clouds. *Reviews of Geophysics* **50**(1), RG1001.

Houze, R. A. 2018. 100 Years of Research on Mesoscale Convective Systems. *Meteorological Monographs* **59**, pp. 17.1–17.54.

Hoyer, S. and J. Hamman. 2017. xarray: N-D labeled Arrays and Datasets in Python. *Journal of Open Research Software* **5**(1), p. 10.

Hoyer, S., M. Roos, H. Joseph, J. Magin, D. Cherian, C. Fitzgerald, M. Hauser, K. Fujii, F. Maussion, G. Imperiale, S. Clark, A. Kleeman, T. Nicholas, T. Kluyver, J. Westling, J. Munroe, A. Amici, A. Barghini, A. Banihirwe, R. Bell, Z. Hatfield-Dodds, R. Abernathey, B. Bovy, J. Omotani, K. Mühlbauer, M. K. Roszko, and P. J. Wolfram. 2022. *xarray*.

Hsieh, J.-S. and K. H. Cook. 2005. Generation of African Easterly Wave Disturbances: Relationship to the African Easterly Jet. *Monthly Weather Review* **133**(5), pp. 1311–1327.

Hsieh, J.-S. and K. H. Cook. 2007. A Study of the Energetics of African Easterly Waves Using a Regional Climate Model. *Journal of the Atmospheric Sciences* **64**(2), pp. 421–440.

Hu, G., S. L. Dance, R. N. Bannister, H. G. Chipilski, O. Guillet, B. Macpherson, M. Weissmann, and N. Yussouf. 2023. Progress, challenges, and future steps in data assimilation for convection-permitting numerical weather prediction: Report on the virtual meeting held on 10 and 12 November 2021. *Atmospheric Science Letters* **24**(1).

Hu, H., L. R. Leung, and Z. Feng. 2021. Early warm-season mesoscale convective systems dominate soil moisture–precipitation feedback for summer rainfall in central United States. *Proceedings of the National Academy of Sciences* **118**(43), e2105260118.

Huang, X., C. Hu, X. Huang, Y. Chu, Y.-h. Tseng, G. J. Zhang, and Y. Lin. 2018. A long-term tropical mesoscale convective systems dataset based on a novel objective automatic tracking algorithm. *Climate Dynamics* **51**(7-8), pp. 3145–3159.

Huffman, G., E. Stocker, D. Bolvin, E. Nelkin, and J. Tan. 2019. *GPM IMERG Final Precipitation L3 Half Hourly 0.1 degree x 0.1 degree V06*.

Inness, P. and S. Dorling. 2013. Operational weather forecasting. Advancing Weather and Climate Science. Chichester, UK: Wiley-Blackwell.

Jackson, L. S., J. H. Marsham, D. J. Parker, D. L. Finney, R. G. J. Fitzpatrick, D. P. Rowell, R. A. Stratton, and S. Tucker. 2022. The Effect of Explicit Convection on Climate Change in the West African Monsoon and Central West African Sahel Rainfall. *Journal of Climate* **35**(5), pp. 1537–1557.

Judt, F., D. Klocke, R. Rios-Berrios, B. Vanniere, F. Ziemen, L. Auger, J. Biercamp, C. Bretherton, X. Chen, P. Düben, C. Hohenegger, M. Khairoutdinov, C. Kodama, L. Kornblueh, S.-J. Lin, M. Nakano, P. Neumann, W. Putman, N. Röber, M. Roberts, M. Satoh, R. Shibuya, B. Stevens, P. L. Vidale, N. Wedi, and L. Zhou. 2021. Tropical Cyclones in Global Storm-Resolving Models. *Journal of the Meteorological Society of Japan. Ser. II* **99**(3), pp. 579–602.

Kendon, E. J., A. F. Prein, C. A. Senior, and A. Stirling. 2021. Challenges and outlook for convection-permitting climate modelling. *Philosophical Transactions of the Royal Society A: Mathematical, Physical and Engineering Sciences* **379**(2195), p. 20190547.

Kendon, E. J., R. A. Stratton, S. Tucker, J. H. Marsham, S. Berthou, D. P. Rowell, and C. A. Senior. 2019. Enhanced future changes in wet and dry extremes over Africa at convection-permitting scale. *Nature Communications* **10**(1), p. 1794.

Kiladis, G. N., C. D. Thorncroft, and N. M. J. Hall. 2006. Three-Dimensional Structure and Dynamics of African Easterly Waves. Part I: Observations. *Journal of the Atmospheric Sciences* **63**(9), pp. 2212–2230.

Kiladis, G. N., M. C. Wheeler, P. T. Haertel, K. H. Straub, and P. E. Roundy. 2009. Convectively coupled equatorial waves. *Reviews of Geophysics* **47**(2), RG2003.

Klein, C., L. S. Jackson, D. J. Parker, J. H. Marsham, C. M. Taylor, D. P. Rowell, F. Guichard, T. Vischel, A. M. Famien, and A. Diedhiou. 2021a. Combining CMIP data with a regional convection-permitting model and observations to project extreme rainfall under climate change. *Environmental Research Letters* **16**(10), p. 104023.

Klein, C., F. Nkrumah, C. M. Taylor, and E. A. Adefisan. 2021b. Seasonality and Trends of Drivers of Mesoscale Convective Systems in Southern West Africa. *Journal of Climate* **34**(1), pp. 71–87.

Klein, C. and C. M. Taylor. 2020. Dry soils can intensify mesoscale convective systems. *Proceedings of the National Academy of Sciences* **117**(35), pp. 21132–21137.

Kniveton, D. R., R. Layberry, C. J. R. Williams, and M. Peck. 2009. Trends in the start of the wet season over Africa. *International Journal of Climatology* **29**(9), pp. 1216–1225.

Kuang, Z. 2008. A Moisture-Stratiform Instability for Convectively Coupled Waves. *Journal of the Atmospheric Sciences* **65**(3), pp. 834–854.

Lafore, J.-P. and M. W. Moncrieff. 1989. A Numerical Investigation of the Organization and Interaction of the Convective and Stratiform Regions of Tropical Squall Lines. *Journal of the Atmospheric Sciences* **46**(4), pp. 521–544.

Lavender, S. L. and A. J. Matthews. 2009. Response of the West African Monsoon to the Madden–Julian Oscillation. *Journal of Climate* **22**(15), pp. 4097–4116.

Lean, H. W., P. A. Clark, M. Dixon, N. M. Roberts, A. Fitch, R. Forbes, and C. Halliwell. 2008. Characteristics of High-Resolution Versions of the Met Office Unified Model for Forecasting Convection over the United Kingdom. *Monthly Weather Review* **136**(9), pp. 3408–3424.

Li, T. and P.-c. Hsu. 2018. Fundamentals of Tropical Climate Dynamics. Springer Atmospheric Sciences. Cham: Springer International Publishing.

Liu, C. and M. W. Moncrieff. 2004. Effects of Convectively Generated Gravity Waves and Rotation on the Organization of Convection. *Journal of the Atmospheric Sciences* **61**(17), pp. 2218–2227.

Lock, A. P., A. R. Brown, M. R. Bush, G. M. Martin, and R. N. B. Smith. 2000. A New Boundary Layer Mixing Scheme. Part I: Scheme Description and Single-Column Model Tests. *Monthly Weather Review* **128**(9), pp. 3187–3199.

Mapes, B. E. 2000. Convective Inhibition, Subgrid-Scale Triggering Energy, and Stratiform Instability in a Toy Tropical Wave Model. *Journal of the Atmospheric Sciences* **57**(10), pp. 1515–1535.

Mapes, B. E. and J. Lin. 2005. Doppler Radar Observations of Mesoscale Wind Divergence in Regions of Tropical Convection. *Monthly Weather Review* **133**(7), pp. 1808–1824.

Maranan, M., A. H. Fink, and P. Knippertz. 2018. Rainfall types over southern West Africa: Objective identification, climatology and synoptic environment. *Quarterly Journal of the Royal Meteorological Society* **144**(714), pp. 1628–1648.

Marsham, J. H., N. S. Dixon, L. Garcia-Carreras, G. M. S. Lister, D. J. Parker, P. Knippertz, and C. E. Birch. 2013. The role of moist convection in the West African monsoon system: Insights from continental-scale convection-permitting simulations. *Geophysical Research Letters* **40**(9), pp. 1843–1849.

Matthews, A. J. 2004. Intraseasonal Variability over Tropical Africa during Northern Summer. *Journal of Climate* **17**(12), pp. 2427–2440.

May, R., S. Arms, P. Marsh, E. Bruning, J. Leeman, Z. Bruick, and M. D. Camron. 2016. *MetPy: A Python Package for Meteorological Data*. Language: en.

Mekonnen, A. and W. B. Rossow. 2018. The Interaction between Deep Convection and Easterly Wave Activity over Africa: Convective Transitions and Mechanisms. *Monthly Weather Review* **146**(6), pp. 1945–1961.

Mekonnen, A., C. D. Thorncroft, and A. R. Aiyyer. 2006. Analysis of Convection and Its Association with African Easterly Waves. *Journal of Climate* **19**(20), pp. 5405–5421.

Mendes, O. and M. Fragoso. 2023. Assessment of the Record-Breaking 2020 Rainfall in Guinea-Bissau and Impacts of Associated Floods. *Geosciences* **13**(2), p. 25.

Meyer, B. and J. O. Haerter. 2020. Mechanical Forcing of Convection by Cold Pools: Collisions and Energy Scaling. *Journal of Advances in Modeling Earth Systems* **12**(11).

Miller, J., C. Taylor, F. Guichard, P. Peyrillé, T. Vischel, T. Fowe, G. Panthou, E. Visman, M. Bologo, K. Traore, G. Coulibaly, N. Chapelon, F. Beucher, D. P. Rowell, and D. J. Parker. 2022. High-impact weather and urban flooding in the West African Sahel – A multidisciplinary case study of the 2009 event in Ouagadougou. *Weather and Climate Extremes* **36**, p. 100462.

Mittermaier, M., J. Wilkinson, G. Csima, S. Goodman, and K. Virts. 2022. Convective-scale numerical weather prediction and warnings over Lake Victoria: Part I—Evaluating a lightning diagnostic. *Meteorological Applications* **29**(3).

Moncrieff, M. W. 1992. Organized Convective Systems: Archetypal Dynamical Models, Mass and Momentum Flux Theory, and Parametrization. *Quarterly Journal of the Royal Meteorological Society* **118**(507), pp. 819–850.

Moncrieff, M. W. 2019. Toward a Dynamical Foundation for Organized Convection Parameterization in GCMs. *Geophysical Research Letters* **46**(23), pp. 14103–14108.

Moncrieff, M. W., C. Liu, and P. Bogenschutz. 2017. Simulation, Modeling, and Dynamically Based Parameterization of Organized Tropical Convection for Global Climate Models. *Journal of the Atmospheric Sciences* **74**(5), pp. 1363–1380.

Monerie, P.-A., C. M. Wainwright, M. Sidibe, and A. A. Akinsanola. 2020. Model uncertainties in climate change impacts on Sahel precipitation in ensembles of CMIP5 and CMIP6 simulations. *Climate Dynamics* **55**(5-6), pp. 1385–1401.

Montgomery, M. T. and R. K. Smith. 2017. Recent Developments in the Fluid Dynamics of Tropical Cyclones. *Annual Review of Fluid Mechanics* **49**(1), pp. 541–574.

Moon, S. and K.-J. Ha. 2020. Future changes in monsoon duration and precipitation using CMIP6. *npj Climate and Atmospheric Science* **3**(1), p. 45.

Moore, R. W. and M. T. Montgomery. 2005. Analysis of an Idealized, Three-Dimensional Diabatic Rossby Vortex: A Coherent Structure of the Moist Baroclinic Atmosphere. *Journal of the Atmospheric Sciences* **62**(8), pp. 2703–2725.

Nesbitt, S. W., R. Cifelli, and S. A. Rutledge. 2006. Storm Morphology and Rainfall Characteristics of TRMM Precipitation Features. *Monthly Weather Review* **134**(10), pp. 2702–2721.

Nkiaka, E., A. Taylor, A. J. Dougill, P. Antwi-Agyei, E. A. Adefisan, M. A. Ahiataku, F. Baffour-Ata, N. Fournier, V. S. Indasi, O. Konte, K. A. Lawal, and A. Toure. 2020. Exploring the Need for Developing Impact-Based Forecasting in West Africa. *Frontiers in Climate* **2**, p. 565500.

Nowottnick, E., J. Zawislak, A. Nehrir, W. McCarty, A. Piña, J. Reid, S.-H. Chen, A. Rowe, N. Sakaeda, S. Chen, E. Zipser, Z. Pu, C. Robinson, R. Ferrare, S. Hristova-Veleva, L. Ziemba, L. Thornhill, K. Bedka, M. Kavaya, S. Tanelli, and CPEX-CV/JATAC Team. 2023. *Overview of NASA's Convective Processes Experiment – Cabo Verde (CPEX-CV) in the East Atlantic in September 2022 and Collaboration with the Joint Aeolus Tropical Atlantic Campaign (JATAC)*. Tech. rep.

Oertel, A. and S. Schemm. 2021. Quantifying the circulation induced by convective clouds in kilometer-scale simulations. *Quarterly Journal of the Royal Meteorological Society* **147**(736), pp. 1752–1766.

Osei, M. A., M. Padi, B. Yahaya, M. Baidu, E. Quansah, J. N. A. Aryee, E. I. Yamba, S. Owusu-Ansah, and L. K. Amekudzi. 2023. The dynamics of dry and wet monsoon MCS formation

over West Africa: Case assessment of February 13, 2018 and June 18, 2018. *Quarterly Journal of the Royal Meteorological Society* **149**(750), pp. 133–151.

Pante, G. and P. Knippertz. 2019. Resolving Sahelian thunderstorms improves mid-latitude weather forecasts. *Nature Communications* **10**(1), p. 3487.

Parker, D. J., R. R. Burton, A. Diongue-Niang, R. J. Ellis, M. Felton, C. M. Taylor, C. D. Thorncroft, P. Bessemoulin, and A. M. Tompkins. 2005. The diurnal cycle of the West African monsoon circulation. *Quarterly Journal of the Royal Meteorological Society* **131**(611), pp. 2839–2860.

Parker, D. J., A. Fink, S. Janicot, J.-B. Ngamini, M. Douglas, E. Afiesimama, A. Agusti-Panareda, A. Beljaars, F. Dide, A. Diedhiou, T. Lebel, J. Polcher, J.-L. Redelsperger, C. Thorncroft, and G. A. Wilson. 2008. The Amma Radiosonde Program and its Implications for the Future of Atmospheric Monitoring Over Africa. *Bulletin of the American Meteorological Society* **89**(7), pp. 1015–1028.

Parker, D. J. and A. J. Thorpe. 1995. Conditional Convective Heating in a Baroclinic Atmosphere: A Model of Convective Frontogenesis. *Journal of the Atmospheric Sciences* **52**(10), pp. 1699–1711.

Patricola, C. M., R. Saravanan, and P. Chang. 2018. The Response of Atlantic Tropical Cyclones to Suppression of African Easterly Waves. *Geophysical Research Letters* **45**(1), pp. 471–479.

Pearson, K. J., R. J. Hogan, R. P. Allan, G. M. S. Lister, and C. E. Holloway. 2010. Evaluation of the model representation of the evolution of convective systems using satellite observations of outgoing longwave radiation. *Journal of Geophysical Research* **115**(D20), p. D20206.

Pendergrass, A. G. and D. L. Hartmann. 2014. The Atmospheric Energy Constraint on Global-Mean Precipitation Change. *Journal of Climate* **27**(2), pp. 757–768.

Plant, R. S., G. C. Craig, and S. L. Gray. 2003. On a threefold classification of extratropical cyclogenesis. *Quarterly Journal of the Royal Meteorological Society* **129**(594), pp. 2989–3012.

Prasanth, S., Z. S. Haddad, R. C. Sawaya, O. O. Sy, M. Van Den Heever, T. Narayana Rao, and S. Hristova-Veleva. 2023. Quantifying the Vertical Transport in Convective Storms Using Time Sequences of Radar Reflectivity Observations. *Journal of Geophysical Research: Atmospheres* **128**(10), e2022JD037701.

Prein, A. F., W. Langhans, G. Fosser, A. Ferrone, N. Ban, K. Goergen, M. Keller, M. Tölle, O. Gutjahr, F. Feser, E. Brisson, S. Kollet, J. Schmidli, N. P. M. Lipzig, and R. Leung. 2015. A

review on regional convection-permitting climate modeling: Demonstrations, prospects, and challenges. *Reviews of Geophysics* **53**(2), pp. 323–361.

Provod, M., J. H. Marsham, D. J. Parker, and C. E. Birch. 2016. A Characterization of Cold Pools in the West African Sahel. *Monthly Weather Review* **144**(5), pp. 1923–1934.

Pscheidt, I., F. Senf, R. Heinze, H. Deneke, S. Trömel, and C. Hohenegger. 2019. How organized is deep convection over Germany? *Quarterly Journal of the Royal Meteorological Society* **145**(723), pp. 2366–2384.

Pytharoulis, I. and C. Thorncroft. 1999. The Low-Level Structure of African Easterly Waves in 1995. *Monthly Weather Review* **127**(10), pp. 2266–2280.

Ramsay, H. 2017. The Global Climatology of Tropical Cyclones. *Oxford Research Encyclopedia of Natural Hazard Science*. Oxford University Press.

Rawlins, F., S. P. Ballard, K. J. Bovis, A. M. Clayton, D. Li, G. W. Inverarity, A. C. Lorenc, and T. J. Payne. 2007. The Met Office global four-dimensional variational data assimilation scheme. *Quarterly Journal of the Royal Meteorological Society* **133**(623), pp. 347–362.

Raymond, D., S. Gjorgjievska, S. Sessions, and K. Fuchs. 2014. Tropical cyclogenesis and mid-level vorticity. *Australian Meteorological and Oceanographic Journal* **64**(1), pp. 11–25.

Riehl, H. 1979. Climate and weather in the tropics. London: Academic Press.

Roberts, A. J., J. K. Fletcher, J. Groves, J. H. Marsham, D. J. Parker, A. M. Blyth, E. A. Adefisan, V. O. Ajayi, R. Barrette, E. De Coning, C. Dione, A. Diop, A. K. Foamouhoue, M. Gijben, P. G. Hill, K. A. Lawal, J. Mutemi, M. Padi, T. I. Popoola, P. Rípodas, T. H. Stein, and B. J. Woodhams. 2022. Nowcasting for Africa: advances, potential and value. *Weather* **77**(7), pp. 250–256.

Roca, R., J. Aublanc, P. Chambon, T. Fiolleau, and N. Viltard. 2014. Robust Observational Quantification of the Contribution of Mesoscale Convective Systems to Rainfall in the Tropics. *Journal of Climate* **27**(13), pp. 4952–4958.

Roehrig, R., D. Bouniol, F. Guichard, F. Hourdin, and J.-L. Redelsperger. 2013. The Present and Future of the West African Monsoon: A Process-Oriented Assessment of CMIP5 Simulations along the AMMA Transect. *Journal of Climate* **26**(17), pp. 6471–6505.

Rotunno, R., J. B. Klemp, and M. L. Weisman. 1988. A Theory for Strong, Long-Lived Squall Lines. *Journal of the Atmospheric Sciences* **45**(3), pp. 463–485.

Roux, F. 1988. The West African Squall Line Observed on 23 June 1981 during COPT 81: Kinematics and Thermodynamics of the Convective Region. *Journal of the Atmospheric Sciences* **45**(3), pp. 406–426.

Russell, J. O., A. Aiyyer, J. D. White, and W. Hannah. 2017. Revisiting the connection between African Easterly Waves and Atlantic tropical cyclogenesis. *Geophysical Research Letters* **44**(1), pp. 587–595.

Russell, J. O. H. and A. Aiyyer. 2020. The Potential Vorticity Structure and Dynamics of African Easterly Waves. *Journal of the Atmospheric Sciences* **77**(3), pp. 871–890.

Sathiyamoorthy, V., P. K. Pal, and P. C. Joshi. 2007. Intraseasonal variability of the Tropical Easterly Jet. *Meteorology and Atmospheric Physics* **96**(3-4), pp. 305–316.

Satoh, M., H. Tomita, H. Yashiro, Y. Kajikawa, Y. Miyamoto, T. Yamaura, T. Miyakawa, M. Nakano, C. Kodama, A. T. Noda, T. Nasuno, Y. Yamada, and Y. Fukutomi. 2017. Outcomes and challenges of global high-resolution non-hydrostatic atmospheric simulations using the K computer. *Progress in Earth and Planetary Science* **4**(1), p. 13.

Schielicke, L., C. P. Gatzen, and P. Ludwig. 2019. Vortex Identification across Different Scales. *Atmosphere* **10**(9), p. 518.

Schubert, W. H., P. E. Ciesielski, D. E. Stevens, and H.-C. Kuo. 1991. Potential Vorticity Modeling of the ITCZ and the Hadley Circulation. *Journal of the Atmospheric Sciences* **48**(12), pp. 1493–1509.

Schumacher, C. and R. A. Houze. 2003. Stratiform Rain in the Tropics as Seen by the TRMM Precipitation Radar. *Journal of Climate* **16**(11), pp. 1739–1756.

Schumacher, C., R. A. Houze, and I. Kraucunas. 2004. The Tropical Dynamical Response to Latent Heating Estimates Derived from the TRMM Precipitation Radar. *Journal of the Atmospheric Sciences* **61**(12), pp. 1341–1358.

Schumacher, R. S. and R. H. Johnson. 2008. Mesoscale Processes Contributing to Extreme Rainfall in a Midlatitude Warm-Season Flash Flood. *Monthly Weather Review* **136**(10), pp. 3964–3986.

Schumacher, R. S. and K. L. Rasmussen. 2020. The formation, character and changing nature of mesoscale convective systems. *Nature Reviews Earth & Environment* **1**(6), pp. 300–314.

Schwendike, J. and S. C. Jones. 2010. Convection in an African Easterly Wave over West Africa and the eastern Atlantic: A model case study of *Helene* (2006). *Quarterly Journal of the Royal Meteorological Society* **136**(S1), pp. 364–396.

Semunegus, H., A. Mekonnen, and C. J. Schreck. 2017. Characterization of convective systems and their association with African easterly waves. *International Journal of Climatology* **37**(12), pp. 4486–4492.

Sen Roy, S. and R. C. Balling Jr. 2013. Diurnal patterns in lightning activity in northern tropical Africa. *Physical Geography* **34**(2), pp. 75–84.

Seneviratne, S., X. Zhang, M. Adnan, W. Badi, C. Dereczynski, A. Di Luca, S. Ghosh, I. Iskandar, J. Kossin, S. Lewis, F. Otto, I. Pinto, M. Satoh, S. Vicente-Serrano, M. Wehner, and B. Zhou. 2021. Weather and Climate Extreme Events in a Changing Climate. *Climate Change 2021: The Physical Science Basis. Contribution of Working Group I to the Sixth Assessment Report of the Intergovernmental Panel on Climate Change*. Ed. by V. Masson-Delmotte, P. Zhai, A. Pirani, S. Connors, C. Péan, S. Berger, N. Caud, Y. Chen, L. Goldfarb, M. Gomis, M. Huang, K. Leitzell, E. Lonnoy, J. Matthews, T. Maycock, T. Waterfield, O. Yelekçi, R. Yu, and B. Zhou. Type: Book Section. Cambridge, United Kingdom and New York, NY, USA: Cambridge University Press, pp. 1513–1766.

Senior, N., A. Matthews, B. Webber, B. Latos, and D. Baranowski. 2023. *Extreme precipitation in South Sulawesi triggered by equatorial waves and its representation in MetUM forecasts.* Tech. rep.

Shea, D. J. and W. M. Gray. 1973. The Hurricane's Inner Core Region. I. Symmetric and Asymmetric Structure. *Journal of the Atmospheric Sciences* **30**(8), pp. 1544–1564.

Sherwood, S. C., S. Bony, and J.-L. Dufresne. 2014. Spread in model climate sensitivity traced to atmospheric convective mixing. *Nature* **505**(7481), pp. 37–42.

Short, C. J. and J. Petch. 2022. Reducing the spin-up of a regional NWP system without data assimilation. *Quarterly Journal of the Royal Meteorological Society* **148**(745), pp. 1623–1643.

Simpson, J., J. B. Halverson, B. S. Ferrier, W. A. Petersen, R. H. Simpson, R. Blakeslee, and S. L. Durden. 1998. On the role of "hot towers" in tropical cyclone formation. *Meteorology and Atmospheric Physics* **67**(1-4), pp. 15–35.

Singh, C., J. Daron, A. Bazaz, G. Ziervogel, D. Spear, J. Krishnaswamy, M. Zaroug, and E. Kituyi. 2018. The utility of weather and climate information for adaptation decision-making: current uses and future prospects in Africa and India. *Climate and Development* **10**(5), pp. 389–405.

Skamarock, W. C., M. L. Weisman, and J. B. Klemp. 1994. Three-Dimensional Evolution of Simulated Long-Lived Squall Lines. *Journal of the Atmospheric Sciences* **51**(17), pp. 2563–2584.

Smagorinsky, J. 1963. General Circulation Experiments with the Primitive Equations I: The Basic Experiment. *Monthly Weather Review* **91**(3), pp. 99–164.

Smith, R. N. B. 1990. A scheme for predicting layer clouds and their water content in a general circulation model. *Quarterly Journal of the Royal Meteorological Society* **116**(492), pp. 435–460.

Staniforth, A. and J. Côté. 1991. Semi-Lagrangian Integration Schemes for Atmospheric Models—A Review. *Monthly Weather Review* **119**(9), pp. 2206–2223.

Stein, T. H. M., R. J. Hogan, K. E. Hanley, J. C. Nicol, H. W. Lean, R. S. Plant, P. A. Clark, and C. E. Halliwell. 2014. The Three-Dimensional Morphology of Simulated and Observed Convective Storms over Southern England. *Monthly Weather Review* **142**(9), pp. 3264–3283.

Stevens, B. and S. Bony. 2013. What Are Climate Models Missing? *Science* **340**(6136), pp. 1053–1054.

Stevens, B., M. Satoh, L. Auger, J. Biercamp, C. S. Bretherton, X. Chen, P. Düben, F. Judt, M. Khairoutdinov, D. Klocke, C. Kodama, L. Kornblueh, S.-J. Lin, P. Neumann, W. M. Putman, N. Röber, R. Shibuya, B. Vanniere, P. L. Vidale, N. Wedi, and L. Zhou. 2019. DYAMOND: the DYnamics of the Atmospheric general circulation Modeled On Non-hydrostatic Domains. *Progress in Earth and Planetary Science* **6**(1), p. 61.

Stratton, R. A., C. A. Senior, S. B. Vosper, S. S. Folwell, I. A. Boutle, P. D. Earnshaw, E. Kendon, A. P. Lock, A. Malcolm, J. Manners, C. J. Morcrette, C. Short, A. J. Stirling, C. M. Taylor, S. Tucker, S. Webster, and J. M. Wilkinson. 2018. A Pan-African Convection-Permitting Regional Climate Simulation with the Met Office Unified Model: CP4-Africa. *Journal of Climate* **31**(9), pp. 3485–3508.

Sultan, B. and S. Janicot. 2003. The West African Monsoon Dynamics. Part II: The "Preonset" and "Onset" of the Summer Monsoon. *Journal of Climate* **16**(21), pp. 3407–3427.

Takayabu, I., R. Rasmussen, E. Nakakita, A. Prein, H. Kawase, S.-I. Watanabe, S. A. Adachi, T. Takemi, K. Yamaguchi, Y. Osakada, and Y.-H. Wu. 2022. Convection-Permitting Models for Climate Research. *Bulletin of the American Meteorological Society* **103**(1), E77–E82.

Tang, B. H., J. Fang, A. Bentley, G. Kilroy, M. Nakano, M.-S. Park, V. Rajasree, Z. Wang, A. A. Wing, and L. Wu. 2020. Recent advances in research on tropical cyclogenesis. *Tropical Cyclone Research and Review* **9**(2), pp. 87–105.

Taylor, C. M., C. E. Birch, D. J. Parker, N. Dixon, F. Guichard, G. Nikulin, and G. M. S. Lister. 2013. Modeling soil moisture-precipitation feedback in the Sahel: Importance of spatial scale versus convective parameterization. *Geophysical Research Letters* **40**(23), pp. 6213–6218.

Taylor, C. M., R. A. M. De Jeu, F. Guichard, P. P. Harris, and W. A. Dorigo. 2012. Afternoon rain more likely over drier soils. *Nature* **489**(7416), pp. 423–426.

Taylor, C. M., A. Gounou, F. Guichard, P. P. Harris, R. J. Ellis, F. Couvreux, and M. De Kauwe. 2011. Frequency of Sahelian storm initiation enhanced over mesoscale soil-moisture patterns. *Nature Geoscience* **4**(7), pp. 430–433.

Thorncroft, C. D. and M. Blackburn. 1999. Maintenance of the African easterly jet. *Quarterly Journal of the Royal Meteorological Society* **125**(555), pp. 763–786.

Thorncroft, C. D., D. J. Parker, R. R. Burton, M. Diop, J. H. Ayers, H. Barjat, S. Devereau, A. Diongue, R. Dumelow, D. R. Kindred, N. M. Price, M. Saloum, C. M. Tayor, and A. M. Tompkins. 2003. The JET2000 Project: Aircraft Observations of the African Easterly Jet and African Easterly Waves: Aircraft Observations of the African Easterly Jet and African Easterly Waves. *Bulletin of the American Meteorological Society* **84**(3), pp. 337–352.

Thorncroft, C. and K. Hodges. 2001. African Easterly Wave Variability and Its Relationship to Atlantic Tropical Cyclone Activity. *Journal of Climate* **14**(6), pp. 1166–1179.

Tiedtke, M. 1989. A Comprehensive Mass Flux Scheme for Cumulus Parameterization in Large-Scale Models. *Monthly Weather Review* **117**(8), pp. 1779–1800.

Tomassini, L. 2018. Mesoscale Circulations and Organized Convection in African Easterly Waves. *Journal of the Atmospheric Sciences* **75**(12), pp. 4357–4381.

Tomassini, L. 2020. The Interaction between Moist Convection and the Atmospheric Circulation in the Tropics. *Bulletin of the American Meteorological Society* **101**(8), E1378–E1396.

Tomassini, L., D. J. Parker, A. Stirling, C. Bain, C. Senior, and S. Milton. 2017. The interaction between moist diabatic processes and the atmospheric circulation in African Easterly Wave propagation. *Quarterly Journal of the Royal Meteorological Society* **143**(709), pp. 3207–3227.

Torri, G., Z. Kuang, and Y. Tian. 2015. Mechanisms for convection triggering by cold pools. *Geophysical Research Letters* **42**(6), pp. 1943–1950.

Van Der Walt, S., J. L. Schönberger, J. Nunez-Iglesias, F. Boulogne, J. D. Warner, N. Yager, E. Gouillart, and T. Yu. 2014. scikit-image: image processing in Python. *PeerJ* **2**, e453.

Vellinga, M., M. Roberts, P. L. Vidale, M. S. Mizielinski, M.-E. Demory, R. Schiemann, J. Strachan, and C. Bain. 2016. Sahel decadal rainfall variability and the role of model horizontal resolution. *Geophysical Research Letters* **43**(1), pp. 326–333.

Vogel, P., P. Knippertz, A. H. Fink, A. Schlueter, and T. Gneiting. 2020. Skill of Global Raw and Postprocessed Ensemble Predictions of Rainfall in the Tropics. *Weather and Forecasting* **35**(6), pp. 2367–2385.

Vogel, P., P. Knippertz, T. Gneiting, A. H. Fink, M. Klar, and A. Schlueter. 2021. Statistical Forecasts for the Occurrence of Precipitation Outperform Global Models over Northern Tropical Africa. *Geophysical Research Letters* **48**(3).

Walters, D., A. J. Baran, I. Boutle, M. Brooks, P. Earnshaw, J. Edwards, K. Furtado, P. Hill, A. Lock, J. Manners, C. Morcrette, J. Mulcahy, C. Sanchez, C. Smith, R. Stratton, W. Tennant, L. Tomassini, K. Van Weverberg, S. Vosper, M. Willett, J. Browse, A. Bushell, K. Carslaw, M. Dalvi, R. Essery, N. Gedney, S. Hardiman, B. Johnson, C. Johnson, A. Jones, C. Jones, G. Mann, S. Milton, H. Rumbold, A. Sellar, M. Ujiie, M. Whitall, K. Williams, and M. Zerroukat. 2019. The Met Office Unified Model Global Atmosphere 7.0/7.1 and JULES Global Land 7.0 configurations. *Geoscientific Model Development* **12**(5), pp. 1909–1963.

Walters, D., I. Boutle, M. Brooks, T. Melvin, R. Stratton, S. Vosper, H. Wells, K. Williams, N. Wood, T. Allen, A. Bushell, D. Copsey, P. Earnshaw, J. Edwards, M. Gross, S. Hardiman, C. Harris, J. Heming, N. Klingaman, R. Levine, J. Manners, G. Martin, S. Milton, M. Mittermaier, C. Morcrette, T. Riddick, M. Roberts, C. Sanchez, P. Selwood, A. Stirling, C. Smith, D. Suri, W. Tennant, P. L. Vidale, J. Wilkinson, M. Willett, S. Woolnough, and P. Xavier. 2017. The Met Office Unified Model Global Atmosphere 6.0/6.1 and JULES Global Land 6.0/6.1 configurations. *Geoscientific Model Development* **10**(4), pp. 1487–1520.

Wang, B. and Q. Ding. 2008. Global monsoon: Dominant mode of annual variation in the tropics. *Dynamics of Atmospheres and Oceans* **44**(3-4), pp. 165–183.

Warner, J. L., J. Petch, C. J. Short, and C. Bain. 2023. Assessing the impact of a NWP warm-start system on model spin-up over tropical Africa. *Quarterly Journal of the Royal Meteorological Society* **149**(751), pp. 621–636.

Wheeler, M. C. and H. H. Hendon. 2004. An All-Season Real-Time Multivariate MJO Index: Development of an Index for Monitoring and Prediction. *Monthly Weather Review* **132**(8), pp. 1917–1932.

White, A. A., B. J. Hoskins, I. Roulstone, and A. Staniforth. 2005. Consistent approximate models of the global atmosphere: shallow, deep, hydrostatic, quasi-hydrostatic and non-hydrostatic. *Quarterly Journal of the Royal Meteorological Society* **131**(609), pp. 2081–2107.

Wilson, D. R. and S. P. Ballard. 1999. A microphysically based precipitation scheme for the UK meteorological office unified model. *Quarterly Journal of the Royal Meteorological Society* **125**(557), pp. 1607–1636.

Wilson, D. R., A. C. Bushell, A. M. Kerr-Munslow, J. D. Price, and C. J. Morcrette. 2008. PC2: A prognostic cloud fraction and condensation scheme. I: Scheme description. *Quarterly Journal of the Royal Meteorological Society* **134**(637), pp. 2093–2107.

Wood, N., A. Staniforth, A. White, T. Allen, M. Diamantakis, M. Gross, T. Melvin, C. Smith, S. Vosper, M. Zerroukat, and J. Thuburn. 2014. An inherently mass-conserving semi-implicit semi-Lagrangian discretization of the deep-atmosphere global non-hydrostatic equations. *Quarterly Journal of the Royal Meteorological Society* **140**(682), pp. 1505–1520.

Woodhams, B. J., C. E. Birch, J. H. Marsham, C. L. Bain, N. M. Roberts, and D. F. A. Boyd. 2018. What Is the Added Value of a Convection-Permitting Model for Forecasting Extreme Rainfall over Tropical East Africa? *Monthly Weather Review* **146**(9), pp. 2757–2780.

Wu, M.-L. C., O. Reale, S. D. Schubert, M. J. Suarez, R. D. Koster, and P. J. Pegion. 2009. African Easterly Jet: Structure and Maintenance. *Journal of Climate* **22**(17), pp. 4459–4480.

Zhang, C., Á. F. Adames, B. Khouider, B. Wang, and D. Yang. 2020. Four Theories of the Madden-Julian Oscillation. *Reviews of Geophysics* **58**(3).